Study of SiGe HPT for radio over fiber applications

Marc Rosales

To cite this version:

Marc Rosales. Study of SiGe HPT for radio over fiber applications. Electronics. Université Paris-Est, 2014. English. NNT : 2014PEST1101 . tel-01133525

HAL Id: tel-01133525

https://theses.hal.science/tel-01133525

Submitted on 19 Mar 2015

UNIVESITÉ PARIS-EST
École Doctorale MSTIC
Mathématiques, sciences et Technologies de l'Information et de la Communication

Ph.D. THESIS
to obtain the title of Doctor of Science
Specialty : Electronics, Optronics and Systems

Defended on June 30, 2014
Marc ROSALES

Study of SiGe HPT for Radio over Fiber Applications

Thesis Director: Prof. Catherine ALGANI
Thesis Advisor: Dr. Jean-Luc POLLEUX

Jury:

Reviewers:	Pierre LECOY, Pr.	Université de Cergy Pontoise
	Laurent VIVIEN, Dr. HDR	Université Paris 11
Advisors:	Catherine ALGANI, Pr.	ESYCOM Le CNAM
	Jean-Luc POLLEUX, Dr.	ESYCOM ESIEE
Examiners	Georges ALQUIÉ ,Pr.	Université Paris 6
	Tarik BOUROUINA,Pr.	ESYCOM ESIEE

Acknowledgments

This dissertation would not have been possible without the guidance and the help of several individuals who have contributed and extended their valuable assistance in the completion of this study.

I would like to express my deepest gratitude to my thesis supervisors. First and foremost to Dr. Jean-Luc Polleux for accepting me to be a part of the laboratory and providing knowledge and guidance for the whole duration of my studies as well as in the writing papers and preparations for presentations for conferences, project meetings up to the final review of my PhD manuscript. Prof. Catherine Algani, for welcoming me in the ESYCOM –Photonics group and her guidance. Most specially in the final stages of my research.

I would like to thank the people of the ORIGIN project for giving me the opportunity to work in research project that helped widen my perspective in terms of doing collaborative research work.

I would also like to thank Prof. Pierre LECOY, and Dr. Laurent VIVIEN for accepting to be the reviewers of my work and having the time to review my PhD dissertation. My sincere thanks also goes to Prof. Georges ALQUIÉ , Prof. Tarik BOUROUINA for accepting to be part of the jury for my defense.

I would like to acknowledge the ESYCOM microwave photonics team, Julien Schiellein Carlos Viana for whom we shared lots of time in discussing and solving technical and scientific problems. This core group helped a lot in the generation of research data and co-authored publications

I thank my fellow labmates at ESIEE-ESYSCOM for sharing their time and giving the another dimension in my PhD studies through their camaraderie and friendship.

My studies in a foreign country could not have been possible without the support Electrical and Electronics Engineering Institute of the University of the Philippines Diliman to help me advance my academic and scientific career. I am very thankful for the ERDT program of DOST by providing the necessary funding to support my doctoral studies.

Finally, and most importantly, I would like to thank my wife, Thet. Her unending support, encouragement and love have kept me going through this stage in our lives. My son Gabriel, who gave me joy of being a parent and being an inspiration to persevere more in my studies.

Table of Contents

List of Figures

List of Tables

1 State of The Art

1.1 Introduction

High-speed wireless data connection for indoor and short-range communications provides data transfers at very high rate between electronic devices up to 1Gbit/s for WiMedia wireless standard [1] and 7Gbit/s for WiGig wireless standard [2]. This allows for the use of wireless connection instead of relying on cables for high-speed interface. One goal is in the use of this wireless connection to transfer uncompressed high definition video signals between a high definition (HD) media player and a HD TV set where high-speed interfaces and cables such as HDMI cables are needed to support the required data rates.

Several high-speed wireless interfaces have been studied and proposed to address very high-speed short-range wireless connections. One of the studies is focused on Ultra-

Wideband technology (UWB) using Multiband Orthogonal Frequency Division Multiplexing (MB-OFDM). In this radio interface, UWB signals are defined to have a bandwidth of at least 500 MHz or more than 20% of the center frequency. This is one of the basis for IEEE 802.15.3a [3] standard for wireless broadband communications where a high communication speed from 110 Mbps up to 480 Mbps is proposed. The coverage distances are limited due to the low power emission standards required for UWB radios (FCC Mask Rules), 3.1-10.6 GHz and very low Effective Isotropic Radiated Power (EIRP). The coverage distance of 110 Mbps bit rate is about 10 meters and even shorter for the higher data rates.

Another approach is the use of higher carrier frequencies such as 60 GHz. At this frequency, the devices are mostly connected via line of sight wireless communication and the range is at most 10 meters. In this range two wireless standards and protocols that are developed. WirelessHD, which operates at 60 GHz, and is designed to be used as video transport method. This standard can achieve data rates in the range of 10-28 Gbit/s range [4]. This allows for the simultaneous transmission of uncompressed HD video and multi-channel audio and data.

In 2012, IEEE adopted the WiGig to be used in the IEEE 802.11.ad standard. The IEEE 802.11.ad standard is a Wi-Fi compatible system that uses 2.4, 5 and 60 GHz bands. In the 60GHz band, the channel is divided into four 2.16 GHz wide channels. It supports data rates of up to 7 Gbits/s and a single channel version for low power operation that can deliver a speed of up to 4.6 Gbit/s [5]. At these data rates, the following can be performed.

- Transfer 1000 photos between laptop computers in 5 seconds (versus ~1.5 minutes with IEEE 802.11n)
- Download a single 1080p movie to a tablet in 3 minutes (versus ~1 hour with IEEE 802.11n)
- Upload a 2-minute HD clip from a camcorder in 3 seconds (versus ~1 minute with IEEE 802.11n)

The 3-10 meter line of sight operating range of these wireless systems; UWB (FCC standard), Wireless HD, 60 GHz band of the IEEE 802.11ad can be increased with the use of Radio over Fiber technologies. There have been several demonstrations in the transmission of UWB signals over fiber [6]-[9]

In this chapter, the different applications and implementations of the Radio over Fiber (RoF) technology will be discussed. It will be followed by the introduction of the ORIGIN project. This project is a French nationally funded project (Fonds Unique Interministériel -FUI). Wherein, several groups from the academe and industry work towards an Optical Radio Infrastructure for Gigabit Indoor Network (ORIGIN) project. This project covers a wide range of research activities in the development of a RoF infrastructure for 60GHz radio systems such as the ECMA 387, WirelessHD and the 60GHz band of the 802.11ad. One particular research aspect of this project is focused on low cost photonic components such as optical sources and photodetectors that could be used in the implementation of RoF systems. Finally, the last section of this chapter will focus on photodetectors that are used for RoF systems and that will be reviewed and analyzed.

1.2 Radio over Fiber Systems and applications

Radio over Fiber technologies – its architectures and its main applications, are analyzed in this section. Using multimode fibers for RoF application will be discussed in detail. In recent years, RoF has proven to be an effective solution to provide high-speed data transfers. This is attributed to the optical fiber's inherently large bandwidth characteristics. The combination of wireless distribution into a fiber infrastructure offers a possibility of a long reach, high data rate wireless mobile communication systems. It is used to increase wireless access coverage, network capacity and mobility and to minimize the cost of an access network.

RoF is a technology where complex electrical signals (i.e. wireless services: GSM, UMTS, Wi-Fi, Internet, and Satellite) are modulated into an optical carrier for transport and distribution over a fiber link or network, and eventually to a wireless emitter. RoF techniques are used in military applications such as antenna remoting and in radar installations. RoF based systems are also used in large commercial environments such as airports [10] [11] stadiums, hotels and shopping malls [12], [13] to provide wireless coverage. Currently, there are studies on RoF technologies in home area networks (HAN) [8] [14], [15]

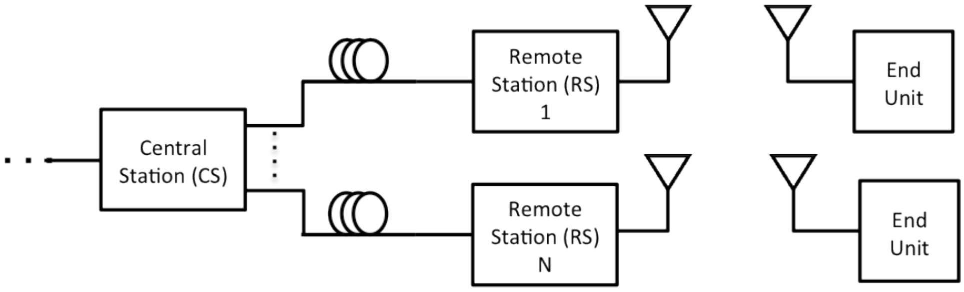

Figure 1.1 Basic Radio over Fiber configuration

The general RoF system implementation is shown in Figure 1.1 [16]. A central station (CS) is connected to one or more remote stations (RS) via two optical fibers for duplex operation. The RSs have wireless connections to end units (EU). Depending on the RoF system application, the EUs could be space satellites, tower antennas or personal wireless devices. The CS connects the RS and it could be connected to an external network. A simplest RoF implementation could be composed of a CS, one RS and one EU. In a RoF network, the radio signal that is transported in the optical fiber is near its final format for wireless transmissions. This means, that the radio signal is already modulated and carrying information following the different format used for different wireless services and applications. The radio signal could be transported from a CS to a RS and finally to an end unit. The RS receives and converts the modulated optical signal to RF and performs wireless transmission via an antenna. All the modulation and complex processing are done in the CS. The CS and RS configuration analogy could be extended to the different wireless applications and services.

An early application of RoF concept in a mobile communication application is described in Figure 1.2 [17]. It was implemented by using one channel of a second-generation cordless telephone standard (CT2) to modulate the intensity of a 1330nm multi-longitudinal mode laser. A 0.5 km single mode fiber served as the fiber link and the RoF signal was detected using a PIN photodiode (PIN PD) and amplifier combination. The CT2 telephony system uses a frequency division multiple access (FDMA) time division duplex (TDD) scheme to provide up to 40 telephony channels of 40 frequencies. Each channel is 100 kHz wide and is located in the frequency band of 864-868MHz.

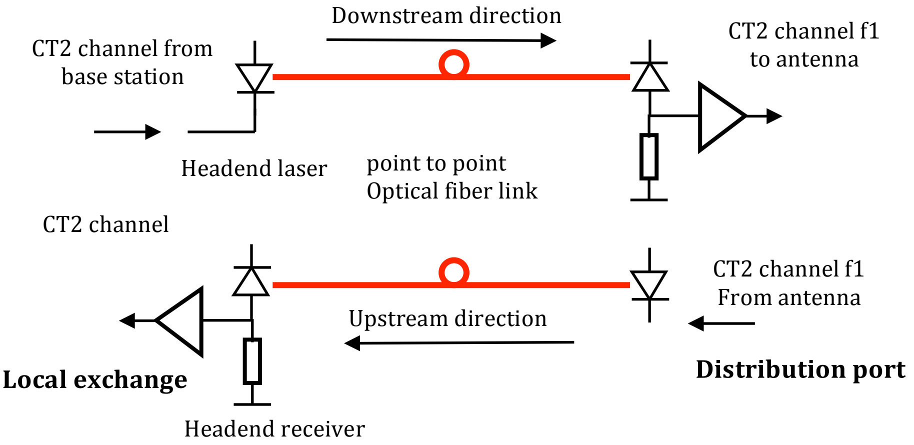

Figure 1.2 Implementation of a RoF Link a single channel cordless telephone access optical system [17].

1.2.1 Intensity Modulated Radio over Fiber

In intensity modulation RoF links, the complex electrical signal is used to modulate the intensity of the optical carrier. There are several methods to implement this, and they are categorized as either direct or external modulation methods. The optical links will be characterized in terms of different Radio Frequency figures of merit such as gain, noise figure and Spurious-free dynamic range (SFDR). Wireless communications standards impose different minimum SFDR requirements that should be considered in the design of RoF links.

An intensity-modulation direct detection (IM-DD) analog optical link is defined in Figure 1.3. The wireless signal centered at ω_{RF} will modulate the intensity of the optical source with a center frequency of ω_{OPT}, which is the frequency associated with the optical wavelength. This will result in mixing of the two frequencies, thus resulting to an optical signal centered at ω_{OPT} with two sidebands centered at the frequency of $\omega_{OPT} \pm \omega_{RF}$. The photodetector performs the detection and demodulation of the RoF signal - resulting in the extraction of the electrical signal that is centered at ω_{RF}

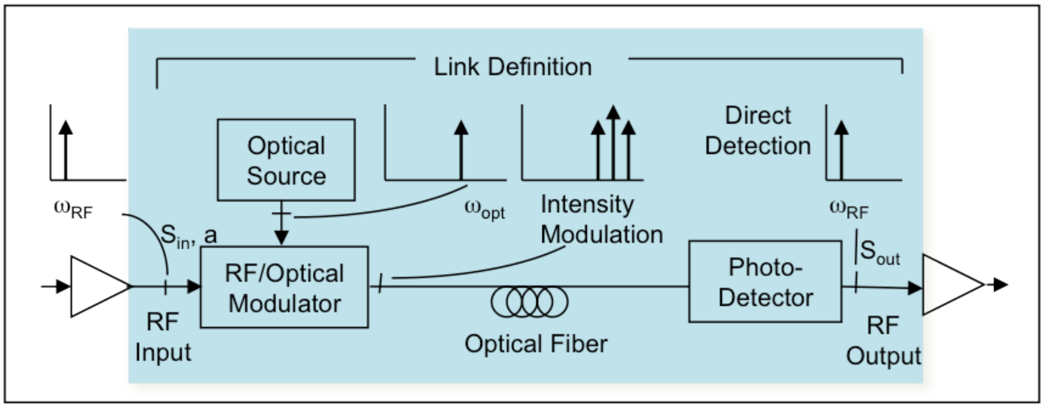

Figure 1.3 An intensity-modulated direct detection (IM-DD) analog optical link [18]

1.2.1.1 Direct Modulation

A direct-modulation link is implemented using a semiconductor laser to directly add a small signal modulation around a bias point set by a DC current of the laser, corresponding to a small signal modulation of the intensity of the photons emitted by the laser. A single device serves as both the optical source and the RF/Optical modulator. Referring to Figure 1.3, the laser is both the optical source and the RF/Optical modulator too. Direct modulation of a laser means adding a time varying current, which results in output optical intensity tracking the changes in the current.

Direct modulation of up to about 30 GHz is possible [19]. However, one of the disadvantages of this scheme is chirp, i.e., the optical frequency is inadvertently modulated. Operating the laser in continuous mode and modulating it externally could avoid the chirp in directly modulated RoF links. There is also the oscillation frequency of the laser limiting the upper value of the RF modulated frequency. Other disadvantages can occur with low-level signals such as RIN and non-linearity at the high level signal including distortions on the transmitted data.

1.2.1.2 External Modulation

In an external modulation link, different devices are needed to act as the optical source and RF/Optical modulator. The optical source could be a semiconductor laser designed for high power output or a solid-state laser. Solid-state lasers exhibit better noise characteristics compared to semiconductor lasers. However, they are much larger and typically more expensive. The chirp, caused by very high frequency direct modulation of laser is eliminated if the laser operates in continuous mode, The external modulators provide the intensity modulated optical output. These external modulators are typically voltage driven devices and have modulation bandwidths beyond 100 GHz for polymer based devices [20]. Using external modulators could also provide phase and frequency modulations. However, detection of phase and frequency modulation requires coherent photo-receivers using local oscillator lasers. Coherent detection offers improved sensitivity. It is more complex to implement than direct modulation.

A commonly used external modulator in RoF Links is the Mach-Zender Interferometric (MZI) modulator. Lithium Niodabate is one of the common materials used for MZI modulators. It offers low optical loss and a sufficiently strong electro optic tensor. An alternative to the MZI modulator is the electro-absorption (EA) modulator. An applied electric field affects the output intensity by shifting the optical absorption band edge in a semiconductor via either the Franz-Keldysh effect or the quantum confined Stark effect. Using these two effects, it is possible to fabricate an EA modulator with a transfer function yielding a better linearity than that of a standard MZI modulator [21]. The interest in EA Modulators is its potential for low cost integration with semiconductor laser source [22] . Externally modulated lasers (EML) products are currently available commercially [23].

The different RoF links are categorized depending on the center frequency of the modulating wireless signal are shown next.

1.2.1.3 Radio Frequency (RF) over Fiber

Radio Frequency over fiber could be considered as the simplest scheme for transporting radio signals over an optical fiber link or network. It involves the direct transport of the radio signals at its designated carrier frequency. This radio signal at its carrier frequency is used to modulate an optical source.

The modulated optical signal is the detected one at the remote station by a high-speed photodetector. The RS does not require any frequency translation. This offers the advantage of implementing simple RS and additional benefits of centralized control, independence for air-interface and the possibility of multi- wireless band operation. However, this scheme requires high-speed modulation techniques that need optoelectronic components with good analog performance over the bandwidth and frequency band of the radio signal being transported. It also requires high-speed photodetection schemes, which convert the modulated optical signals back to the original radio signals.

An implementation of the RF-over-Fiber scheme is shown in Figure 1.4. For single mode fibers, the carrier frequency will be limited by the chromatic dispersion and the O/E and E/O bandwidths. The chromatic dispersion depends both upon the length of the fiber and the RF carrier, for short distances it could be neglected at low RF.

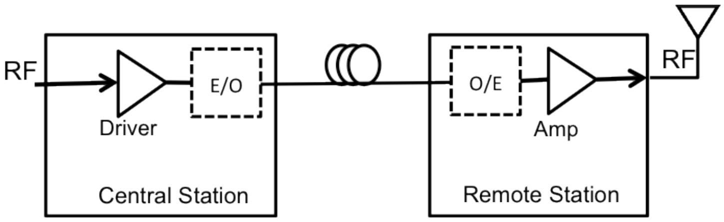

Figure 1.4 RF-over –Fiber representation (one way)

1.2.1.4 Intermediate Frequency over Fiber

In this scheme, an intermediate frequency (IF) of the RF signal is generated or initially available in the central station CS. It is then transmitted to the fiber link, In the RS side, the detected signal of the photodetector is frequency translated to the RF using a mixer and a local oscillator.

An implementation of the IF over fiber is shown in Figure 1.5. In an IF over fiber scheme, the frequency limitations of the components used in the RoF link are taken cared off. The requirements on the optoelectronic devices are relaxed. Lower speed and lower cost optoelectronics devices could be used in the fiber optic link. As mentioned earlier, the presence of the high frequency mixer and stable local oscillator (LO) in the remote unit side presents an increase of complexity in the RS side. This scheme also presents some possible limitations on its upgradability of reconfigurability as may be dictated by future revisions in the wireless network.

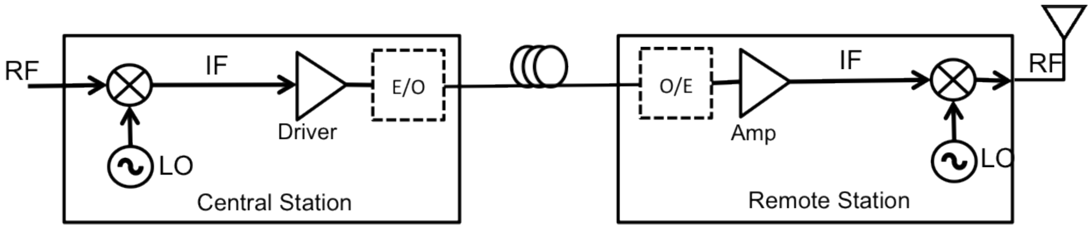

Figure 1.5 IF over Fiber (one way)

Low cost multimode fiber (MMF) can be used for the transmission of optical signals in IF over Fiber scheme. Several commercial RoF products are based on the distribution of radio signals over MMF since many buildings have legacy optical fiber infrastructure networks based on MMFs. [24]

1.2.1.5 Baseband over Fiber

The third scheme transports the wireless signal as a baseband (BB) signal over the fiber link or network. The received optical signal is detected and then upconverted to the required radio frequency in the RS. This scheme has the advantage of using mature digital and electronic circuitry for signal processing at the RS. Low-speed optoelectronic devices are used within the RS. Like IF over Fiber, the effects of fiber chromatic dispersion are also greatly reduced. However, the need for frequency conversion at the remote station complicates its architecture design as the air interface frequency increases. The additional LO source and extensive signal processing hardware in the antenna BS may also limit the upgradeability of the overall fiber radio system. Using the BB over fiber scheme, the BB spectrum cannot be allocated to the application on the RoF Link. Remote delivery of the LO signal from the central office can also be implemented in this scheme. Figure 1.6 shows a schematic representation of a baseband over fiber implementation of a RoF link.

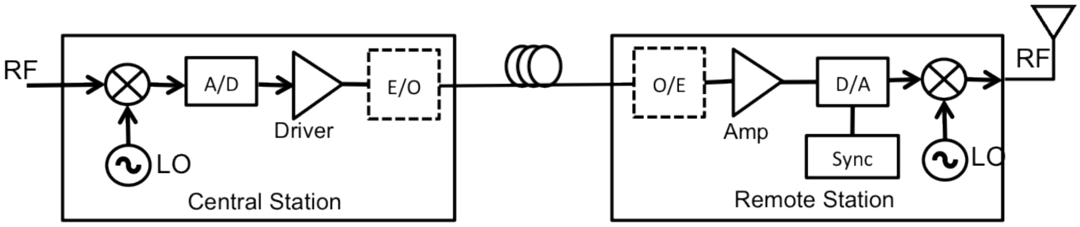

Figure 1.6 Baseband over Fiber (BB-RoF)

1.2.2 Radio over Single Mode Fiber

Most implementations of RoF applications utilize single mode optical fiber (SMF) this allows for long span RoF links. This is important in remote antennas for satellite communications and RoF repeater based systems for outdoor environments. One limitation of SMF is the chromatic dispersion. Figure 1.7(a) shows the RF losses in an intensity modulated RoF link with a 80 km fiber length [25]. It suffers from destructive interferences of the sidebands, which will lead to null at certain RF carrier frequencies. Figure 1.7(b) shows the topographical map showing the optical losses due to the chromatic dispersion as a function of the fiber length and carrier frequency. A carrier frequency of 10 GHz with a fiber length of maximum 10 km will have a 0dB chromatic dispersion loss. However, for a carrier Frequency of 60 GHz, it will have a 20dB optical loss at around 800 meters. Fiber links with 60 GHz RF carriers should be at the maximum 800 meters while employing very high bandwidth electro-optical (EO) and optoelectronic (OE) components.

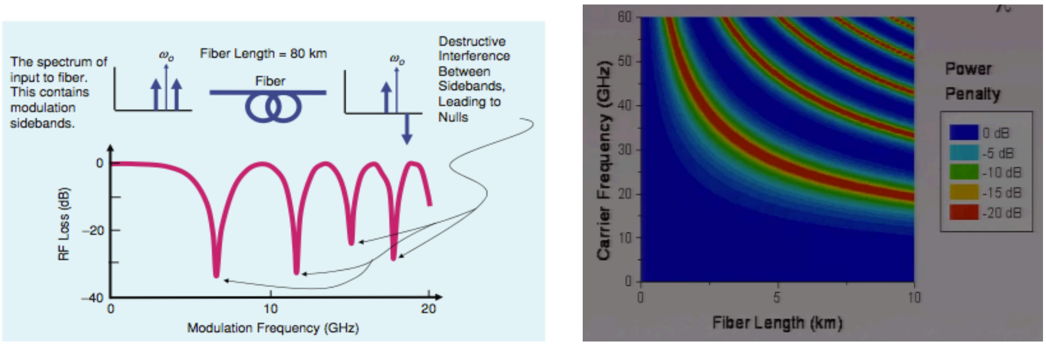

a) b)

Figure 1.7 (a) Effects of chromatic dispersions on the loss of optical fiber as a function of modulating frequency.[25]. (b). Topographical map showing the effect after optical losses due to chromatic dispersion

1.2.3 Radio over Multimode Fiber

A multimode fiber (MMF) is designed to allow numerous modes of light to be transmitted simultaneously as opposed to SMF, which is designed to carry one propagation mode of light. Physically, the main difference of the two types of fibers is the diameter of the core of the fiber. A typical SMF will have a core of 5µm or 9µm and a cladding of 125µm. A typical MMF will have a 62.5µm core and a cladding of 125µm. Having a larger core size simplifies the connections allowing the use of lower cost optoelectronic components such as light emitting diodes (LEDs) to be used as optical sources. However, modal dispersion limits the performance on a MMF compared to a SMF. A MMF has higher pulse spreading rates than a SMF. This limits the MMF's information transmission capacity. SMF are therefore better at retaining the fidelity of each light pulse over longer distances than MMF. With this property, most of optical fibers for very long distances use SMF. MMF is mostly used for communication over short distances, such as within a building or on a campus. It supports links with data rates of 10 Mbit/s to 10 Gbit/s over link lengths of up to 600 meters (300 m for 10 Gbit/s). This is sufficient for the majority of in building applications. MMF generally is used for backbone applications in buildings. The modal characteristic of the MMF limits the system bandwidth and RF carrier frequency that can be used in a RoF link. Figure 1.8 shows a summary of the different optical fibers that are installed in a building. It highlights that in premises MMF dominates over SMF for link lengths up to 300m [26].This trend continues even for new installations due to the improvements in MMF manufacturing to enable the requirements of higher speed Ethernet systems.

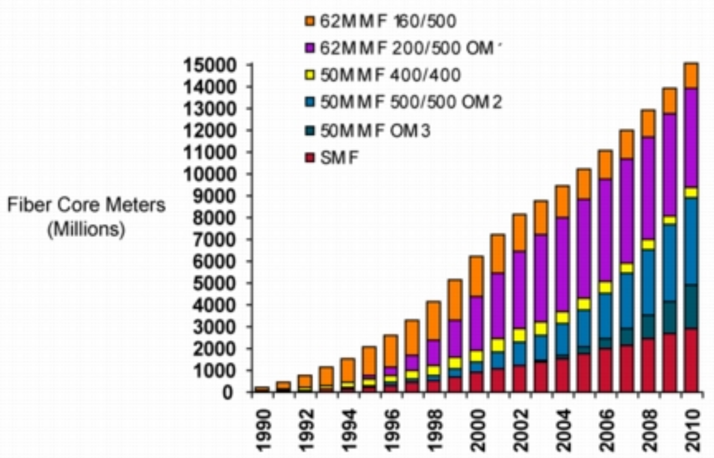

Figure 1.8 In premises optical fiber install base analysis to 2007 [26]

The different optical fibers using ISO classifications of a Corning branded MMF fibers is shown in Table 1.1. These classifications are used for Ethernet based systems. It summarizes the different bandwidths of different MMF fiber categories at 850m and 1310nm. This shows that an optical multi-mode 2 (OM2) fiber and using 850nm wavelength will have an attenuation of 2.3dB/km and its bandwidth is 500MHz·km under overfill launch conditions (OFL) and enhanced modal bandwidth (EMB) of 510 MHz·km. If a link is 500 meters of OM2 MMF it will have a 3 dB bandwidth of 1.0 GHz

Table 1.1 Summary of Glass multimode fiber properties

ISO	Core/Cladding Diameter (µm)	850nm (dB/km)	1300nm (dB/km)	OFL 850nm (MHz·km)	OFL 1300nm (MHz·km)	EMB 850nm (MHz·km)
OM1	62.5/125	2.9	0.6	200	500	385
OM1	62.5/125	2.9	0.6	200	500	220
OM2	50/125	2.3	0.6	500	500	510
OM3	50/125	2.3	0.6	1500	500	2000
OM4	50/125	2.3	0.6	1500	500	4700

The 3dB modal band of the MMF limits its use for short fiber links. There are techniques like offset launch and restricted mode excitations, used to overcome the limit of the modal bandwidth of the MMF. This requires precision in the coupling of the light source to the MMF. In situations where the optical source, i.e. VCSEL, is coupled to the MMF fiber or it is a commercial off the shelf (COTS) Receiver Optical Sub-Assembly (ROSA) where the launching conditions could not be controlled.

Subcarrier multiplexing of wired LAN data signals with VCSELs is another solution that offers viable data transmission at carrier frequencies that is 20 times above the 3dB modal bandwidth of the MMF[27]. This is possible due to the high frequency components of the impulse response of a MMF.

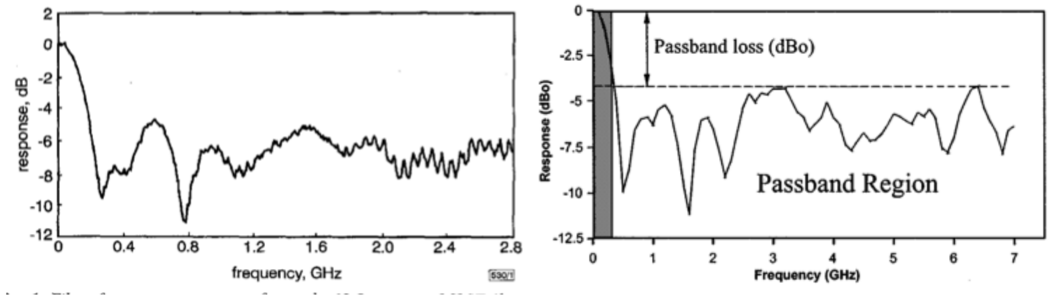

a) b)

Figure 1.9 Frequency response of: a) 1km-length 62.um core MMF [27] b)500m 62.5um core MMF at 850nm [28]

Figure 1.9(a) shows the frequency response of a 1km-length 62.5μm core fiber. This measurement used a research grade vertical cavity surface emitting laser (VCSEL) is used as a source. The low frequency response gives a 3dB bandwidth of 180MHz·km. However, at higher frequencies, there is a relatively flat response with a level -7dB below the low frequency region. This area is a suitable band for communications. Figure 1.9(b) is a similar plot, but shows a response of a 500m length of MMF fiber. The subcarrier modulation (SCM) is somewhat similar to a RoF signal with a carrier in the low GHz range.

Another demonstration shows how MMF could be used for RoF Distributed antenna Systems (DAS) applications [29]. They showed that a 2GHz carrier signals which carry complex modulation scheme (32 QAM) of 10 Mbps could be transmitted over a 2km OM2 fiber (500MHzkm) using a 1310nm distributed feedback (DFB) laser with a low degradation in the received constellation diagram and an error vector magnitude (EVM) in the range of 3-5%. Figure 1.10 shows comparison of the constellation and eye diagram for a coaxial cable and a radio over link using an MMF fiber.

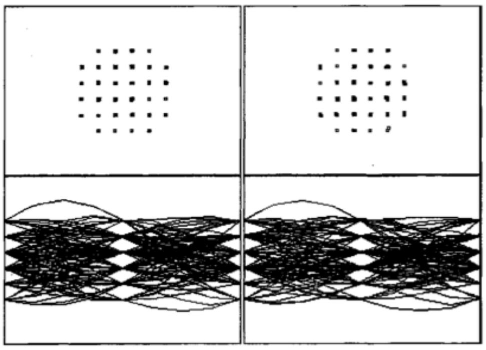

a) b)

Figure 1.10 Constellation and eye diagrams for a 32-QAM showing a) coaxial cable b) 1km MMF transmission [29].

Studies in optical links using a butt coupled VCSEL to a 300m-length and 50µm-core MMF (2000MHz·km) and a commercial PD with 0.4 A/W responsivity followed by 1000Ω transimpedance amplifier (TIA) and wideband amplifiers showed that spurious free dynamic range of SFDR of 97dbHz$^{2/3}$ was achieved. This demonstrates that MMF, already installed in most buildings used as short indoor RoF links have performance comparable to short SMF links without the need for new SMF installations. MMF operation in the low gigahertz ranges allows for the implementation of a RF intensity modulated-direct detection (RF IM-DD) RoF based systems using lower cost optoelectronic components. RF IM-DD results in the lower overall system cost and reduced link complexity because the need to make an IF IM-DD fitting the bandwidth of the MMF is removed.

Several aspects of the MMF RoF systems were studied to verify its performance with respect to the ones required by different wireless standards. Some research focused on its performance, depending upon the optical sources: DFB sources [30] [31], as compared to VCSELs [32], [33] [34], [35]. However as VCSELs continue to improve their performances and lower their costs, more RoF over MMF are studied using VCSELS.

The performances of the RoF MMF over different samples and different lengths of multimode fiber are of particular interest in several studies. [36], [35] [37] [38]. They focused on low and high modal bandwidth MMF and lengths of 100, 300, 500 and 600 meters. The performance of different wireless standards that will use RoF over MMF as a transport medium should be studied. Different standards such as Cellular systems AMPS and GSM [35] [39] WCDMA UMTS [34] [39]wireless LAN 2.4GHz[33] , [30] ,[35],[40] [39] and 5 GHz[33],[30],[37]. UWB impulse [41] [40]and MB-OFDM UWB[42]. were studied as individual standards transporter over the MMF RoF link. and also as a combination of different standards when they are co-distributed. They verified different figures of merit such as link gain[32], SFDR[32], [36], EVM [33] , [35], [39] throughput, and signal to noise ratio[30]

MMF fiber with enhanced modal bandwidth (EMB) greater than 1400 MHz·km is used with less signal degradation for WLAN 2.4GHz and 5GHz RoF remote antenna feeding for fiber length from 300-500 meters [37],[33] [35]. Figure 1.11 shows the results of bandwidth measurements of a VNA and VSCEL with different samples of 62.5µm and 50µm core MMF fiber with a length of 300 meters. It shows that the 50µm fibers have a bandwidth that is >4.5GHz for the 300m lengths that are used in the measurement. The measured EVM of different IEEE 802.11(x) signals over MMF shows that at 1Km an EVM of 10-12% could be achieved [33] [38]

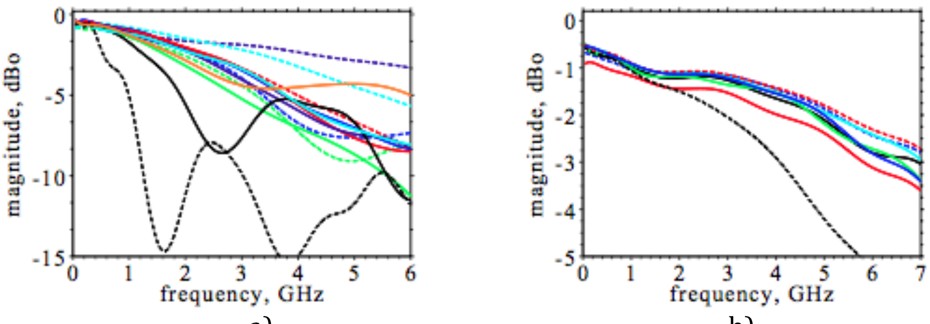

a) b)

Figure 1.11 Bandwidth measurements of different fibers with the VCSEL used for WLAN transmission a) 62.5um fibers, b) 50um fibers [37]

Several research groups demonstrated actual RF signal propagation over MMF fiber. Transmission experiments on uncooled DFB lasers on the RoF MMF transmission of

802.11a/b signals results with low penalty at 70°C [30]. A video transmission link of 1Mb/s on 1km-long worst case MMF fiber was used. The co-distribution of different standards WLAN and impulse UWB along cable television (CATV) based RF signals for in building distribution over 500m MMF achieved acceptable SNR and EVM for successful transmission of the different signals[40], [43]. A set of distributed antennas from a single access point showed the improved coverage and reduction of the total emission power [44]. A throughput of 20Mb/s was demonstrated for this setup. A pico-cellular WLAN using radio over MMF was demonstrated [45].It is composed of 14 picocells with cells of 4m radius. At the 2.4GHz bandwidth, each picocell is associated with a different access point. RF ID and Zigbee was also inserted in the system and with the fiber fed WLAN still provided 20Mb/s throughput and hand-off between picocells was implemented. Figure 1.12 shows the schematic of the system architecture.

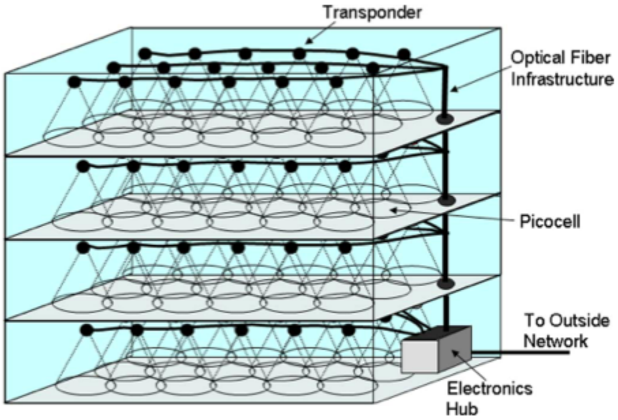

Figure 1.12 General schematic of the pico-cellular WLAN using radio over MMF [45]

Another application of Radio over MMF is the distribution of ultrawideband (UWB) radio signals. This is of particular interest because UWB signals offer over short range of distance, high data rates at the expense of occupying a large bandwidth. Impulse UWB modulated on VCSELs and MMF was demonstrated in [41], [46] using a commercial product Wisair® to generate the multiband orthogonal frequency division multiplexing MB-OFDM signal through a MMF RoF system. Data rates of 480 Mbps are achieved over 400 metes in length [42].

The possibility of transmitting MB-OFDM UWB signal with a data rate of 1.92 Gbits/s over a 500m OM2 MMF at 850 nm was demonstrated in [47]. A BER of 10^{-8} in the (3.1-4.7) GHz range and 10^{-6} in the (6-7.6) GHz range was achieved with a use of transmitter optical sub-assembly (TOSA)/ receiver optical sub-assembly (ROSA) components in a point to point topology. A multipoint topology was also demonstrated for the distribution of UWB MB-OFDM signal over MMF with low cost devices [8].

1.3 ORIGIN PROJECT

The Optical-Radio Infrastructure for Gibabits/s Indoor Networks (ORIGIN) is a collaborative project funded by DGCIS (Direction Générale de la Compétitivité, de l'Industrie et des Services), a unit of the French minister of the Economy, Industry and Employment). It is in collaboration with the industry: Orange Labs / France Télécom ACOME, Niji and SIRADEL – and academic institutions - ESYCOM , Télécom Bretagne, and IREENA (joined IETR in 2012).This project aims to improve indoor very high data rate radio coverage using RoF. The goal is to produce a prototype of a Home Area

Network using a RoF architecture composed of RoF transducers, domestic cabling and a central node.

The expected results of the project are the following:

- Analysis of the market and its players,
- Identification of service scenarios,
- System specifications,
- RoF transducers prototyping,
- Performances measurement and validation,
- Simulation of the complete system to write engineering rules,
- Pre-industrial demonstration platform,
- Business plan.

The project is divided into seven Sub Projects as illustrated in Figure 1.13

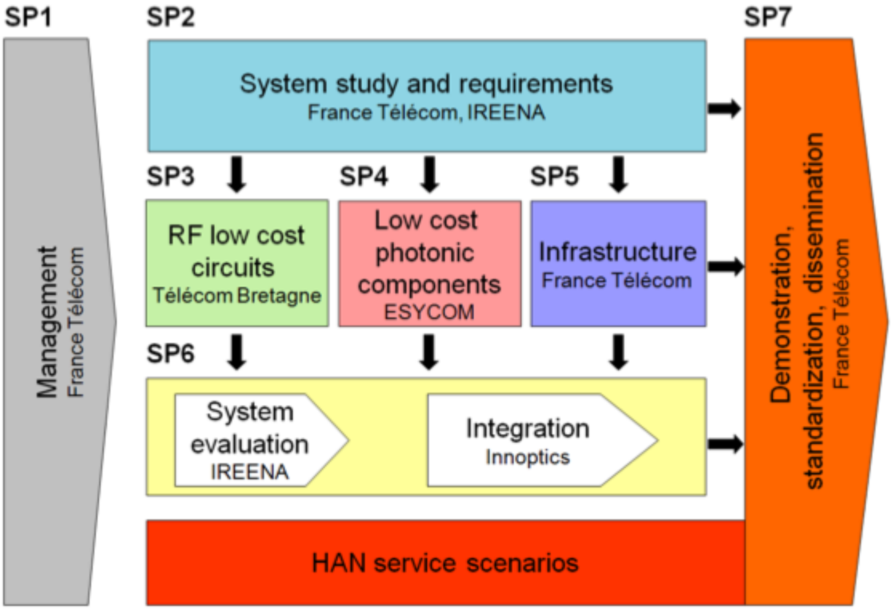

Figure 1.13 The ORIGIN Project structure and subdivision

ESYCOM is in charge of Work Package 4 (SP4), focused on the implementation of low cost photonic components. The main tracks of this research component are the following: Silicon Germanium HPTs, VCSELs, and Hybrid microwave-photonic integration on Siilcon.

This thesis involves research on SiGe HPTs. SiGe HPTs are used because it affords the potential of direct integration of the detector and amplification circuits, towards opto-electronic monolithic microwave integrated circuits (OE-MMIC). Initial research suggests promising linearity. This photodetector structure offers amplification and matching properties at the same time allowing for direct integration with high speed SiGe-based circuits.

1.3.1 System Block Diagram

The ORIGIN project aims to develop new infrastructures in building allowing communications at high data rates between a domestic bridge and different wireless devices operating at 60GHz carrier frequencies in all different areas of a house. RoF technology is used as the main infrastructure of the system implementation. Multimode Fiber is chosen as the optical medium to connect the different Transceiver Radio over

Fiber (TRoF) modules. Direct Modulation IF over MMF fiber is chosen to be the main architecture of the system. A simplified implementation of the RoF channel to connect two rooms to one another is presented in Figure 1.14.

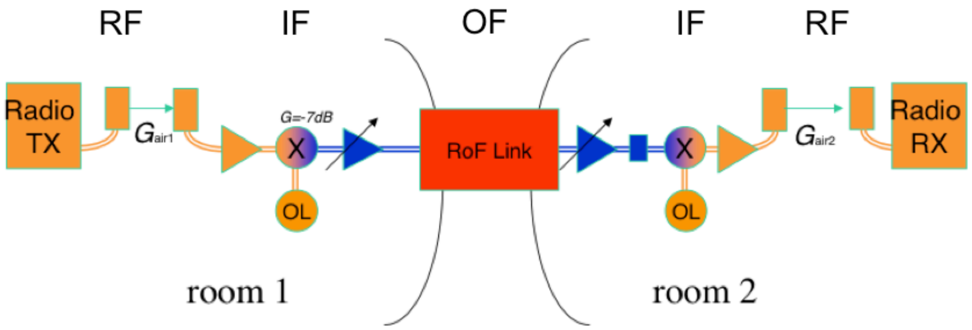

Figure 1.14 Simplified schematic representation of the IF-RoF channel that is used to connect two rooms.

A 60 GHz transmitting (TX) radio device is placed in room 1 while in room 2 a 60 GHz receiving device. They are both separated such that the receiver could not receive the signal from the transmitter. The initial hop from the radio TX is a receiving antenna at 60 GHz. This is then amplified and down converted to an intermediate frequency. This signal is then used to directly modulate a VCSEL. The modulated optical beam is transported through a multimode fiber, where a PD receives this signal and converts it to an electrical one. These signals are then amplified and upconverted to 60 GHz. A 60 GHz transmitting antenna radiates the wireless signal to the radio receiver.

Different implementations of the ORIGIN system are developed to:

1. provide verification of the system functionality and performances.,
2. improve performances of the systems, and
3. use low cost photonic component for the implementation of the system.

1.4 Photodetectors

This section targets to provide a state-of-the-art on photodetectors with a focus on low cost technologies. Photodetectors are devices, which convert optical signals to electrical signals. Discrete type, high speed photodetectors are typically used in the implementation of RoF links. This means that a single device such as a photodiode that is packaged to have an access for optical coupling and electrical access via RF or microwave connectors. Another form will be of a photodiode and an amplifying stage via the use of a transimpedance amplifier (TIA). These components are hybrid packaged together and provided with an access for optical coupling to the photodetector and an electrical access to the output of the amplifying stage.

In the succeeding sections, we will give a brief review of the figures of merit that are used to measure the performances of different photodetectors. The different discrete high-speed photodetector implementations and how they are optimized for the wavelength and speed of their operation will be discussed. The different discrete photodetector performances at 850nm are then summarized. The different research efforts to implement optoelectronic integrated circuits (OEIC) front ends composed of photodetectors and initial amplifying stages on the same die or processing technology are then reviewed. Photodetectors implemented in silicon based processing technologies are analyzed. Heterojunction bipolar phototransistors (HPT) implemented using a SiGe Bipolar process technology are assessed.

1.4.1 Photodetector Figures of merit

1.4.1.1 Quantum efficiency

Quantum efficiency is defined as the probability that a single photon incident on a detector generates an electron-hole pair. The internal quantum efficiency is given by the Eq. 1.1

$$\eta_{int} = \frac{number\ of\ e-h\ pairs\ generated}{number\ of\ incident\ photons} \leq 1 \qquad \textbf{Eq. 1.1}$$

The external quantum efficiency is due to number of collected electron hole pairs due to the number of photons that are incident in the semiconductor material. Eq. 1.2 shows the external quantum efficiency. It can also be described from measureable quantities such as the photo generated current I_{ph}, the optical power that is incident on the material P_{opt} and the wavelength of the optical signal λ as presented in Eq. 1.3

$$\eta_{ext} = \frac{number\ of\ collected\ e-h\ pairs}{number\ of\ incident\ photons} \qquad \textbf{Eq. 1.2}$$

$$\eta_{ext} = \frac{I_{ph}(\lambda)/q}{P_{opt}/hv} = \frac{1.24}{\lambda(\mu m)} \cdot \frac{I_{ph}(\lambda)}{P_{opt}} \qquad \textbf{Eq. 1.3}$$

If the external quantum efficiency is greater than 1, it signifies that the photo generated current is amplified and that the photodetector processes a gain mechanism. External quantum efficiency as a function of the internal quantum efficiency is presented below.

$$\eta_{ext} = \eta_{int} \cdot (1-R) \cdot (1-e^{-\propto W}) \qquad \textbf{Eq. 1.4}$$

where α is the absorption coefficient of the material at the wavelength of operation and R is the coefficient of reflection onto the photodetector surface and W is the width of the absorption region.

1.4.1.2 Responsivity

Responsivity is a measure of light-to-current conversion efficiency of the detector. A high detector responsivity improves the signal to noise ratio of the receiver system. It is possible to have gain in photodetectors (as in avalanche photodetectors) due to impact ionization and avalanche multiplication that can lead to high responsivity. But these mechanisms are usually accompanied by a penalty in bandwidth and noise performance. Mathematically, the responsivity of a detector R is defined as

$$R = \frac{I_{ph}}{P_{inc}} \qquad \textbf{Eq. 1.5}$$

where I_{ph} is the photocurrent and, P_{inc} is the incident optical power, η is sometimes defined as external quantum efficiency representing the fraction of incident photons leading to I_{ph}. In reverse bias junction photodiodes where the depletion region (high field region) constitutes the bulk of the absorption region, it can be approximated by

$$\eta = \eta_{int}(1-R)(1-\frac{e^{-\alpha d}}{1+\alpha L_n}) \quad \text{Eq. 1.6}$$

where R is the optical reflectivity between the air and the semiconductor, α is the absorption coefficient of the intrinsic region, d is the depletion region thickness and η_{int} is the internal quantum efficiency defined as the ration of the number of electron hole pairs created to the number of absorbed protons. In pure materials, η_{int} is almost unity. L_n is the minority carrier diffusion length, i.e. for electrons in the p-type substrate. In the absence of a diffusive transport, the term αL_n is missing in Eq. 1.6 and $(1-e^{-\alpha d})$ represents the fraction of light absorbed in the depletion width of the detecting junction. Note $L_n = \sqrt{D_n \tau_n}$ where D_n is the diffusion constant and τ_n is the minority carrier lifetime.

Because the quantum mechanical process of absorption transforms a photon to an electron–hole pair regardless of the energy of the absorbed photon, the maximum possible responsivity varies with photon energy. For example, at a wavelength of 850nm (1.45eV) the maximum possible responsivity (in a material with 100% absorption and is 0.69A/W, while at a wavelength of 1550nm (0.79eV), responsivity can be as large as 1.25A/W. [48]

1.4.1.3 3dB Bandwidth

The bandwidth of a photodetector is defined as the modulated RF frequency at which the responsivity of the detector has fallen by 3dB from its low frequency value. It is mainly limited by carrier transit time, RC time constant, diffusion time by photogenerated carriers outside the depletion region. Carrier transit time is the time taken by the photogenerated carriers to travel across the high-field region. It is usually dominated by a hole transit time as holes typically have lower drift velocity than electrons in common photodetector materials. The RC time constant is determined by the equivalent circuit parameters of the photodiode and the load circuit. Diode series resistance (due to ohmic contacts and bulk resistances), load impedance and the junction and parasitic capacitances contribute to the RC time constant. Diffusion time becomes important when the photocurrent due to carriers absorbed in the p and n contact regions within about one diffusion length of the edge of the depletion region becomes comparable to the current arising from the photo generated carriers within the depletion region.

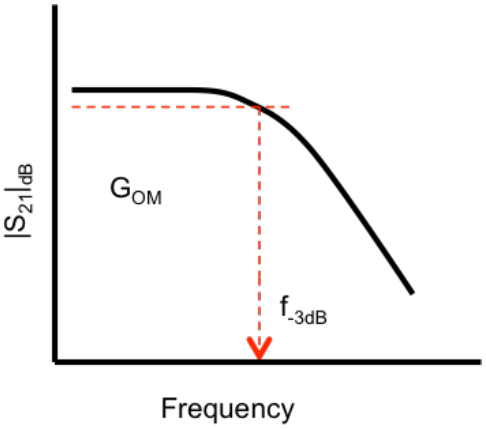

Figure 1.15 Representation of the 3dB bandwidth of the photodetector

1.4.2 High Speed Photodetectors

Discrete high-speed photodetectors are implemented to reach high performances with regards to maximum detection and speed. Since these devices are discrete in nature, they are not limited to constraints such as process compatibility to electronic circuits, in processing or supply voltage levels. Indeed, most optical receiver modules are packaged as a hybrid device. This is shown in Figure 1.16 where an optical receiver module is composed of a means to couple the light to the detector and it is wafer bonded to the first stage of an electronic circuit.

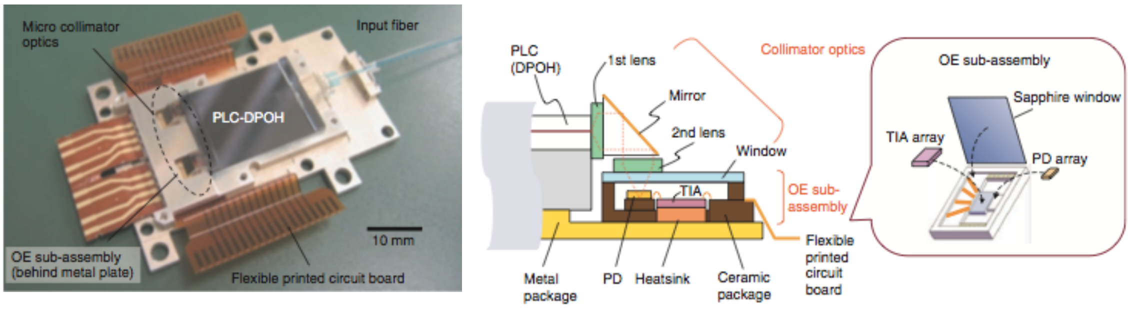

a)　　　b)

Figure 1.16 Example OE receiver module that is composed of hybrid packaged discrete photodetector and amplifiers [49]

In order to achieve good performances, these photodetectors use direct band gap materials like GaAs for example that are matched to the particular wavelength of application. The detection layers and area are optimized form to achieve a good balance between detection and speed. The speed of the photodetector is primarily limited by the diffusion parameters and the RC delays.

High-speed photodetectors are used in the different radio over fiber implementations as discussed in the previous section. These devices are required for telecommunications systems and for high capacity optical based networks. Different materials are used in the implementation of these detectors as well as photodetector structures. Non- direct band gap materials such as Silicon are commonly used to implement photodetectors for wavelengths from 400nm up to 1000nm and another indirect bandgap material Germanium is used at long wavelengths up to 1800nm. Due to the indirect bandgap of silicon and germanium at these wavelengths, they have relatively small bandwidth efficiency products. Direct bandgap materials such as III-V semiconductors are more adapted for high-speed operation. GaAs has as cutoff wavelength of around 900nm and is ideal for visible and near infrared operation of the telecom wavelength of 850nm. Alloys of GaInAs ternary semiconductors with a cutoff wavelength of 1650nm are specially useful for the telecommunication photodetectors at 1310nm and 1550nm.

The use of the materials that are matched to a specific wavelength and optimized for high-speed operation is a key activity in the research for very high speed discrete photodetectors. This is specially the case in telecoms applications where the performance is the primary criteria. However, silicon is abundant and has the relatively lower cost related processing. There has been a lot of research activity to develop high-speed photodetectors that are based on silicon. This offers the availability of monolithically integrating these detectors with high-speed electronic circuits that are needed for the processing of the detected optical signals. One aspect of this research involves extending the spectral response of silicon-based detectors so that it can be used in the telecoms wavelength such as 1310nm. This involves the use of germanium and silicon as a platform for Ge based photodetectors. Heterojunction such as SiGe is used with Silicon in order to increase the spectral response and to improve its high- speed operation. Another approach is to push for higher frequencies of operation which is achieved by using novel photodetector structures, i.e., heterojunction and SOI technologies. These researches focus on the fact that the photodetectors should be processed to be compatible to silicon based processing technologies such as Silicon/SiGe CMOS, Bipolar and BiCMOS which will help in its future monolithic integration with silicon based electronic circuits. Lastly, there is a lot or research activities, which are focused on implementing high-speed photodetectors directly on commercial silicon, based processing technologies with little or no modification in the mask set and processing steps. This assures that these devices are process compatible and could be easily included as part of list of available devices for these silicon based process technologies.

In the following section we will discuss two primary implementations of high-speed photodetectors; photodiodes and phototransistors. Photodiodes are the most common high-speed photodetectors. These photodiodes could be classified according to their structure; PIN photodiode, MSM photodiode, Avalanche photodiode (APD),

1.4.2.1 PIN Photodiode.

A PIN photodiode is a variation of a simple PN junction photodiode. This PN junction photodiode is reversed biased to obtain a large space charge region (SCR) or a depleted zone to accommodate the photodetection. In PIN photodiode, the absorption region is augmented by the insertion of an intrinsic layer in between the p-type and n-type semiconductor. This intrinsic layer is undoped or could be lightly doped. This is used to artificially augment the space charge region. It can be said the depletion region is almost entirely contained in the intrinsic region. This helps increase the optical absorption. In this type of photodiode, the light absorbed in the semiconductor produces electron hole pairs. The electric field in the depletion region causes the separation of the electron hole pairs, which leads to the flow of current in the external circuit. The frequency response of this PD is limited by the transit time, which is the time it takes to for the carriers to cross the depletion region and the RC time constant effects due to the photodiode bulk resistance and contact resistances. The photodiode capacitance is due to the separation of charge at the depletion region. The tradeoff for speed versus sensitivity is very evident in a surface illuminated PIN PD. In order to increase the frequency response of a vertically illuminated PIN PD the sensitivity is always sacrificed. The decrease in the length of the depletion region will reduce the transit time of the carriers which will increase the bandwidth of the photodiode. However this will result in the decrease of its quantum efficiency. A simple representation of the PIN PD is shown in Figure 1.17. It shows an illumination that is perpendicular to the PIN structure.

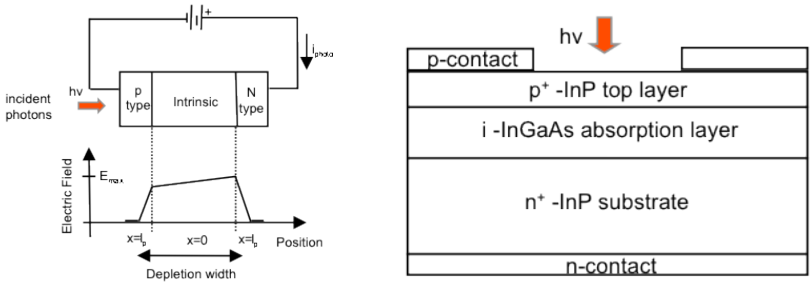

a) b)

Figure 1.17 example p-i-n photodiode. (a) diode structure (b) electric field profile[50], [51] For a PIN PD, its quantum efficiency can be expressed by the following equation.

$$\eta_{ext} = \eta_{int} \cdot (1 - R) \cdot (1 - e^{\propto W}) \qquad \textbf{Eq. 1.7}$$

Where R is the reflection coefficient, α is the absorption coefficient and W is the thickness of the intrinsic layer. It is considered that $\eta_{int} \approx 1, \alpha(\lambda) \cdot W \ll 1$

The PIN PD bandwidth is limited by the transit time and RC time constant of the equivalent circuit of the PIN PD [52], [53], [54], [51] .

$$\frac{1}{f_{3dB}^2} = \frac{1}{f_t^2} + \frac{1}{f_{RC}^2}\,; f_{3dB} = \left[\left(\frac{2\pi w}{3.5\bar{v}}\right)^2 + \left(\frac{2\pi\varepsilon_0\varepsilon_r RS}{w}\right)^2\right]^{-\frac{1}{2}} \qquad \textbf{Eq. 1.8}$$

Where
$$\frac{1}{\bar{v}^4} = \frac{1}{2} \times \left(\frac{1}{v_e^4} + \frac{1}{v_h^4}\right) \qquad \textbf{Eq. 1.9}$$

In this equation, R is the total resistance which includes the series resistance of the diode and load resistance of the diode, S is the surface of the photodiode ε_0 is the dielectric constant and the ε_r is the relative permittivity, w is the thickness of the depletion region and $v_e \, and \, v_h$ are the saturation speeds of electrons and holes. The Eq. 1.8 shows that, in order to increase the transit time, it is necessary to decrease the intrinsic absorption layer thickness. From this equation, the PIN PD bandwidth is maximal for a given photosensitive area S.

$$w = \sqrt{3.5\bar{v}\varepsilon_0\varepsilon_r RS} \approx \sqrt{S} \qquad \textbf{Eq. 1.10}$$

The optimum absorption layer thickness is proportional to the diameter of the PIN PD photosensitive area. By reducing the photosensitive area S, the bandwidth of the PIN PD can be increased. However this reduces the series resistance, decreases the saturation current and makes the coupling to fiber-optic cable more difficult.

Very high-speed compound semiconductor PIN photodiodes have been reported in literature most of which are bandgap engineered to operate in the long wavelength operations 1350 and 1510nm. Simulations of InP/GaInAs/InP PIN photodiodes suggested bandwidths greater than 60 GHz at 1550nm [55]. Waveguide PIN PD which are laterally illuminated PIN PD have 3dB bandwidth greater 40 GHz at 1550nm have been demonstrated [56]. Cutoff frequencies in the range of 110-120 GHz at 1350nm operation were reported, [57], [58], and at 970nm operation a 100GHz cutoff frequency of a vertically illuminated GaInAs/InP PIN [59].

High speed Silicon PIN PD has been reported to achieve a bandwidth of 34GHz and peak efficiencies ranging from 42% at 704nm and 31% at 836nm[60]. Silicon based PIN PD operated at long wavelengths were implemented by using SiGe and Ge on Si due to their compatibility to silicon CMOS processing and their high optical absorption coefficients at 1300nm and 1550nm. One implementation is a Germanium PIN PD that is grown on silicon. Recent literature shows cutoff frequencies in the range of 40GHz [61],[62]-[64]. Another approach using Germanium as a means to extend the spectral response of silicon for the long wavelength region is to use heterostructure of Si and Ge. Many successful reports of PIN SiGe/Si superlattice photodetectors have been made for wavelengths of 850-1300nm. A GeSi/Si waveguide PIN photodiode that operated at speeds greater than 1GHz at 1300nm with an internal quantum efficiency of 40% [65]. A planar SiGe/Si based PIN PD was demonstrated with a 10.5GHz cutoff frequency at 980nm with an external quantum efficiency of 25-29%.[66]. Several SiGe/Si PIN photodiode exhibited a responsivity of 0.3A/W and a bandwidth of 0.8 GHz at 880nm [67], [68] [69]

Using standard silicon based CMOS, BiCMOS and Bipolar process profits from a lot of interest to make monolithically integrated OEIC's. Si waveguide PIN photodiodes have been developed using standard CMOS processing with a bandwidth of 10-20GHz and an internal responsivity of 0.8A/W at 1550nm [70]. By using additional mask in a standard CMOS twin well process, high-speed PIN PD with cutoff frequency of 1.4GHz at 622nm was used in monolithic a CMOS based photoreceiver [71]. Other groups used modified BiCMOS and Bipolar process. Planar PIN PD that are fabricated on CMOS-compatible silicon on insulator (SOI) substrates were presented in several researches. [72]-[74]. Using different PIN PD structure is seen as a solution to fabricate PDs in an unmodified CMOS process. They were able to achieve 2-3GHz of cutoff frequency at 850nm wavelength. [75]

1.4.2.2 Metal Semiconductor Metal Photodiode

The metal semiconductor metal (MSM) photodiode consists of thin metal electrodes on a semiconductor substrate. It is essentially made of back-to-back Schottky diodes that use interdigitated electrode configuration on an undoped semiconductor layer. Figure 1.18 shows a top view and cross section view of an MSM photodiode. The metal fingers of the metal electrodes have finger width of w and are separated by a distance s. The spacing s should be greater than the finger width, in order to have a high quantum efficiency for the photodiode. One advantage of the MSM PD is that it has a simple planar structure which is compatible with the production process of field-effect transistors [76] , [77] and other planar semiconductor processes. A MSM PD is used in FET-based monolithic OEIC receivers with 11GHz bandwidth [78]. MSM Photodiodes in Si-based standard CMOS technologies was also demonstrated [79]. It has been applied to several opto-microwave applications [80], [81], [82], [83], [84], [85], [86], [87].

In an MSM PD, when the light hits the semiconductor surface, it is absorbed and generates electron-hole pairs within the active region. The holes drift towards the negative electrodes, and the electrons travel to the positive electrode due to the influence of an electric field when a reverse bias voltage is applied. The bandwidth of an MSM PD is similar to that of a PIN PD in the sense that it is limited by the RC time constant and the transit time values.

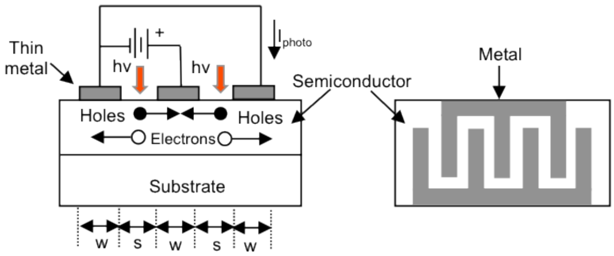

a) b)

Figure 1.18 MSM photodiode, (a) cross sections (b) top view [88]

The external quantum efficiency of a MSM PD is given by the equation:

$$\eta = (1 - R)\frac{L}{L + l}(1 - e^{-\alpha \cdot w}) \qquad \text{Eq. 1.11}$$

where $L, l\ and\ w$ are the dimensions of the component as indicated in the Figure 1.18 $\propto$ is the absorption coefficient of the material and R is the reflection coefficient of the air semiconductor interface. In order to have increased quantum efficiency, L should be much greater than l. It is also possible to improve the quantum efficiency by using semi-transparent electrodes[89] or by back side illumination [90] , [91].

The MSM PD bandwidth, as well as for the PIN PD, is limited by drift time and RC-time. Although in the MSM PD optical radiation propagates perpendicular to the direction of the charge carrier transport, it has the similar trade-off between the quantum efficiency and bandwidth. In order to increase the transit time the interdigital spacing has to be reduced which will result to higher cutoff frequencies [92]-[94]. In order to increase quantum efficiency and to decrease the capacitance, it is necessary to enlarge the interdigital spacing.

Since the MSM PD bas lower capacitance per unit area compared to the PDs based on pn junctions, the MSM PD bandwidth is usually limited by transit time. Also it is necessary to note that the interdigital spacing reduction increases both dark current and degradation probability of the MSM PDs due to high surface currents. The nature of a saturation of a photocurrent in the MSM PD and Schottky PD is the same as in the PIN PD. However, the internal electrical field of the Schottky barrier is usually lower than in the PIN structure and also there is a large barrier for holes at the metal-semiconductor interface. This results in lower saturation current of the PD based on Schottky barrier comparing with the PIN PD.

Cutoff frequencies of 375GHz and 510GHz have been reported [95],[96]. It is based on low temperature grown GaAs. In bulk silicon, cutoff frequencies of 110 GHz was reported [97] another group at 85GHz for 633 and 850nm operation [98]. MSM PD on SOI has also been reported [99] .

1.4.2.3 Avalanche Photodiode

Avalanche Photodiodes (APD) offers high sensitivity due to internal amplification and avalanche gain of the photocarriers. It incorporates a high field region that multiplies the photocurrent through the avalanche generation of the additional electron hole pairs. APD's have internal gain, as a result they have very high responsivity and are used in the implementation of high sensitivity photoreceivers. However, APDs present stronger noise level compared to PIN PD. For APD's, silicon are used to increase the photoreceiver sensitivity of fiber-optic links. With increase sensitivity in the links, the APDs help increase the distance between repeaters. The increase in APD sensitivity is due to internal amplification during an avalanche gain of the photocarriers. A large reverse bias is needed to supply the ionization field in the multiplication layer. This avalanche gain is characterized by ionization rates for electrons $\alpha_n$and holes α_p. In an approaching of a constant electric field inside of the multiplication layer, the multiplication factor M can be expressed through ionization rates and multiplication layer thickness d_m:

$$M = \frac{(\alpha_n - \alpha_p)}{\left(\alpha_n - \alpha_p e^{(\alpha_n - \alpha_p) d_m}\right)} = \frac{1 - k_\propto}{e^{-[(1-k_\propto)\propto_n \cdot d_m]} - k_\propto} \qquad \textbf{Eq. 1.12}$$

where $k_\propto = \frac{\alpha_p}{\alpha_n}$

For low noise, fast response times and high multiplication factor, the ionization coefficients should significantly differ from each other. Silicon has been long recognized as the best APD multiplication material in terms of gain-bandwidth product and excess noise. Excess noise is present in APDs due to the multiplications process. This is due to the large ratio of electron and hole ionization coefficients. These coefficients define the probability that a carrier causes an ionization, and generates additional carriers. Very high or very small ratios $k_{\propto}$ of these coefficients results in APDs with little noise and high gain bandwidth products[100]. There are studies on APDs in silicon that are focused on integration with CMOS and Bipolar process and reduction of the operating voltages [101]-[103] [104], [105],[106],[107].

For long wavelength applications APDs use of composite heterostructures with separate absorption layers and wide bandgap multiplication layers based on material that have distinguishable ionization rates for the holes and electrons. These are called separate absorption and multiplication (SAM) structures. A narrow bandgap material is used in the absorption region, but a higher bandgap material such as InP is used in the multiplication region[108], [109]. Figure 1.19 shows a cross section of a high speed InGaAs APD. The difference in bandgap between the two materials causes an accumulation of charge at the interface, which tends to slow the device. A solution to this problem has been to use a graded bandgap profile by incorporating a superlattice. These devices are called a separate absorption grading and multiplication APD (SAGM–APD) [110], [111] Several variations of the SAGM–APD have also been developed including, the separate absorption, grading, charge and multiplication APD (SAGCM–APD) [112], [113].the superlattice APD (SL–APD) [114], [115] and the ‘staircase’ APD [116], [117].

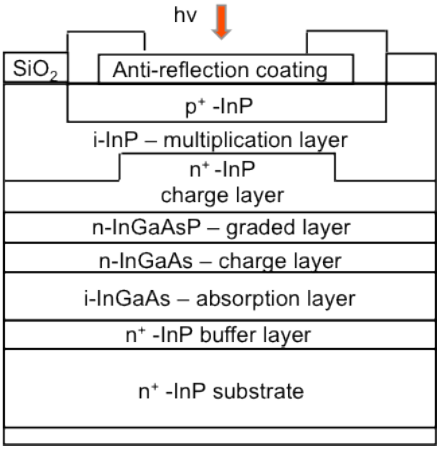

Figure 1.19 Typical structure of high speed InGaAs APD [51]

The gain of the APD is equal to one when it is biased in small reverse voltages. The amplification occurs only at large reverse bias. Its bandwidth is determined by RC time constant, drift time of photocarriers and time for avalanche formation.

$$\tau_{av} = \frac{1}{\partial_n + \partial_p} \frac{1 - e^{-(\alpha_n - \alpha_p)d_m}}{\alpha_n - \alpha_p} \qquad \text{Eq. 1.13}$$

Where ∂_n and $\partial_p$are the electron an hole velocities in the multiplication layer. In order to increase the APD bandwidth, it is necessary to reduce both the absorption, and multiplication layer thickness. The minimum absorption thickness is limited by the required quantum efficiency. The quantum efficiency could be increased by means of

Resonant Cavity Enhanced (RCE) or edge coupling. The multiplication layer thickness is limited by the minimum space necessary for photocarriers to obtain the sufficient energy for ionization. This means that the bandwidth of the high speed APD is limited by the avalanche formation time τ_{av} The APD performance could be improved with the use of superlattices in the heterojunctions. If the avalanche is formed by fast electrons, it results in decreasing the avalanche formation time to increase of bandwidth.

In the literature, An APD with a 17 GHz unity gain operating at 1300 nm. It has InGaAs for the absorption zone and InGaAsP-InAlAs for the multiplication zone. Through backside illumination it has a quantum efficiency of 74% and a gain bandwidth product of 110GHz. [118]. Using Silicon as the multiplication zone, an avalanche PD with a unity gain of 10 GHz with a quantum efficiency of 42% and the gain bandwidth is estimated in the environment of 400GHz [119].

Table 1.2 shows the summary of the properties of the different photodiodes that were discussed.

Table 1.2 Summary of different Photodiodes

PD Type	Year	Reference	Material	-3dB (GHz)	Wavelength (nm)
PIN	1995	[59]	GaInAs/InP	100	970
	2002	[56]	---	40	1550
	1994	[57]	---	110	1350
	1995	[58]	GaAs	120	1300
	2005	[61]	Ge on Si	25.1	1552
	2008	[62]	Ge on Si	40	1550
	2009	[63]	Ge on Si	49	1550
	1986	[65]	GeSi/Si	1G	1300
	1997	[66]	SiGe/Si	10.5	1300
MSM	1991	[76]	InGaAs	---	1300,1550
	2000	[77]	InGaAs	3	1300,1500
	1993	[78]	GaAs	11	850
	2009	[79]	Si	0.919	850
	1985	[80]	GaAs	---	800
	1996	[81]	AlGaAs/GaAs	8.2	840
	1993	[82]	AlGaAs/InGaAs/GaAs	1.0	850
	1996	[83],	InAlAs-InGaAs-InP	18	1550
	1998	[84]	SiGe	1.1	850
	1998	[85]	AlGaAs/GaAs	17	1550
	2001	[86]	GaAs	2	850
	1992	[89]	GaAs	6	850
	1992	[91]	InGaAs/InAlAs	5	1300
	1996	[92]	InGaAs	40	1300
	1988	[93]	GaAs	105	532
	1998	[94]	InGaAs	70	1550
	1991	[95]	GaAs	375	---
	1992	[96].	GaAs	510	---
	1993	[97]	Si	110	725
	1997	[98].	Si	85	850,633
APD	1997	[100].	Si-InGaAs	9	1300
	2002	[101]-[103]	Si	--	470
	2010	[102]	Si	1.44	850
	2009	[103]	Si	---	850
	2012	[104]	Si	6.3	850
	2012	[105]	Si	2	850
	2012	[106]	Si	0.300/1.0	400/830
	2000	[109]	InAlAs	GB=140	---
	1983	[110]]	InGaAsP	---	1300
	2002	[110], [111]	InGaAs-InP	---	1300/1550
	1995	[113]	InP-InGaAs	6.1	1300
	1997	[114], [115]	InAlGaAs-InAlAs	15.2	----
	2000	[115]	InAlGaAs-InAlAs	15	---

1.4.2.4 Phototransistors

Phototransistors are devices that offer photodetection and signal amplification in a single device. A bipolar phototransistor is a transistor in which the current into the base terminal is influenced by photoelectric effects. This current is then amplified by the transistor action of the device. A common schematic representation of a phototransistor is shown in Figure 1.20, a switch in the 2T position shows no base connection this is called 2T phototransistor configuration and a switch in the 3T position shows a base connection that could be used and is called 3T phototransistor configuration.

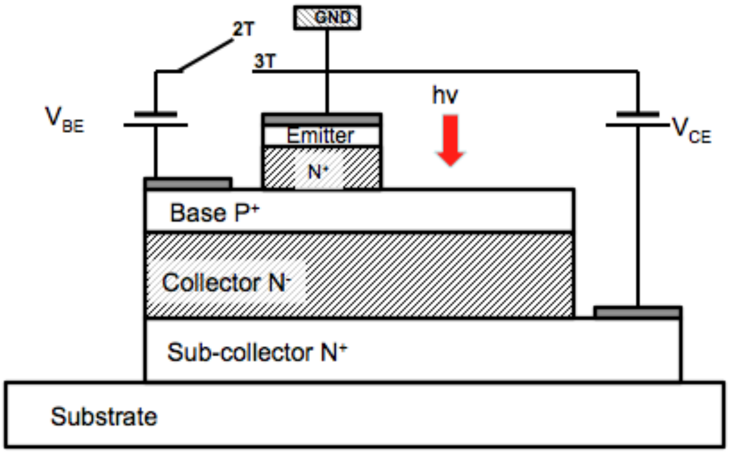

Figure 1.20 Schematic diagram of an npn transistor with a bias circuit in the common emitter configuration. The shaded region are free from mobile charges. The base, collector and sub collector could be tough of as a PIN photodiode

Figure 1.20 also shows a representative cross section of a phototransistor. The structure of the device is similar to a bipolar transistor device except for the enlarged area in the base and collector region. This serves as the optical window of the phototransistor where, illumination passes through this opening.

The npn phototransistor is normally operated in the common emitter configuration where the Vbe and Vce voltages are greater than 0. This means that the phototransistor is in the forward active mode, the base-collector (BC) junction is reverse biased and the BE junction is forward biased. The forward bias of the BE junction could come from the illumination of the HPT or by providing an external base bias. The biasing of the base-emitter BE junction from the illumination is called a two terminal phototransistor configuration (2T-HPT), where in the base contact does not exist [120] or the base electrical contact exist but is left floating [121], [122]. Providing an external bias for the base is called a three terminal HPT configuration (3T-HPT) which is reported to provide enhanced HPT performance [123] [124], [125], [126]. For HPT's operated in the "floating base" and a reverse biased base-collector junction, the vertical illumination of the HPT will be incident on the vertical stack of the HPT. The reversed biased base-collector will act as a reversed biased photodiode and the illumination will be absorbed in the base, base-collector depletion regions or the bulk collector of the HPT. For simplicity, it is assumed that no absorption takes place in the sub-collector and the collector is free of mobile charges. The photoelectric effect generates an electron-hole pair for every photon that is absorbed. The electron-hole pairs generated in the BC depletion region and within the diffusion lengths of the minority carriers in the base and collector will be separated and collected by the field of the BC junction leading to a current flow in the external circuit. This is known as the primary photocurrent. The holes are swept into the base, thereby increasing the base potential. This increases the base-emitter forward bias. To maintain the charge-neutrality condition in the base, a large injection of electrons occurs from the emitter into the thin base resulting in a large electron-current flow from the emitter to the collector. This is the traditional behavior of a bipolar transistor. The amplification of the photocurrent is a purely electrical phenomenon due to the transistor action.

In a common emitter configuration, the phototransistor currents can be characterized in terms of the following currents. Initially, the emitter injects electrons into the base region. The electrons in the base region are minority carriers, they diffuse in the perpendicular direction to the junction layout and if the base is thin enough that recombination can be ignored, they reach the depletion region of the base-collector junction. The presence of a high electric field clears them out toward the collector region. The flow of these charge carriers gives the contribution I_{ne}. Conversely, a current I_{pe} of holes, which are majority carriers in the base is injected from the base towards the emitter. The generation-recombination phenomena mostly occur at the level of the base-emitter junction, I_{reb}, and in the base I_{rb}. I_{reb} comes from the recombination of electrons in the space charge region of the base-emitter junction. I_{rb} is caused by the recombination of electrons with holes, majority carriers in the base. The illumination produces the primary photocurrent I_{ϕ}. This is mostly created in the SCR of the base-collector junction. The primary photocurrent originates from a current of electrons, which migrate directly towards the collector contact, and from a current of holes, which accumulate at the level of the base.

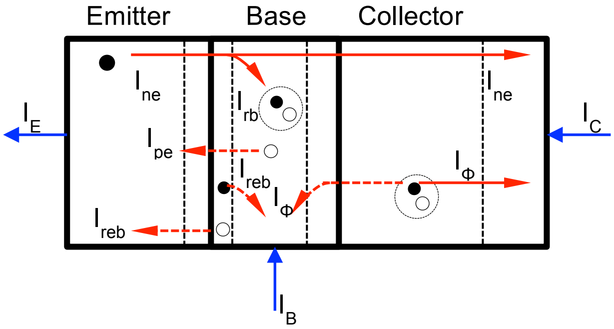

Figure 1.21 Different currents in the phototransistor which include the electrical and optical origins. The SCRs near the emitter-base and base collector junctions are shown by the dotted lines

Using the different contributions of currents that are crossing the junctions. The total currents at the emitter, base and collector. These currents are given by the equations:

$$I_E = I_{ne} + I_{pe} + I_{reb} \quad \text{Eq. 1.14}$$

$$I_B = I_{pe} + I_{rb} + I_{reb} - I_{\phi} \quad \text{Eq. 1.15}$$

$$I_C = I_{ne} - I_{rb} + I_{\phi} \quad \text{Eq. 1.16}$$

1.4.2.5 Responsivity of a phototransistor

The responsivity of the base-collector photodiode part of the phototransistor is defined as the ratio of the primary photocurrent I_{ϕ} to the received optical power P_{opt}

$$R_0 = \frac{I_{\phi}}{P_{opt}} \ A/W \quad \text{Eq. 1.17}$$

The quantum efficiency is the ratio of the number electrons collected to the number of incident photons. It is used to characterize the opto-electical conversion of the base collector photodiode. This efficiency is typically called external quantum efficiency, and is given by the following equation

$$\eta = \frac{I_\phi/q}{P_{opt}/hv} = \frac{hv}{q} \cdot\ R_0 \qquad \textbf{Eq. 1.18}$$

The responsivity of the phototransistor is characterized by the ratio of the component due to the optical excitation Ic_{opt} of the current leaving the device Ic due to the same incident optical power.

$$R_{hpt} = \frac{Ic_{opt}}{P_{opt}} = \frac{Ic_{opt}}{I_\phi} \cdot \frac{I_\phi}{P_{opt}}\ A/W \qquad \textbf{Eq. 1.19}$$

Using the previous equations. We can express Ic_{opt} as:

$$Ic_{opt} = \frac{q}{hv} \cdot \eta \cdot G_{opt} \cdot P_{opt} =\ R_0 \cdot G_{opt} \cdot P_{opt} \qquad \textbf{Eq. 1.20}$$

This shows that the phototransistor has a responsivity that is G_{opt} times greater than the responsivity associated base-collector photodiode. Where G_{opt} is the optical gain of the HPT.

The DC responsivity of the HPT can be extracted from the measurement of the terminal currents. In the base floating base configuration, the DC responsivity is extracted from collector current measurements and is given by the equation [127].

$$R_{hpt} = \frac{I_{C\_illum}}{P_{opt}} \qquad \textbf{Eq. 1.21}$$

where I_{C_illum} is the measured collector current under illumination of optical power of P_{opt}. In the floating base configuration, the current gain of the HPT is associated to the current gain of the HPT in the dark as a function of Ib. the floating base assures that the measured Ic is the amplified photocurrent.

For 3T-HPT operation, one definition of the DC HPT responsivity uses the responsivity definition for a floating base operation [128]. The collector current that is measured under a constant base bias is the amplified photocurrent plus dc biasing current. Another way to define the DC responsivity for 3T-HPT configuration is by subtracting the dark collector current from the illuminated collector current measurements. This assures that the reference for the responsivity computation is the amplified photo generated current. [129].

$$R_{hpt} = \frac{I_{C_{illum}} - I_{C_{dark}}}{P_{opt}} \qquad \textbf{Eq. 1.22}$$

1.4.2.6 Optical transition frequency

The optical transition frequency $f_{T\,opt}$ is the frequency at which the optical gain is unity or zero in dB. This sets the limit for the use of phototransistor as a photocurrent amplifier. It can also be seen as the frequency for which the responsivity of the phototransistor in phototransistor mode is equal to the low frequency responsivity in photodiode mode, which mean that there is no more amplification. Figure 1.22 shows the graphical representation of the $f_{T\,opt}$

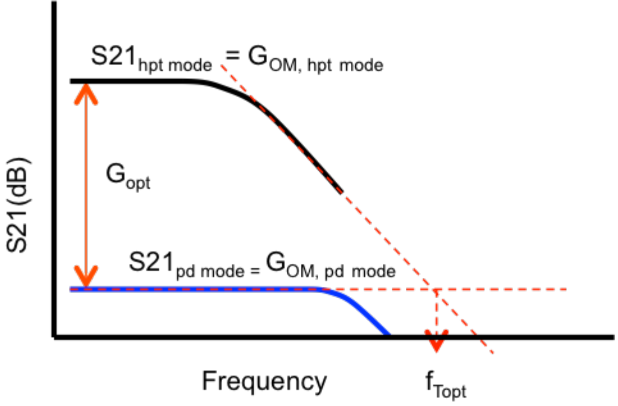

Figure 1.22 Definition of the optical transition frequency and the optical-microwave gain

1.4.2.7 Opto-microwave gain (G_{OM})

This gain represents how much the output signal power is compared to a photodiode with a 1A/W responsivity that is feeding a 50Ω load. [130]-[132]. This is of particular use due to the fact that it is equal to the square of the responsivity (i.e., same value in dB) under a 50Ω loading condition. This provides an effective means of evaluating the efficiency of matching networks compared to a 50Ω loaded network as reference case.

$$G_{OM} = \frac{P_{out-hpt}}{P_{1A/W-photodiode-over-50\Omega}} \qquad \text{Eq. 1.23}$$

if loaded with 50 Ohms

$$\mathrm{G_{OM}(f)} = \frac{\frac{1}{2}\cdot \mathrm{R_0}\cdot \mathrm{I_c}^2}{\frac{1}{2}\cdot \mathrm{R_0}\cdot \mathrm{P_{opt}}^2} = \mathrm{R_{hpt}}^2 \qquad \text{Eq. 1.24}$$

$$G_{OM}|_{dB} = R_{hpt}|_{dB} \qquad \text{Eq. 1.25}$$

The extension relies on the modeling of the optical port as an electrical port whose input impedance is 50Ω. A current of the same amplitude as the modulated optical power models the optical signal. It can be considered as if the signal is detected by a 1 A/W photodiode before entering the internal phototransistor. Both the amplitude and phase information available and power waves theory can be transposed [130], [131]. This approach is the origin of the opto-microwave power gain definition [131] and the OM noise figure definition. A further description of the capability of the opto-microwave gain to deal with matching effects will be dealt with in Chapter 4.

1.4.2.8 Optical Gain (G_{OPT})

The optical gain in current (G_{OPT}) is the coefficient which characterizes the internal amplification of the photocurrent. It is defined as the ratio of the illuminated collector current Ic_{illum} over the photogenerated current in the base in the photodiode mode I_{ph}. It can also be defined as the ratio of the The responsivity in the phototransistor mode, $R_{hpt} = Ic_{illum}/P_{opt}$ over the responsvity photodiode mode $R_{pd} = I_{ph}/P_{opt}$ and in

$$G_{OPT} = \frac{Ic_{illum}}{I_{ph}} = \frac{R_{hpt}}{R_{pd}}$$

Eq. 1.26

The optical gain in current allows for the characterization of the amplification of the photogenerated current but also the frequency limitation of the phototransistor through the variation of Ic_{illum} in frequency. . Figure 1.22 shows the graphical representation of the G_{OPT} as well. Eq. 1.27 show G_{OPT} in dB mode from extracted responsivity in both PD mode and HPT mode from opto-microwave measuements

$$G_{OPT}|_{dB} = G_{OM}|_{HPT\ mode\ dB} - G_{OM}|_{PD\ mode\ dB}$$

Eq. 1.27

1.4.2.9 HPT illumination

The phototransistor structure could be illuminated vertically or laterally. Vertical illumination of the phototransistor could be achieved in different ways. A simple way is to illuminate the phototransistor between base-emitter contact (Figure 1.23 a). This is simply illuminating a transistor structure [133], [134]. The optical beam can be injected via the emitter through an opening in in the emitter contact. [135]-[137] (Figure 1.23 b)or by utilizing a transparent emitter contact[138] (Figure 1.23 c) Finally, one of the base contacts could be removed or omitted to allow for the direct illumination of the base collector junction [139], [140],[141], [142](Figure 1.23 d).

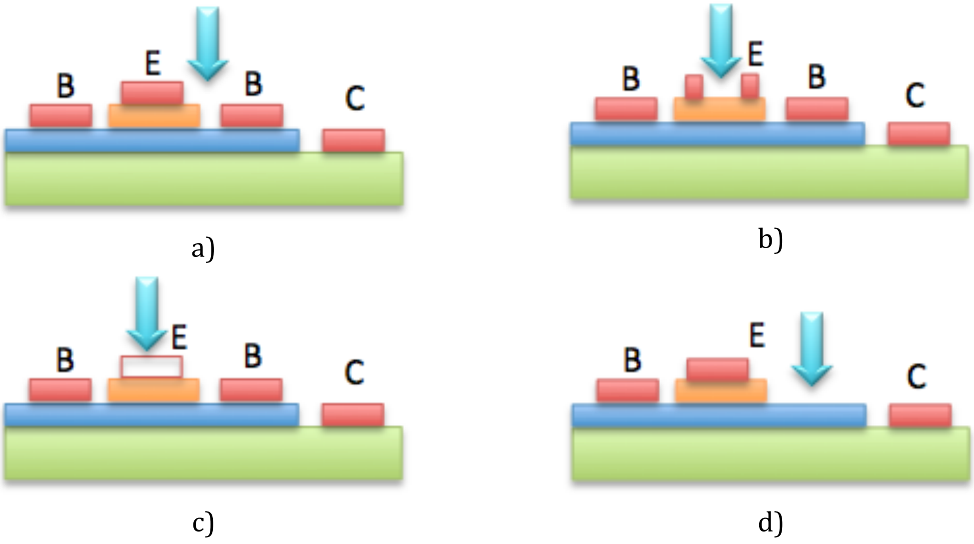

a) b) c) d)

Figure 1.23 Different configurations of vertical illumination of phototransistor (a) the HPT between the base-emitter contact. (b) though the emitter via an opening in the emitter contact. (c) through the emitter via a transparent emitter contact (d) direct illumination of the via removal of a base contact.

Another form of vertical illumination is through the backside of the phototransistor [143]-[147] Lateral illumination of the HPT is one method to improve the coupling efficiency. This allows for the propagation distance be long enough for the optical absorption to be complete while the absorption layer remains thin enough to ensure short transit times. Illumination of the phototransistors through the edge in which the light is inputted on the cleaved side of the device [148], [149]. Lateral illumination is also achieved by using an integrated optical waveguide into the device structure [150].

1.4.3 InP Phototransistors

Phototransistors could be implemented from field effect transistors (FET) or from heterojunction bipolar transistors (HBT). The phototransistor effect in GaAs MESFETs, where studied to provide optical components could be integrated in Monolithic Microwave Integrated Circuits (MMIC) [151]. However studies have shown that these structures suffer from poor dynamic performance with bandwidths of less than 100 MHz under illumination [152].

Using HBT structure to implement a phototransistor is another approach to develop optical components for MMICs. The early implementation of InP/InGaAs HPT was designed for detection in the wavelength range of 960 nm up to 1650nm [143]. It was a 2T-HPT configuration that was illuminated from the bottom. Theoretical studies suggested that the performance of HPTs in optical communication systems could exceed those of PIN-FET base receivers. [153]. Studies on 3T-HPT configurations showed that using a base contact for external biasing could improve frequency response by extracting the excess holes in the base [123]. A gain-bandwidth of 10GHz was reported in the first generation InP/InGaAs 3T-HPT [124].

One of the techniques to improve HBT performances was focused on its size reduction, which directly influences the capacitance of the devices. This capacitance limits the dynamic performance of the device. Also base and collector thickness have been reduced in order to reduce the transit time. The epitaxial structure of the HPT eventually follows any improvement techniques used in a HBT. This reduction in base thickness can increase the gain of the HPT. It is accompanied by an increase in the doping for holding an access resistance reasonable value. However, there is a limit in the reduction of geometric dimension and layer thickness. To have a good quantum efficiency, the layer thickness should be thick enough to have sufficient absorption at a specific range of wavelengths. The absorbing layer should also maintain a size that is comparable to the diameter of the optical beam. The study in illuminated HBTs highlighted this concern [154] [155]. Illumination on to the topside becomes difficult with small area. An edge-coupled two terminal HPT is a proposed solution to take advantage of the benefits of small area HPT and to solve the issue in optical coupling[156]. A three-terminal edge-coupled InGaAs/InP phototransistor is reported with a DC photocurrent gain near 60 and an optical unity gain frequency of 40 GHz. [148]. Evanescent coupling via waveguides in HPT was reported to have f_{Topt} of 20 GHz [157]. The first HPT with a f_{Topt} above 100 GHz is achieved by CNET (III-V lab) [158]. HPTs with optical-gain cutoff frequency above 100GHz was developed using InP-base double-heterostructure with a cutoff frequency of 135GHz [159] and 447Ghz [160]. Table 1.3 presents a summary of the main characteristics of various HPTs, including the materials forming the epitaxial structure, thickness and doping base, the thickness of collector surface, the type of illumination and the wavelength, the current gain (H_{21}), the f_T and f_{MAX}, the responsivity, the f_{Topt}, the optical gain and quantum yield were measured [161].

.

Table 1.3 Summary of InGaAs based HPT [161]

Year	Laboratory	Type	Material	Wb [Å]	Base Doping [cm^{-3}]	Wc [Å]	Surface [µm^2]	λ [µm]	Illumination	H_{21} [dB]	f_t [GHz]	f_{max} [GHz]	R [A/W]	G_{OPT} [dB]	$f_{t\,OPT}$ [GHz]	η_{ext}
1980	Bell Laboratories	2T-HPT	InP/InGaAs				7,850		Under	X	X	X	X	60	2	X
1981	Bundespost	3T-HPT	InP/InGaAs	2,000 to 6,000	1e18, Zn	30,000	10,800	1.15	Under, Emitter window	63	15	X	0.56	19	2	70%
1991	AT&T Laboratories	3T-HPT	InP/InGaAs	2,000	7E+17	10,000	144	1.3	Under	39<>58	2<>16			46	10	35%
1991	Naval Research Laboratory	Illuminated HBT	InP/InGaAs	1,000	1E+19	2,900	80	0.62 and 1.53	Under, Inter-electrode	X	X	X	X	X	15 (pulse)	X
1991	Allied-Signal Aerospace Company	2T-HPT	InP/InGaAs/ GaAs/Si	2,000	1E+19	X	9,944	1.3	X	X	X	X	X	X	4.4 (pulse)	X
1993	AT&T Laboratories	3T-HPT	InP/InGaAs	X	X	10,000	24	1.5	Under	38<>42	52	33		X	X	52%
1993	ATR	Illuminated HBT	GaAs/ AlGaAs	X	X	X	120	0.83	Under, illuminated inter-electrodes	36 (DC)	30	X		25	>20	31%
1993	University of Michigan	3T-HPT	AlGaAs/ GaAs MQW	1,000	1E+19	5,700	92	0.853	Under, Emitter window	30	20	6	4.56	10	12 (pulse)	
1993	BT Laboratories	2T-HPT waveguide	InP/InGaAs	1,000	1e19, Zn	4,000	50	1.48	Lateral, Lens fiber	45	X	X	0.4	X	30	50%
1994	NTT	3T-HPT	InP/InGaAs	1,000	2e19^2e18, gradual	3,000	9	1.55	Under, reflexion sur electrode d'emetteur	44	128 (HBT)	53 (HBT)		36	14	21%
1995	KAIST, Korea	2T-HPT	GaInP/GaAs	800	1e19^1e18, gradual	5,000	1260	0.827	Under, Emitter window	X	X	X	X	29	2	X
1995	NTT	3T-HPT	InP/InGaAs	550	3.5E+19	3,300	20	1.3	Under, Emitter window	X	107	95	0.23	28	60	
1995	NTT	3T-HPT	AlGaAs/GaAs	X	X	X	20	0.83	Under, Entre electrodes	X	44	40	X	X	14	X
1996	King's College	3T-HPT	InP/InGaAs	2,500	6E+18	10,000	7,800	1.5	Under, Transparent electrodes	29	X	X	0.2	28	X	
1996	III-V lab (CNET)	3T-HPT	InP/InGaAs	1,000	2e19, C	5,000	70	1.55	Under, Emitter window	X	35 (HBT)	14 (HBT)		X	>20	11%
1996	IEMN	2T-HPT wave guide	InP/InGaAs	1,000	1e19, Be	4,000	72	1.3	Lateral, Lens fiber	X	X	X		X	25	43%
1996	IEMN	3T-HPT waveguide	InP/InGaAs	1,000	1e19, Be	4,000	32	1.3	Lateral, Lens fiber	X	20	X		X	40	43%
1996									Lateral, guide	28	32	48	0.21	X	X	
1997	III-V lab (CNET)	3T-HPT	InP/InGaAs	600	2E+19	5,000	48	1.5	Under, Base window	25	58	20	0.32	24	42	
1997	III-V lab (CNET)	3T-HPT	InP/InGaAs	600	2e19, C	5,000	70	1.55	Under, Emitter window	25	58	20	0.2	21	33	16%
1997	University of California	HPT a ondes progressives	AlInAs/ InGaAs	600	2.6E+19	7,000	40,000	1.3	Lateral, couplage evanescent par guide polymere	X	X	X		13	20	50%
1998	University of California	3T-HPT	InP/InGaAs	550	5E+19	4,000	36	1.5	Under, Base window	38	65	35	0.13	7	X	
1998	IEMN	3T-HPT	InP/InGaAs						Lateral, Lens fiber	36	X	X	0.29	17	X	
1999	III-V lab (CNET)	3T-HPT	InP/InGaAs	600	3E+19	5,000	14	1.5	Under, Base window	42	71	X	0.42	35	62	
1999	University of California	3T-HPT	InP/InGaAs	500	3E+19	7,500	44	1.5	Under, Base window	X	70	50				29%
2002	III-V Lab (Opto+)	3T-HPT	InP/InGaAs	600	3E+19	4,500	16	1.5	Under, Base window	X	121	51	0.2	32	110	
2002	NTT	3T-HPT	InP/InGaAs				34	1.5	Under, Emitter window	X	153	94	0.22	20	60	
2003	NTT	3T-HPT	InP/InGaAs			3,500	20	1.5	Under	X	163	135	0.26	X	80	
2007	NTT	3T-HPT	InP/InGaAs			3,500	20	1.5	Under, Emitter window	X	168 165	145	0.25 0.13	X	X	
2009	University of Maryland	UTC-HPT	InP/InGaAs	2,350	1e18 to 5e18 (multicouche)	(InP)	25	1.5	Under, Base window	X	X	X	0.2	37	52	

1.4.3.1 InP HPT based photoreceivers state of the art

InP based phototransistors are used for microwave photonic applications. The use of InP HPTs in an all-bipolar integrated photoreceiver circuit was demonstrated in 1988 [162]. It utilized a three terminal HPT as a photodetector and a bipolar amplifier circuit. Figure 1.24 shows the schematic diagram of the photoreceiver circuit. It used a transimpedance configuration due to its inherently wide bandwidth and large dynamic range. There have been several implementations of HPT based optoelectronic circuits and modules have been reported such as: opto-electronic amplifiers, opto-electronic mixers, and photo-oscillators.

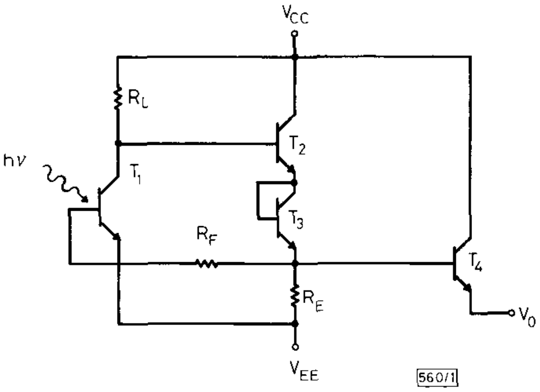

Figure 1.24 circuit diagram of a monolithic bipolar photoreceiver [162].

The monolithically integrated opto-electronic receivers using InP based HPT have been implemented using different amplifier configurations. A basic design of an inductively base loaded HPT first stage serves as a detector and initial amplification stage followed by a second stage HBT based amplifier was reported [163]. Figure 1.25 shows the schematic of this photoreceiver. A 40 GHz-Bandwidth photoreceiver with a photodetection gain of 22dB was achieved with a circuit design which consists of and HPT detection and amplification stage followed by a two stage amplifier [164]. This circuit design is shown in Figure 1.26.

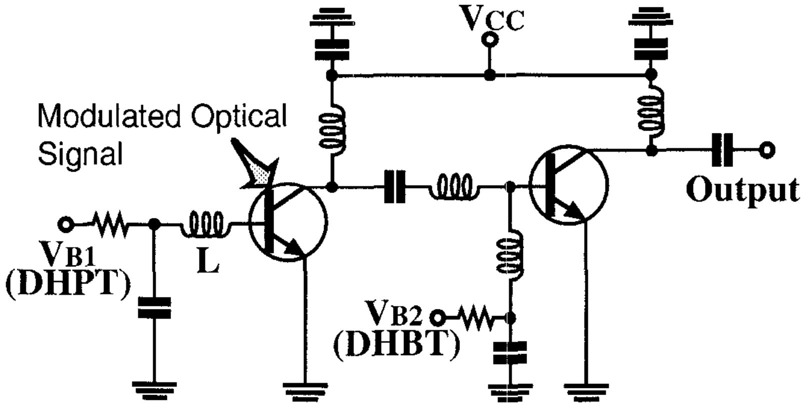

Figure 1.25 Schematic diagram of a HPT-HBT based photoreceiver [163].

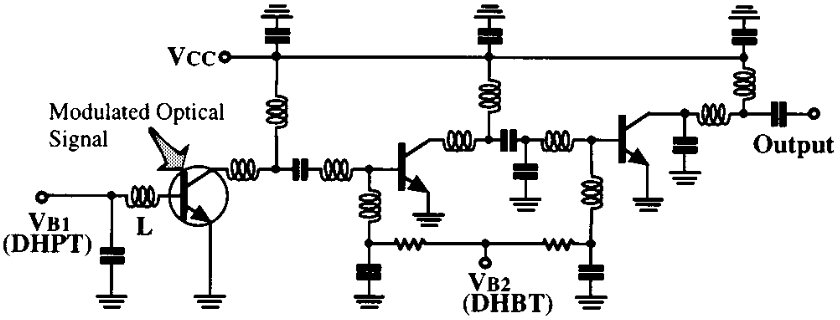

Figure 1.26 Schematic diagram of a photoreceiver composed of an HPT photodetection/amplifying stage and 2 stage amplifiers [164].

Another circuit implementation uses two cascode cells in the design of a 28 GHz narrowband amplifier [139]. The first cascode cell is composed of an HPT and an HBT, and the second cascode cell is purely HBTs. In a cascode cell the first device provides current gain while the second device provides voltage gain. Cascode configuration amplifier has a high frequency response because of the way the transistors are interconnected, the amplifier does not suffer from the Miller multiplication effects on the parasitic impedances, which limit the high frequency response. Figure 1.27 shows this implementation.

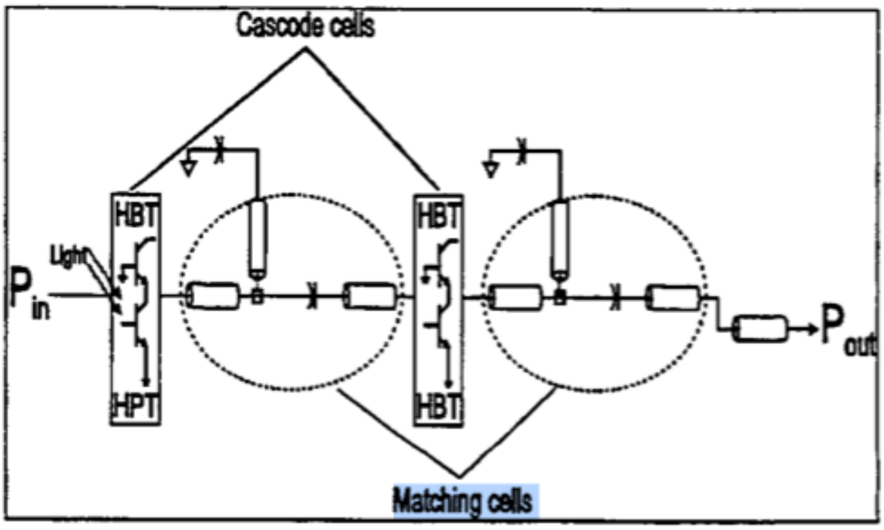

Figure 1.27 Narrowband OE amp using cascode cells [139].

A photoreceiver with an opto-microwave gain of 7.5dB at 32GHz was demonstrated using an HPT as the initial stage for detection and pre-amplification followed by a single transistor common emitter amplifier and a cascode cell for the final stage of amplification[130]. Figure 1.28 shows the schematic of the photoreceiver circuit.

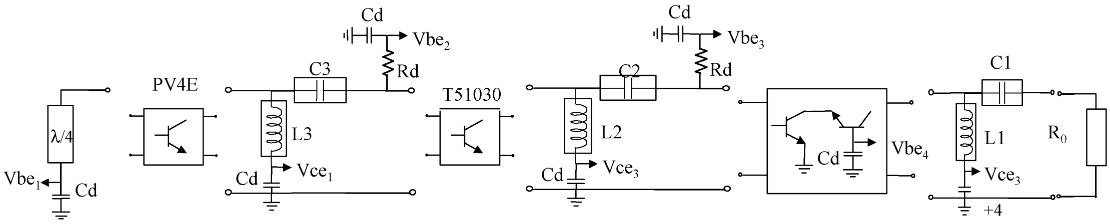

Figure 1.28 Photoreceiver composed of HPT plus two stage amplification [130].

1.4.3.2 InP HPT based mixers state of the art

The inherent non-linear properties of HPTs allow it to be used in an opto-electronic mixer [148], [165], [166]. HPTs have been demonstrated for optoelectronic mixing applications, where the local oscillator (LO) signal was provided electrically [167],[165],[168],and optically [169] , [170]. A single HPT and supporting passive elements for biasing was used to demonstrate its capabilities to be used as on OE mixer. An upconversion O/E mixer was reported using the base as an input for the local oscillator LO of 30GHz, and an optical signal that was modulated with an IF signal from 200MHz up to 2GHz [165]. It had a conversion ratio of 26dB (loss). A single stage downconversion mixer was demonstrated using 3.1GHz as the LO and a 3.1GHz modulated optical beam with conversion gain of -5.1dB [134]. Figure 1.29 shows the schematic diagram of the experiment on single-stage HPT downconverter mixer.

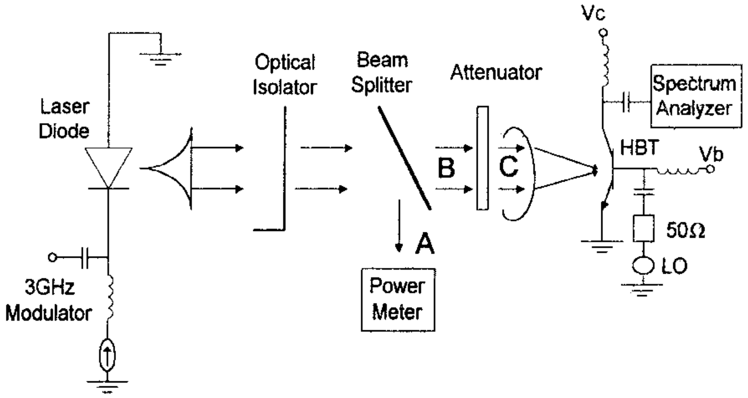

Figure 1.29 Single stage HPT mixer with input LO in the base [134]

A demonstration of a two-terminal edge coupled InP base HPT shows a conversion gain of 7dB [167]. Figure 1.30 shows the schematic diagram of the two-terminal single stage mixer. The HPT emitter was connected to an external SMA connector via a short 50Ω microstrip transmission line. A microstrip coupled line diplexer was employed to separate the 500-MHz intermediate frequency (IF) and 3-GHz LO signals at the HPT emitter. The diplexer loss was 2.13 dB for the LO and 0.07 dB for the IF. The optical signal is modulated by 2.5GHz

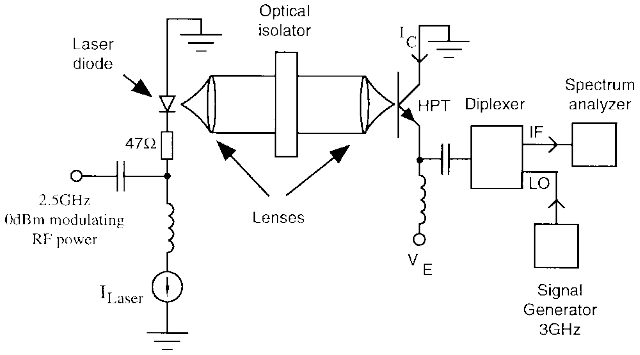

Figure 1.30 Single stage two terminal HPT OE mixer [167].

A narrow band upconversion mixer circuit was designed to upconvert an IF signal of 2GHz to 28GHz or 42GHz by mixing it with a 26GHz or 40 GHz LO signal that is fed to the base of a single stage HPT with a matching cell in the base designed to match the characteristic impedance of the LO [171]. Figure 1.31 shows the schematic diagram of the LO matched single stage HPT based OE mixer. The conversion gains achieved with this circuit are of 12dB and 9.2dB at respectively 28GHz and 42GHz.

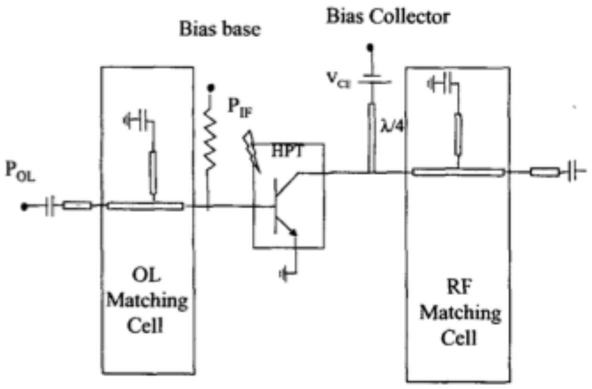

Figure 1.31 Single stage HPT OE mixer with LO matching circuit [171].

A study on a single stage UTC-HPT based OE upconversion and down conversion mixer shows that the HPT mode of operation shows better performances compared to PD mode of operation[172]. A difference of 24dB was observed in the output power of the mixer between HPT mode and PD mode due high internal gain of the HPTs. Figure 1.32 shows the experimental setup for the up conversion measurements.

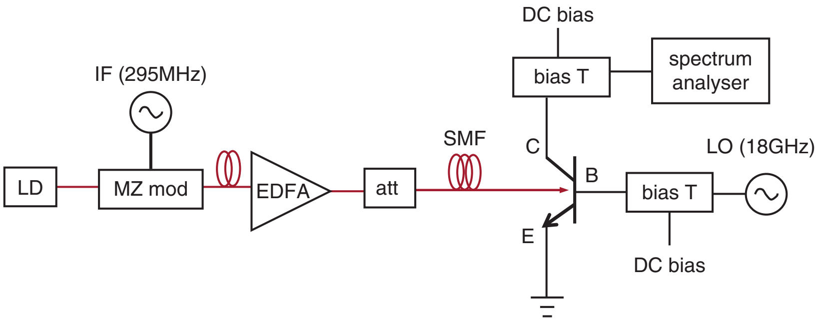

Figure 1.32 UTC HPT in OE upconversion and downconverstion mixer [172].

Demonstration of single stage HPT OE mixer in more complex operations are shown in a 30Ghz optical injection locked self oscillating optoelectronic mixer [170]. This mixer is used as a harmonic upconverter for a 60 GHz RoF downlink transmission of a 20Mbps 16 QAM. Figure 1.33 shows the schematic diagram of 30GHz optical injection locked (OIL-SOM) based on an InP/InGaAs HPT with a simple feedback loop connecting collector port to base port through a 30GHz-band band pass filter

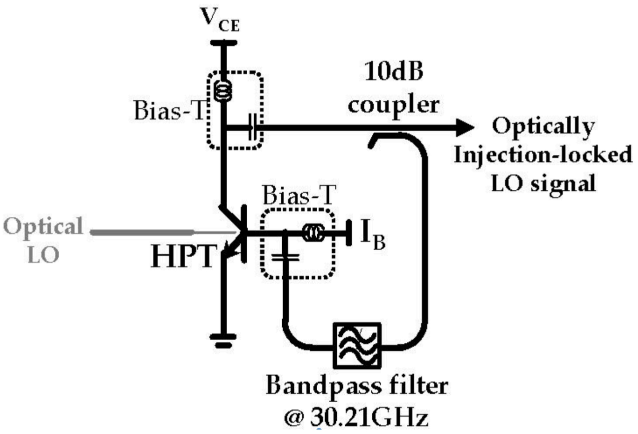

Figure 1.33 Schematic diagram of a 30GHz OIL-SOM [170].

The HPT based OE mixer is used in a 60-GHz band remote up/down conversion bidirectional RoF link [168]. The configuration of proposed bidirectional RoF link is schematically shown in Figure 1.34. With the help of remotely delivered optical LO signals, a single HPT optoelectronic mixer can perform both frequency up- and down-conversion. This approach provides the possibility of eliminating frequency mixers and phase-locked oscillators in base stations, it is expected to reduce the complexity and cost of bidirectional RoF base stations.

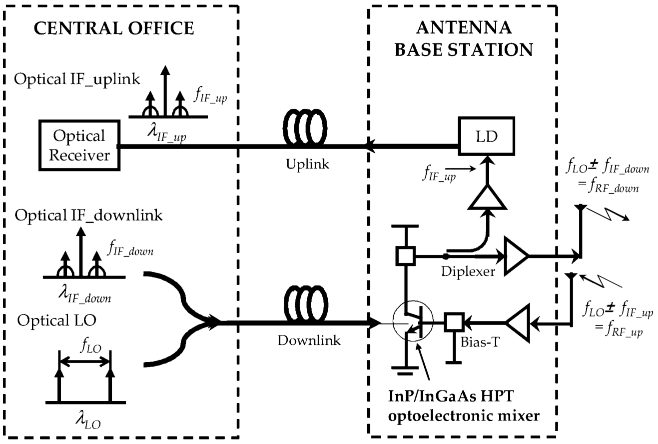

Figure 1.34 Bidirectional OE mixer [168]

The cascode configuration is known to provide wider bandwidth compared to a single device amplifier configuration and used in the design of OE mixers. An HPT based OE cascode OE mixer was demonstrated in a single stage configuration [173], and two stage configuration [171], [158]. The single cascode HPT optoelectronic mixer has a maximum intrinsic and extrinsic down-conversion gains of 18.2dB and 7.4 dB, respectively, for an RF optical–intensity modulation frequency of 3GHz and LO frequency of 3.5 GHz. The intrinsic up-conversion gain varied from 6.9dB to 5.7dB for output frequencies in the range of 6.5GHz-19.5GHz respectively.

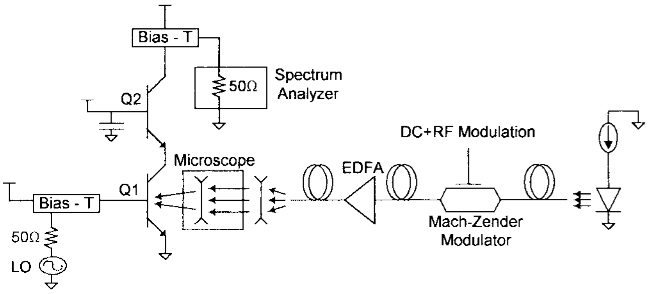

Figure 1.35 HPT based OE Mixer using single cascode configuration [173]

Figure 1.36 shows the schematic diagram of the single stage cascode OE mixer. In the two stage cascode configuration, the first cascode cell comprises one HPT and one HBT, the second one comprises two HBTs. All the three HBTs are identical. In the first cascode pair, the HPT acts as the opto-electronic mixer while the HBT acts as the first amplifier stage. The matching cell between the two cascode cells was designed to maximize the power gain of the circuit at the 28GHz upconverted signal and the second cascode pair achieves further amplification of this signal. Figure 1.36 shows the schematic diagram of the two-stage cascode OE mixer. The optimum mixing results were achieved by biasing the cascode connected HPT/HBT in its active region, and to avoid intermodulation effects, the second HBT/HBT cascode was biased into its dynamic range, lower to the 1dB compression point. The conversion gain achieved with this circuit is 17.8dB at 28GHz.

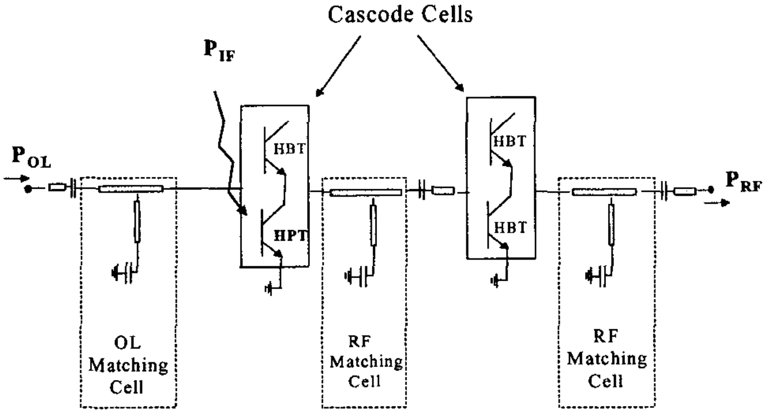

Figure 1.36 Schematic diagram of an HPT based OE mixer using a two stage cascode configuration [158], [171]

1.4.3.3 InP HPT based oscillators

HPTs have been proposed for the monolithic integration of direct optical injection-locked oscillators (D-OILOs) [174] [150]. In this type of oscillators, the optical control signal is intensity modulated by the locking signal (or reference signal) at a frequency f_{ref}, close to the free running frequency f_o of the oscillator. Figure 1.37 shows a schematic diagram of the D-OILO . It consists of an HPT and a resonant circuit which includes a variable resistor and inductor. The HPT is both the photosensitive and amplifying element of the oscillator.

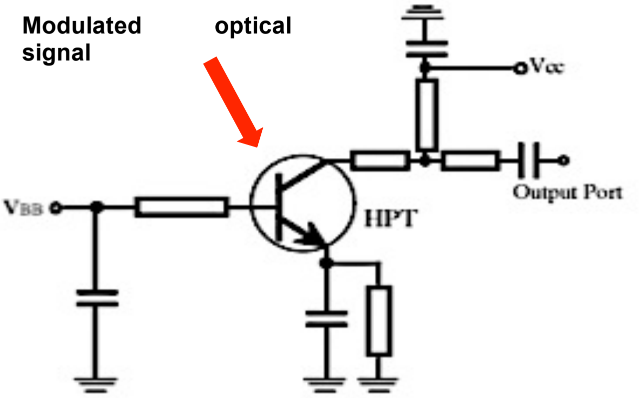

Figure 1.37 D-OILO [175]

The modulated optical signal illuminates the active region of the photo-HBT and is absorbed. In this manner, the locking signal is injected into the oscillator circuit. If f_{ref}, is equal to f_o , fundamental frequency injection-locking occurs. Two D-OILOs at 10GHz and 39GHz have been reported to have an injection-locking range measured was 14% and 2% of the oscillator free-running frequency, respectively [175]. Using a backside illuminated HPT, a D-OILO at 96GHz was demonstrated. [176]. An OILO oscillator running a 60 GHZ offers flexibility in the injection of the optical locking signal by having both the top and back side illumination windows [177]. Low cost HPT based self-injection locked oscillators have been reported to have 55dB phase noise reduction at 10kHz frequency offset from the center frequency of 10.8GHz by injecting 8dBm optical signals without using any high speed optoelectronic components [178].

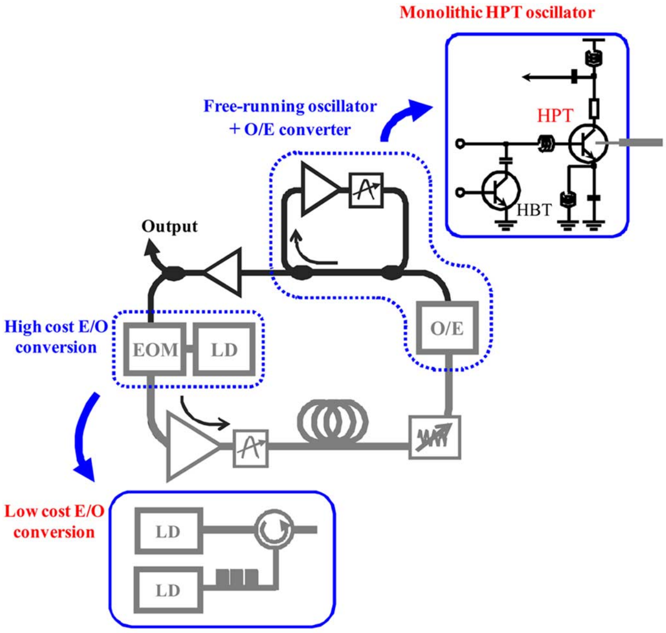

Figure 1.38 Configuration of the HPT based SiL oscillator [178]

The different use of an HPT in an optoelectronic system shows its versatility and a potential in the implementation of low-cost high performance monolithic opto-electronic circuits and systems.

1.4.4 SiGe Phototransistors

The use of a SiGe heterojunction enhances the absorption of Si-based detectors and help extending the cutoff wavelength to longer wavelengths such as 1310 nm and 1550nm. Using this material with phototransistor structure allows for high- speed photodetectors with an internal gain due to the transistor effect. The intrinsic gain results in a high responsivity, and high-speed operation is due to the heterojunction bandgap-offset. This also allows monolithic integration with microelectronic circuit of electronic signal processing. This latter point is actually the main advantage that can be foreseen.

Early studies in $Si_{0.4}Ge_{.0.6}$ phototransistor that are compatible to silicon utilized silicon on insulator via separation of by implantation of oxygen (SIMOX) processing. It used multi-quantum wells (MQW) that are inserted in a vertical resonant cavity which operates at 1300nm wavelength [179]. The structure is a multi quantum well resonant cavity heterojunction phototransistor. The structure is shown in the Figure 1.39. The SiGe/Si MQW acts as the base and the absorption layer. The cavity is defined by the lower SIMOX substrate and the upper $Si0_2$/Si mirror.

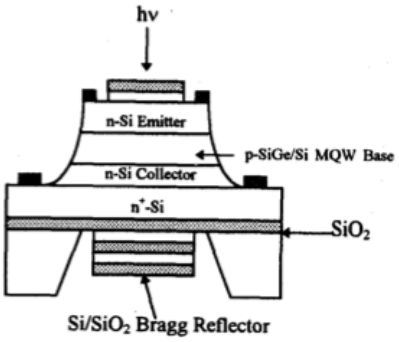

Figure 1.39 Cross section of a SiGe/Si resonant cavity phototransistor on SIMOX [179].

Several years after the study of MQW SiGe/Si on SIMOX, multi-quantum well $Si_{0.5}Ge_{0.5}$ /Si HPT that operates at 850nm and 1310nm with a 1.25 GHz bandwidth was reported [180]. The Figure 1.40 shows the schematic and the electron microscopy photograph of the HPT. The phototransistor is fabricated using a baseline process of HBT with f_T of 50 GHz. The multiple $Si_{0.5}Ge_{0.5}$/Si quantum wells (MQW) are placed between the base and the collector of the Si/SiGe heterojunction bipolar transistors as light absorbing layers. The HPT has an emitter area of 6μm^2 and an optical opening of 14.4 μm^2 through the base collector junction. The phototransistor's f_T is 25GHz which is lower value due to the MQW. In PD mode operation where the emitter is open, the phototransistor has a responsivity of 14mA/W. This low responsivity is due the relatively thin absorption layer of 0.15μm as compared to the absorption length of $Si_{0.5}Ge_{0.5}$ at 850nm which is 3μm. In a base open 2T-HPT operation, the responsivity of the SiGe HPT is at 1.47A/W At 1310nm, the 2T-HPT responsivity is 0.15 A/W. The HPT's cutoff frequency was extracted through impulse response measurements using an 830nm mode-locked Titanium- Sapphire pulse laser. Using the same HPT implementation, a larger HPT device exhibits 17A/W with a cutoff frequency of 0.55 GHz [181], [182].

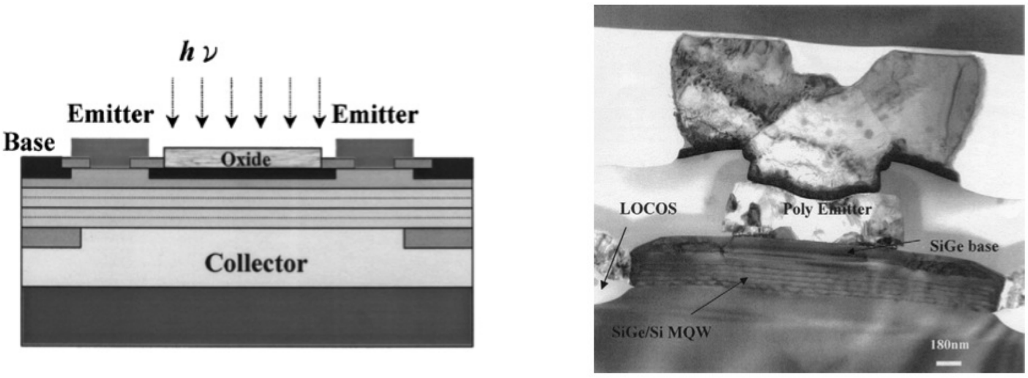

a) b)

Figure 1.40 MQW HPT a) schematic b) electron microscopy photograph [121]

The use of MQW SiGe/Si has demonstrated high responsivity and high bandwidth detection in the 1310nm and 155nm wavelengths, which makes it a viable alternative for use in the various optical communication applications. This approach is not straight forward to implement in commercial SiGe-based processes and at 850nm wavelength detection, a single SiGe layer could be used. The SiGe HPT should be fully compatible with the SiGe HBT structure that is found in commercial SiGe based technologies. This allows for monolithic integration with electronic signal processing circuits, and extends the existing application list of SiGe based technologies to include OE functionalities without the addition of masks and processing steps. These microwave SiGe phototransistors provide an innovative solution for the integration of optoelectronic functions in commercial SiGe bipolar or BiCMOS process technologies, as opposed to SiGe MQW structures. These devices have since been fabricated using several industrial process technologies: Atmel [132], [183], TSMC [182], IBM[184] , and AMS [185] [186].

Integrated phototransistors allows for the adding of new functionality to existing process technologies without the need for process modifications. The transistor action allows amplification that is readily available in the detector device. Low bias voltages are sufficient and there is no need for very high avalanche voltages. Monolithically integrated detectors offer benefits over hybrid or external detector that can be exploited.

First generation HPTs fabricated in the ATMEL SiGe Bipolar process shows a responsivity of 1.49A/W at 940nm in the 3T-HPT mode with constant current base bias and biasing values of 1.5 V V_{CE} and I_B of 60µA. Its frequency bandwidth is in the order of 400 MHz [132] [172]. Figure 1.41 shows a cross section of the reference HBT for the HPT structure and a top view of the 10x10µm^2 HPT. The phototransistor structure is made without any additional absorption structure and is purely based on the SiGe bipolar technology process. The base profile is abrupt with a Ge content in the range of 20%-25%. The heterojunction allows for a high base doping when compared to a pure Si BJT. This is taken into account for the enlargement of the lateral size of the HPT. The enlargement allows for optical coupling of the fiber. The HPT is vertically illuminated through a 10x10µm^2 optical window above the emitter. This HPT structure has a measured f_T of approximately 20GHz. It has a lower f_T as compared to the HBT devices with f_T of 30GHz in this process due to the enlargement of the structure to accommodate an optical window. However it is still considerably high due the high base doping that is greater than 10^{19}cm^{-3}.

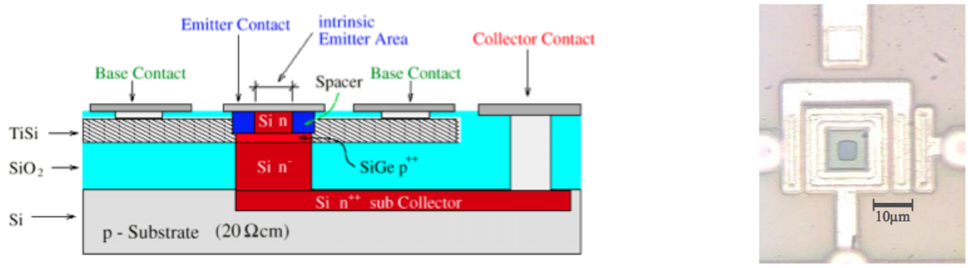

a) b)

Figure 1.41 1st Generation SiGe HPT using Atmel technologies (a) sketch of the vertical structure of the SiGe HBT. (b) Chip photograph of the 1st Generation SiGe HPT with a 10x10um^2 optical window in the emitter [132]

In a SiGe BiCMOS process and at 850nm wavelength of operation, a responsivity of 0.43A/W with a frequency bandwidth of 3GHz bias at V_{CE} = 2V and V_{BE} =0.4V was reported from a SiGe HPT implemented in TSMC process [182]. Using a 0.25µm IBM SiGe BiCMOS process an HPT with responsivities of 2.4A/W and 0.12A/W were achieved under 850nm and 1060nm operation respectively under 2T phototransistor mode (base open). And a bandwidth of above 500MHz for a 10x10µm^2 HPT was demonstrated [187]. In this paper, phototransistors were made by modifying the commercial SiGe HBT structure in IBM 0.25μm SiGe BiCMOS process. The photo detecting window was incorporated by removing silicide layers that block the optical absorption and the existing layers were manipulated The HPT has a dimension of 51x43µm^2 which is approximately the area of the base region. [187].

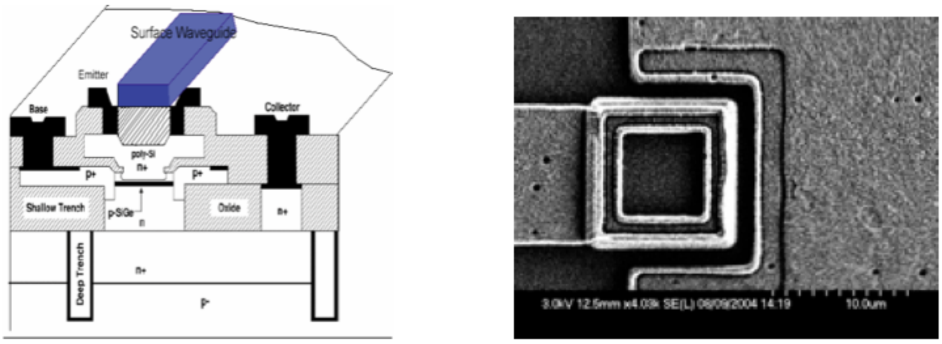

a) b)

Figure 1.42 HPT fabricated using an IBM BiCMOS process technology [188] (a) schematic cross section (b)Chip photograph of HPT (electron microscopy)

Smaller sized HPTs using the IBM SiGe BiCMOS process show that a 6x10µm^2 has a responsivity of 2.7A/W with an electrical cutoff frequency of 2.3 GHz with Vce = 1.5V and Ib = 10µA The opto-microwave cutoff frequencies of these devices measured from pulsed laser measurement are 2.0GHz, 2.1GHz and 5GHz from the HPT sizes of 6x10µm², 5x5µm² and 2x2 µm² finger structure at 850nm and a biasing point of Ib= 2μA and Vce = 2V. It is not clear from the papers of those values were measured in the HPT of PD mode.

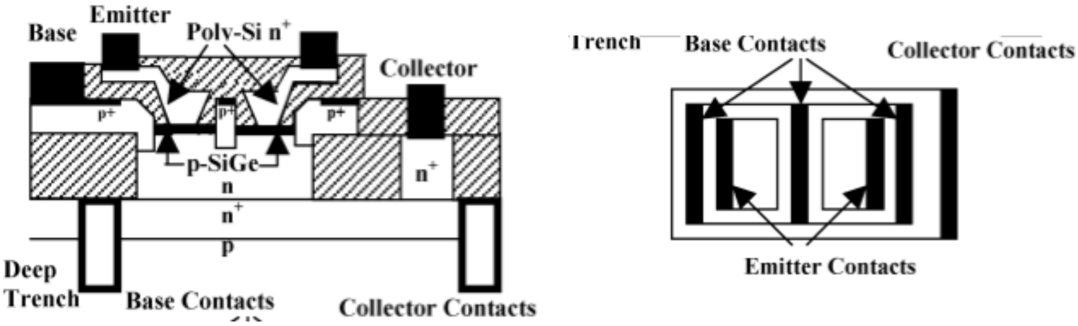

a) b)

Figure 1.43 Second Generation of HPT in IBM BiCMOS using fingered layout a) cross section b) top view [184]

SiGe HPTs implemented on AMS 0.35µm SiGe BiCMOS process were studied by [186]. They have studied extended base collector HPTs with different optical window sizes. Special emphasis was on measurements of link opto-microwave performances using VCSEL of wavelengths 410nm, 675nm, 785nm, and 850nm. This technology has no silicide layers. The transistors are designed with an enlarged base-collector junction area which serves as a photodiode in which, the photocurrent is amplified by the intrinsic transistor part of the device. It has a base node, which is used for base biasing to help speed up the detectors response and to slightly raise responsivity. The emitter capacitance is maintained low and kept as small as possible to avoid slowing the device by making the emitter area as small as possible.

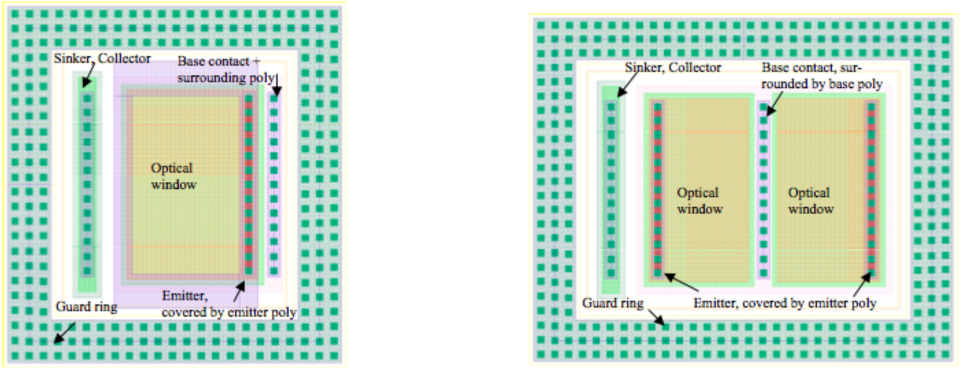

a) b)

Figure 1.44 HPT layout of enlarged BC region fabricated in AMS (a) 6μm x 10μm b) 10μm x 10μm [186]

The Table 1.4 shows a summary of the different SiGe based HPT that were reported in literature. It highlights the size of the intrinsic transistor and the vertical structure configuration of the semiconductor materials, whether is its and extended base and collector (xBC) HPT or an extended emitter base and collector (xEBC) HPT. It also summarizes the DC responsivity of the HPT and how it was extracted as well as the opto-microwave cutoff frequency. .

Table 1.4 State of the art of SiGe HPTs.

Group	Process	Year	Reference	SiGe layer	f_T of Process (GHz)	f_T of HPT Electrical (GHz)	Intrinsic transistor Size (um)	Optical window Size(um)	HPT vertical structure	HPT MODE 2T/3T	DC Responisivity A/W	Lambda (nm)	Q.E	Beta (elect)	Beta Opt	-3db optical	-3bB elect	Product GHzA/W
ITRI (TWN)	ITRI	2002	[180]	MQW	50	25	0.6x10	14.4 um²	xBC	2T	1.47 (1)	850	-----	300	120 (2)	1.25GHz (3)	-----	1.84
										2T	0.15 (1)	1310	14%	300	-------	-----	-----	
ITRI (TWN)	ITRI	2003	[121]	MQW	-------	25	0.6x10	(4)	xBC	2T	1.90 (1)	850	2.78%	160	-----	----	-----	
										2T	1.25mA (1)	1310	$1.18x10^{-3}$	160			-----	
ITRI (TWN)	ITRI	2003	[181]	MQW	----	28	---	----		2T	17 (1)	830	---	----	140 (2)	0.55GHz (3)	-----	9.35
	TSMC			single	------	------	---	----		2T	0.4 (1)	830	----	---	70 (2)	1.5 GHz (3)	-----	
ITRI (TWN)	TSMC	2004	[189]	single	50	----	0.6x10.8	----	xBC	2T	0.7(1)	830	----	81	70(2)	1.8 GHz (3)	-----	1.26
ITRI (TWN)	ITRI	2004	[190]	MWQ	---	---	---	---		2T	17.5(1)	850	---	3000	---	0.55 (3)	-----	9.63
				MQW	---	---	----	---		2T nkt	1.2[(a)	850	---	200	---	1.2 GHZ(3)	-----	1.44
ITRI (TWN)	TSMC	2004	[190], [182]	single	---	---	---	---		2T	0.36(1)	850	---	100	---	1.5 GHz(3)	-----	0.54
				single	---	---	---	---		2T nkt	0.43 (1a)	850	---	100	---	3GHZ(3)	-----	1.29
ESYCOM (FR)	Atmel	2003	[132].	single	30	18.9	~10x10	10x10	xEBC	3T CV	1.49 (B)	940	----	145	---	0.4GHz (6)		0.59
Cornell (USA)	IBM SiGe	2004	[122]	single	47	-------	~51x43	51x43	xEBC	2T	2.4 (1)	850				N/A	-----	N/A
										2T	0.2 (1)	1060				N/A	-----	N/A
				single		-------	~10x16	10x16	xEBC	2T	2.1 (1)	850		100	78	N/A	-----	N/A
										2T		1060				N/A	-----	N/A
Cornell (USA)	IBM SiGe	2004	[187], [188]	single	47	------	~10x16	10x16	xEBC	2T	2.4 (1)	850				0.518 GHz (5)	-----	1.24
	IBM SiGe	2004							xEBC	2T	0.2(1)	1060					-----	
Cornell (USA)	IBM SiGe	2006	[184]	single	47	------	~6x10	6x10	xEBC	3T CC w finger	2.7 (C)	850	393%	68		2.0GHz (2)	2.3	5.94
						------			xEBC		0.13 (C)	1060	----			----	-----	
						-----			xEBC		0.07 (C)	1310	-----			----	-----	
				single		------	~5x5	5x5	xEBC	3T CC	----	850	----			2.1 GHz (2)	-----	
				single		------	~2x2	2x2	xEBC	3T CC w finger	-----	850	230%	90		5.3 GHz (2)	7.7	
IMCD (AW)	AMS	2008	[186]	single	60		0.35x10	10x10	xBC	3T CV	1.10 (B)	675	----	----	----	87MHz	476MHz	
										3T CV	---	850	---	-----	---	70MHz		0.09
				single			0.35x10	6x10	xBC	3T CV	1.76 (B)	675	---	---	---	110MHz	349MHz	
										3T CV	----	850	----	---	---	140MHz		0.19
				single			0.35x4	1x4	xBC	3T CV	0.93 (B)	675	----	---	---	279MHz	1.25GHz	
										3T CV	-----	850	---	---	---	250MHz		0.26
				single			0.35x20	20x20	xBC	3T CV	---	410	----	---	---	62MHz	321MHz	
										3T CV	1 [B]	675	---	---	---	------		

----- not mentioned
MQW = multi quantum well SiGe
Single = single layer SiGe
xBC = extended base and collector
xEBC = extended emitter base and collector
(1) base contact floating common emitter , 2T
(2) beta opt = ic (hpt mode) /ic(pd mode)
(3) from impulse response--- also called * FFT transformed electrical bandwidth, *calls it also optical bandwidth
(4) ratio of spot to optical window = 340
(5) illunated base open sparameter measurements
(6) OM link gain measurements
(1a) floating base,grounded emitter
(B) constant voltage base bias
(C) constant current base bias

Developments on SiGe based HPTs are still in the research and prototype stages. Commercial SiGe HPT based products are not yet available in the market. Device modeling and circuit designs are essential research activities which are necessary in the inroads to favorable utilization of the SiGe HPT in commercial products. In SiGe HPT modeling, a MEXTRAM based equivalent model was developed [191]. It used a MEXTRAM HBT model, and a parallel base-collector photodiode. A model of the optical dependence of the capacitance of a SiGe HPT was studied in order to build an optically controlled oscillator [185], [192]. The base-load effect on SiGe HPT is one point that is needed to be studied to help in the design of optoelectronic circuits. A work on InP/InGaAs HPT in which the RF base load impacts in a current biased base terminal [130] serves as reference point for this study. A fully analytical approach in modeling HPTs help provide and insight in the difference on the effect of voltage and current biasing schemes [193]. An approach to deal with the RF and DC contribution of the base in the three terminal of the HPT has been initiated using physical modeling and virtual experimentation [194],[129]. SiGe HPT was utilized in the implementation of optical interconnects [122] and photo oscillators [192], [195]

The development of SiGe HPTs in ESYCOM started in the modeling of the optical absorption properties of SiGe/Si photodetectors [196] [131]. The first SiGe HPT was developed using a commercial SiGe Bipolar process from Atmel GmbH [132]. The physical modeling of the HPT structure was developed using semiconductor device modeling software [183]. The 1st generation of SiGe HPT used a SiGe processing technology that has an abrupt profile in the base which was evaluated to be 23% using physical simulations[183]. This favors optical absorption in the base and supports fast HBT even with increased physical dimensions, a condition that is favorable in the implementation of HPT with large optical window while having high-speed properties.

1.4.4.1 SiGe HPT based circuits

The integration of a high speed photodetection element operating at 800nm to 1000nm in a silicon based process technology extends its application into the optoelectronics domain. A digital optical receiver topology is shown in Figure 1.45 [197]. It is composed of a photodetection element, the induced photocurrent goes to a transimpedance amplifier. The converted signal is further amplified by a low noise amplifier before it is decoded as a logic 1 or logic 0. A SiGe HPT is used to replace a photodiode as an optical detector.

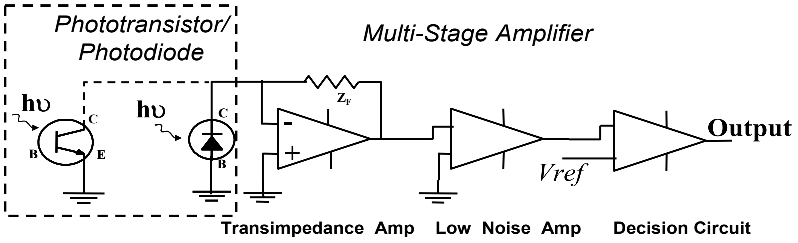

Figure 1.45 Architecture for a SiGe HPT based optical receiver circuit [197]

An circuit implementation of the digital optical receiver topology is presented in Figure 1.46a) [198]. It is a low-voltage supply optoelectronic detector-receiver circuit designed for fabrication using in a commercial silicon-based process. Figure 1.46a) shows a layout view of this circuit.

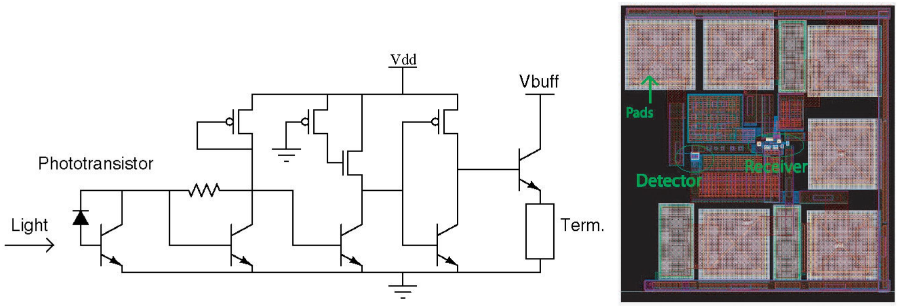

Figure 1.46 a) schematic b) layout [198]

A monolithic integrated SiGe optical receiver and detector was implemented using a the IBM SiGe BiCMOS process [199]. It is composed of a SiGe HPT, a transimpedance amplify, three post amplifier stages and an output driver. Figure 1.47 (a) shows the die photo of the SiGe HPT based integrated optical receiver. The receiver is characterized using a high speed 850nm laser that is vertically coupled using a multimode fiber probe. The resulting eye diagram from the output of the optical receiver with a pseudo random binary sequence at 1GHz input is shown in Figure 1.47 (b).

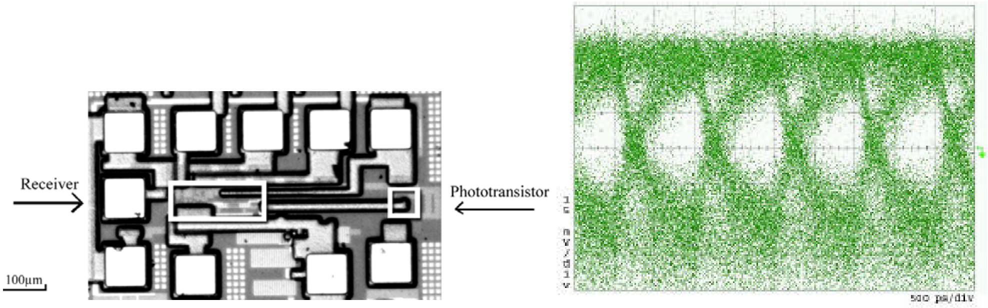

Figure 1.47 (a)Die photo of fabricated integrated optical receiver using SiGe HPT (b) Eye diagram from output of SiGe based optical receiver (2^7-1 PRBS at 1Gbps) [199]

SiGe HPTs are also studied for its use radio over fiber systems. The SiGe HPT is used as an opto-microwave conversion device to produce the radiated microwave carrier. It is a fully integrated a SiGe HPT based oscillator with an active inductor in the base and an active resonator in the emitter [192]. The schematic diagram and the layout of the photo-oscillator implemented using the Austria Mikro Systems 0.8µm BiCMOS process is shown in Figure 1.48. An improved SiGe HPT based light controlled photo-oscillator is also investigated to be used as a component of an optical network-on-chip (ONoC) [195].

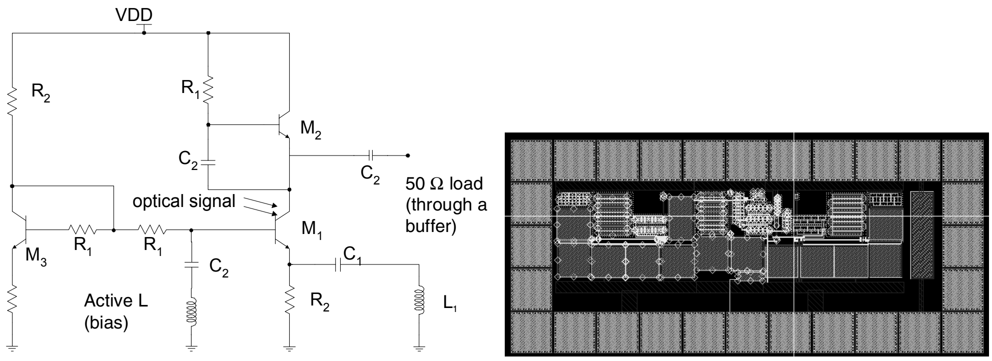

a) b)

Figure 1.48 (a) Schematic diagram of a SiGe HPT based photo-oscillator for radio over fiber systems at 5.2GHz (b) Layout of the photo-oscillator circuit [192]

1.5 Conclusion

In this chapter, we have presented the radio over fiber technology, which is the merging of wireless network applications and optical networks application. RoF, a technology that is traditionally used to extend the reach of wireless signals in an external environment, is now under study for use in indoor environments such as the home. The home is currently the frontier of high data rate environment where approximately 10Gbits/s are currently exchanged Radio over fiber technologies for home applications need to have low system costs. SiGe-based phototransistors as photodetectors in these systems would offer lower cost remote antenna units. This offers the solution of monolithically integrated optoelectronic receiver circuits as well as a monolithically integrated optoelectronic receiver and electro-optical driver circuits.

2 SiGe HPT Technology for 850nm, Operation and Characterization Techniques

2.1 Introduction

A bipolar phototransistor is essentially a bipolar transistor whose base collector junction is reversed biased and acts as a photodiode. As the photo generated current is amplified by the transistor action, a phototransistor can achieve higher responsivity as compared to a PIN photodiode.

The idea of a phototransistor was first proposed by William Shockley who introduced the bipolar configuration for phototransistor operations [200]. He proposed a bipolar transistor structure in which the base current is generated by an optical wave. The first phototransistor was demonstrated in 1953 using Germanium (Ge) in Bell Laboratories [201]. The early phototransistors that were realized are based on Ge and Silicon (Si) for detection in the visible range up to the infrared range. However, they are regarded as slow photodetectors. The III-V materials like Gallium Arsenide (GaAs) and Indium Phosphide (InP) are used mainly as sensors because of their superior high frequency performances in the detection of higher wavelength region up to 1550nm.

This chapter is focused on the SiGe based phototransistors, providing a discussion on the material used in the implementation of the phototransistor the. In Section 2, the electrical and optical properties of SiGe alloys of unstrained (bulk) and strained (pseudomorphic) types are discussed. This provides the understanding of the material that is utilized in a compound semiconductor processing technology. Section 3 gives an overview of a specific 80GHz SiGe bipolar technology from Telefunken GmbH that will be our target for the next generation integrated SiGe HPT. The characteristics of SiGe

HBT that is available in this process technology provides an achievable DC and RF performance. This is an essential step as this provides the baseline electrical performance reference for the phototransistor that will be implemented in this processing technology. The different SiGe Heterojunction Bipolar Phototransistors (HPT) are essentially modified versions of SiGe HBT that are also presented in this section. Section 5 shows the electrical validation of the HPTs. It includes the DC characterization, and RF characterizations of the fabricated HPTs. The measurement setups for optical and opto-microwave characterizations are then detailed in section 6 as well as the reference analog optical links that will be used for the absolute characterizations of the opto-microwave response of the HPTs.

2.2 Silicon Germanium Alloys: Electrical and Optical Properties

The first transistor on Si was presented in 1954. The Si-based transistors developed rapidly because they have less expensive production cost as well as the ease of use of Si as opposed to Ge. Si became one of the main materials for electronics. Texas Instruments played a major role in the early days of the use of Si for electronics; the first transistor on Si in 1954; the first integrated circuit in 1958.

In William Shockley's patent on the first BJT and first phototransistor in 1951 [202], he already mentioned the concept of a heterojunction and hence, an heterojunction bipolar transistor (HBT). He envisioned a mix of Si and Ge, and thus obtained a SiGe alloy that could be integrated with Si-based components. The early theoretical studies on phototransistors were made by Kroemer in 1957[203] until 1980's [204], [205]. The early studies on relaxed bulk SiGe materials were made in the 1958 as well. [206]. Two decades after, the first SiGe layer constrained over Si [207] was fabricated, and in 1987 first SiGe HBT using molecular beam epitaxy was presented [208] .

During those days the main issues in the development of a heterojunction in a Si process is the lack of materials compatible with Si. The crystal structure of Si is diamond-like lattice. Certain materials like Gallium Phosphide (GaP), Aluminum phosphide (AIP), and Zinc Sulfide (ZnS) have lattice constants that are the same for Si (a = 0.5431nm). However, their crystal follows a Zincblende structure, which is different from a diamond structure, and as a result, could not be used for heterostructures with Si.

2.1.1 Bulk SiGe Alloy

Silicon and Germanium are chemical compatible semiconductors. Both are from the Group IV elemental semiconductors and crystallize in a diamond lattice structure. Table 2.1 shows the properties of bulk Si and Ge.

Table 2.1. Properties of Bulk Si and Ge

Parameter	Units	Silicon	Germanium
Atomic number	-	14	**32**
Atomic density	(atoms/cm^3)	5.02 x 10^{22}	**4.42 x 10^{22}**
Atomic weight	(g/mole)	28.09	**72.6**
Density	(g/cm^3)	2.329	**5.323**
Electronic orbital configuration	-	(Ne)$3s^2 3p^2$	**(Ar)$3d^{10} 4s^2 4p^2$**
Crystal structure	-	diamond	**diamond**
Lattice constant (298 K)	(Å)	5.43107	**5.65791**
Energy band gap (low doping)	(eV)	1.12 (300° K)	**0.664 (291K)**
		1.17 (77K)	**0.741 (4.2K)**
Equiv. conduction band minima	-	6	**8**
Effective electron mass (300° K)	(x m_0)	1.18	**-**
Effective hole mass (300° K)	(x m_0)	0.81	**-**
Intrinsic carrier density (300° K)	(cm^{-3})	1.02 x 10^{10}	**2.33 x 10^{13}**
Eff. conductive band DoS (300° K)	(cm^{-3})	2.8 x 10^{19}	**1.04 x 10^{19}**
Eff. Valance band DoS (300° K)	(cm^{-3})	1.04 x 10^{19}	**6.00 x 10^{18}**
Electron mobility (300° K)	(cm^2/V-sec)	1450	**3900**
Hole mobility (300° K)	(cm^2/V-sec)	500	**1900**
Electron diffusivity (300° K)	(cm^2/ sec)	37.5	**100**
Hole diffusivity (300° K)	(cm^2/ sec)	13	**49**
Optical phonon energy	(meV)	63	**37**
Phonon mean free path length	Å	76	**105**
Intrinsic resistivity (300° K)	(Ωcm)	3.16 x 10^5	**47.62**

Table 2.1 shows a lattice mismatch of 4.2% between Si and Ge. This is comparable to widely used III-V systems such as GaAs and InAs (7.16%) and GaAs and InP (3.81%). It is possible to create a SiGe alloy, which is completely miscible over the full range of composition and can be combined to form $Si_{1-x}Ge_x$ alloys, where the Ge content x can range from 0 to 1.

The lattice constant of $Si_{1-x}Ge_x$ from the diffraction measurements follows a parabolic relation in the form of the equation [209].

$$a(Si_{1-x}Ge_x) = 0.002733x^2 + 0.01992x + 0.5431(nm) \tag{Eq. 2.1}$$

The fraction x of Ge will also influence the other parameters of the alloy: the band gap, the relative dielectric constant, the effective density of states, the valence band and the conduction band. The energy bands of the two extremes are represented in k-space direction at 300° K as shown in Figure 2.1.

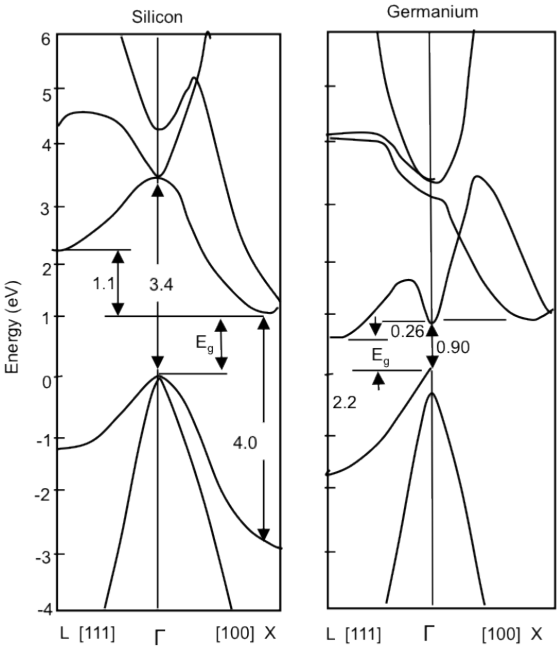

Figure 2.1 Energy band structure of the conduction band and valence bands of Si and Ge as a function of the k-space direction [210]

Ge and Si are both indirect gap materials. The top of the valence energy band is located at k = 0 (Γ region), while the bottom of the conduction energy band is located in L valley for Ge and X- Valley for Si.

Figure 2.2 shows the band gap for a bulk SiGe alloy as a function of percentage of Si [206]. It shows that the smallest indirect gap acquires a Ge-like characteristics and occurs near the L Brillouin Zone (BZ) boundary. When the alloy is from 15% to 100% Si, the characteristics have a Si-like structure with the smallest band gap occurring near the X BZ boundary.

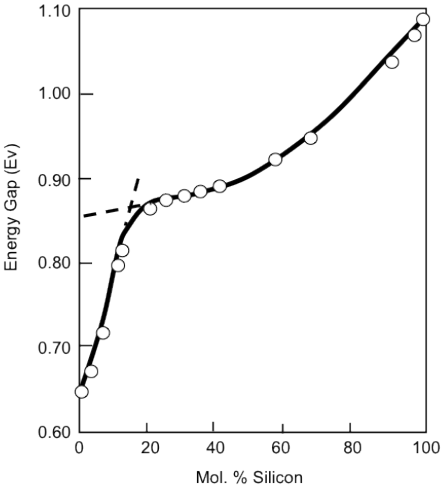

Figure 2.2 Energy gap in SiGe alloys a 296K based on the one-phonon MacFarlane-Roberts expression [206]

As an indirect band gap material, a phonon is required for the conservation of momentum in order to enable the radiative transmission of an electron from the minimum conduction band to the maximum of the valence band. Phonon energy is generated whenever a photon energy is emitted. For an alloy of 20% Ge, the phonon energy is calculated as $E_p \sim 50\ meV$ [211]

The indirect band gap optical absorption edge is determined by the sum of the indirect band gap energy and the phonon energy.

The absorption spectra for Si-rich and Ge-rich SiGe alloys are presented in Figure 2.3 and Figure 2.4 respectively. Note that for the Si-rich alloy, the absorption coefficient shifts slowly to lower energy as Ge is added up to 30%. The absorption coefficient also shows that there is little change in shape. This is because the band gap varies only slightly for this composition. As a first approximation, the material behaves like Si. In addition, in the case of SiGe alloys rich in Ge, the absorption spectrum is changing rapidly with the composition close to the spectrum of pure Ge. Ultimately, the bulk SiGe alloy presents an increased wavelength as compared to pure Si when the proportion of Ge is significant or greater than 30%. These results will be different for the case of a strained SiGe alloy .

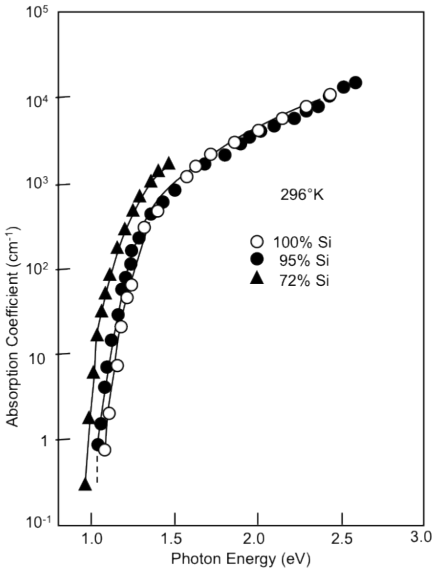

Figure 2.3 Intrinsic absorption spectra in a series of SiGe alloys at 295° K. [206]

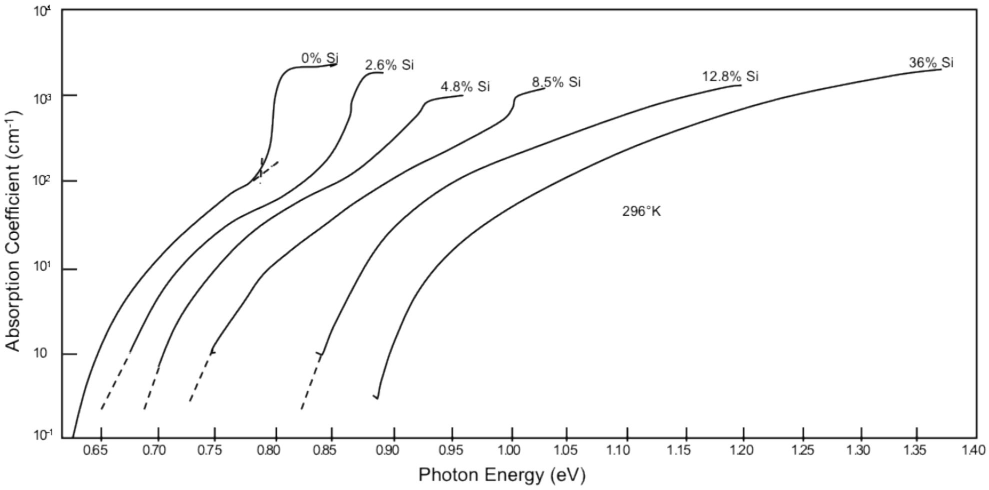

Figure 2.4 Intrinsic absoption spectra of Germnanium rich SiGe alloys [206]

2.1.2 Strained SiGe

The lattice mismatch between Silicon and Germanium of 4.17% at 300°K slightly increases with increasing temperature. When a $Si_{1-x}Ge_x$ is grown on a thick Si substrate and the Si has to be accommodated, the inherent mismatch can be handled in two ways.

One way is the compression of the lattice of the $Si_{1-x}Ge_x$ layer to fit with the underlying lattice of the Si. This is called pseudomorphic growth. This results in $Si_{1-x}Ge_x$ that is under strain. The second way is when the $Si_{1-x}Ge_x$ layer is unstrained or relaxed, and the lattice mismatch at the interface is accommodated by the formation of misfit dislocations. This results in a break in crystallinity across the growth interface, and a defected film unsuitable for high yielding device applications. These misfit dislocations generally lie in the plane of the interface, but dislocations can also thread vertically through the $Si_{1x}Ge_x$ layer. Figure 2.5(a) shows the schematic of the lattice structure of Si and SiGe. Figure 2.5(b) illustrates the pseudomorphic growth on top of Si substrate resulting in the compression of the SiGe lattice. Figure 2.5(c) presents the relaxed growth of SiGe lattice and the misfit dislocation in the interface.

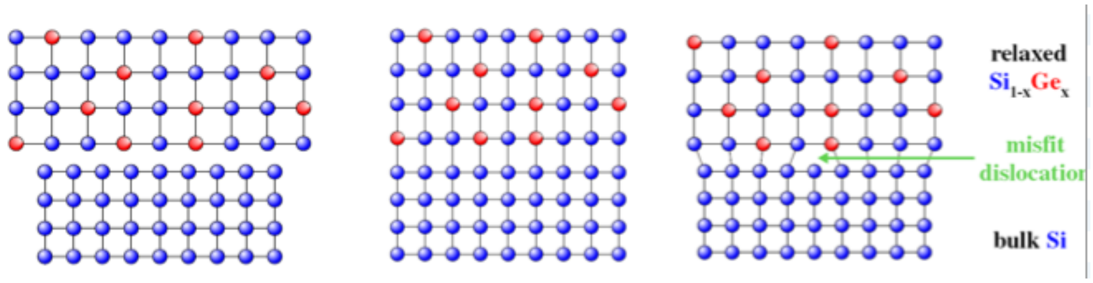

a) b) c)

Figure 2.5 Schematic illustrations of a) lattice structure of SiGe on top and Si on the bottom; b) resulting lattice from strained SiGe pseudomorphic growth; c) relaxed growth with the presence of misfit dislocation

The critical thickness is the maximum thickness of a strained SiGe layer growth without relaxation of the stain through the formation of misfit dislocations. This sets a limit on the device structure design. It is strongly dependent on the Ge content. The Matthews-Blakeslee equation is one of the early computations of the critical thickness in terms of the mechanical equilibrium of a pre-existing threading dislocation. In this case, the force of the dislocation segment residing at the hetero-interface is balanced with the component of the force per unit length acting on the threading component of the dislocation in growth plane. The thickness at which these two forces are equal is defined to be the critical thickness [212]. In Figure 2.6 the Matthews-Blakeslee equation shows that, the critical thickness of $Si_{1-x}Ge_x$ alloy on Silicon (100) substrate is less than (100 Å) 10nm for x>0.2, which places a severe restriction for practical device applications.

Another calculation known as the People-Bean equation, assumes that the misfit dislocation generation is determined solely by energy balance, which shows good agreement with experimental data[213]. Also in Figure 2.6, the line representing the People-Bean equation is shown. It shows larger critical thickness which exceeds (100Å) 10nm up to x=0.5. This calculation may be used as a reference for the practical device growth and fabrication, that the thermal budget during the epitaxial layer growth and device processing is kept low enough to maintain the strained layer.

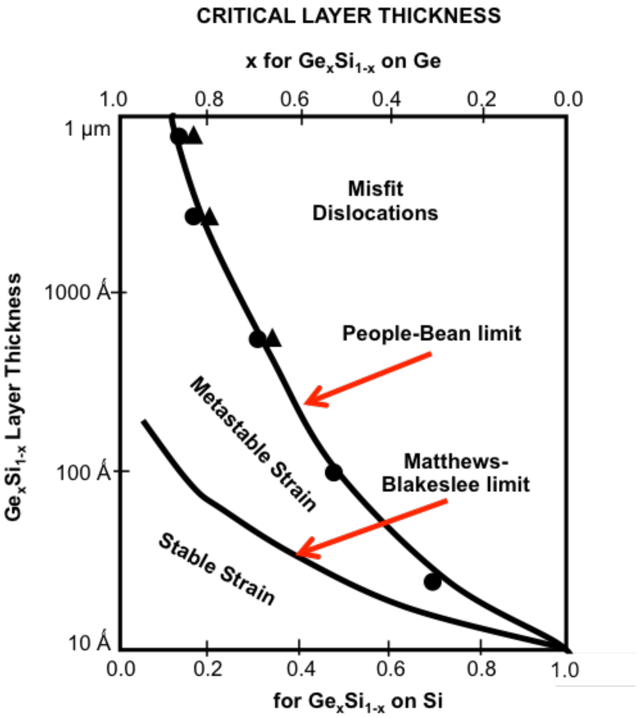

Figure 2.6 Limits of strained layer (defect-free) growth for GeSi /Si on Si (100) [214] .

The discrepancy between these two types of calculation can be explained by the observation that strain relaxation in $Si_{1-x}Ge_x$ layers occurs gradually. Layers thicknesses above the People-Bean curve can be considered to be completely relaxed, whereas layers below the Matthews-Blakeslee curve can be considered to be fully strained. These fully strained layers are stable and will not relax during any subsequent high-temperature processing. Layers lying between the two curves are termed meta-stable. These layers may be free of dislocations after growth, but are susceptible to relaxation during later high-temperature processing.

The band gap of SiGe alloys has a dominant impact on the optical and electrical characteristics of the alloys. Figure 2.7 shows the SiGe energy band gap as a function of Ge content of relaxed and strained SiGe at 300°K. The profile of the strained SiGe is different from the bulk SiGe band gap. The strain lifts the degeneracies in the conduction and valence bands, causing the relative position of the energy valleys to change. The six-fold degeneracy in the conduction band is split into four and two fold degeneracies, while the heavy hole band and light hole band are split in the valence band [215]. The two band gap curves appearing in Figure 2.7 for strained alloys correspond to the heavy hole band (lower curve) and the light hole band (upper curve). The cross-hatched region represents the uncertainties arising from the deformation potential employed for the calculation. The band gap of the heavy hole band should be regarded as the actual band gap, as this is usually defined as the energy difference between the lowest conduction band-edge and the highest valence band-edge.

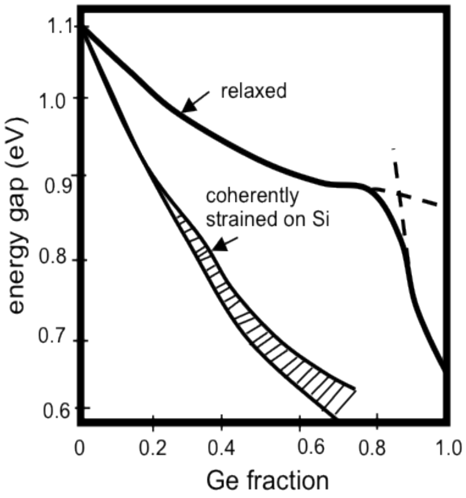

Figure 2.7 Energy band gap of relaxed(bulk) and compressively strained $Si_{1-x}Ge_x$ alloys on Si (100) substrate at 300° K[215]

As shown previously, $Si_{1-x}Ge_x$ alloys have a smaller band gap than Si partly because of the larger lattice constant and partly because of the strain. It can be seen that the strain has a dramatic effect on the band gap of $Si_{1-x}Ge_x$. For 10% Ge, the reduction in band gap is 92meV for strained $Si_{1-x}Ge_x$, compared with 50meV for unstrained $Si_{1-x}Ge_x$. The variation of band gap with Ge content for strained $Si_{1-x}Ge_x$ can be described by the following empirical equation based from a linear approximation which is dependent on the Ge fraction in the film and in the substrate[215].

$$\Delta E_{G\ SiGe\ strained}(x) = (0.74 - 0.53x_s)x \qquad \text{Eq. 2.2}$$

Where x is the Ge content in the film and x_s is the Ge content in the substrate. Another approximation is made which a polynomial approximation of the third order [214].

$$\Delta E_{G\ SiGe\ strained}(x) = 0.96x + 0.42x^2 - 0.17x^3 \qquad \text{Eq. 2.3}$$

It is noticeable that the band gap of the strained alloys decreases so rapidly that it becomes even smaller than that of bulk Ge when $x>0.6$. Note that the band gap is indirect for both strained and unstrained SiGe alloys.

The band alignment for compressively strained $Si_{1-x}Ge_x$ on unstrained Si is a Type 1 band alignment. The majority of the band offset at the heterojunction interface occurs in the valence band, with only a small offset in the conduction band. It is generally accepted that conduction band offset comprises less than 10%-15% of the total band offset, depending on the Ge composition. The valence band offset can be approximated as a function of Ge composition x [213]

The optical absorption of strained SiGe will also be different from relaxed or bulk SiGe. Early measurements were made at 90°K, the normalized measured absorption coefficient data are shown in Figure 2.8 [216]. It shows results for three Ge fractions of 25%, 40% and 60%

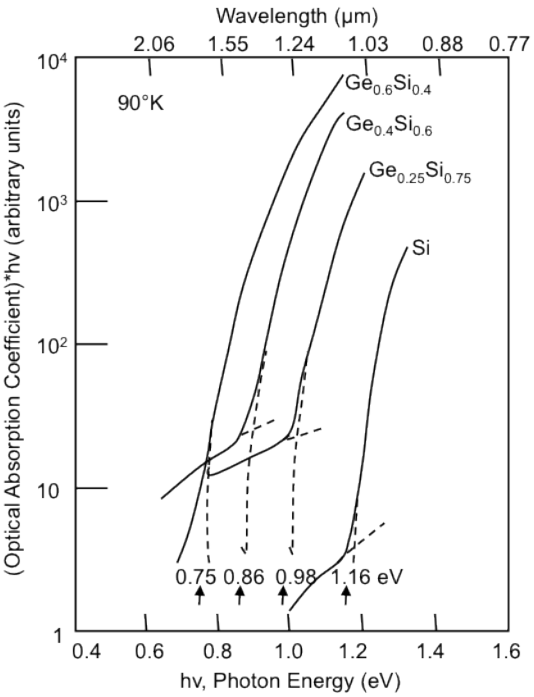

Figure 2.8 Absorption Coefficient of Strained SiGe at 90K [216]

One model of the absorption coefficient for constrained SiGe used the one phonon MacFarlane model as a reference [131],[196]. This model takes into consideration the Ge fraction, temperature of operation and wavelength of the incident optical wave.

$$\alpha_{absorption} = A(x) \cdot \left[\frac{\left(hv - E_g - E_{phonon}(x)\right)^2}{1 - e^{\left(E_{phonon}(x)/_{kT}\right)}} + \frac{\left(hv - E_g + E_{phonon}(x)\right)^2}{e^{\left(-E_{phonon}(x)/_{kT}\right)} - 1} \right] \quad \text{Eq. 2.4}$$

The model is a function of Ge content x and the parameters $A(x)$ and $E_{phonon}(x)$ which are extracted from stained SiGe measurements [216].

$$A(x) \approx 3200 \cdot (1 - 1.61x + 9.581x^2) \quad \text{Eq. 2.5}$$

$$E_{phonon}(x) = 0.0408 + 0.0013x + 0.0533x^2 \quad \text{Eq. 2.6}$$

This model is valid for Ge fraction of up to 40%. Figure 2.9 shows the absorption coefficient at 300°K for strained SiGe as a fraction of Ge for different wavelengths of 800nm, 980nm, 1300nm and 1550 nm. This shows that the absorption coefficient has lower values as the frequency increases. The two data points show estimated absorption coefficients of $Si_{0.8}G_{0.2}$ [217]

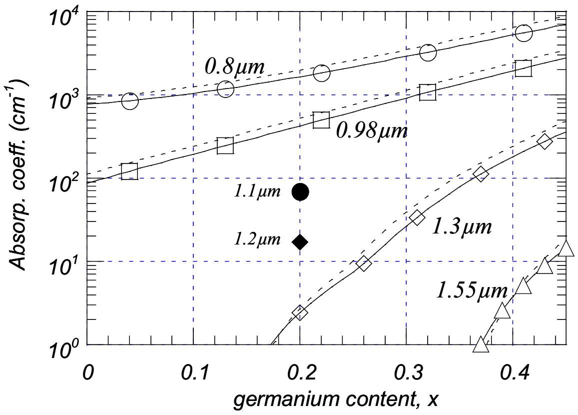

Figure 2.9 Absorption coefficients of strained SiGe at different wavelengths: 0.8μm (circle), 0.98μm (square) , 1.3μm (diamond) , 1.55μm (triangle) Plain circle and diamond respectively provide measured values at [196]

The absorption coefficient as modeled in Eq. 2.4 was used in the estimation of the quantum efficiency of a SiGe HPT which should good agreement with measured values [184].

2.2 SiGe HPT Technology and design rules validations

The HPT's that are the subject of this study are implemented using the Telefunken GmbH SiGe Bipolar process technology. One key aspect to this research is to implement in such a commercial technology without the addition of masks and processing steps.

The Telefunken SIGE2-RF Bipolar Silicon Germanium process technology is tailored specifically for maximum RF performance. This has an f_T of up to 80GHz and f_{MAX} of up to 90GHz. This RF bipolar technology allows the production of wafer with applications in high-speed cellular, high-speed networking, wireless LAN and high performance standard RF devices and used is for different applications [218]-[220] [221].

This process is a 0.8μm lithography double polysilicon heterojunction bipolar technology. The minimum emitter size is 0.8x1.4μm^2 (layout size) for vertical NPN HBT transistors which provides actual size after processing of 0.5x1.1μm^2. This process technology offers NPN HBTs (f_T = 50GHz and f_{MAX} ≈ 90GHz) and selectively implanted collector (SIC) NPN (with f_T = 80GHz and f_{MAX} ≈ 90GHz), lateral PNP transistors, diodes (PN, Zener, ESD, Varactor and Schottky), passive devices such as inductors capacitors and resistors. This technology provides circuits working above 10GHz and potentially up to 60GHz in some configurations [219] .

Table 2.2 Electrical parameters of the SiGe2-RF process technology

NPN TFSiGe2 RF @ 32°C (0.5 μm x 10 μm, CEB)					
Parameter	Condition non SIC	Condition SIC	Value non SIC	Value SIC	Units
f_T	V_{CE} = 2.8 V	V_{CE} = 1.5 V	50	80	GHz
f_{MAX}			90	90	GHz
HFE	I_E = -1 mA, V_{CB} = 0 V		300	360	
VAFI	I_B = 10 μA, V_{SUB} = 0 V		40	60	V
BVCEO	I_C = 2 μA, V_E = 0 V		4.3	2.4	V
BVCBO	I_C = 2 μA, V_B = 0 V		11	10	V

Figure 2.10 shows the simplified schematic of the cross section of the SiGe HBT.

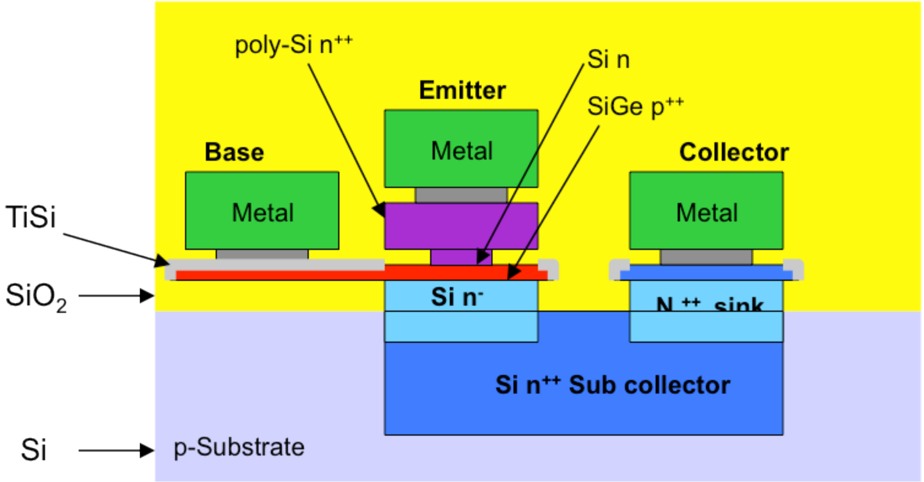

Figure 2.10 Schematic cross-section of SiGe2-RF technology from Telefunken

A typical transition frequency curve is given in Figure 2.11 for a typical size 0.9x10µm² HBT with and without collector selective implantation. The SIC transistor reaches up to 75-80GHz, while non-SIC transistor reaches 50GHz only.

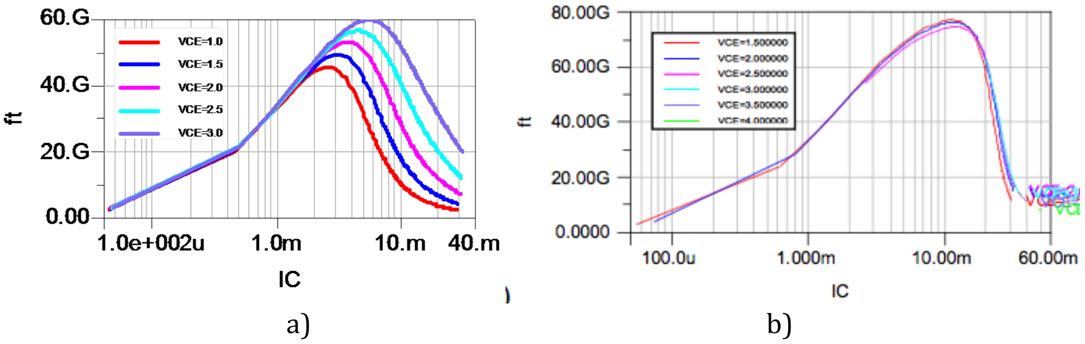

Figure 2.11 Simulation of f_T versus Ic curve of a 0.9x10µm² SiGe HBT from SiGE2RF Telefunken GmbH technology; a) without SIC option; b)with SIC option

2.2.1 Simulation of SiGe HBT characteristics (Sizes Related to the HPT)

The characteristics and performance of a reference HBT are discussed in this section. This will provide some insights on how modifications to implement HPT will influence the DC and RF performance. The reference HBT has the dimensions of 0.5x10µm² for the emitter width and length respectively. The plots are generated from simulations of the models provided by the foundry.

Output characteristics (Ic-Vce) of a transistor show the collector current (Ic) as a function of the collector voltage (Vce) and the base currents (Ib). These curves will help shows a transistor as a linear amplifier. This provides a guide on where AC signals can be superimposed on DC bias levels. The collector current can be expressed in Eq. 2.7, where B' and E' are the internal nodes of the intrinsic transistor as shown in Figure 2.13. Eq. 2.8 shows the value of the collector current as a function of the external series resistances of the HBT.

$$I_C = I_S exp\frac{qV_{B'E'}}{kT} \quad \text{Eq. 2.7}$$

$$I_C = I_S exp\frac{\left(V_{BE} - I_B R_B - I_B R_E(1+\beta)\right)}{kT} \quad \text{Eq. 2.8}$$

The Ic-Vce plot shows a finite slope in the collector current in the liner region that is due to the base width modulation see Figure 2.13 and Figure 2.14 . It is used to extract the Early Voltage. It also show that the plots will not be equally spaced which means that the current gain β varies with the base current Ib.

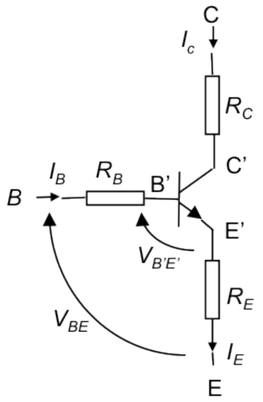

Figure 2.12 Schematic diagram of an HBT showing the internal collector, internal base, internal emitter.

Figure 2.13 shows the output characteristics of a 0.5x10μm^2 HBT. The Vce values are swept from 0V to 3.5 V at different constant Ib values starting from 500nA up to 2uA. In this plot, the saturation region from 0-0.2V Vce.; the cut-off region near Ic = 0 line; and the active region from 0.5V-2.5V and the breakdown region above 3V are shown.

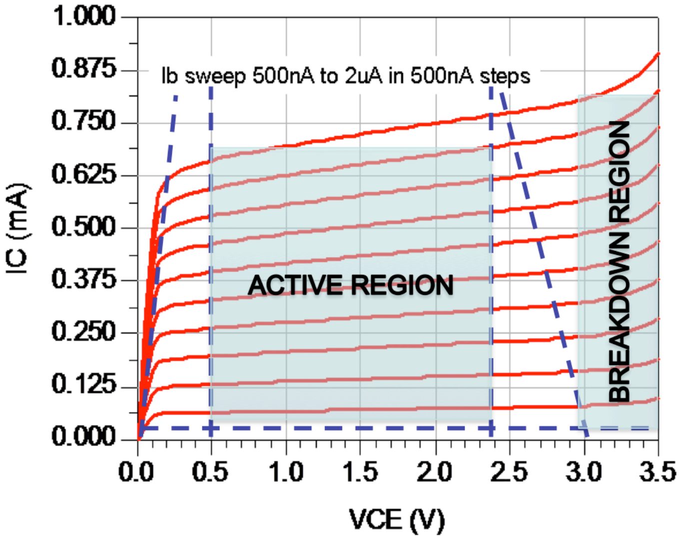

Figure 2.13 Output response of a 0.5x10μm^2 HBT (simulation) with Vce = 0V- 3.5V and Ib is swept from 500nA up to 2μA in 500nA steps.

The output response exhibits an Early voltage of 10-12V as shown in Figure 2.14. The output characteristics also show that the transistor starts to show avalanche currents at 3V.

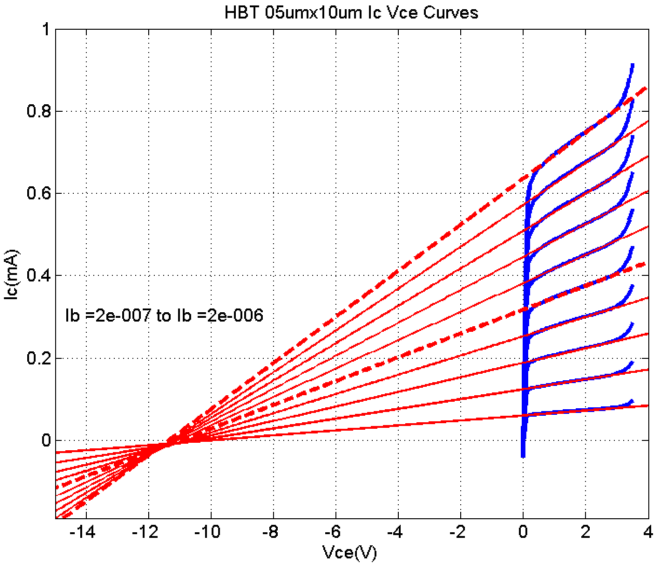

Figure 2.14 Early Voltage of 0.5x10µm² non sic HBT (simulation)

The output conductance is a measure of collector variation with base-collector reverse bias. The base-collector depletion region widens and reduces the neutral base width as the reversed biased-collector voltage increases, while keeping a fixed emitter-base voltage. The reduction of the neutral base width leads to an increase in the gradient of the injected electron distribution in the p-type base. Since the electron diffusion current across the base is directly proportional to this gradient, the collector current will increase. A low output conductance is desirable to achieve invariant output current in low-frequency analog applications.

Figure 2.15 shows the output response of different sized HBTs under 1µA Ib. There are two sets of sizes 0.5µm emitter width, with different lengths and 0.9µm emitter width, with different lengths. These simulations show that at a fixed width, the change in length from 5µm to 40µm results in a very slight increase in output current. This will be relevant in the discussion of HPT types where the intrinsic transistor emitter width is at a fixed value and the emitter length is also the length of the optical window. While at a fixed length of 10µm the difference in output current between 0.5µm and 0.9µm is significant. This will be relevant to HPTs with the same intrinsic transistor emitter length and a different emitter.

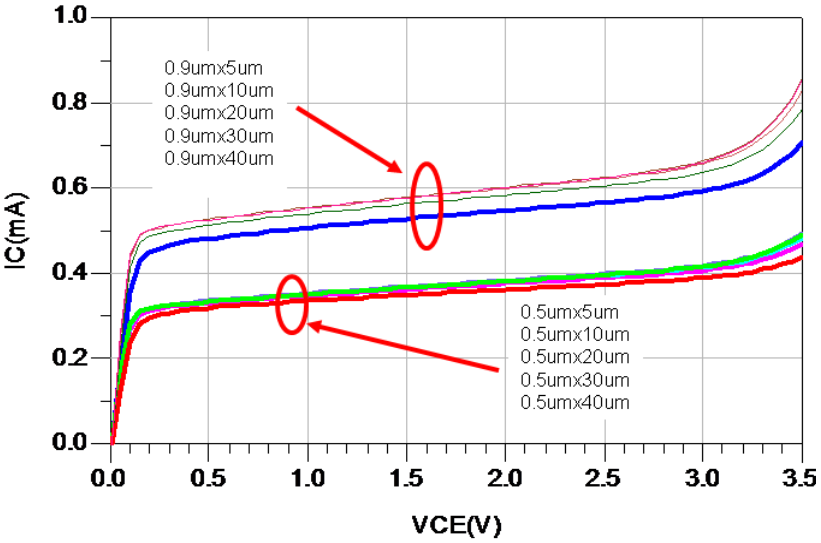

Figure 2.15 Output response of 0.5 x3.0µm², 0.5 x 5.0µm², 0.5 x 10µm², 0.5x 20.0 µm² HBTs at Ib = 1µA

The Gummel plots are combined plots of the base current Ib and the collector current Ic as a function of the base emitter voltage Vbe which is plotted in a semi logarithmic scale when the base collector voltage (Vbc) is 0 or constant. This plot is used in device characterization as is reflects the quality of the base emitter junction. Different parameters can be extracted from this plot, such as the common emitter current gain β, the base and collector ideality factors η, series resistances and leakage currents. In the Gummel plot, the log of collector current of an ideal bipolar transistor should be proportional to Vbe/kT, corresponding to an inverse slope of approximately 60mV/decade of collector current at room temperature. The increase in the collector current (and the current gain) of the HBT compared to the homo-junction transistor is due to the narrower band gap in the base since both devices have the same integrated base dopant concentration. Since the base current of Silicon and SiGe HBTs are virtually identical, the current gain enhancement due to Germanium incorporation is similar to the collector current enhancement. Therefore, the superior current gain potential of a SiGe HBT can be traded for an increased f_{MAX} and reduced base resistance leading to higher power gain, faster switching speed and a lower noise figure.

Figure 2.16 shows the simulated Gummel plot of the reference HBT. Superimposed on the figure is the common emitter current gain. It has a peak value of around 360. The different regions in this plot are identified. The low current region shows the recombination and tunneling effects. A linear region is observed for both Ic and Ib in the Vbe range of 0.55V to 0.85V and the high current region is seen where there is a change in slope of Ic. This is where the series resistance and Kirk effect are exhibited.

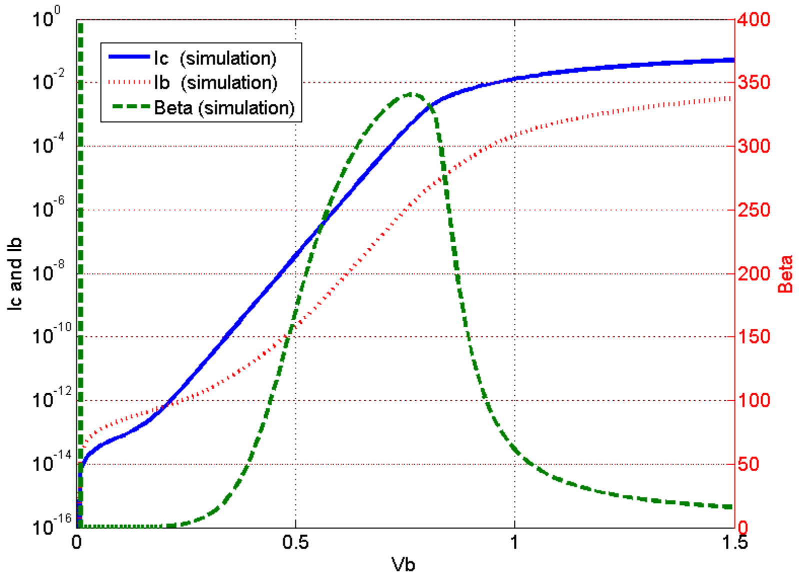

Figure 2.16 Gummel plot of a 0.5 x10µm² HBT at Vbc = 0V (simulation)

Another similar Gummel plot is made where Vce is set to 2V and the Vbe is swept from 0V – 3.5 V. This biasing reflects a typical biasing scenario under normal forward biasing conditions. In Figure 2.17, Ib is the absolute value of Ib. This means that at low values of Vbe up to 0.3V with 2V Vce, the Ib current is flowing out of the base.

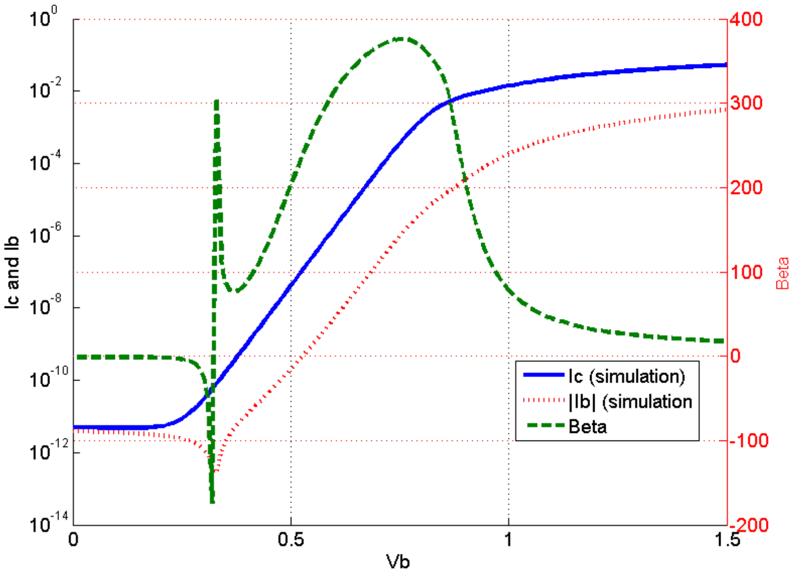

Figure 2.17 Gummel Plot of a 0.5x10µm² HBT at fixed Vce = 2V (simulation)

The current gain of the different sized HBTs are also extracted to show the characteristics of different devices. Figure 2.18 shows the current gain β of the different HBT sizes. It presents a summary of all the extracted current gain β as a function of the length of the HBT. Two line series are shown with one series having a width of 0.5µm and the other is 0.9µm. Larger devices, whatever the length is, will have a higher current gain than smaller devices. This behavior will be used in the analysis of the characteristics of the fabricated HPTs.

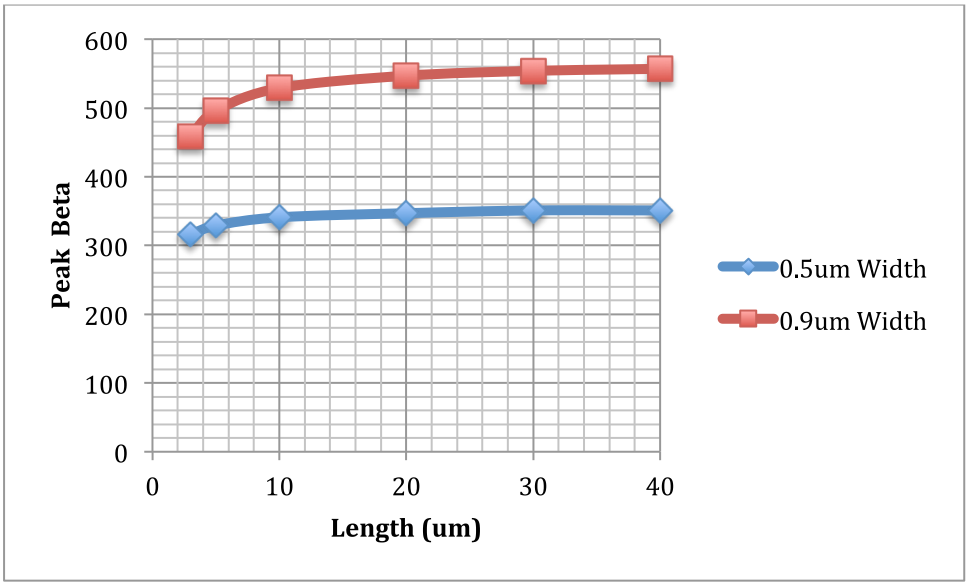

Figure 2.18 Beta of different HBT sizes (Simulated)

Table 2.3 provides a summary of the biasing conditions for the peak beta of the different devices. From the table, the length increases from 3µm, 5µm, 10µm, 20µm, 30µm and 40µm with a constant width of 0.5µm. The current gain slowly increases from 316 to 351. With fixed length of 10µm, the β from width 0.5µm to 0.9µm increases from 341 to 529. This increase in current gain is achieved at higher collector currents and is primarily due to the change in the cross sectional area of the emitter in which the current gain β is directly proportional.

Table 2.3 Biasing conditions for the peak beta of different devices (Simulations)

Width μm	Length μm	Area μm^2	Beta (Peak)	Vb (V)	Vc (V)	Ib (μA)	Ic (mA)	Jc (A/μm^2)
0.5	3	1.5	316	0.76	0.76	0.45	0.14	9.47E-05
0.5	5	2.5	329	0.76	0.76	0.70	0.22	9.28E-05
0.5	10	5	341	0.76	0.76	1.34	0.46	9.12E-05
0.5	20	10	347	0.76	0.76	2.57	1.00	1.00E-04
0.5	30	15	351	0.76	0.76	5.13	2.00	1.33E-04
0.5	40	20	351	0.77	0.77	6.70	2.00	1.00E-04
0.9	3	2.7	459	0.77	0.77	0.70	3.20	1.19E-04
0.9	5	4.5	496	0.77	0.77	1.10	1.00	2.22E-04
0.9	10	9	529	0.77	0.77	1.91	1.00	1.11E-04
0.9	20	18	547	0.77	0.77	3.57	2.00	1.11E-04
0.9	30	27	554	0.77	0.77	5.13	3.00	1.11E-04
0.9	40	36	557	0.77	0.77	6.60	4.00	1.11E-04

The S-Parameters of the transistor provide the high frequency characteristics of the device. The RF electrical gain of the transistor is a key indicator of the behavior of the carriers into the structure. The transition frequency f_T of the transistor can be extracted from S-Parameters under different bias conditions. A typical representation is usually f_T as a function of the collector current Ic. This is not a direct description of the speed of the transistor. It gives a good indication on the transit times (maximum f_T of the curve) and capacitances (linear slope for the increase in f_T in the low collector current region).

For the reference HBT, at 2V Vce a peak f_T of almost 50GHz is achieved with an Ic of approximately 3mA. Figure 2.19 shows the f_T and f_{MAX} of this transistor at 1.5V and 2V V_{ce}. The f_T is maximized at 49GHz when Ib is 8.5μA and Ic is 3mA . The f_{MAX} is maximized at 60GHz when Ib is 8μA and Ic is 3mA.

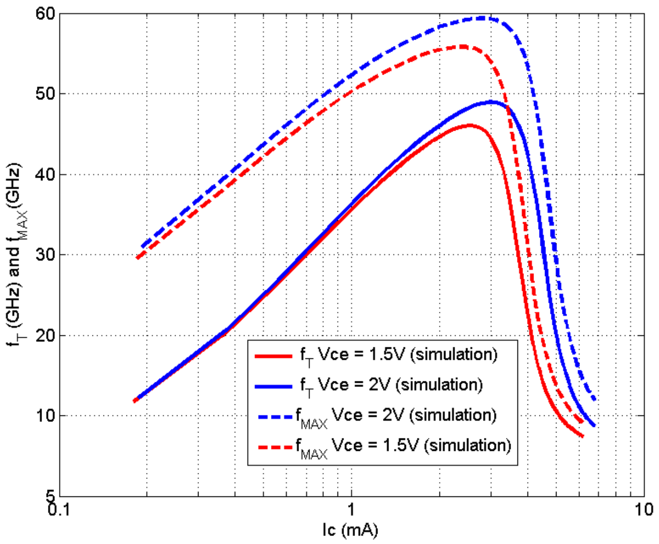

Figure 2.19 f_T and f_{MAX} vs. Ic of reference HBT at Vce values of 1.5V and 2V

Table 2.4 shows a summary of peak f_T of differently sized non-SIC transistors. It shows that the peak f_T is around 47Ghz for all the devices and is achieved at higher collector currents as the size of the transistor increases.

Table 2.4 Peak f_T of different HBT sizes

Width µm	Length µm	Area µm^2	f_T (peak) GHz	Vce V	Ib µA	Ic mA	Jc A/µm^2
0.5	3	1.5	45	2	3	1	6.67E+08
0.5	5	2.5	46	2	5	2.	8.00E+08
0.5	10	5	47	2	9	3	6.00E+08
0.5	20	10	47	2	17	6	6.00E+08
0.5	30	1.5	47	2	25	9	6.00E+08
0.5	40	20	47	2	33	12	6.00E+08
0.9	3	2.7	47	2	3	2	7.41E+08
0.9	5	4.5	47	2	5	3	6.67E+08
0.9	10	9	48	2	8	4	4.44E+08
0.9	20	18	48	2	16	9	5.00E+08
0.9	30	27	48	2	23	13	4.81E+08
0.9	40	36	47	2	31	18	5.00E+08

Figure 2.20 shows all the simulated S-Parameters of the reference 0.5x10µm^2 HBT at Vce = 1.5V and different base currents that maximizes either f_T or f_{MAX}, max S_{21} and 0dB S_{21}. This analysis is of interest to take comparisons with HPTs loaded with 50Ω. The 3dB cutoff frequency is of special interest as it is the main frequency characteristics that could be extracted in an easy way from the HPT responsivity curves versus frequency, and that could be related to the device optimizations as will be seen in Chapter 3 and 4.

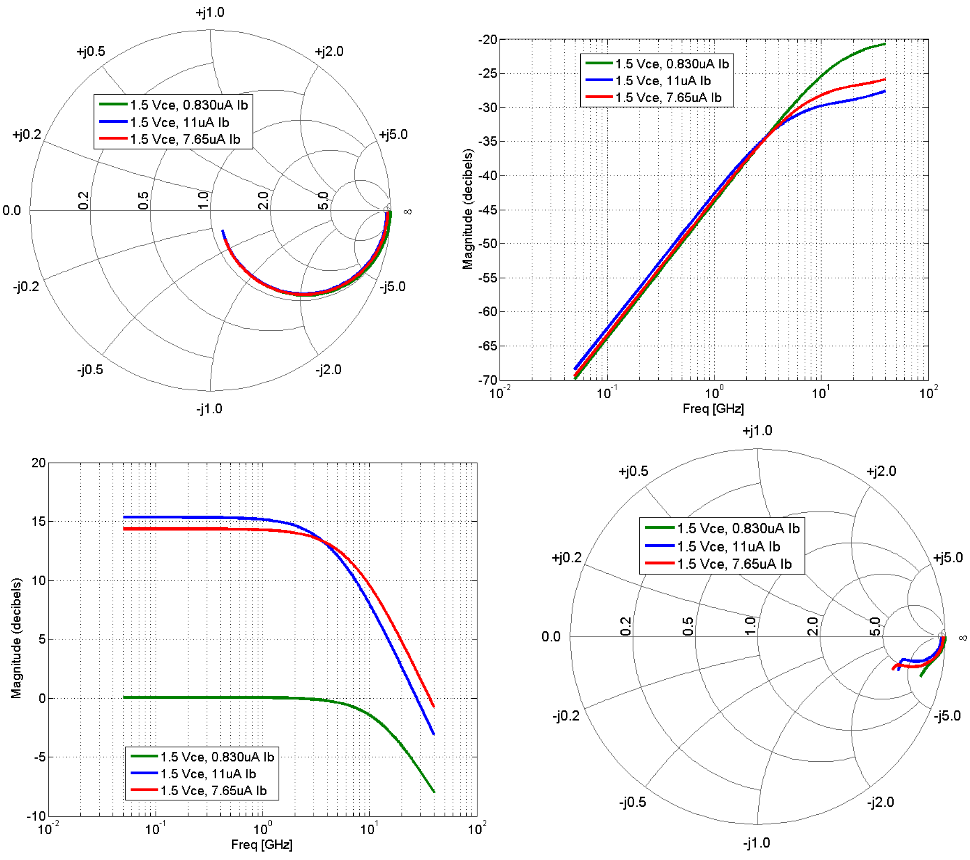

Figure 2.20 Simulated S-Parameters from 50 MHz to 40 GHz of the reference HBT at different biasing points (Max S_{21} , 0dB S_{21} , Peak f_T and f_{MAX})

A summary of the S_{21} values is presented in Table 2.5. When the transistor is biased to have the maximum 50Ω gain, its cutoff frequency is 4.5GHz. A biasing with 0dB 50Ω gain shows a cutoff frequency of approximately 15GHz. This gives a basis of comparison for further HPT analysis with f_{-3dB} ranging from 4.5GHz to 16GHz depending on the biasing. This is also useful to know for a circuit designer.

Table 2.5 Summary of simulated S21 of the reference 0.5x10µm² HBT

	Gain dB	Cutoff GHz	Ib (µA)	Vb(V)	Ic(mA)	Vc (V)
Max Gain(50MHz)	15.34	4.5	11	0.841	3.59	1.5
0 db (50MHz)	0	16	0.830	0.746	0.300	1.5
Peak f_T	14.36	7	7.65	0.824	2.6	1.5
Peak f_{MAX}	14.36	7	7.65	0.824	2.6	1.5

2.2.2 Fabricated HPT Structures

The design of the HPT using the SiGe2RF involves using the material and semiconductor layers that are available to define a standard HBT using this technology. To ensure compatibility with the process technology, there are no new material layers and/or processing masks added. The HPT's are designed using the available masks and layers. of a CEB type non-SIC HBT with a cross section as shown in Figure 2.10 While enlarging the structure an creating an optical window opening for a vertical illumination.

The first HPT structure type (xBC type) is implemented by extending the base-collector region while keeping the emitter width at a minimum size of 0.8µm in the layout view and an actual emitter width of 0.5µm. This allows for a faster intrinsic transistor, which is defined by the area under emitter. The extended base-collector region defines the optical window and the intrinsic base-collector PN photodiode. This structure is similar to other III-V HPTs and SiGe HPT [189], [192] , [186]

In a vertical device, the base layer should be as thin as possible. This aids in the improvement of the transit time resulting to faster transistors. The emitter stripe width should be as small as possible such that the base emitter capacitance is small. These principles that helps to make fast transistors could be applied in the design of fast phototransistors as well.

In the reference HBT mask layout, the exposed base polysilicon is always silicided to keep the polysilicon resistances at a minimum. This means that a Titanium Silicide (TiSi) layer will be grown on top of the extended base polysilicon layer of the HPT.

Figure 2.21 shows the resulting HPT structure. This structure is called and extended base collector HPT (xBC HPT) The bottom layer is the P-type substrate. All over the structure is a yellow layer that represents all the oxide and nitride layers as the result of the processing steps. All the green parts represent the first metal layer that is in contact with the different semiconductor materials.

The transistor base is a SiGe material that is approximately 20% of Germanium with an abrupt doping profile. These are assumed properties and are not supplied by the foundry. The emitter is the violet part with a small width that is N-type material of 0.5µm. On top of it is another violet layer, which represents the emitter polysilicon. The collector is connected to a N+ sub-collector contact. The resulting intrinsic transistor is the layers under the emitter region. The optical window is defined by the extended base and collector and the resulting TiSi layer on top of it. The illumination will pass through the oxide and the nitride layers. Then it passes through the TiSi where high reflections are expected. And finally, it goes through the base and collector layers.

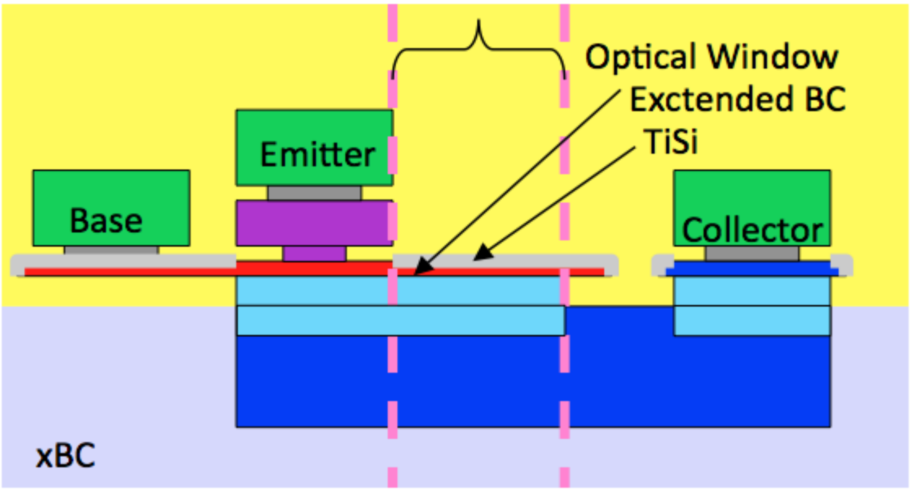

Figure 2.21 Simplified schematic cross section of an extended Base Collector HPT (xBC)

The second HPT structure type (xEBC type) is designed by extending the emitter base and collector altogether. This is similar to a SiGe HPT structure in the previous studies of Polleux [131] , and Yin [184]. This structure is intended to handle higher currents and provide high current gains due to the increase in the emitter stripe width. This HPT is essentially one large HBT. It is composed of two intrinsic transistors: The area under the emitter contact defines the first intrinsic transistor and this could not be vertically illuminated; The optical window defines the second intrinsic transistor. Figure 2.22 shows the resulting HPT structure: xEBC HPT. Illumination is only available in the EBC layer that is defined by the optical window that is at the edge of the emitter metal contact.

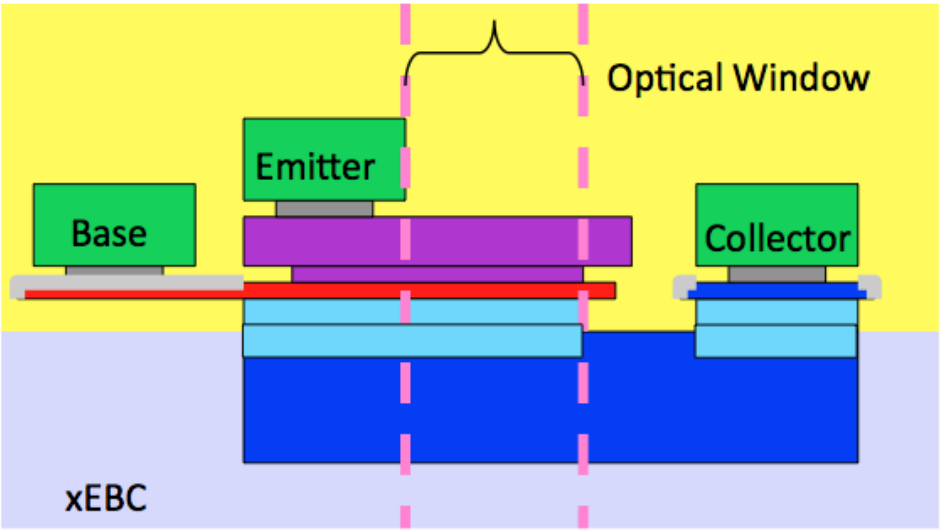

Figure 2.22 Simplified schematic cross section of an extended Emitter Base Collector HPT (xEBC)

Different HPT structures were designed to minimize the optical losses in the optical signal. One technique is to remove the silicidation in the extended base polysilicon. This is accomplished with the use of the mask used to define a silicide block out. This mask is used in the design of polysilicon resistors. This is applicable to an HPT structure that is of extended base collector (xBC) type. Figure 2.23 shows the resulting HPT structure: xBCrT HPT. This is similar to the xBC structure however the TiSi layer is omitted. As the reflection from the TiSi are removed, it is expected that it will have an increase in optical signal penetrating the structure. It is also expected that there will be an increase in the resistance in the base.

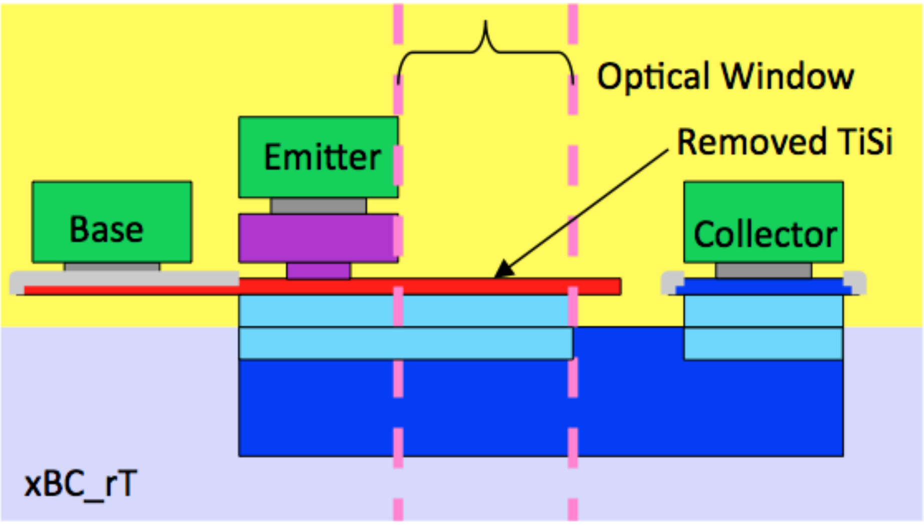

Figure 2.23 Simplified schematic cross section of an extended Base Collector with removed TiSi layer (xBCrT)

Another way to improve the amount of optical signal passing through the device is by removing the oxide and nitride layers on top of the optical window. This approach is used in an xBC, xEBC and xEBCrT type of HPTs. The mask layer that is used to define the pad access for wirebonding or flip chip is used to define the area where the oxide and nitride layers will be etched. There is an expected increase in the optical signal going to the device using this approach. However, the actual depth of the etched oxide could not be determined because this etching process is time controlled to etched down to a topmost metal layer. The etching is at least this value but could be made deeper. Figure 2.24 represents the final HPT when the etched oxide is applied to an xBCrT structure. This structure is called xBCrTeO.

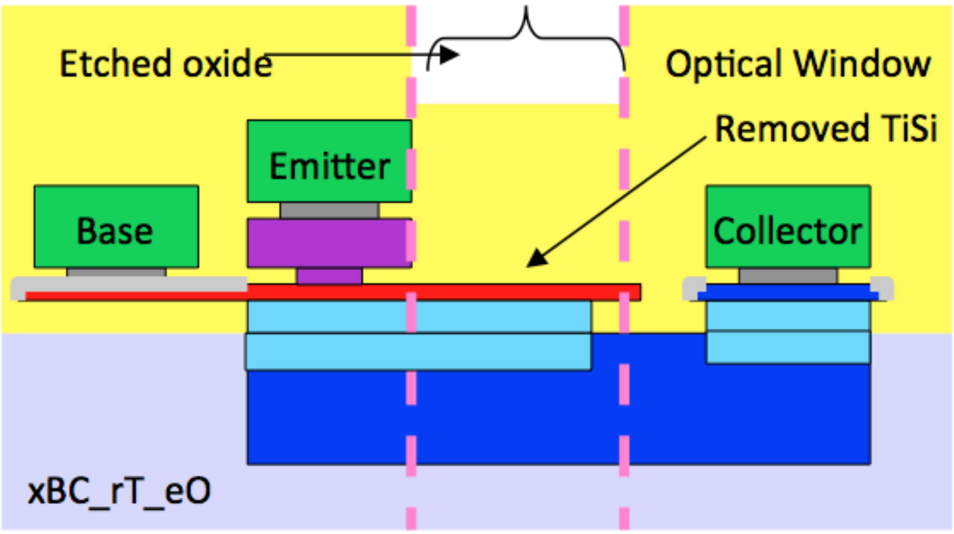

Figure 2.24 Simplified schematic cross section of an extended Base Collector with removed TiSi and etched oxide HPT (xBCrTeO)

Different structures were implemented in three prototyping runs during the thesis study. The variations in the design included different window the mentioned different sizes, the type of optical windows, and the addition of a SIC option in the HPT. The naming scheme for the fabricated HPTs is:

<Prototype Run Number>-<Optical Window Size><optical window type>
<xBC or xEBC><extras><extras>

Prototype Run Number	R1, R2, R3
Optical Window Size	03 = 3x3μm^2 05 = 5x5μm^2 10 = 10x10μm^2 20 = 20x20μm^2 30 = 30x30μm^2 40 = 40x40μm^2 50 = 50x50μm^2
Optical Window Type	xBC = extended Base Collector xEBC = extended Emitter Base Collector
Optical Window Shape	SQ = Square CR = circular, applicable to xEBC type only
Extras	rT = removed Titanium, applicable only to xBC type eO = etched oxide sic = if the collector uses SIC.

As an example, R1-10SQxBCrTeO corresponds to Prototype Run 1, with square optical window size of 10x10μm^2 of an extended base and collector with an removed titanium and etched oxide. The complete list of tested HPT structures among those which were fabricated in this research is provided in Table 2.6.

Table 2.6 Complete list of tested HPT structures

CODE	Device Name	Emitter Width(μm)	Emitter Length (μm)
1	R1-03SQxBCrT	0.5	1.6
2	R1-05SQxBCrT	0.5	3.9
3	R1-10SQxBCrT	0.5	8.9
4	R1-30SQxBCrT	0.5	28.9
5	R1-50SQxBCrT	0.5	48.9
6	R1-03SQxBC	0.5	1.6
7	R1-05SQxBC	0.5	3.9
8	R1-10SQxBC	0.5	8.9
9	R1-30SQxBC	0.5	28.9
10	R1-50SQxBC	0.5	48.9
38	R1-05SQxBCrTeO	0.5	3.9
39	R1-10SQxBCrTeO	0.5	8.9
40	R1-30SQxBCrTeO	0.5	28.9
41	R1-50SQxBCrTeO	0.5	48.9
57	R1-05SQxEBC	5.9	3.9
58	R1-10SQxEBC	11	8.9
62	R1-03xBCrTsic	0.5	1.6

63	R1-10xBCrTsic	0.5	8.9
R1C1	R2-10SQxEBC	11	8.9
R1C2	R2-10SQxEBCeO	11	8.9
R1C3	R2-10SQxEBCsic	11	8.9
R1C4	R2-10SQxEBC_sic_eO	11	8.9
R1C7	R2-20SQxEBC	20.9	18.9
R1C8	R2-20SQxEBCeO	20.9	18.9
R1C9	R2-20SQxEBCsic	20.9	18.9
R1C10	R2-20SQxEBCsiceO	20.9	18.9
R1C13	R2-30SQxEBC	30.9	28.9
R1C14	R2-30SQxEBCeO	30.9	28.9
R1C15	R2-30SQxEBCsic	30.9	28.9
R1C16	R2-30SQxEBCsiceO	30.9	28.9
R2C2	R2-50SQxEBC	50.9	48.9
R2C3	R2-50SQxEBCeO	50.9	48.9
R2C4	R2-50SQxEBCsic	50.9	48.9
R2C5	R2-50SQxEBCsiceO	50.9	48.9

In order to facilitate on wafer testing, all the HPT structures are placed in a fixture with ground signal ground (GSG) RF probing pads with a 100µm pitch. RF 50Ω pads are shielded to have improved noise performance. This is illustrated in Figure 2.25 which shows the mask layout design for a 10x10µm^2 and a 50x50µm^2 HPT.

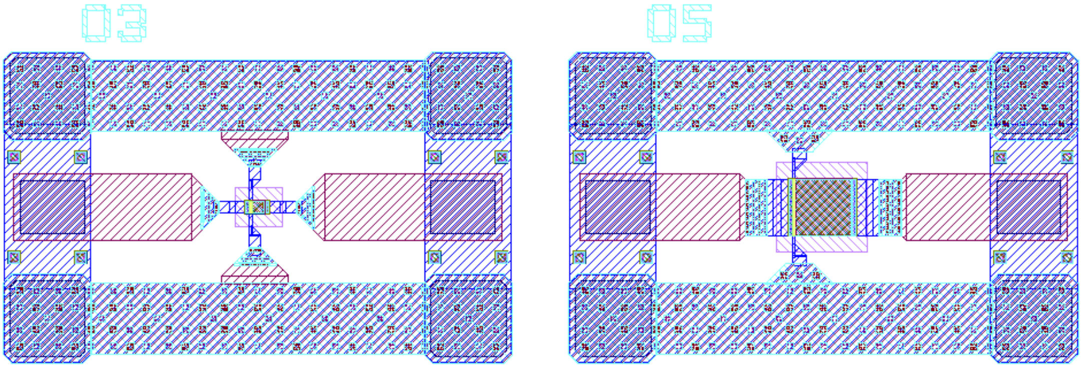

a) b)

Figure 2.25 Illustration of the layout of two SiGe HPT structures: a) 10x10µm^2 xBCrT ;b) 50x 50µm^2 xBCrT. Figure 2.26 shows chip microphotograph of the fabricated (R1-10SQxBCrT) and (R1-50SQxBCrT) HPTs.

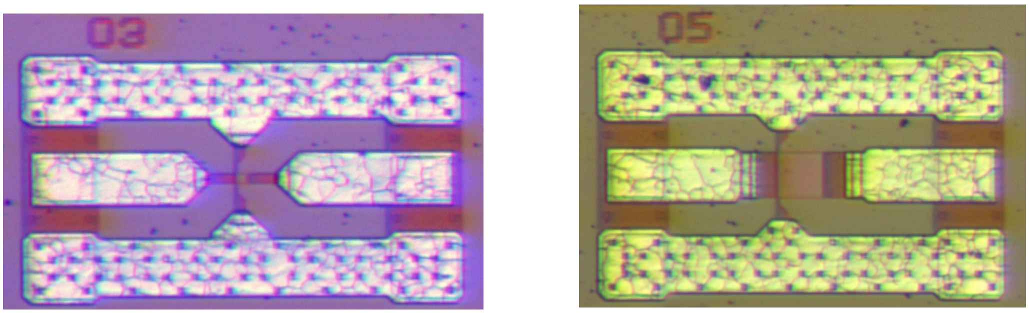

a) b)

Figure 2.26 Photograph of two fabricated cells of low noise RF GSG pads and a) 10x10µm^2 HPT R1-10SQxBCrT and b) 50x50µm^2 HPT R1-50xBCrT

2.3 Electrical validation of the HPT structures

The implemented HPTs are modified versions of a reference HBT. It is important thus to verify if the modifications made in the mask layout for the design of HPT are compatible to the fabrication process. In the dark conditions, the electrical characteristics of the HPT should exhibit similarities to HBTs in terms of DC and in RF responses.

2.3.1 DC Characterization

DC characterization of the HPT involves measuring the output Ic-Vce characteristics of the HPT and the Gummel measurements. Figure 2.27 shows the photograph of the measurement bench for DC and RF measurements. A semiconductor parametric analyzer was used to supply and measure the base and emitter currents and voltages through bias tees integrated in a vector network analyzers. The output characteristics of the HPT were measured by sweeping the collector voltage Vce from 0V to 3V while setting Ib at different current levels.

Figure 2.27 On- wafer DC and RF characterization bench

Figure 2.28 shows the measured output characteristics of the R1-10SQxBC HPT and the simulation of the 0.5x10μm^2 non-sic HBT superimposed. They have the same intrinsic HBT size with an enlarged BC junction in the case of the HPT. Comparing the HPT output characteristics to the HBT characteristics, the following are observed:

- a lower collector current
- a wider saturation region,
- a higher Early voltage ~30V, and

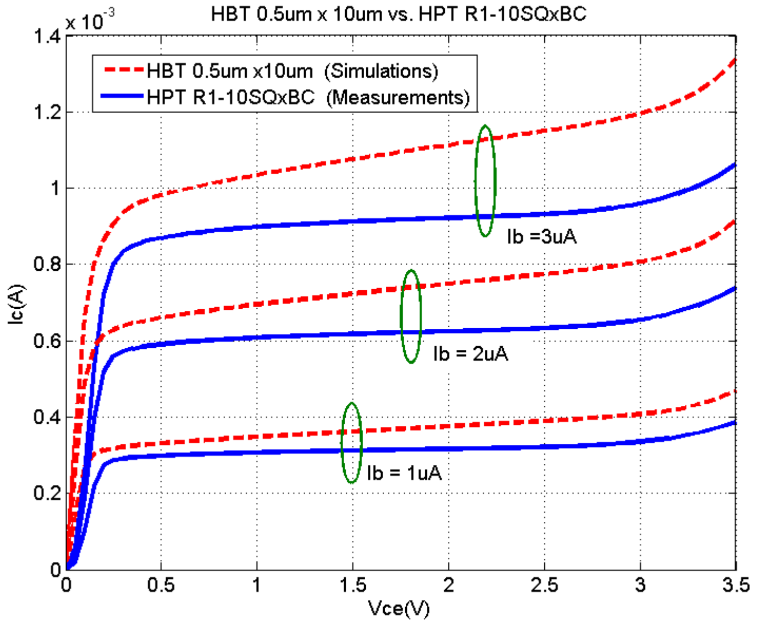

Figure 2.28 Ic vs.Vce of R1_10x10SQxBC HPT (measurements) as compared with simulation of the reference HBT (0.5x10µm²).

The modification in the structure of an HBT to implement an HPT affects the series resistances and passive capacitances of the device. According to Eq. 2.7 the external base and emitter and emitter resistance has an impact in the collector current. The enlargement in the HPT thus reduce the current gain as shown in Figure 2.28. The transistor series resistances could be estimated using Figure 2.29 as a reference R_B is the resistance of the base. It is sum of two resistance components: 1) the R_{BX}, is the resistance between the edge of the active transistor area and the base contact. The transistor geometry, and the extrinsic base sheet resistance estimate this resistance. 2) The intrinsic base resistance of the active base region, which is located beneath the emitter. It can be estimated as from the transistor geometry and the intrinsic base resistance.

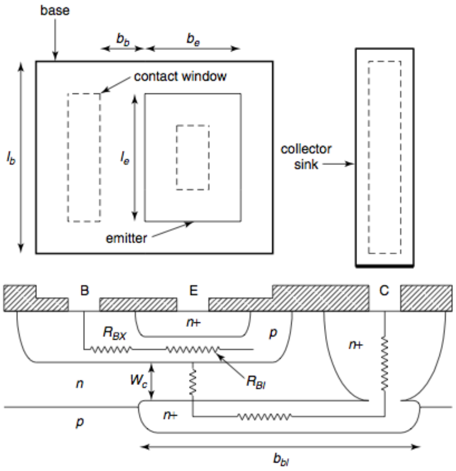

Figure 2.29 Cross section of a basic bipolar transistor showing the components of the base and collector resistance. [222]

In an xBC HPT, the second component in the base resistance increases due to the increased extrinsic base forming the optical window. This results to an increased base resistance. The HPT with xBC thus results in a lower collector current given the same base current as illustrated in Figure 2.28. The collector resistance R_C will also increase due to the extended collector. The extrinsic transistor is enlarged to form the optical window. The extrinsic base resistance is thus increased. The intrinsic base resistance maybe also be increased, but in a less extent as the distance from the base contact of the active intrinsic transistor is kept constant.

Figure 2.30 shows the Gummel plot of R1-10SQxBC HPT and the 0.5x10µm² non-sic HBT. The lowering of the Ic is slightly visible due to log scale of the plot line. Ib is lower in the linear region and is slightly higher in the high injection region. The current measurements tend to flatten out in the order of 10^{-10}A in the low Vbe region. This shows actually the limits of the measurement equipment (current leakage in RF cables) and not the recombination currents.

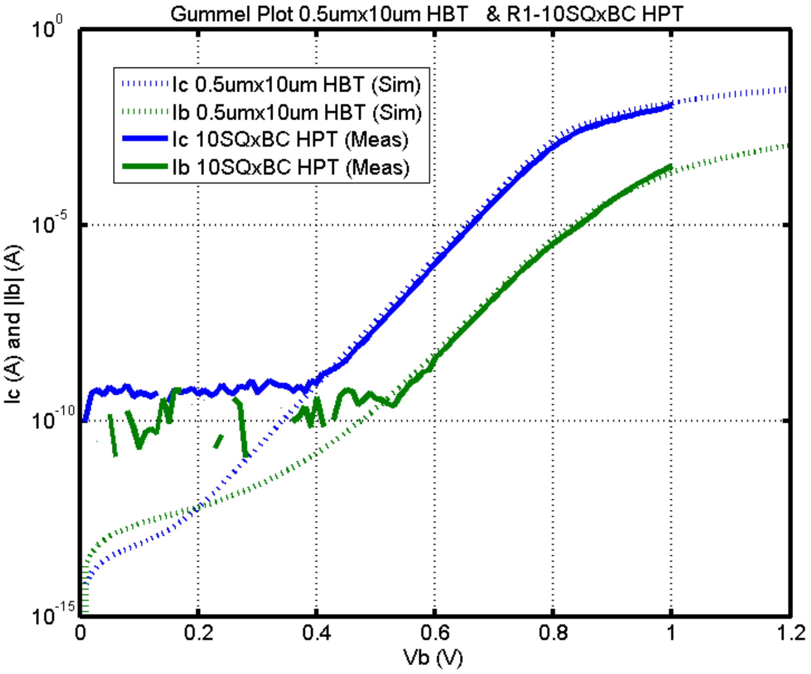

Figure 2.30 Gummel Plot of R1-10SQxBCrT HPT (measurements) as compared with simulation of the reference HBT 0.5x10µm² HBT

Figure 2.31 shows the extracted current gain β of the two devices. In the HPT as explained previously, a decrease of the peak current gain is seen. In this figure, the location of the biasing point for the peak current gain is the same in both devices.

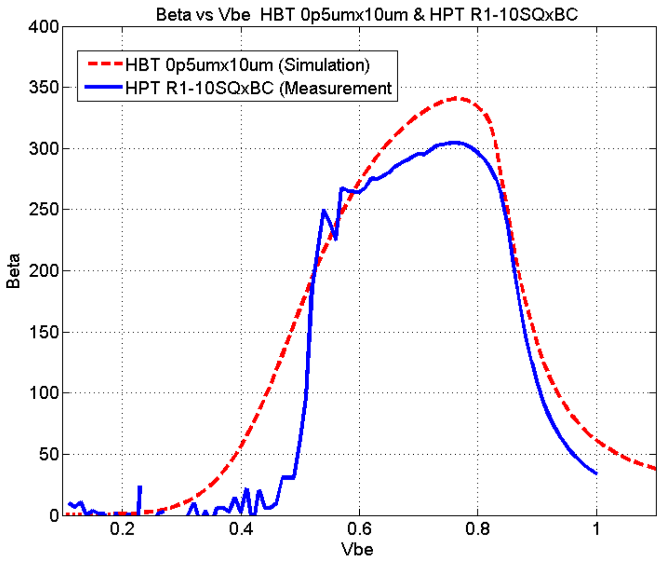

Figure 2.31 Beta plot of R1-10QSxBC_ HPT, Ic ,Ib and β of 0.5x10μm²

The DC tests enable to verify the electrical behavior of the transistor and help to identify non-functioning devices as well as to identify proper biasing values. It is also an essential test to extract DC parameters for the non-linear model of the HPT.

We have seen that extending the base and the collector to make an HPT lowers the output current Ic and lowers of the current gain as compared to and HBT having the same intrinsic transistor. The DC verification of several HPTs are presented. The HPTs are sorted by size. The different HPT types are represented with different colors.

- XX SQxBC (blue)
- XX SQxBCrT (red)
- XX SQxBRrTeO (green)
- XX SQxBCrTsic (brown)
- XX SQxEBC (violet)

2.3.1.1 3x3μm^2 HPTs

Figure 2.32 shows the output characteristics Ic-Vce of the different kinds of 3x3μm² square HPTs. Namely xBC, xBCrT, xBCrT_sic (a) is for measurement made with Ib = 1μA and (b) for Ib = 10μA. In this measurement the extended base collector HPT show a value of 261μA when Vce = 1.5V and Ib = 1μA . The extended base collector with removed titanium shows a lower collector current in the active region with a value of 217μA under the same biasing condition. This is attributed in the increase in resistance of the extrinsic base of the HPT due to the removal of the silicided titanium. The collector resistance for both the xBC and xBCrT is has the same values as can be seen in the slopes of the HPTs at the start of the active region. This means that the difference between the two HPT types changes the base resistance only and the collector resistance remains the unchanged. The extended base collector with removed titanium and sic HPT exhibits and increase in collector current due to the selective implantation of the collector with a value of 330μA at the same bias conditions. This is accompanied by the early appearance of the avalanche currents and breakdown voltage at 2V. The same trends could be observed in the 10μA base bias.

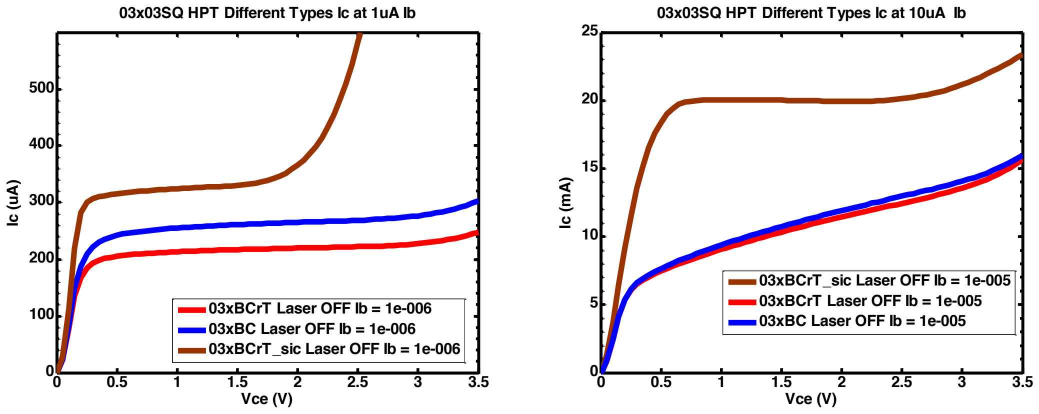

a) b)

Figure 2.32 Ic-Vce curves of different 3x3µm² HPTs (a) Ib = 1µ A (b) Ib= 10µA

Figure 2.33 shows the 3x3µm² HPTs (a) Gummel measurements and the (b) common emitter current gain β as a function of Vbe. The highest beta is seen in the xBCrTsic HPT with a peak value of 327 which is attributed to the increase in collector current which is the effect of using SIC. This is followed by the xBC with a β of 244 and a reduced β of 210 for the xBCrT. This is related to the characteristics of the collector current.

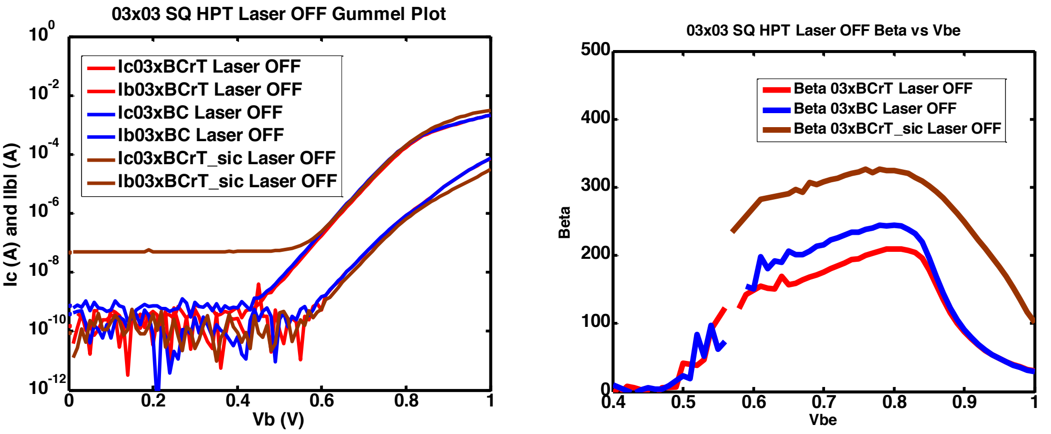

a) b)

Figure 2.33 Different 3x3µm² HPTs a)Gummel plot of the different 3x3 HPTs b)extracted β

2.3.1.2 5x5 μm^2 HPTs

Figure 2.34 shows the output characteristics of the 5x5µm² HPTs: xBCrT, xBCrTeO, and xEBC. The etched oxide is expected to have no any effect in the DC characteristics of the HPT, since this process happens at the top most oxide layer, which is in the surface of the wafer and away from the active device. It is observed at 1.5V and 1µA that there is a 2% change in collector current and 0.05% change when Ib = 10µA. The low percentage of change in collector current means that for this size, oxide etching barely affects the DC characteristics of the HPT when compare to a non oxide etched version. The xEBC shows increase in collector current due to increase in size of the intrinsic transistor which is almost the same size as the optical window. The output characteristics also shows that collector resistance (Rc) the for the xBC is higher than xEBC. This is seen in the in the slope of the collector current in the saturation region. This indicates that the transistor active region is more distributed in the xEBC HPT, thus providing vertical electron flow closer to the collector contact.

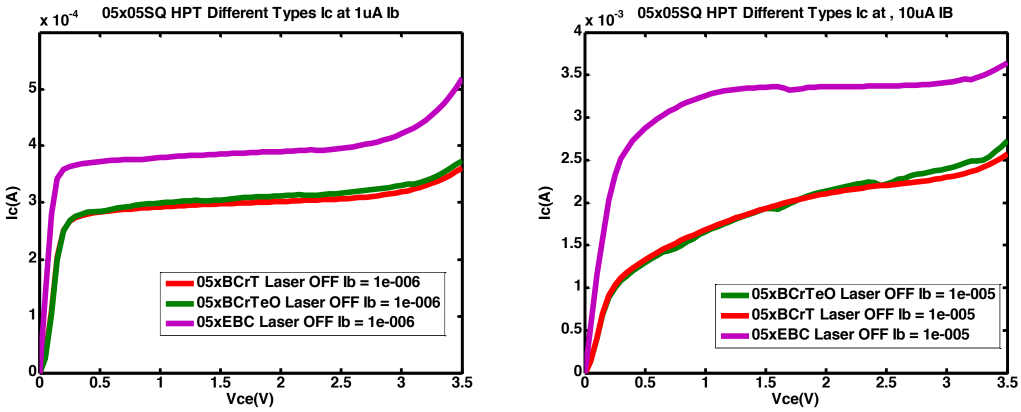

a) b)

Figure 2.34 Ic-Vce curves of different 5x5µm² HPTs (a) Ib = 1µA (b) Ib= 10µA

Figure 2.35 shows that the Gummel plot of the xBCrT and xBCrTeO are essentially the same value. Ic and Ib increases for the xEBC HPT which is expected from a larger intrinsic transistor. The resulting current gain β of the two xBC types are the same region of peak value approximately 298 and the current gain β of xEBC is higher and reaches a value of 382.

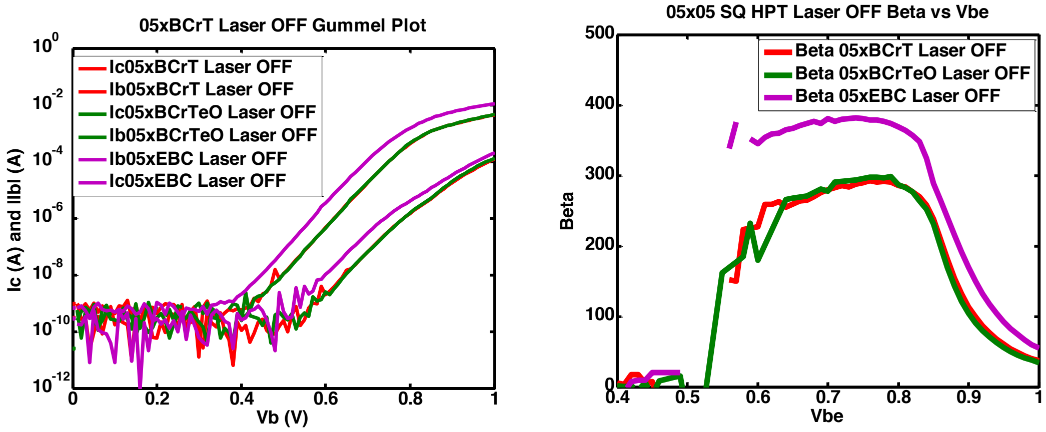

a) b

Figure 2.35 Different 5x5µm² HPTs a)Gummel plot of the different 3x3 HPTs b)extracted beta

2.3.1.3 10x10 µm² HPTs

In this optical window size 10x10µm², it is noted the measurement for xBC exists and this will starting point of the discussion. Removal of titanium (rT) results in decrease of collector current as in the case of the 3x3µm² HPT measurements. For this size, the value of the collector current of the etched oxide HPT is different from the non etched oxide HPT with a value that is lower. This is due to the large surface for the etching which may deepen the etched region, thus affecting the active layer, altering the base region which is not protected by the Titanium.

The measurement of the SIC HPT version is similar to that of removed titanium HPT below the start of its breakdown voltage which starts to appear at 1.75V Vce for the low current biasing. In the higher current biasing, the SIC HPT shows a higher Rc resistance as with the smaller SIC HPT, however with less pronounced increase. Finally, xEBC results in higher collector currents, similar to that of observed in the 5x5µm² HPTs , both in the 1µA bias and 10µA bias.

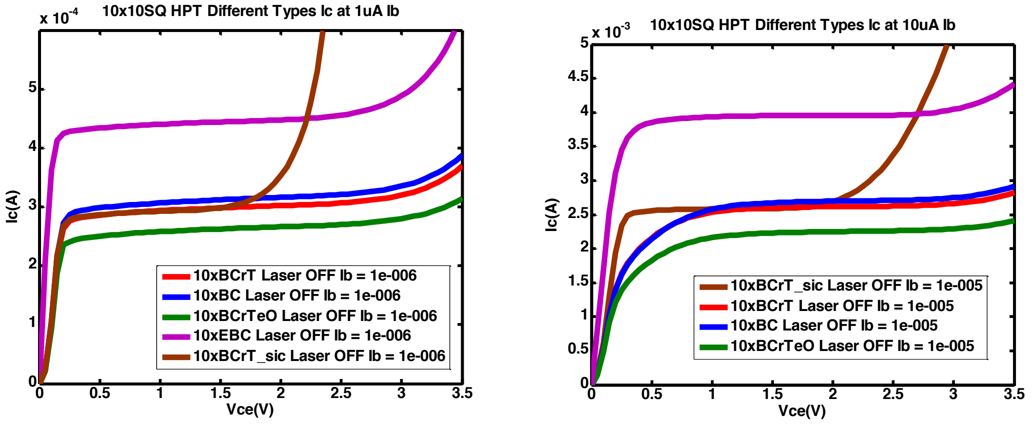

a) b)

Figure 2.36 Ic-Vce curves of different 10x10μm² HPTs (a) Ib = 1μA (b) Ib= 10μA

Figure 2.37 shows the Gummel plot and the extracted current gain β . The β of the xEBC HPT is the highest of all 10x10μm² HPTs. This is attributed to the increased intrinsic transistor size. This is followed by the xBC with a peak value of 305. The xBCrT HPT shows a slightly lower peak beta of 292. The xBCrTsic HPT has approximately the same β of 290 but rolls off at a slower rate compared to the xBCrT HPT. It can be said the effect of using SIC has little impact on the DC characteristics of large HPTs. The xBCrTeO HPT shows a lower beta curve with approximately a 18% reduction compared to the xBCrT HPT , this may be attributed to some issues during the oxide etching as observed in the Ic-Vce curves.

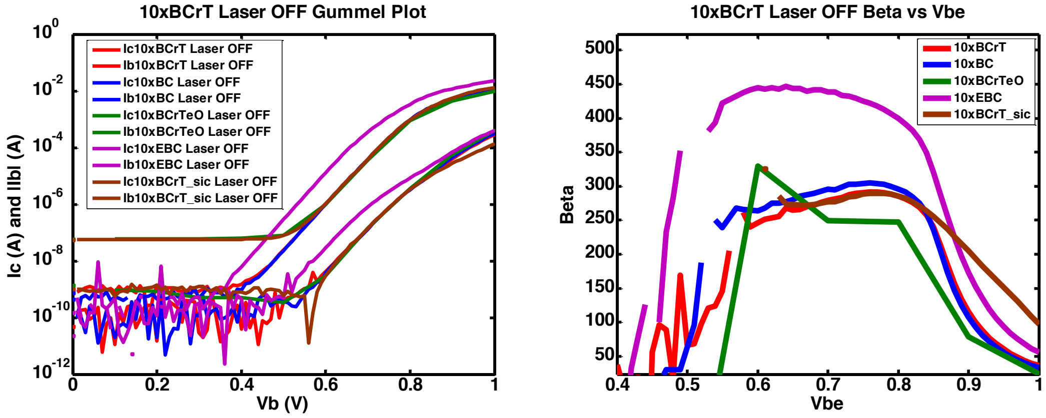

a) b)

Figure 2.37 Different 10x10μm² HPTs a)Gummel plot of the different 3x3 HPTs b)extracted beta

2.3.1.4 50x50μm² HPTs.

In this size, there are no significant change in the xBC and xBCrT. The xBCrTeO results in a slightly lower collector current. A similar trend that was seen in the 10x10μm² HPT. The series resistances dominate the DC characteristics of the HPT.

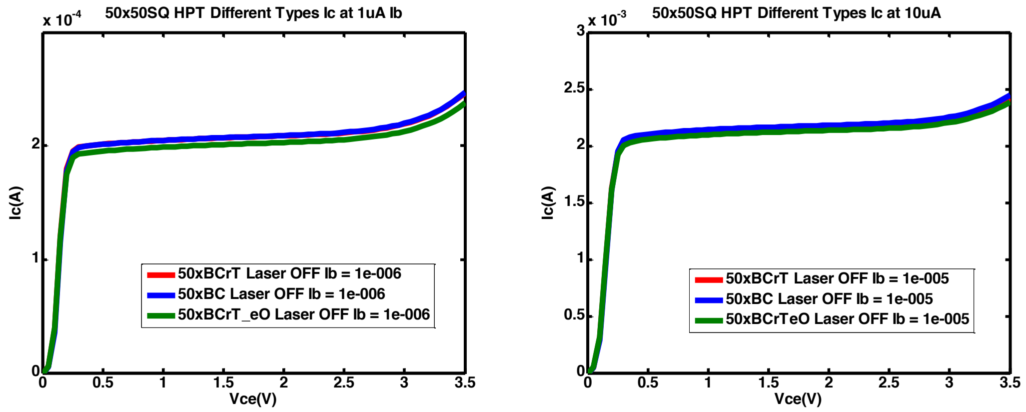

a) b)

Figure 2.38 Ic-Vce curves of different 50x05 HPTs (a) Ib = 1uA (b) Ib= 10uA

The beta curve for all the measured 50x50μm^2 HPTS showed that there is no significant change in the different types. It is primarily due to the large size of the optical window that, the extrinsic resistances dominate the HPT resistances.

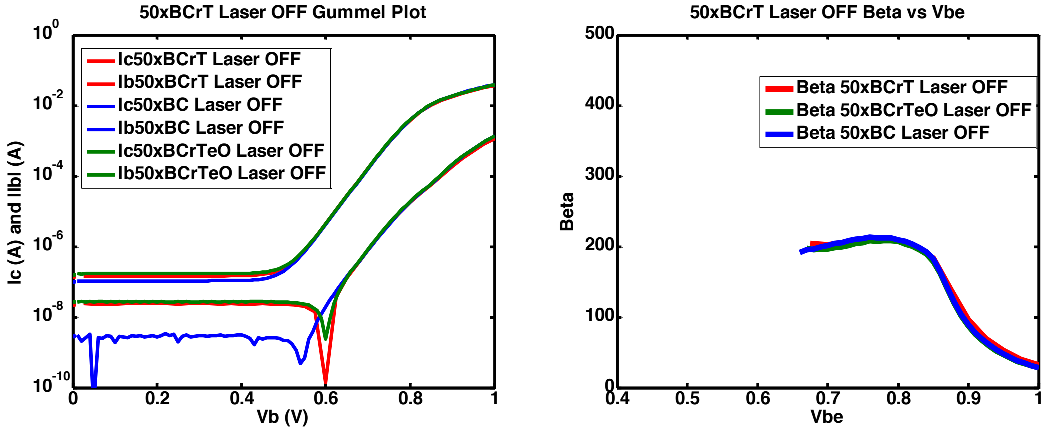

a) b)

Figure 2.39 Different 50x50µm^2 HPTs a)Gummel plot of the different 3x3 HPTs b)extracted beta

The measured peak current gain of the different HPTs are summarized in Table 2.7. It shows that for xBC HPTs, the 10x10µm^2 HPT has the highest peak current gain β of 305 with a Vbe of 0.78V. The xBCrT HPTs shows that that 10x10µm^2 HPT has the highest peak value of 292 with 0.77V. In xBCrTeO HPTs, the 5x5µm^2 HPT has the peak value of 299 at 0.79V for its current gain β. The smallest HPT with the xBCrTsic HPT structure benefits from the increase in Ic due to the selective implantation of the collector. It has a peak β of 299 at 0.76V. Finally for xEBC HPTs, the largest optical window of 50x50µm^2 presents the highest measured β of 803 at 0.65V.

Table 2.7 Summary of measured peak β and corresponding Vbe value

Device Name	Peak Beta Values	Vbe
R1-03SQxBC	244	0.8
R1-10SQxBC	305	0.76
R1-50SQxBC	213	0.78
R1-03SQxBCrT	210	0.81
R1-05SQxBCrT	292	0.78
R1-10SQxBCrT	292	0.77
R1-50SQxBCrT	211	0.775
R1-05SQxBCrteO	299	0.79
R1-10SQxBCrteO	249	0.7
R1-50SQxBCrteO	208	0.79
R1-03xBCrTsic	326.7	0.76
R1-10SQxBCrTsic	290	0.76
R1-05SQxEBC	382	0.74
R1-10SQxEBC	446.6	0.64
R2-10SQxEBC	612	0.675
R2-20SQxEBC	707	0.65
R2-30SQxEBC	737	0.675
R2-50SQxEBC	803	0.65

2.3.2 Dynamic behavior and RF characterization

RF characterization consists of measuring the four S-parameters of the transistor in common-emitter configuration over the 10MHz-40GHz range. The non-illuminated S-Parameters of the HPTs show the electric frequency characteristics of the HPT. It is expected that the S-Parameters will show similarities to the reference HBT. It is expected however that the modifications will have a pronounced effect in the cut-off frequencies of the different HPT structures.

Figure 2.40 shows the photo of the measurement platform. RF response is obtained with a 40GHz vector network analyzer from Agilent. The measurement provides S-parameters of the electrical two ports of the phototransistor. Biasing is performed using the Agilent B1500, with the same process as previously mentioned. Collector voltage, Vce, and base current, Ib, are swept in order to provide a complete set of S-parameters measurement across the Ic-Vce network.

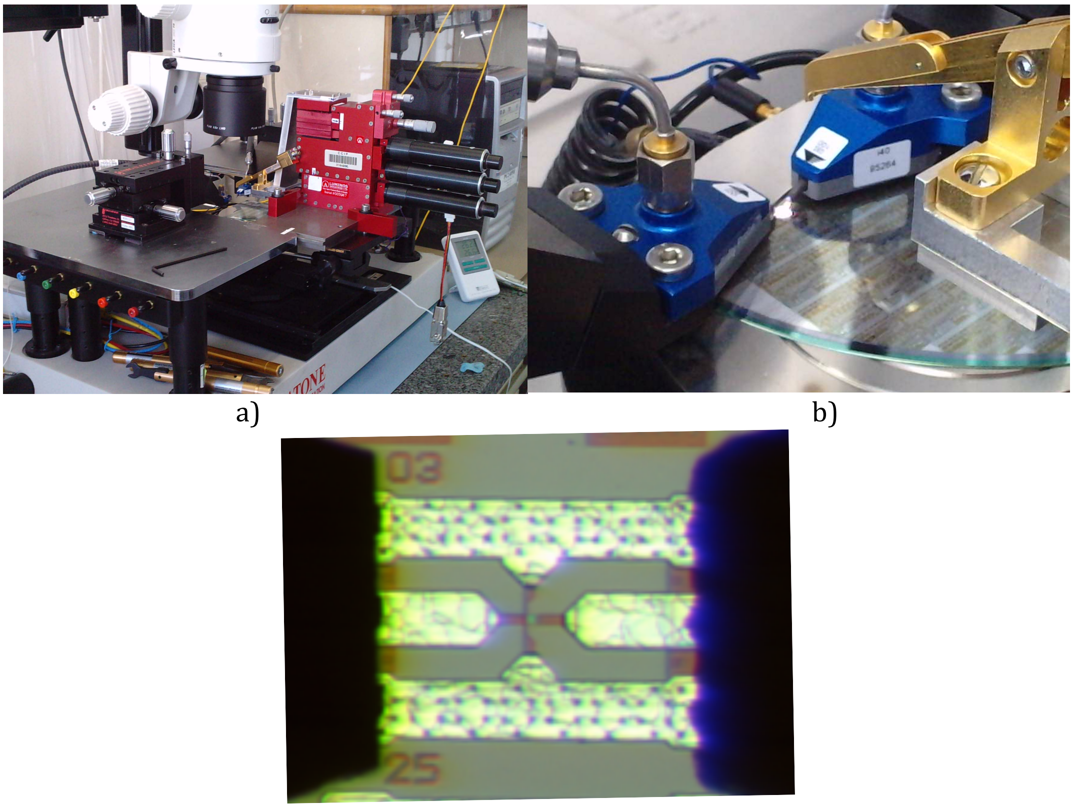

a) b)

c)

Figure 2.40 The series of photographs show (a) the on wafer measurement bench, (b) the GSG probes with the HPT test chip, and (c) microscope view of the R1-10SQxBCrT HPT

Using GSG fixtures for on-wafer measurement requires de-embedding of the GSG fixtures' effect on the measurement. Structures for de-embedding the on wafer measurements were included in the runs. They are shown in Figure 2.41

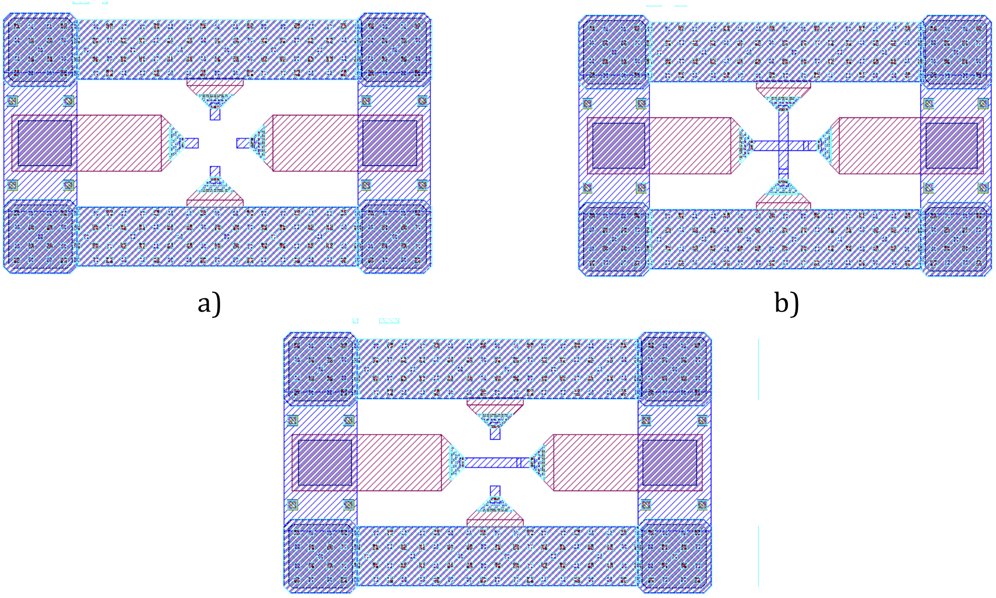

a) b)

c)

Figure 2.41 RF de-embedding structures. (a) open (b) short (c) thru

Post-processing of the measurements includes the measurements of the de-embedding structures and using the de-embedding equations. Open-de-embedding (OPD) is one of the simplest de-embedding procedures as it only uses one de-embedding structure. To perform open de-embedding, a set of open pads are used. This method assumes that the parasitics leading to the DUT is modeled by a parallel admittance. This admittance is determined form the measured admittance of the OPEN pads. De-embedding is implemented by subtracting the open admittance from the admittance of the DUT with pad and interconnects. This allows to have de-embedded measurements that are sufficient for the frequencies under study. The two-step de-embedding uses an open and a short standard. This method assumes that the parasitics leading to the DUT is modeled by a parallel admittance and a series impedance. The first step for this de-embedding is performed by subtracting the Y-parameters of the open standard from the Y-parameters of the DUR with pad and interconnects. This Y-parameter is then converted to Z-parameters. The second step is subtracting the Z-parameters of the series impedance from the Z-parameters computed from step one. This series impedance is computed as the difference of the admittance of the short standard and the admittance of the open standard. Figure 2.42 shows the S-Parameters of the R1-SQ10xBC HPT at a bias point of Vce= 1.5V and Vbe = 0.84V. Three sets of measurements are presented, raw measurements (RAW), open-deembedded measurements (OPD) and two step de-embedded measurements (2STD). OPD and 2TSD shows similar results in the measurements up to 40GHz. Using simpler structures would suffice for the characterizations.

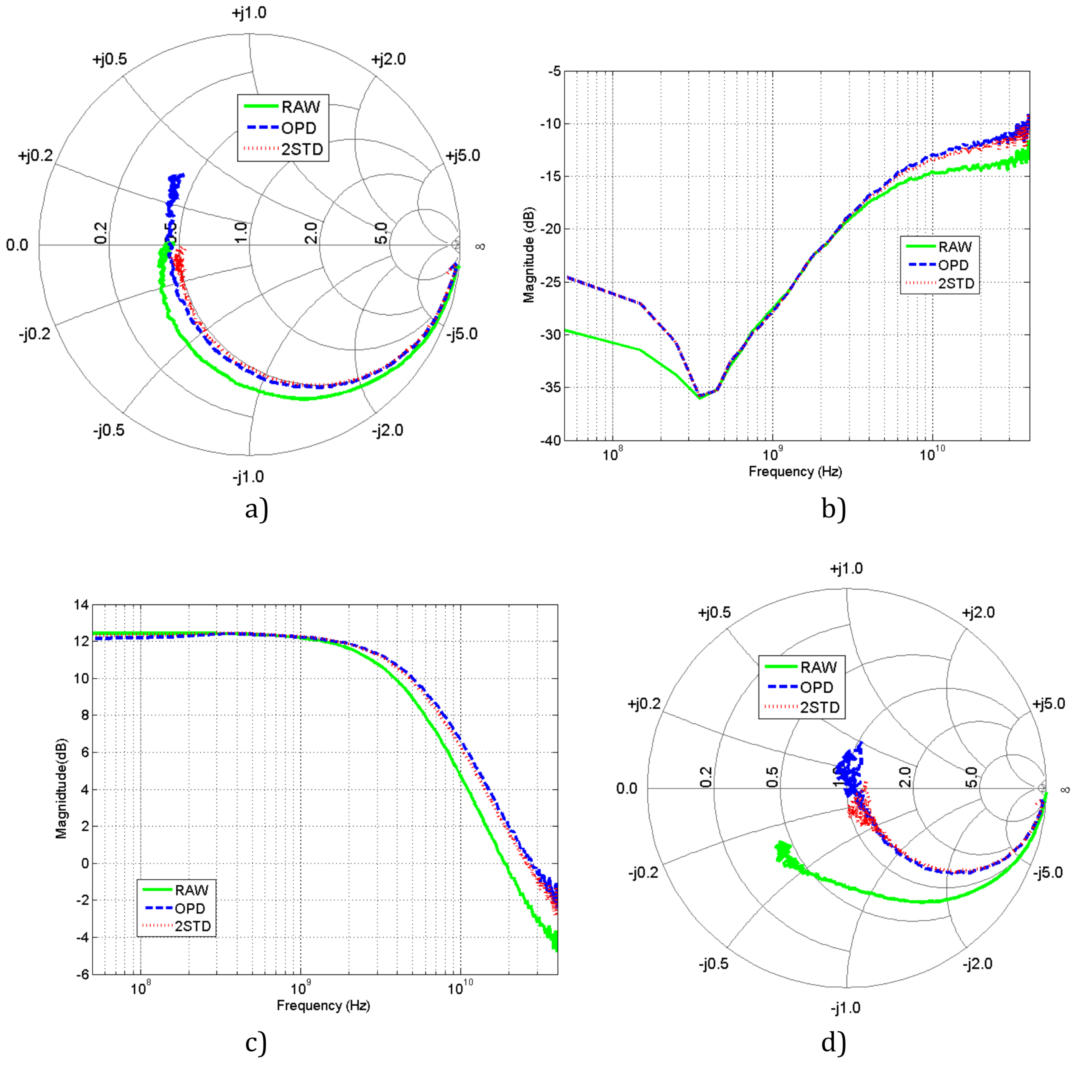

a) b) c) d)

Figure 2.42 Complete S-Parameters of R1-10SQxBCrT HPT, raw measurement compared with OPD and 2STD de-embedding

Figure 2.43 shows the f_T at 1.5V and V_{ce} of the RAW and de-embedded measurements. It show a peak f_T of around 40GHz for the de-embedded measurements. The simulation results of a reference device with a peak f_T at 47GHz is also superimposed. The modifications to make an extended base collector HPT results in the reduction of f_T which is primarily due to the higher capacitance in the base and collector region.

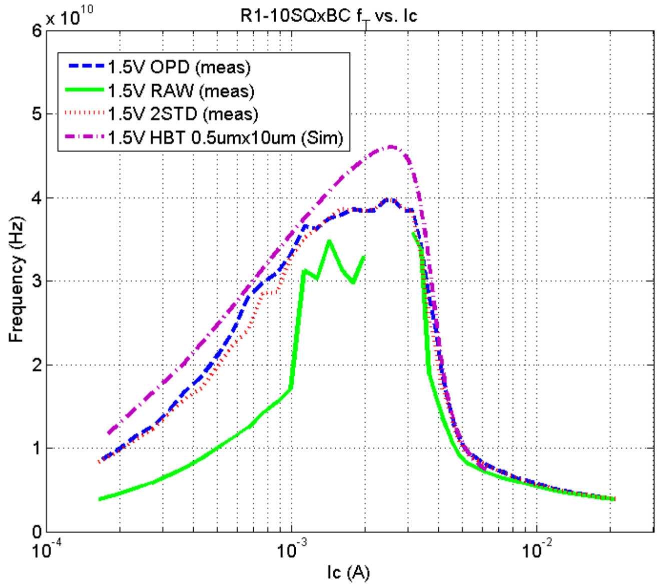

Figure 2.43 Extracted f_T of R1-10SQxBC HPT with different de-embedding techniques (measurements) and the f_T of the 0.5x10µm² reference HBT superimposed (simulation)

We present hereafter the extracted f_T of the different HPTs following the color scheme presented in the extracted current gain β of the different HPTs that were grouped according to the size. Figure 2.44 shows the extracted f_T versus Ic plot of the different 3x3 HPTs namely xBC, xBCrT. and xBCrTsic. The f_T of the xBC and xBCrT is in the same region of 43GHz. Using the selective implanted collector in the structure, increases the peak f_T to 46 GHz. However, this is achieved at higher collector currents but falls abruptly after the f_T reaches its peak value.

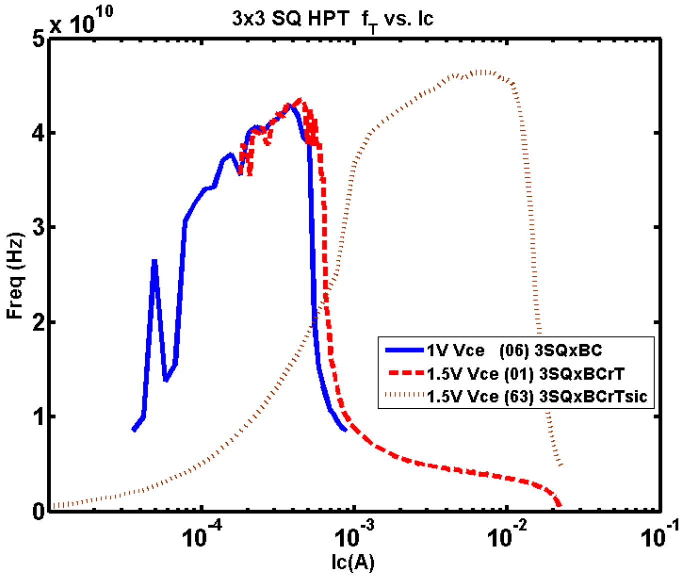

Figure 2.44 Measured f_T vs. Ic of R1-03SQxBC, R1-03SQxBCrT, R1-03SQxBCrTsic

Figure 2.45 shows the f_T vs Ic of the different 5x5µm² HPTs. It shows that etching the oxide above the optical window does not severely affect the f_T of the device. Both the R1-05SQxBCrT HPT and R1-05SQxBCrTeO HPT has a peak f_T of 47GHz and fall off at the same rate. The R1-05SQxEBC HPT has approximately the same f_T but is achieved at higher collector currents. This is due to the enlarged intrinsic transistor.

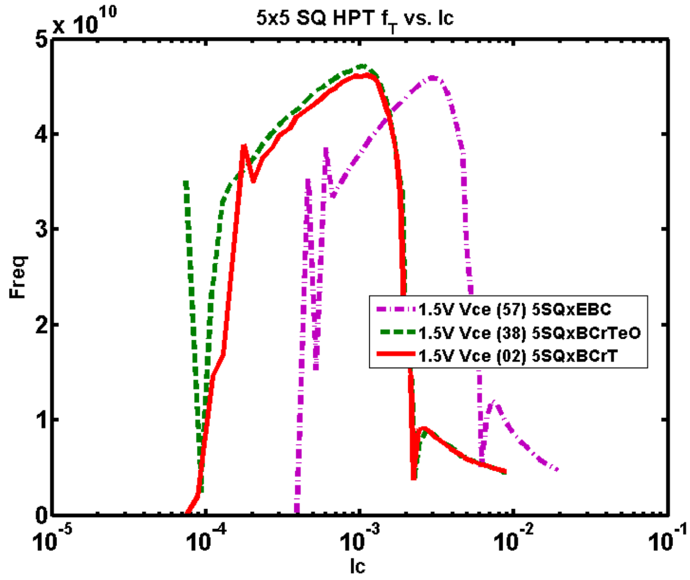

Figure 2.45 Measured f_T vs. Ic of R1-05SQxBCrT, R1-05SQxBCrTeO, R1-05SQxEBC

Figure 2.46 shows the extracted f_T of the different types of 10x10µm² HPT. The R1-10SQxBC HPT shows a peak f_T of 42 GHz. R1-10SQxBCrT HPT version shows a narrowing of the f_T curve due to the TiSi removal but with approximately the same peak f_T of 42GHz.

Due to the increased Rc, both the R1-10SQxBCrT HPT and R1-10SQxBCrTeO HPT has the approximately the same peak f_T value which means that the RF performance is not degraded by the oxide etching. Despite the DC behavior is affected by a 20% β reduction, capacitances and transit times are not affected by the electrical active part of the HPT. The sic version keeps the wide f_T curve while benefiting from an increase in the peak f_T. The xEBC has a slight higher peak value of 44GHz as compared to the non-sic xBC types. Similarly to the 5x5µm² xEBC HPT, it requires a higher collector current to achieve its peak value due to the increased intrinsic transistor size.

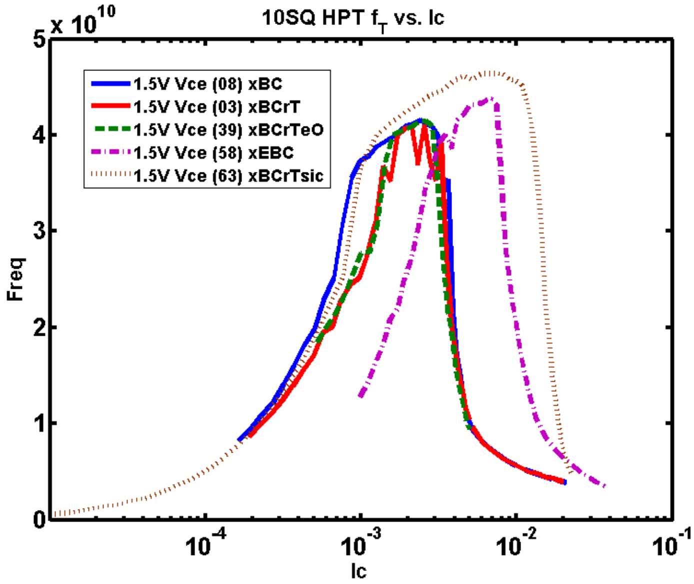

Figure 2.46 f_T vs. Ic of different 10x10 HPTs

Figure 2.47 shows the 50x50µm² HPTs. Both the R1-50SQxBCrT and R1-50SQxBCrTeO HPT shows a peak f_T of 17GHz. Even for these large HPTs, oxide etching does not severely affect the RF performance of the HPT, while it had some effects on dc performances.

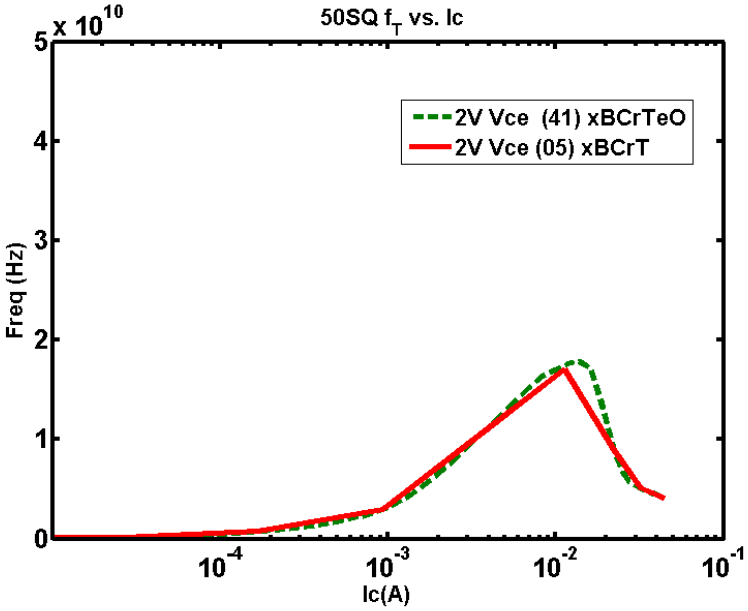

Figure 2.47 f_T vs. Ic of, R1-50SQxBCrT HPT and R1-50SQxBCrTeOHPT

Table 2.8 shows a summary of the RF characteristics of the various HPTs with the values of the peak f_T and the bias current that is required to reach it. All xBC HPTs from 3x3µm², 5x5µm² and 10x10µm² have an f_T in the range of 42GHz-47GHz. Only the 50x50µm² sized optical window HPTs suffers a severe penalty in f_T. The extended Emitter, Base and Collector (xEBC) HPTs exhibits lower values of f_T as optical window size is increased. Their f_T range from 32GHz to 40GHz This is primarily due to the increase in the base collector capacitance of the intrinsic transistor, which is directly proportional to the optical window size. Finally, the required current to reach the peak f_T of the transistors increases as a function of the optical window size for all the different HPT types. The table also lists the maximum measured maximum gain of the device and its corresponding -3dB cutoff frequency. Generally we can classify the xBC types as Group 1 and xEBC types as Group 2 HPTs. Group one HPTs benefit from smaller intrinsic transistor which can be seen in the measured cutoff frequencies as high as 13GHz for a 5x5 µm² optical window size and as low as 250 MHz for the 50x50µm² optical window size. In the group 2 HPTs which has larger intrinsic transistors, the cutoff frequencies are 500 MHz for the 10x10 and as low as 275 MHz for the 50x50 µm². This will be important for the opto-microwave HPT behavior analysis in further chapters.

Table 2.8 Summary of peak f_T and maximum S21 values.

Device Name	FT (GHz)	IC (mA)	Vce (V)	RF Max S21 at 50 MHz (dB)	F-3dB (GHz)	Gain Bandwidth
R1-03SQxBCrT	43.48	0.46	1.5	----	-----	--
R1-05SQxBCrT	46.19	1.1	1.5	5.7	12.6	71.82
R1-10SQxBCrT	49.01	2.5	1.5	13.12	4.35	57.072
R1-50SQxBCrT	17.03	11.25	2	22	0.25	5.5
R1-03SQxBC	42.96	0.39	1	----	---	--
R1-10SQxBC	41.54	2.4	1.5	12.31	5.6	68.936
R1-50SQxBC	7.54	15	2	23	0.25	5.75
R1-05SQxBCrteO	47.12	1.05	1.5	5.8	13.93	80.794
R1-10SQxBCrteO	41.6	2.6	1.5	12.5	3.15	39.375
R1-50SQxBCrteO	17.83	13.8	2	23	0.25	5.75
R1-05SQxEBC	45.85	3.15	1.5	13	3	39
R1-10SQxEBC	43.77	6.9	1.5	19.3	1.3	25.09
R1-03xBCrTsic	46.4	7.4	1.5	----	---	----
R1-10SQxBCrTsic	45.31	7.8	1.5	17.54	2.95	51.743
R2-10SQxEBC	35 GHz	7mA	2V	19.26	0.499	9.61074
R2-20SQxEBC	33 GHz	10mA	2V	23.86	0.35	8.351
R2-30SQxEBC	34 GHz	19mA	2V	25.2	0.25	6.3
R2-50SQxEBC	32 GHz	30mA	2V	26.02	0.275	7.1555

In summary, for the DC and RF characterization of the HPT, The extended base collector HPT (xBC) sets the reference characteristics as this is the most simple modification in the reference HBT structure which keeps the size of the intrinsic transistor as small as possible with the emitter width of 0.5µm and the emitter length is dependent on the optical window size. Removing the Titanium in the extrinsic base polysilicon reduces the collector current and the peak current gain β of the HPT by up to 20% and shows only little degradation on the cutoff frequency of the HPT. Etching the oxide on top of the optical window, shows minimal variations on the DC and RF characteristics of the HPT. It can be concluded that this processing step does not affect the HPT electrically. Finally, the extended base emitter and collector HPT benefits from enhancement in peak electrical beta but suffers from low cutoff frequencies as compared to the Group 1 HPTS of the same optical window size.

2.4 Optical and Opto-Microwave Characterization Setups for HPTs

Optical and opto-microwave characterization is the most direct analysis of the phototransistor behavior. This section aims at providing a brief illustration on the impact of illumination on the DC measurements to validated the sensitivity of our bench and to set up the experimental bench for opto-microwave measurements that will be used in the succeeding chapters.

In opto-microwave characterization, two operation modes have to be measured: the phototransistor mode, i.e. with a biasing suited for the transistor mode activation (Vbe above 0.7V roughly), and the photodiode mode (Vbe below 0.4V roughly). Some relevant opto-microwave parameters are: opto-microwave gain G_{OM} , optical transition frequency f_{Topt} and opto-microwave S-parameters S_{OM}.

Figure 2.48 shows the schematic of the opto-microwave measurement bench. The Network Under Test (NUT) is the network in between A and B. It includes the VCSEL, optical splitter, optical probe, HPT and the GSG probe. The measured S_{21} as shown by the VNA is the link gain of this network (dB). Port 1 of the VNA directly modulates an 850nm VCSEL. The directly modulated optical signal is connected to a 90/10 optical splitter. The 10% value of the optical signal is continuously monitored to ensure proper the system is properly connected. This is also used to compute for the optical power that is inserted to the optical probe. The 90% of the optical signal is used to illuminate the phototransistor. Illuminating the phototransistor is achieved by using an optical probe, which is attached to a nanopositioner. The nanopositioner allows the optical probe to be positioned to about 50μm above the optical window with the aid of a 45° mirror to observe the height of the probe through a microscope as seen in Figure 2.49. The optical probe has a lensed fiber with a spot size that is determined experimentally to be 26μm [223].The base of the HPT is connected to a GSG probe. The base is biased with a bias tee with a 50Ω load attached to the RF input of the bias tee. The collector is connected via GSG probe to the port 2 of the VNA. Port 2 of the VNA is a port used for the measurement and to provide the collector bias. The VNA used for the experiment is an 8753ES 40GHz VNA and it is connected to an Agilent B1500 semiconductor parametric analyzer. Control and automation of measurements are implement using customized Easy Expert application tests and Matlab scripts.

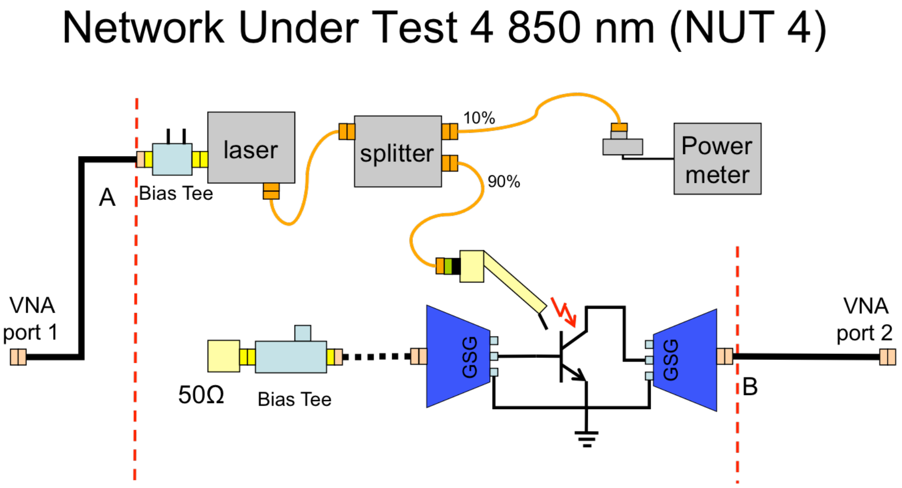

Figure 2.48 Measurement bench for the opto-microwave characterization of HPTs

It is then important to note that the measurement of the HPT is actually the measurement of the link composed of the laser, the injection fiber and the phototransistor. A 10Gbps Avalon VCSEL was used for the measurements. Figure 2.49 shows the photographs of the opto-microwave measurement of the R1-10SQxBC HPT as an example. The GSG probes are on the GSG pads and the Lightwave probe is positioned on top of the HPT. The center of location of the optical window of the HPT is determined by scanning the optical probe in the X and Y the vicinity of the optical window as can be seen in Figure 2.49(b). The location with the highest measured link gain for the PD mode of operation is set to be the center of the HPT optical window.

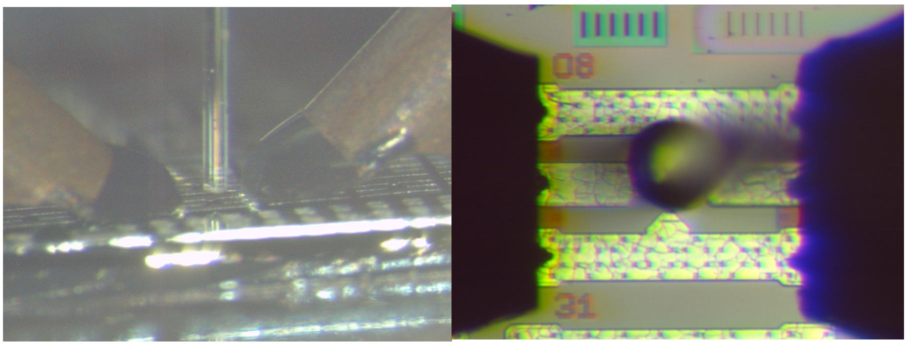

a) b)

Figure 2.49 Lightwave probe on top of HPT structure.

Figure 2.50 shows the measured link gain of the laser and HPT in two modes of operation of the HPT, the PD mode and HPT mode at Vce = 2V. In PD mode, the base of the HPT is set to 0V, the emitter is grounded and the collector is set at 2V. In HPT mode, the base is biased at 25µA, the emitter is grounded and Vce = 2V. The low frequency link gain in the PD mode is -41dB with an opto-microwave cutoff frequency of approximately 180MHz. In the HPT mode of operation, the low frequency link gain is -39dB and the opto-microwave cut-off frequency of approximately 190MHz. The optical gain is at 2dB for the 10SQxBC HPT at this specific biasing point.

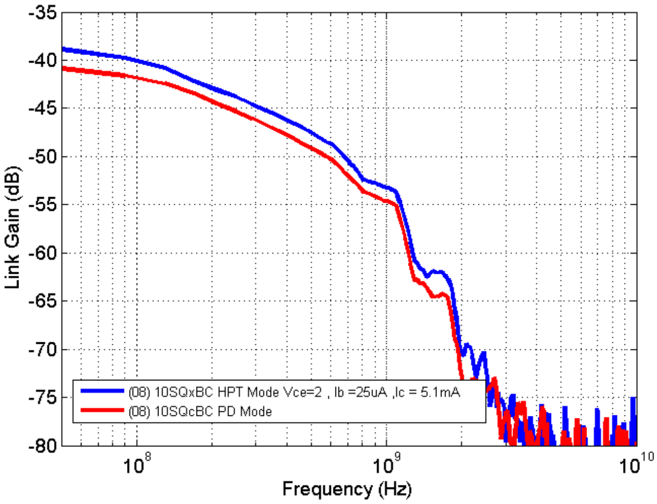

Figure 2.50 Link Gain of 10xBC HPT mode and PD Mode

2.4.1 Absolute characterization and de-normalization

The measurement of any analog optical link with a VNA needs some calibration procedure on the electrical reference plane: one at the input of the laser, and one at the output of the photo-detector. Thus, an absolute value for the link power transfer is available, in phase and in module. However, it is important to extract the phototransistor response from the laser and fiber characteristics. It is done through opto-electrical de-embedding that requires a separate characterization of the laser used for measurements with a calibrated photodiode.

For this thesis, the opto-microwave measurements of the phototransistors were implemented at different times and conditions. Thus, different phototransistor opto-microwave measurement sets were made. This means that each measurement set should have at least a reference link measurement, which is composed of the laser providing the same optical power as with the phototransistor measurements and a reference photodiode. At the minimum, this provides normalized HPT responsivity measurements. A characterized photodiode allows for the extraction of the responsivity of the HPT.

Figure 2.51 shows a schematic representation of the opto-microwave measurement bench for the characterization of one reference analog optical link. The Network Under Test (NUT) 1 is the network between the VNA port 1 and VNA port 2. It includes a VCSEL, an optical splitter (10/90), a photodiode and an optical power meter. VNA port 1 of the directly modulates an 850nm Avalon VCSEL rated for 10Gbps operation. The directly modulated optical signal is connected to a 10/90 optical splitter. The 10% optical signal is used for system monitoring and the 90% optical signal is used to illuminate the Adopco photodiode. Port 2 of the VNA is connected the output of the photodiode.

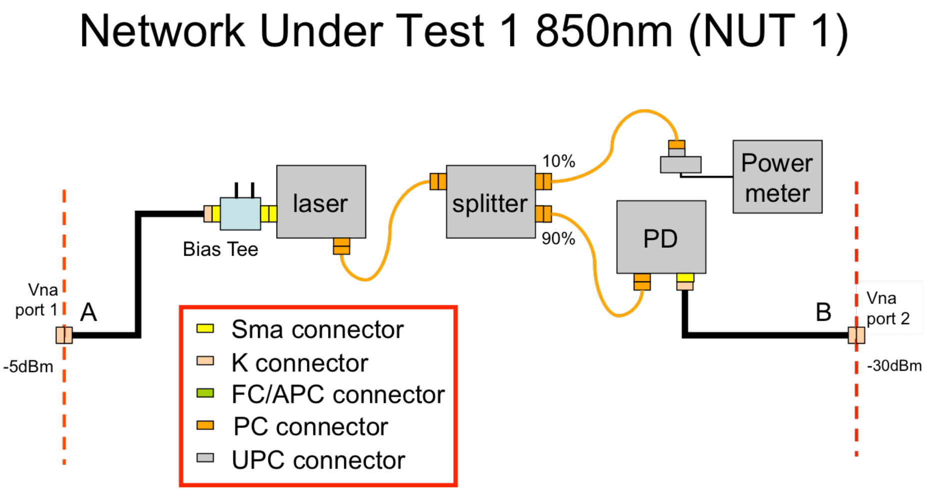

Figure 2.51 Measurement bench for the characterization of reference link made with an Avalon laser and Adopco photodiode.

The cutoff frequency from the measured link gain is dominated by the device with the lower cutoff frequency. The measured opto-microwave link gain is shown in Figure 2.52 with the monitored 10% power of the optical signal that is -18.47dBm. It will be identified as Reference Link 01 in succeeding discussions. It can be seen that there is a flat response in the region from 50 MHz to 700MHz and a lowering in response afterwards. The measurements do not show a very clean roll off in the opto-microwave link measurement response, which is primarily due to poor electrical connections and possible issues in the PCB assembly mount of the VSCEL module. The Avalon VCSEL is rated for 10Gbps operation with cutoff frequency in the 9GHz region [224]. The Adopco photodiode is rated for 10Gps operation and an expected cutoff frequency of 7.5GHz [225]. The cutoff frequency that is observed in the reference link is dominated by the cutoff frequency of the PCB assembly of the laser module. The limits of the flat response will help in the identification the optical cutoff frequency of the phototransistors.

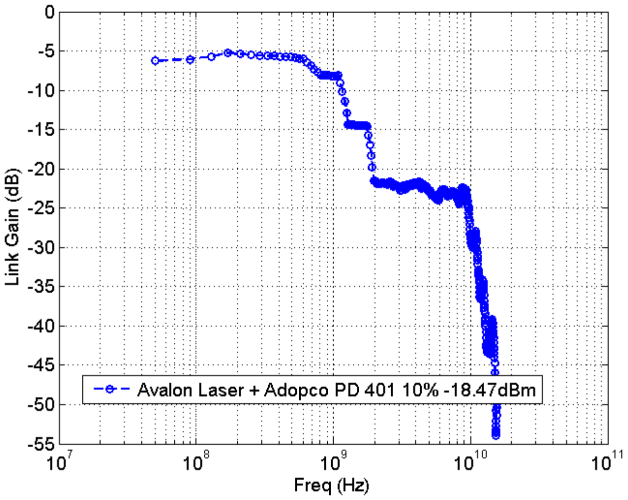

Figure 2.52 Measured G_{OM_Link} of the reference analog optical link composed of an Avalon VCSEL with an Adopco PD connected to the 90% optical output of the VCSEL. The monitored 10% value of the optical signal is -18.47dB.

Reference Link 02 is implemented using the same measurement setup in Figure 2.51. However, different components were used. It used a VI Systems Laser Module operating at 850nm with a slope efficiency of 0.3W/A thru fiber probe and Photometer, and a New Focus Photodiode Module with a responsivity of 0.11 A/W at 850nm. As specified in the data sheet , the laser has a cutoff frequency of 25GHz as specified in the datasheet and the PD a cutoff frequency of 25GHz.

Simple computation of the link gain from the given responsivity and slope efficiency shows that the link gain is :

Link Gain = 20 log10 (0.3 W/A * 0.1 1A/W) = -29.62 dB

This value is consistent with the measured link gain. The resonance of the link gain occurs at 10 GHz, and the cutoff frequency is at 18GHz which is near the -3dB cutoff frequency of the VCSEL as specified in the datasheet. This cutoff frequency is primarily due to the cut off frequency of the VCSEL module. Inserting a 50/50 splitter after the 90% branch produces an optical loss of -3dB. This results in a -6dB loss in the optical link gain which can be observed in the blue line. This blue line is labeled as Reference Link 03 . Reference Link 04 is the link gain measured using an ESYCOM assembled Transceiver optical sub-assembly (TOSA) and the New Focus photodiode. Reference Link 02 injects 2.44mW at the input of the lensed fiber. Reference Link 03 injects 1.22mW and Reference Link 04 injects 1.8mW .

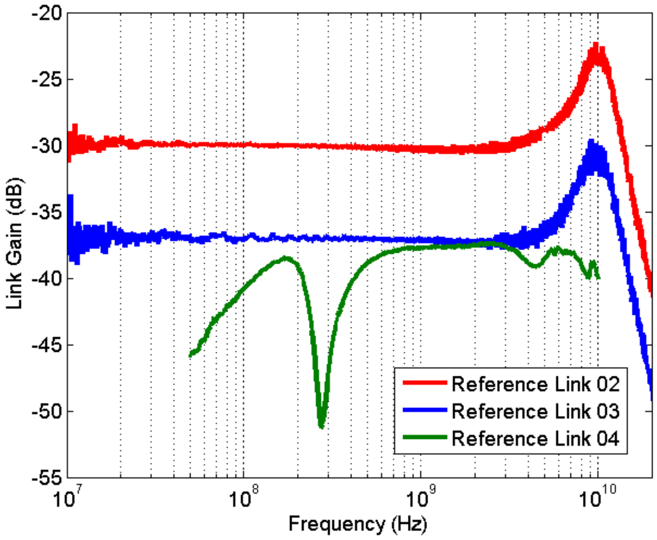

Figure 2.53 Measured reference link using New Focus photodiode with VI systems laser (Reference Link 02 and 03) and ESYCOM TOSA [226] (Reference Link 04)

The opto-microwave gain of the HPT $G_{OM\_HPT,dB}$ is the ratio between the output power of the receiver and the output power of a reference photodiode calibrated to 1A/W. Practically this is extracted using two G_{OM} measurements:

$$G_{OM\ HPT,dB} = S_{21(Link_{Laser}+HPT)dB} - S_{21(Link_{Laser}+\ PD)dB} + R_{ph(PD\ ref),dB}$$

with $S_{21(link\ DUT)dB}$ the measured gain for the analog optical link composed of the VSCEL and HPT. $S_{21(link\ PD)dB}$ is the link gain measured for the link with the reference photodiode and $R_{ph(PD\ ref),dB}$ is the known responsivity of the reference photodiode.

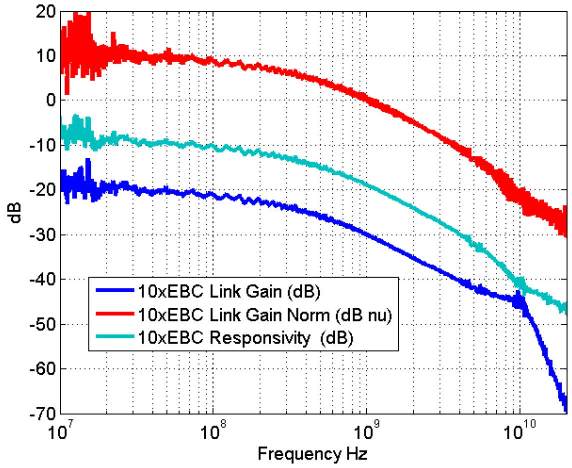

Figure 2.54 Extraction step of the HPT responsivity of R2-10xEBC from opto-microwave link measurements. HPT bias: Vce = 2V,Vb = 0.85V, Ib = -6.375uA,Ic = 9.71mA. At 50MHz Responsivity is 0.336A/W, cutoff is 295MHz and Gain bandwidth = 0.98898 GHz A/W

Figure 2.54. shows the resulting plots from the extraction of the GOM HPT (dB) of R2-10xEBC HPT. It shows the final extracted GOM of the HPT together with the initial measured link gain of the HPT and the reference link gain used for the removing the VCSEL characteristics. The REF link gain line is subtracted from the Link Gain line, which results in link Gain norm. The responsivity (dB) of the reference photodiode is added to the Link Gain norm which results in the HPT responsivity (dB). At 50MHz, the link gain

is measured as -20.46dB, the reference link is at -30.01dB and the responsivity of the reference PD in dB is -19.17dB. The HPT opto-microwave responsivity is thus -9.46(dB) and 0.34 A/W in linear terms at low frequency.

2.4.2 Optical influence on electrical DC performance

Optical responsivity in DC of the phototransistor can be measured by using the same DC characterization used for electrical measurements such as the Ic-Vce curves and Gummel plots with the difference of having illumination in the optical window. Figure 2.55 shows a schematic of measuring the optical influence on the DC and RF performance of the HPT. The biasing and measurements of the base and collector are done using a semiconductor parametric analyzer that is directly connected to a VNA. The optical illumination and alignment procedure follows the procedure described earlier.

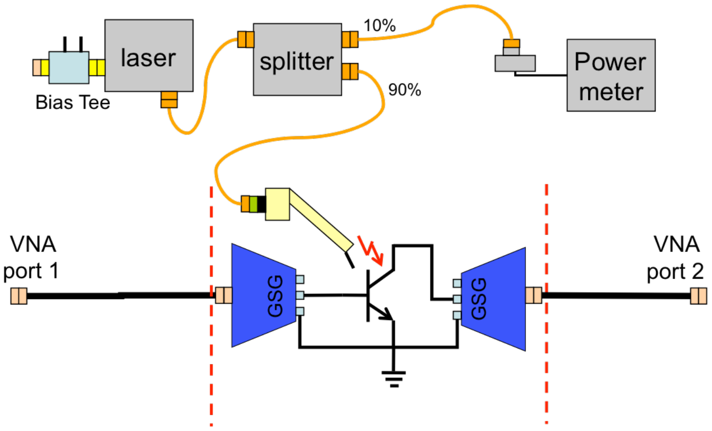

Figure 2.55 Measurement setup to measure the optical influence on DC performance of HPTs

Figure 2.56 shows the Ic-Vce curve of the R1-10SQxBCrT HPT under illuminated and non-illuminated conditions. The non-illuminated condition (blue curves) shows the electrical output characteristics of the HPT. Vce is swept from 0V to 3.5V and Ib is swept from 5µA to 20µA in 5µA steps. Under the same biasing conditions, the HPT is vertically illuminated with an 850nm VCSEL and a 1.2mW output power is fed to the optical probe. This results in an illuminated Ic-Vce curve (red curves) with a noticeable increase in the output collector current. It can be observed for the plots that as Ib is increased, the change in collector current becomes less. A DC responsivity can be extracted from these measurements by subtracting the non-illuminated collector current from the illuminated collector current with same base current bias dividing the difference by the optical power of the illumination. An equation for this DC responsivity is presented in Eq. 1.22.

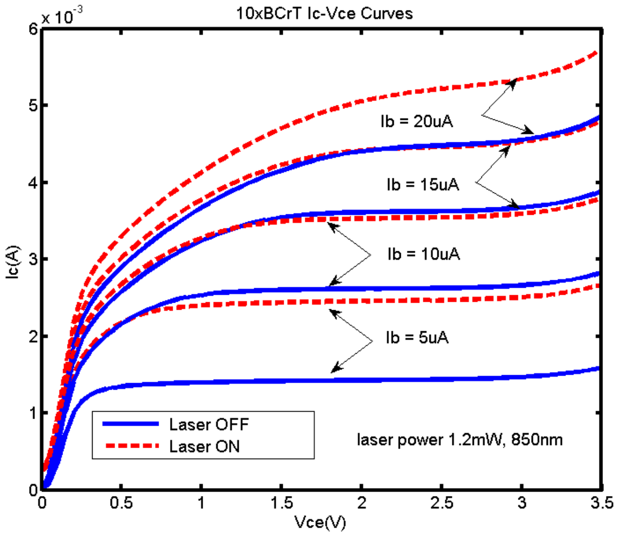

Figure 2.56 Ic-Vce curves of R1-10xBCrT under illuminated and non-illuminated conditions

Figure 2.57 shows the extracted DC responsivity for a 5µA biased R1-SQxBCrT HPT. It has a flat DC responsivity of 0.86 A/W in the Vce range of 1V-2.8V. We can see a decreasing responsivity is noticed as Ib is increased, especially at the love Vce value. This can be explained by the modulation of the BC space-charge region, which affects the photogenerated current. This observation is consistent with the fact that the BC photocurrent is exclusively responsible for the DC HPT photoresponse control.

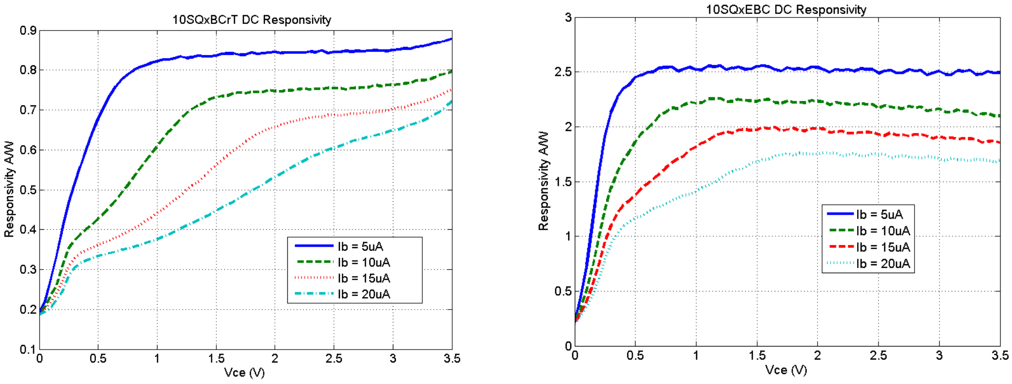

Figure 2.57 Extracted DC responsivity of R1-10SQxBCrT HPT and R1-10SQxEBC HPT under different bias conditions, including coupling losses with 1.2mW output from VCSEL

Figure 2.58 shows the extracted DC responsivity of the different 10x10µm^2 square HPTs of prototyping Run 1 having a 5µA Ib as the bias value. The extended Base-Collector HPT has the lowest responsivity, at high Vce values, the non illuminated measurements are higher than the illuminated measurements. Removal of the silicided titanium (TiSi) shows a pronounced increase in responsivity as high as 0.82 A/W for the 2V Vce biasing condition. Further increase in responsivity is seen due to the etching of the oxides with a responsivity of 1.2A/W at 2V. Finally the extended Emitter- Base-Collector HPT exhibits the highest extracted responsivity of 2.5A/W at 2V Vce. Compared to xBCrTeO the current gain increases from 240 up to 415 at Ib = 5µA and Vce = 2V. The current gain increases thus by a factor of 1.73x and the DC HPT responsivity increases by 3 times.

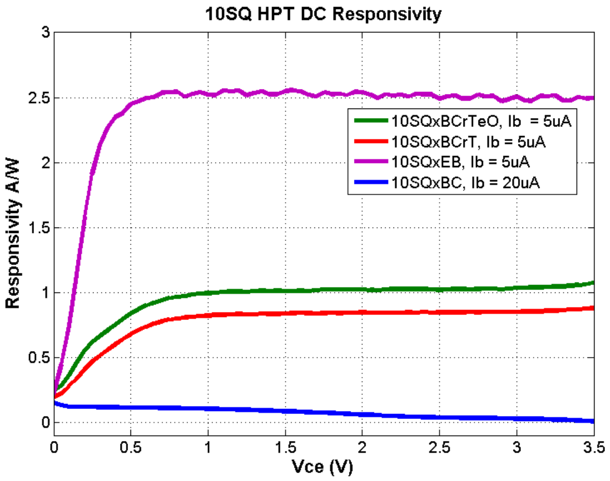

Figure 2.58. Extracted responsivity of different 10x10µm^2 square HPTs from RUN1 including coupling losses with 1.2mW output from VCSEL

Figure 2.59 shows the extracted responsivity of the 50x50µm^2 HPTs. The extended base collector (xBC) HPT has a responsivity of 0.3A/W at 2V Vce. Removing the titanium increases the responsivity to 4.2A/W at 2V. The etched oxide version exhibits the highest responsivity at 4.8A/W at 2V Vce. The trend in the increase of responsivity due to layer modifications is the same as observed in the 10x10µm^2 HPTs.

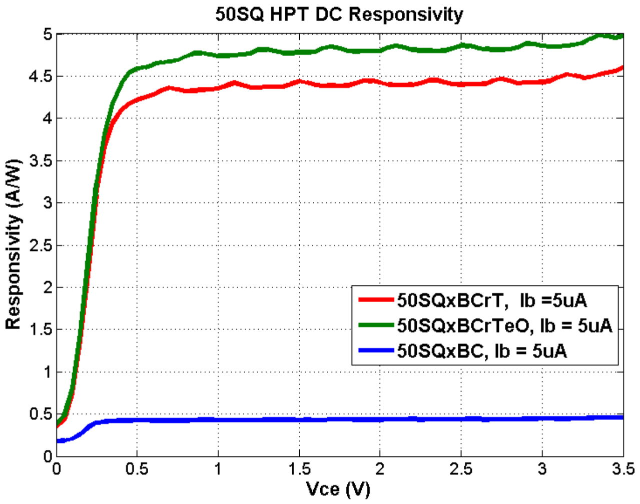

Figure 2.59 Extracted DC responsivity of different 50x50µm^2 HPTs

2.5 Conclusion

In this chapter the electrical and optical characteristics of relaxed and strained SiGe alloys were presented. We briefly discussed the SiGe HBTs of the Telefunken process. Their characteristics and performances were presented and put as a reference point for the further HPTs fabricated in this process. In the last part of the chapter we have introduced the 1st HPTs implemented using the Telefunken SiGe2RF Process. The main topologies of HPT were fabricated are: xBC HPT where only the Base and Collector regions are enlarged to collect the light; and the xEBC HPT where all the emitter, base and collector regions are extended

We then, presented the different methods for the characterization of the HPT. The performances of a 0.5x10µm^2 HBT and a 10SQxBC HPT with identical intrinsic transistor size of 0.5x10µm^2 are compared. It showed decrease in current gain β , increase in Early Voltage, less max RF gain at 50 MHz, reduction in cutoff frequency at max RF gain bias. The different HPTs structure were verified electrically and the modifications in a reference HBT to design an HPT showed process compatibility despite process rule violations. This confirms the viability of our approach.

The DC optical measurements showed that extending the base and collector results in measurable optical responsivities. The removal of silicided titanium and the etching of the oxide provide the needed vertical stack variation to improve responsivites by a factor of 5.7 times and 6.7 times with values of 0.85 A/W and 1 A/W respectively, with only decrease of the transistor current gain from 305 to 292.

Finally the extended emitter base and collector HPT exhibits the highest DC responsivity with a value of 2.5 A/W, including the coupling losses from the optical probe. This is due to the high gain of this structure. It also proved that illumination through the emitter does not interfere with the optical absorption in the base and collector.

The opto-microwave characterization of R1-10xSQxBCrT showed a 2dB optical gain is available when comparing the PD and HPT mode, with an opto-microwave cutoff frequency of the HPT in the 170MHz range. This is only an illustration of one case and is better studied in the next chapters. The following chapters will further investigate the opto-microwave behavior of these SiGe HPT.

3 SiGe HPT Opto-microwave behavior

3.1 Introduction

This chapter is focused on the study and analysis of the different fabricated SiGe HPT structures using the techniques and measurement systems presented in Chapter 2. It presents the operating modes of the SiGe HPT; photodiode PD mode and phototransistor (HPT) mode. In Section 2, the PD mode of operation of the SiGe HPT is used to provide an understanding on how the optimizations used for the different SiGe HPT structures provide improvements in its response. The efficacy of the different optimization are studied. In Section 3 the three terminal configuration of the SiGe HPTs (3T-HPT) is put into perspective. The presence of the base contact in the fabricated HPT provides another parameter to optimize the optical HPT performance. The base contact could be biased using voltage sources or current sources. It's effect in the DC optical response will be analyzed in depth. Finally, Section 4 focuses on the phototransistor mode of operation of the different HPTs. The opto-microwave responsivity of the HPTs are extracted at different bias points. This allows to find an optimum bias point that maximizes the gain and the frequency response of the HPT.

3.2 Optimization on the optical path of the HPT

This section deals with the optimization of the technology to improve the optical injection in the phototransistor. The photodiode response will be best suited for this analysis. In vertical illumination of the SiGe HPT, the optical signal enters into the phototransistor through different nitride and oxide layers which are by products of the planar processing of the fabrication technology. The optical signal then passes through the opening defined by the optical window and down to the semiconductor layers of the SiGe HPT structure. Optimizations for the transmission of the optical signal can be achieved in two ways. The first is variations in the vertical stack in of the HPT structure that minimizes the optical losses due to transmissions and reflections thus preserving the transistor effect that is inherent in the SiGe HPT. The second is matching the optical window to the optical spot size of the optical signal in order to maximize the overall response. This assumes that the optical signal has fixed spot size.

3.2.1 HPT vertical stack optimizations

Opto-microwave measurements are used in analyzing the performances of different SiGe HPT structures with different vertical stack. The HPT response under photodiode (PD) mode of operation is used to illustrate the effect of the variation in the upper vertical stack of the different HPTs on the optical injection into the device. Indeed, the photodiode mode of operation shows the response of the HPT without the effect of the electrical amplification from the intrinsic transistor of the HPT. This provides a clear indication that the observed response is due only to the photodetection of the HPT. It will illustrate the efficacy of the techniques used in the different HPT structure to improve the transmission of the optical signal. The PD mode of operation is implemented by setting the collector voltage Vce at 2V. This reverse biases the base-collector junction of the SiGe HPT. The base-emitter voltage, Vbe is then set to 0V, which turns off the base-emitter junction of the SiGe HPT. Figure 3.1 shows a representation of the 850nm optical beam with a 26µm diameter spot size illuminating the R1-10SQxBC HPT. The rectangle that covers the area of the entire HPT defines the undoped P-Type substrate and everywhere else is the p+ channel stop. It shows that the optical beam fully covers the entire surface area of the 10x10µm^2 HPT. However, there are optical power losses due to the larger optical beam as compared to the optical window of the HPT. Using the opto-microwave measurement bench presented in Chapter 2, the optical signal power that is fed to the optical probe is estimated to be 1.08mW when the laser monitored output power is of 0.014mW.

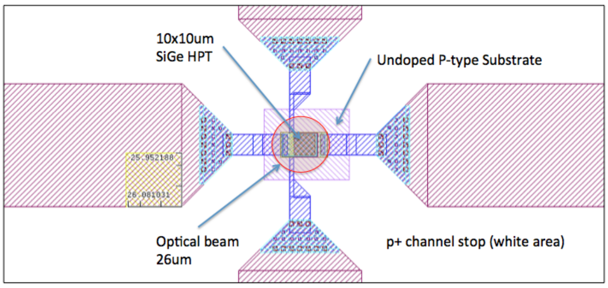

Figure 3.1 Layout view of the R1-10SQxBCrT HPT and sketch of the 26µm spot size optical beam used for the illuminated measurements.

The opto-microwave measurement results of the laser + HPT in photodiode mode link for the operation of the different types of 10x10µm^2 square HPTs are presented in Figure 3.2. It presents the measured link gain as a function of frequency for the different HPTs: 10x10µm^2 HPT with reduced emitter (R1-10SQxBC), 10x10µm^2 HPT with reduced emitter shape and TiSi removed (R1-10SQxBCrT), 10x10µm^2 HPT with reduced emitter shape, TiSi and superficial oxide layer removed (R1-10SQxBCrTeO) and the 10x10µm^2 HPT with extended emitter base and collector regions (R1-10SQxEBC). We focus on the 10x10µm^2 HPTs to keep the optical window constant and to therefore analyze more directly the difference of the optical stack only.

The different values of the measured responses are attributed to the difference in the optical powers that reach the active area of the phototransistor. The measurements of the 10x10µm^2 HPTs initially suffer from optical losses brought about by the optical beam having a spot size that is greater than the optical window. This mismatch amounts to 81% of the optical beam signal to illuminate the area outside the active collection region of emitter, base and collector of the phototransistor. Comparing the different HPT implementations that have the same optical window sizes ensures that this mismatch is the same for each type. The simplified cross-section of the R1-10SQxBC HPT under non-illuminated and illuminated conditions is shown in Figure 3.3 illustrating the path of the optical beam. Table 3.1 shows the optical properties of the different materials that constitute the vertical stack of the HPT at 850nm illumination. In the PD mode of operation, the analog optical link using the extended Base-Collector (xBC) HPT has the lowest response with a link gain of -40.9dB at 50MHz with a measured collector current Ic of 193µA. This low response is due to reflections caused by the TiSi layer in the silicided extended base polysilicon to the optical beam that is detected by the HPT. The removal of the TiSi layer in the (xBCrT) HPT results in a higher link gain of -37.2dB and a measured Ic of 244µA. This increase is due to the removal of the reflections caused by the TiSi layer. Removing the nitride and oxide layers on top of the optical window in addition to the absence of the TiSi in the (xBCrTeO) HPT further increases the optical power reaching the active layers. It shows further improvement resulting to a link gain of -35.1dB and a measured Ic of 320µA. Finally, the extended emitter base and collector (xEBC) HPT has the highest link gain at 50MHz with a value of -33.3dB. For the xEBC HPT, the optical signal passes through a one less oxide layer due to the extension of the emitter polysilicon that is not silicided. The emitter polysilicon replaces the area occupied by the oxide in extended Base-Collector type HPTs and appears having a higher transmittance as compared to the oxide layer of the same thickness.

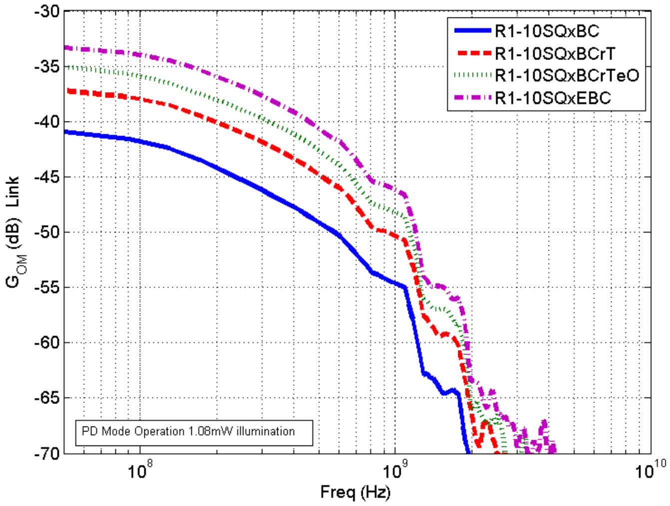

Figure 3.2 Link gain (dB) of laser + HPT in PD mode operation. Vce = 2V, Vbe = 0V. Optical power is estimated to be 1.08mW. The spot size of beam is measured to be 26µm[223].

The measured link gains are normalized to the Reference 01 link measurement as shown in Chapter 2. In Figure 3.4, the normalized G_{OM} relative to 0dB of the different 10x10µm^2 HPTs are presented. This helps to illustrate the difference in the frequency response of the HPTs. The extracted f_{-3dBom} of the four HPT types are in the range of 154MHz up to 170MHz. The lowest cutoff frequency is observed in the xBC HPT, followed by the xBCrTeO HPT with 156MHz, the xBCrT HPT with 163MHz and the highest is from xEBC HPT. The low frequency link gain (50MHz) PD mode response of the HPTs are summarized in Table 3.2. The DC responsivity is extracted using the equation presented earlier in Chapter 1.

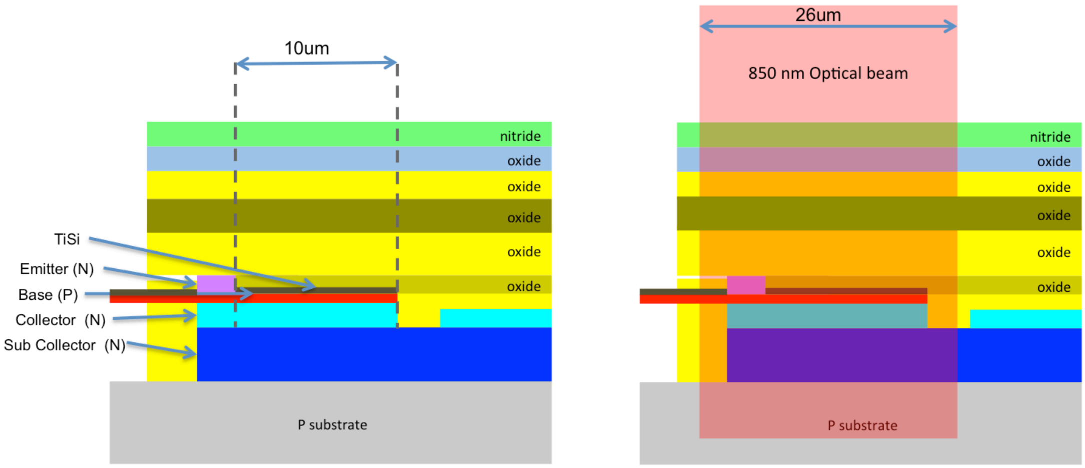

a) b)

Figure 3.3 Simplified cross section of the R1-10SQxBC HPT, without illumination and under illumination of an 850nm optical beam with a 26µm spot size. (a) non-illuminated (b)illuminated

Material	λ	n	R	T
oxide	850	1.5379	0.04485	0.9104
nitride	850	1.99354	0.11015	
TiSi	850	2.982	0.52527	0.010543
Polysilicon (n+)	840	3.71562	0.33165	0.95711
Polysilicon (p)-	840	3.71562	0.33165	0.96554
(n-) epitaxy collector (si)	850	3.66208	0.32605	0.97192
Nburriedlayer(n+) (subcollecor)(si)	850	3.66208	0.32605	0.85364

Table 3.1 Optical Properties of different material that are in the vertical stack of the HPT [227]

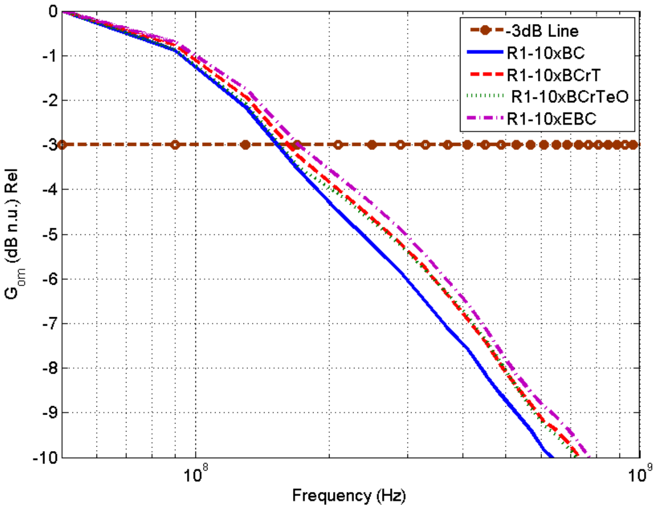

Figure 3.4 Relative opto-microwave measurements of the laser +HPT (PD Mode)

HPT	Link Gain (@50 MHz) (dB)	Vce (V)	Vb (V)	Ic Illum (µA)	Ic Dark (A) (Gummel Meas)	DC Responsivity PD Mode A/W	Opto-microwave cutoff frequency f_{-3dBom} (MHz) PD Mode
10xBC	-40.89	2	0	193	1.46E-10	0.179	154.0
10xBCrT	-37.20	2	0	244	8.70E-10	0.226	162.6
10xBCrTeO	-35.05	2	0	320	5.89E-08	0.297	155.8
10xEBC	-33.34	2	0	331	1.49E-10	0.306	170.6

Table 3.2 Low frequency opto-microwave response link gain (PD Mode Vce = 2, Vbe =0) of the different 10x10µm² Run1 HPTs under an illumination of 1.08mW and a spot size of 26µm in diameter.

In summary, the optimizations in the optical stack of a 10x10µm² HPT shows that the removal of TiSi layer and oxide etching improves optical responsivity when used separately or combined in extended Base and Collector HPTs with minimal penalty in the opto-microwave cutoff frequency. Extending the emitter, to prevent having silicided polysilicon layers produces an HPT with an increased intrinsic transistor size which benefits from increased electrical current gain β but suffers from low electrical cutoff frequency. However, the opto-microwave measurement shows that for this size of HPTs, illumination through the emitter polysilicon instead of the base polysilicon reduces optical losses and exhibits enhancement in responsivity and opto-microwave cutoff frequency. It indicates that the transit time of the photo generated carriers is the most limiting parameters in a SiGe HPT at 850nm.

3.2.2 Maximizing coupling efficiency

Optical transmission could also be improved by maximizing the coupling of the optical beam to the detector surface. This minimizes the optical power that is not detected. An optical detector surface area, which is equal to or greater than the optical spot size used in an opto-microwave system will greatly improve measured analog optical link gains. The current measurement system uses an optical beam with a spot size of 26µm in diameter as discussed previously. Table 3.3 shows a summary of calculated percentages of the optical beam entering the optical window of the different HPTs.

Optical beam Spot Size area (µm²)	Optical Window(um²) Square	Detector area (µm²)	% of Light hitting the optical window	% Loss	Loss in dB
531	5x5	25	5	95	13
531	10x10	100	19	81	7
531	20x20	400	75	25	1.25
531	30x30	900	100	100	0
531	50x50	2500	100	100	0

Table 3.3 Estimation of the amount of optical power that passes through the optical window from an illumination with 26µm diameter spot size.

Figure 3.5 shows the top view of the 10x10µm² HPT and 50x50µm² HPT and the 26µm spot size that is used to illuminate the HPT. The 81% loss of optical signal is seen in the top view of the 10x10µm² HPT and the 100% coupling is clearly shown in the 50x50µm² HPT. In both conditions, the illuminating beam is inside the undoped P-type substrate.

This results to photocurrents from the photodiode that is formed by the subcollector (n+) and the substrate (p). This is illustrated in the next section. Figure 3.6 shows the simplified cross section of the R1-50SQxBC HPT without illumination and with illumination from a 26µm optical beam.

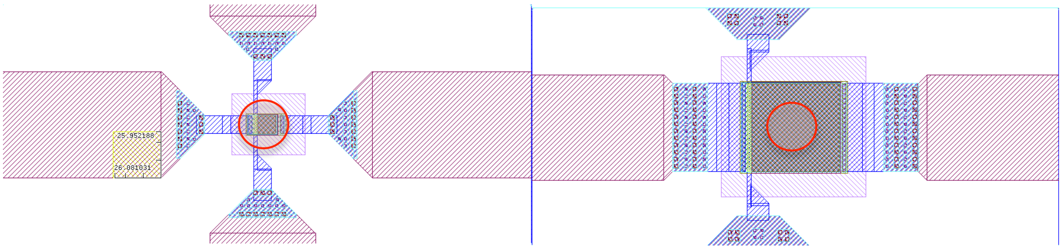

a) b)

Figure 3.5 Comparison of the of the spot size with respect to the (a) 10x10µm^2 HPT and the (b) 50x50µm^2 HPT

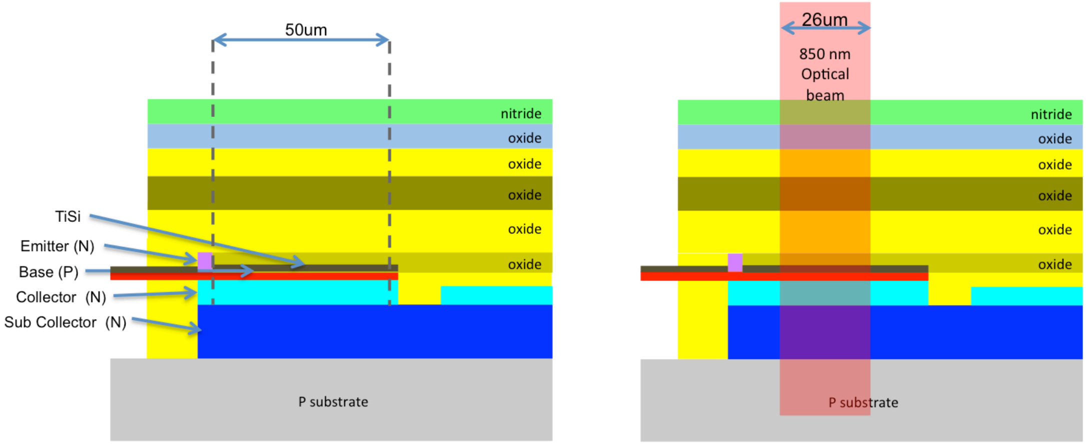

a) b)

Figure 3.6 Simplified cross section of the R1-50SQxBC HPT and 850nm optical beam with a 26µm spot size.(a) without illumination and (b) with illumination

The response of the laser and HPT in PD mode will be compared for similar types of HPT having an optical window of 10x10µm^2 and 50x50µm^2. This will illustrate the effects of the optical window size under an illumination of the same optical beam since the amplification due to the intrinsic transistor is not present. Figure 3.7(a) shows the normalized G_{OM} (PD mode) response of R1-10SQxBC HPT and R1-50SQxBC HPT. The 10x10µm^2 HPT has a response of -34.61dB and the 50x50µm^2 HPT has a -31.87dB response. The increase in response between the different sized extended Base-Collector (xBC) HPTs is 2.74dB. It is due to the 100% coupling of the 26µm diameter spot size to the 50x50µm^2 HPT. The low increase in response of the R1-50SQxBC as opposed to R1-10SQxBC may be attributed to the fact that, with 100% coupling of the power of the optical beam, the optical signal is subjected to greater reflection losses due to the larger surface area of the TiSi layer in the R1-50SQxBC HPT but also an mainly to greater recombination of photo generated carriers before reaching the contact. Figure 3.7(b) shows a normalized 0dB optical frequency response of the two HPTs the 10x10 HPT has a cutoff of 154.05MHz and the 50x50 HPT has a cutoff of 153.81MHz. For this type of HPT, the increase in optical window shows negligible change in the optical cutoff frequency $f_{-3dB\ OM}$ of the HPTs. However, at higher frequencies, R1-50SQxBC exhibits higher frequency slope at higher frequencies. That proves that the frequency limitations on the PD mode are rather on the transit time even if capacitance limitations sharpen further the frequency slope.

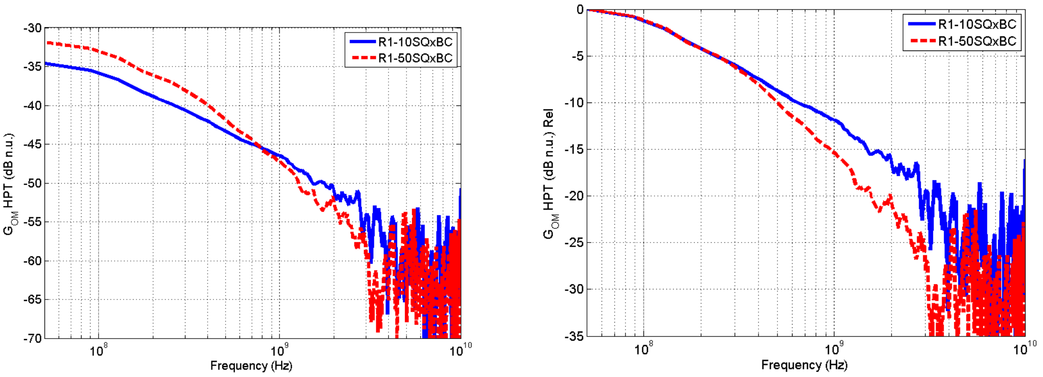

a) b)

Figure 3.7 G_{OM} of laser + 10xBC HPT and laser + 50xBC HPT in PD mode operation (a) measured link gain and (b) normalized to 0dB

Figure 3.8(a) shows the normalized G_{OM} (PD mode) response of response of the 10SQxBCrT HPT and a 50SQxBCrT HPT. The 10x10µm^{2} has a response of -30.91dB and the 50x50µm^{2} HPT has a response of -24.37dB. The 50x50µm^{2} HPT photodiode mode response has 6.6dB improvement over the 10x10µm^{2} HPT. This is almost as expected due to the 100% optical coupling provided by the larger optical, window which is 7dB improvement expected from the coupling ratio. In terms of the difference in response between R1-50SQxBC HPT and R1-50SQxBCrT HPT, a 7.5dB increase in response is due to the removal of the silided titanium (TiSi), which causes very high reflection losses. In the 10x10µm^{2} HPTs, the removal of TiSi layer results to an increase of only 3.7dB as opposed the 10x10µm^{2} HPT with the TiSi layer. Both devices suffer from coupling losses due to the mismatch in the optical window size and the benefits of the removal of the TiSi layer is limited to the illuminated surface of the 10x10µm^{2} HPT. In terms of opto-microwave frequency response, the 50xBCrT HPT has a lower opto-microwave cutoff frequency of 140MHz as compared to 163MHz of the 10xBCrT HPT. It can be observed that the change in optical cutoff frequency for this type of HPT is minimal given that the difference in the optical window is huge. The transit times are the most limiting factor as seen previously. The lack of TiSi layer however brings out two effects: the base resistance is increased, and makes the RC limitation competing with transit times within the 50x50µm^{2} HPT.

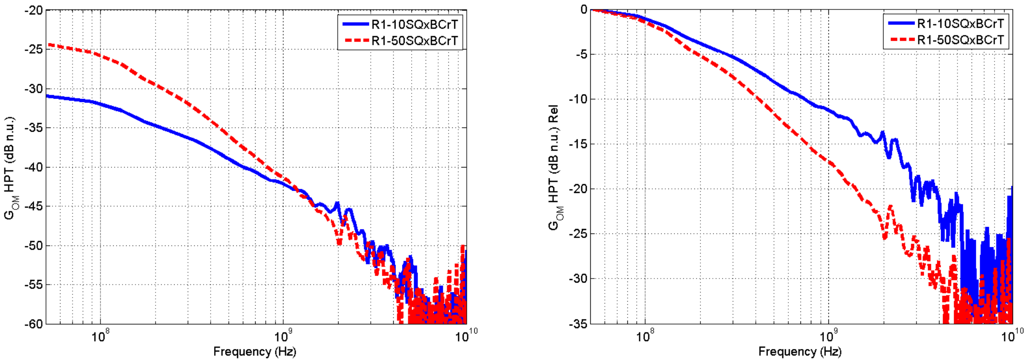

a) b)

Figure 3.8 G_{OM} of laser + 10xBCrT HPT and laser + 50xBCrT HPT in PD mode operation (a) measured link gain (b) normalized to 0dB

Figure 3.9 a shows the normalized G_{OM} PD mode response of the R1-10SQxBCrT_eO HPT and the 50xBCrTeO HPT. The 10x10µm^{2} HPT has a response of -30.91dB and the 50x50µm^{2} HPT has a response of -24.37dB. For this type of HPT, the increase in the optical window size results in a 6.54dB increase response. As in the case before, the removal of TiSi may have reduced the recombination of holes at the BC junction, and thus the device benefits fully from the size enlargement.

The R1-10SQxBCrTeO HPT has an improvement of 2.15dB as compared to the R1-10SQxBCrT HPT. Whereas, only 0.12dB increase is observed between the R1-50SqxBCrT HPT and the R1-50SQxBCrTeO HPT. In terms of opto-microwave frequency response, the R1-50SQxBCrTeO HPT has a lower -3dB opto-microwave cutoff frequency of 144MHz as compared to 156MHz of the R1-10SQxBCrTeO HPT. Thus, etching the superficial oxide on the xBCrTeO HPT does not affect the frequency limitations and benefits to the reduction of coupling losses.

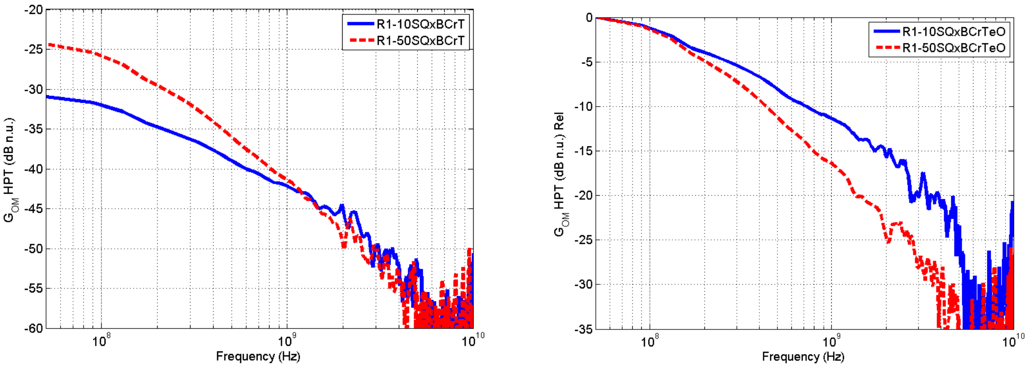

a) b)

Figure 3.9 G_{OM} of laser + R1-10SQxBCrTeO HPT and laser + R1-50SQxBCrTeO HPT in PD mode operation (a) measured link gain (b) normalized to 0dB

Prototyping Run 2 has extended Emitter, Base and Collector (xEBC) HPTs with different optical window sizes of 10x10μm^2, 20x20μm^2, 30x30μm^2 and 50x50μm^2. The opto-microwave measurements of these HPTs were implemented with a VCSEL from VI Systems and the reference Photodiode is from New Focus. Figure 3.10 shows the G_{OM} (dB n.u) in PD mode of the phototransistors with different optical window sizes of extended emitter, base and collector. These measurements are relative to the Reference Link 2 as presented earlier in Chapter 2. In 10MHz of operation, the R2-10SQxEBC HPT has a response of 6.68dB, the R2-20SQxEBC HPT has a response of 10.7dB, the R2-30SQxEBC has 9.1dB and the R2-50SQxEBC HPT has 8.4dB. From the measurements, at 75% to 100% coupling, the relative response is approximately 10dB at 10MHz which shows an approximated 3dB increase in response as compared to the R2-10SQxEBC HPT with 19% coupling.

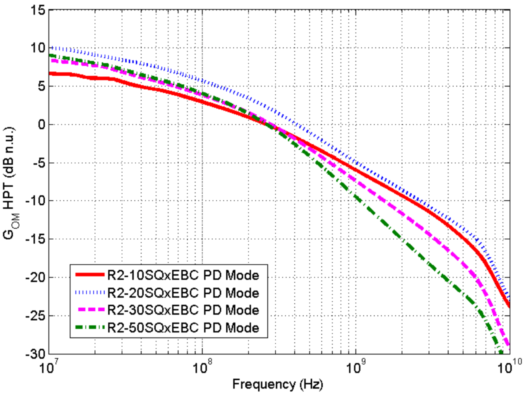

Figure 3.10 relative G_{OM} of xEBC HPTs from 10x10μm^2 to 50x50μm^2 in PD mode operation

Table 3.4 shows a summary of the performance of the HPT in PD mode operation of 10x10 and 50x50 HPTs of different HPT types.

	Link Gain (@50 MHz) (dB)	Cutoff In PD mode	Ic las on (µA) Vbe=0V Vce=2V	Ic las off (µA) Vbe =0 V Vce = Vbe	Popt in (mW)	DC Responsivty (A/W) PD Mode
R1-10SQxBC	-40.89	187 (1)	193	0.00015	1.08	0.179
R1-10SQxBCrT	-37.2	205 (1)	244	0.00087	1.08	0.226
R1-10SQxBCrTeO	-35.05	198 (1)	320	0.0059	1.08	0.297
R1-10SQxEBC	-33.34	221 (1)	331	0.00015	1.08	0.306
R1-50SQxBC	-38.13	186 (1)	235	0.11	1.08	0.217
R1-50SQxBCrT	-30.66	159 (1)	465	0.14	1.08	0.430
R1-50SQxBCrTeO	-30.54	166 (1)	498	0.17	1.08	0.461
R2-10SQxEBC	-25.39	295 (2)	798	0.00068	2.44	0.327
R2-20SQxEBC	-22.44	199 (2)	1114	0.00056	2.44	0.457
R2-30SQxEBC	-24.31	125 (2)	927	0.00096	2.44	0.379
R2-50SQxEBC	-23.97	97.5 (2)	975	0.00065	2.44	0.400

Table 3.4 Summary of measured performance of different HPTs with (1) measured with an Avalon VCSEL and Reference Link01 and (2) measured with VI systems VCSEL and Reference Link 02

In summary, the measurements show that coupling losses are avoided if the spot size of the optical beam is fully enclosed by the optical window of the HPT. This is best observed in between the R1-10SQxBCrT HPT and R2-50SQxBCrT HPT wherein there is approximately a 7dB increase in the HPT response of in the larger HPT. 7dB is the estimated coupling loss in 10x10µm^2 under a 26µm spot size illumination. The extended Base-Collector HPTs and its variants show that its frequency response is not severely affected from the improvements brought by the reduction of coupling losses via optical window size optimization.

Finally, the effect of the vertical stack is in the PD mode of operation of the HPT with 100% coupling. This limits the effects of the transistor action of the HPT and the effects of coupling mismatch. The R1-50SQxBC HPT has a response of -38.13 dB which is used as the base line responses. The removal of the TiSi layer in R1-50SQxBCrT gives an increase in response of 7dB, and the additional removal of the oxide on top of the optical window in R1-50SQxBCrTeO HPT gives a total increase of 7.4dB. This means the TiSi layer produces a severe amount of reflections and the oxide and nitride layer has lesser transmission losses associated to it. Using and emitter-base-collector extended HPT structure (xEBC) provides a further increase by 6.5dB. It is seen by comparing the R1-10xSQxBC and R1-SQxEBC.

3.3 Effect of Base Biasing on SiGe HPT

The early implementation of HPTs in the literature was implemented with the base is left floating. [143].This has been referred to as two-terminal HPTs (2T-HPTs). In this configuration, the average power of the incident light provides the bias current for the HPT. The incident power on the HPT dictates the operating point of the HPT, and when the incident power is low, the HPT may be biased in low current gain region which results in low optical response. The presence of a base contact in three terminal HPTs (3T-HPT) configurations were shown to produce improved performance [228] [229]. In a typical common emitter 3T HPT biasing, the base is supplied with a voltage source or current source to provide more control to the optical response of the HPT by having a means to push the HPT operating point to a level where the current gain is of optimum value. The HPT base can be either voltage or current biased.

The HPT performance is very much dependent on its biasing. It controls the different modes of operation of the HPT. A detailed analysis of the HPT performance as a function of bias values provides a clear picture of the HPT operation and provides a means to optimize HPT response. This study is implemented by closely monitoring the supplied bias and the response that is associated with the specific bias values. The R2-10SQxEBC HPT is initially used to illustrate the performance of the HPT under the two biasing conditions: current base biasing and voltage base biasing.

3.3.1 SiGe HPT Base Biasing in dark conditions

The biasing range of the SiGe HPT can be explored by sweeping the bias in the base of the HPT while setting a fixed voltage bias in the collector of the HPT. Gummel measurements are produced where the base is supplied with a voltage source that is swept from an initial value to a final value. This illustrates the base biasing with a constant voltage (CV). On the other hand, the Ic-Vce measurements for the output characteristics of the HPT illustrate the HPTs characteristics under constant current (CC) biasing that is applied to the base.

Figure 3.11(a) shows the Gummel curve of the HPT with Vcb =0V. The base voltage is initially provided with 0V, which puts the HPT in a reverse active mode. It is then increased up to 1V where the HPT goes to a forward active mode up to saturation. The collector and base currents are measured as a function of the supplied voltage in the base. In this non-illuminated condition, the measured Ic and Ib clearly shows the different regions in the HPT operation: the low current region, the linear region and the high current region. In the low Vbe bias range, the measured Ic and Ib saturates in the range of 10^{-10}A. In the linear region, the Ic and Ib has an ideality factor of 0.96 and 0.94 respectively. Finally in the high current region, the change in the slope of Ic and Ib are evident.

The typical Ic-Vce output characteristics of the HPT as shown in Figure 3.11(b), illustrates how an input base current influences the output collector current. Dark condition is respected. The base current Ib are swept from 1µA-20µA in steps of 1µA and 20µA -100µA in steps of 10µA. With 2V Vce, the collector current Ic is equal to 650µA with an Ib of 1µA and equal to 17.5mA with an Ib of 100µA.

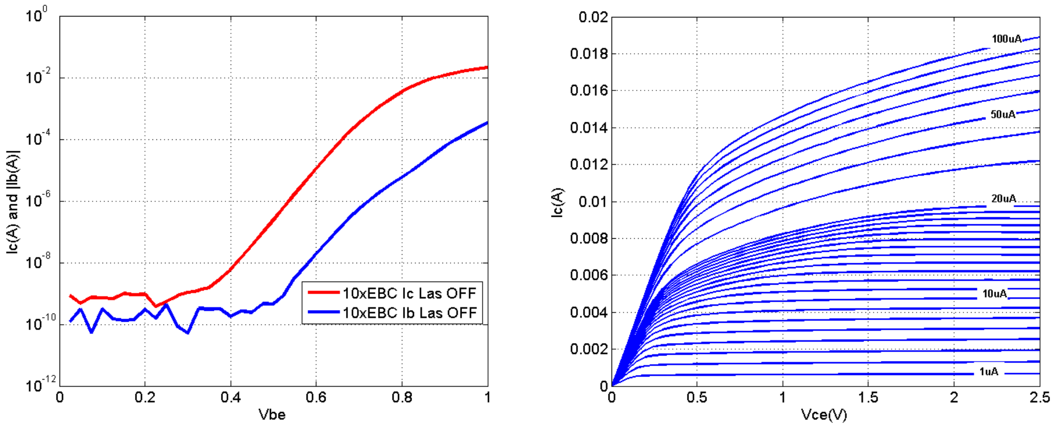

a) b)

Figure 3.11 R2-10SQxEBC HPT (a) Gummel curve, Vcb =0V, Vb is swept from 0V to1 V (b) Ic –Vce curves Ib is swept from 1µA-100µA

Using the Ic-Vce measurements, the measured Vbe is presented as a function of the supplied Ib, at selected Vce values. It represents the induced voltage in the Base-Emitter junction due the Vce bias and the Ib bias. This is shown in Figure 3.12(a) where each line series in this plot corresponds to a fixed Vce value. A fixed base bias Ib of 1µA corresponds to a Vbe value of 0.72V when Vce is 2V. Following the 2V Vce series, a Vbe value of 0.82V at 10µA Ib and 0.92V at 100µA Ib are achieved. These values will have approximately the same values when referred to Gummel curves shown in Figure 3.11(a).

Shown in Figure 3.12(b) is the collector current as a function of the measured base voltage and the different curves shows varying Vce from 1V to 2.5V. The collector current shows increase as Vce is increased.

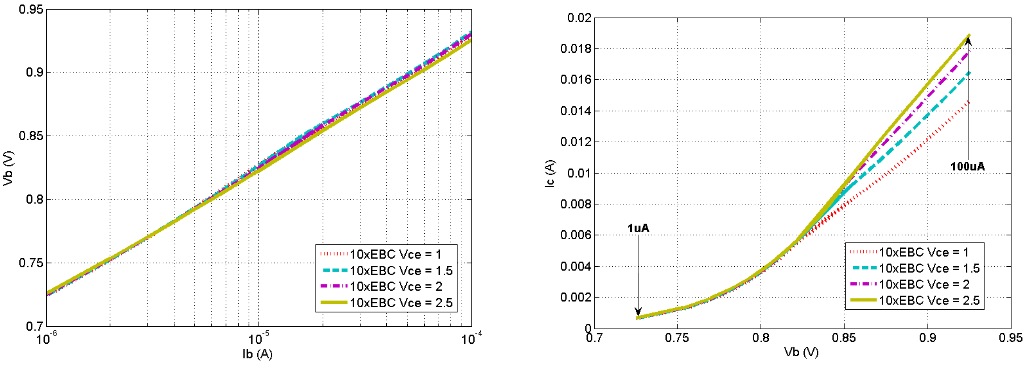

a) b)

Figure 3.12 R210xEBC Vbe vs Ib plot extracted from Ic-Vce measurements at selected Vce values of 0V,0.5V 1V, 1.5v,2V and 2.5V. (a) Vb vs. Ib (b) Ic vs Vb

The current gain β can be extracted using the two type measurements; Gummel curves from Vbe = 0V to 1V, and Ic-Vce curves from 1µA to 100µA. The extracted current gain curves are presented as a function of the input parameters Vbe and Ib in Figure 3.13 (a) and (b). Figure 3.13 (a), shows the extracted current gain β vs. Vbe. The first curve is from the Gummel measurements with Vcb =0 and Vbe is from 0 to 1V. The second curve is from the Ic-Vce measurements with Vce =2V and Ib is swept from 1µA -100µA which results in a Vbe from 0.73V to 0.93V as presented in Figure 3.12(a). From the Gummel measurements, β has a peak value of 610 with Vbe in the range of 0.65 to 0.725V. The Ic-Vce measurements show that the peak current gain is with Ib equal to 1µA.

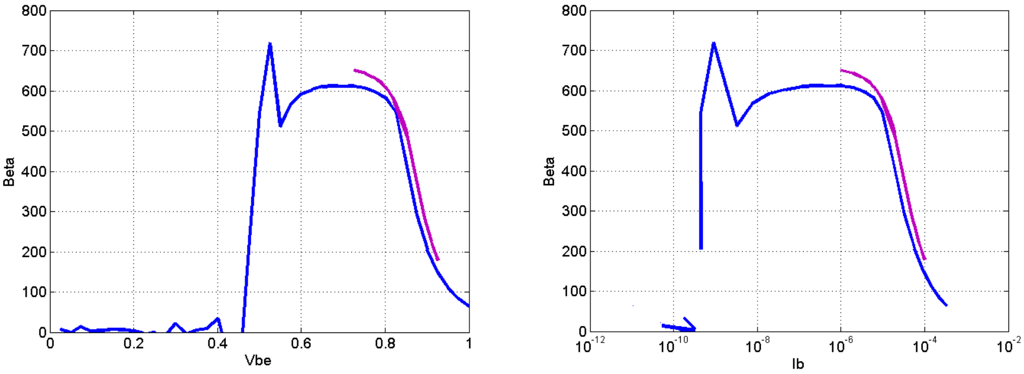

a) b)

Figure 3.13 Extracted β of the R2-10xEBC (a) Beta vs Vbe from (b) Beta vs. Ib

Shown in Figure 3.14(a) is the current gain β as a function of an output parameter, the collector current. In both measurement types the collector current is a measured parameter. The voltage sweep from 01-1V results in a collector current that has a value from 1.42x10^{-8}A up to 21.6mA and for the Ic-Vce measurement the resulting collector current is from 668uA to 18.9mA. Figure 3.14(b) shows the current gain β for the R3-10xEBCeO HPT with constant voltage and constant current in the base to further illustrate that the resulting unilluminated DC current gain β of the HPT yields the same current gain β as long as the resulting current in the collector will have the same value whether it is from a voltage bias or a current bias.

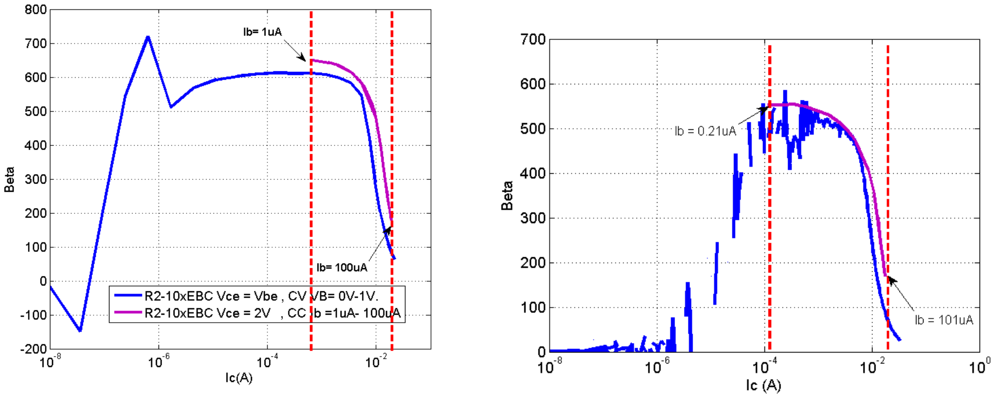

a) b)

Figure 3.14 Extracted β vs. the measured collector current . a) of the R2-10xEBC HPT b) R3-10SQxEBC_eO HPT

In the non-illuminated condition, a desired current gain could be achieved either by a voltage bias or a current bias in the base CV biasing starting from 0V-1V offers a wide range of collector currents from 10^{-8}A up to hundreds of mA and CC biasing could achieve the same range as long as very low current could be provided in the base of the HPT. A gain of 650 could be achieved with a 1μA or 0.725V biasing in the base. However, as seen from the output characteristics of the HPT, this very low biasing could not support large swings in the collector current. In order to allow for larger DC swings, the HPT should be biased in the lower gain region of 400 to 500 which is 20μA to 30μA Ib, or 0.825V to 0.85V Vb or 5.5mA to 7mA in terms of the collector current Ic.

The electrical frequency response is also analyzed in terms of the type of bias presented in the base of the HPT. The S-Parameters of the HPT are measured using constant voltage in the base. The measured RF Gain (S$_{21}$) of the HPT at 50MHz as a function of the collector current is shown in Figure 3.15(a) (CV) bias in the base The peak S$_{21}$ occurs at 0.95V or 21.22mA with a value of 19.26dB for this HPT. The effect of the type of the base bias in the measured low frequency S$_{21}$ is shown in Figure 3.15(b) with the R3-10SQxEBCeO HPT. Similarly, from the DC current gain β results as shown in Figure 3.14(b). The measured S$_{21}$ results at 50 MHz will have the approximately the same value, as long as the resulting collector current has the same value. While trivial, this mainly validates our measurement bench and will help us conclude on the optoelectronic behavior later on.

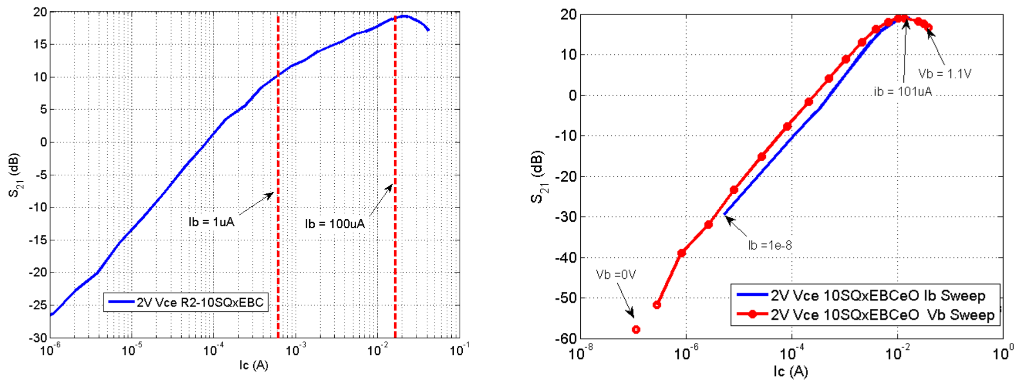

a) b)

Figure 3.15 S_{21} (50MHz) vs. Ic of (a) R2-10SQxEBC (b)R3-10QxEBC_eO

Figure 3.16(a)shows the extracted f_T as a function of the measured collector current from voltage biasing the base. It shows that the peak f_T is achieved in the region of 2.7mA to 9.2mA Ic, which corresponds to 0.78V to 0.85V in terms of base voltage input or 4.5μA to 18.8mA in base current input. Figure 3.16(b) shows the extracted f_T using CV and CC measurements of the R3-10SQxEBC_eO HPT. Again, it illustrates the extracted f_T will have the same results as long the collector current is the same value.

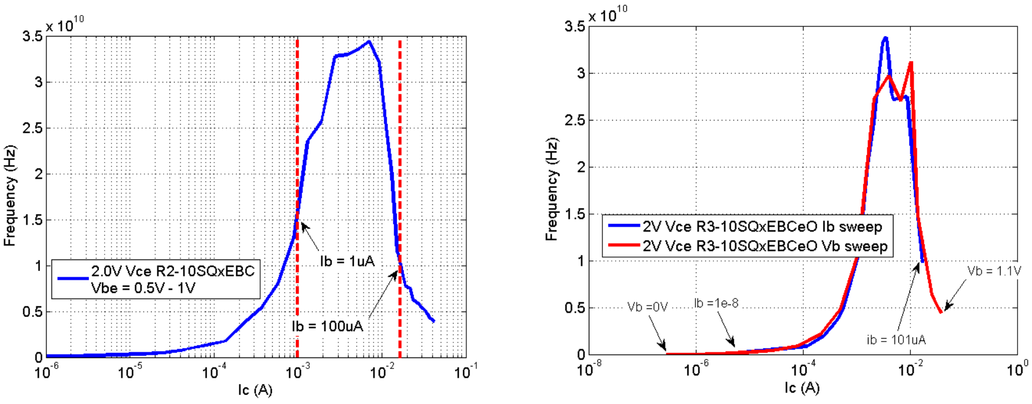

a) b)

Figure 3.16 Extracted f_T vs. Ic of (a) R2-10SQxEBC HPT (b)R3-10QxEBC_eO HPT

In summary, under the non-illuminated condition, CC sweeps and CV sweeps only provide variations in the range of measured collector currents. Furthermore it appears that the HPT could be biased in the high current gain region, however, this region results in low S_{21} values. The frequency response requirements in the HPT provides a good parameter to optimize for DC biasing. Finally, the measurements shows that the R2-10SQxEBC HPT will have an RF gain of 15dB with a collector current of 2.8mA. In this collector bias level, the f_T of the HPT is at 32 GHz and the DC current gain is approximately 590.

3.3.2 Illuminated SiGe HPT and DC Responsivity

The presence of the illumination in the HPT affects the DC bias of the HPT. This sections shows how the bias currents and voltages are affected by the average optical power that is used to illuminate the HPT. The DC responsivity of the HPT is extracted under CV bias and CC bias in the base shows significant differences.

3.3.2.1 Constant Voltage Biasing

Figure 3.17 shows the Gummel plot of the R2-10SQxEBC HPT in the non-illuminated condition and under illumination of an 850nm 2.44mW optical beam.

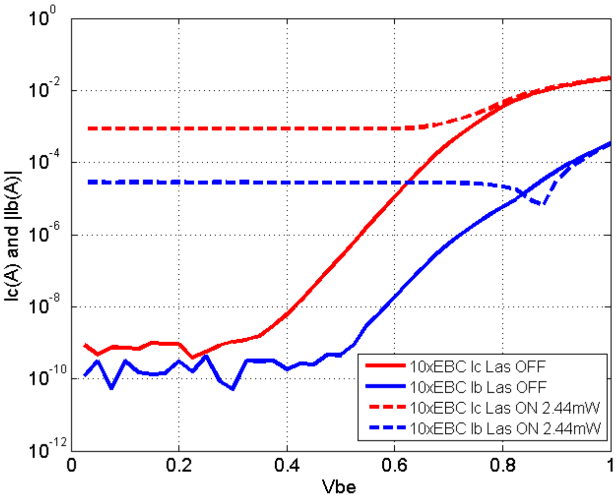

Figure 3.17 Gummel Plot of R2-10SQxEBC under no illumination and illuminated condition of 2.44mW.

Under the illuminated condition, it is observed that at high base bias, > 0.97V the effects of the optical absorption are negligible on the biasing level as compared to the dark currents from the transistor operation of the HPT. At low Vbe bias, the base current Ib saturates at around 28µA flowing out of the base contact and the collector current Ic saturates at around 856µA. These currents correspond to the photocurrent generated by the optical absorption, which are far greater than the HPT's transistor action at this bias level.

The base current is plotted as the absolute value of the measured illuminated base current. The notch shows the reversal in the direction of the base current. In the low base bias, and with adequate optical power, the hole injection into the base due to the optical absorption can exceed than what is required for recombination with electrons that are injected from the emitter. This produces a net flow of holes out of the base connection. This results in illuminated base currents that have lower value as compared to the dark base current. At high base-emitter bias, the hole injection due to the optical absorption is negligible compared the that of the base contact.

The difference in the value of Ic and Ib at low vbe shows that at 850nm of operation, the increase in collector current is attributed to the optical absorption in the parasitic photodiode that is formed by the HPT sub-collector and the p-type substrate. This is a clear difference with respect to InGaAs/InP HPTs.

The effects of the intensity of the illumination are illustrated in Figure 3.18 (a) and (b) where the illuminated HPTs collector and base current are shown at 1.22mW and 2.44mW of illumination. Photocurrent levels increase with the intensity of the optical power as expected. The location of the notch on the Ib curve also moves to a higher base-emitter voltage bias as the optical power increases.

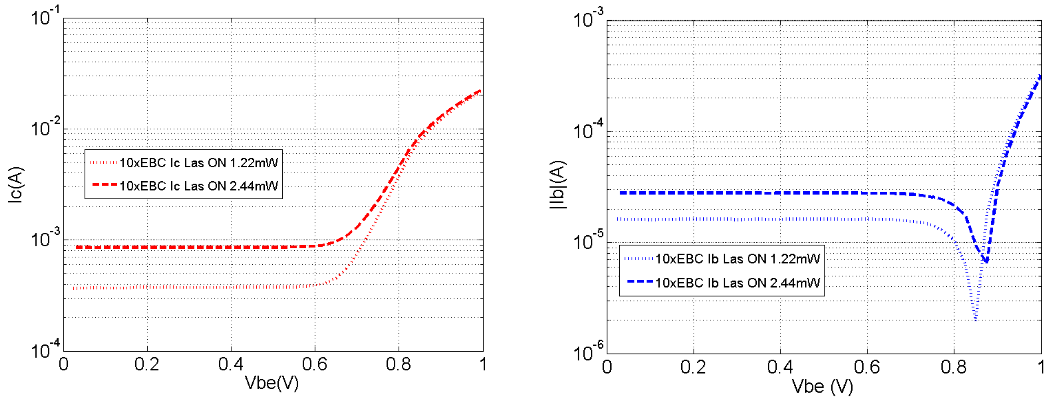

a) b)

Figure 3.18 Collector and base currents of R2-10SQxEBC under different illumination power levels(a) Ic vs Vbe (b) |Ib| vs Vbe of

In summary, at low base-emitter junction bias and high enough optical power, the base, collector and subcollector together operate as a photodiode whose photocurrent generation swamps out the device's transistor action. That is, the effects of electron injection into the base from the emitter are negligible. By contrast, at high base-emitter bias the transistor action is well established and the photocurrent constitutes a small base current injected into the device, which becomes amplified by the device's operation to provide the device's optical gain. The substrate parasitic photodiode proves however to have a deep impact on Ic.

The measured collector current from the illuminated and dark Gummel measurements is used to extract the DC responsivity of the HPT. The HPT responsivity equation initially presented in Chapter 1 is again presented

$$R\left(\frac{A}{W}\right)=\frac{Ic_{illum}-Ic_{dark}}{P_{in\ opt}}$$

The illumination of the HPT under constant voltage bias causes an initial significant increase in the measured collector current due to the photocurrent from the parasitic substrate photodiode. As the base-emitter region becomes forward biased the difference between the illuminated Ic and dark Ic starts to increase until it reaches a peak value where it starts to descend at a lower values as Vbe is increased. Figure 3.19(a) shows the resulting DC responsivity for the 10x10µm^2 HPT in xEBC configuration under 2.44mW of illumination as function of the supplied Vbe.

The peak responsivity is at 0.49A/W with Vbe equal to 0.825. While it is 0.35 A/W in the photodiode mode (Vbe =0V)Shown in Figure 3.19(b) is the DC HPT responsivity as a function of the measured Ib. The peak responsivity has a measured Ib of -17.6µA. Figure 3.19(c) shows the responsivity as a function of the measured collector current, and the peak occurs at Ic = 6.51mA.

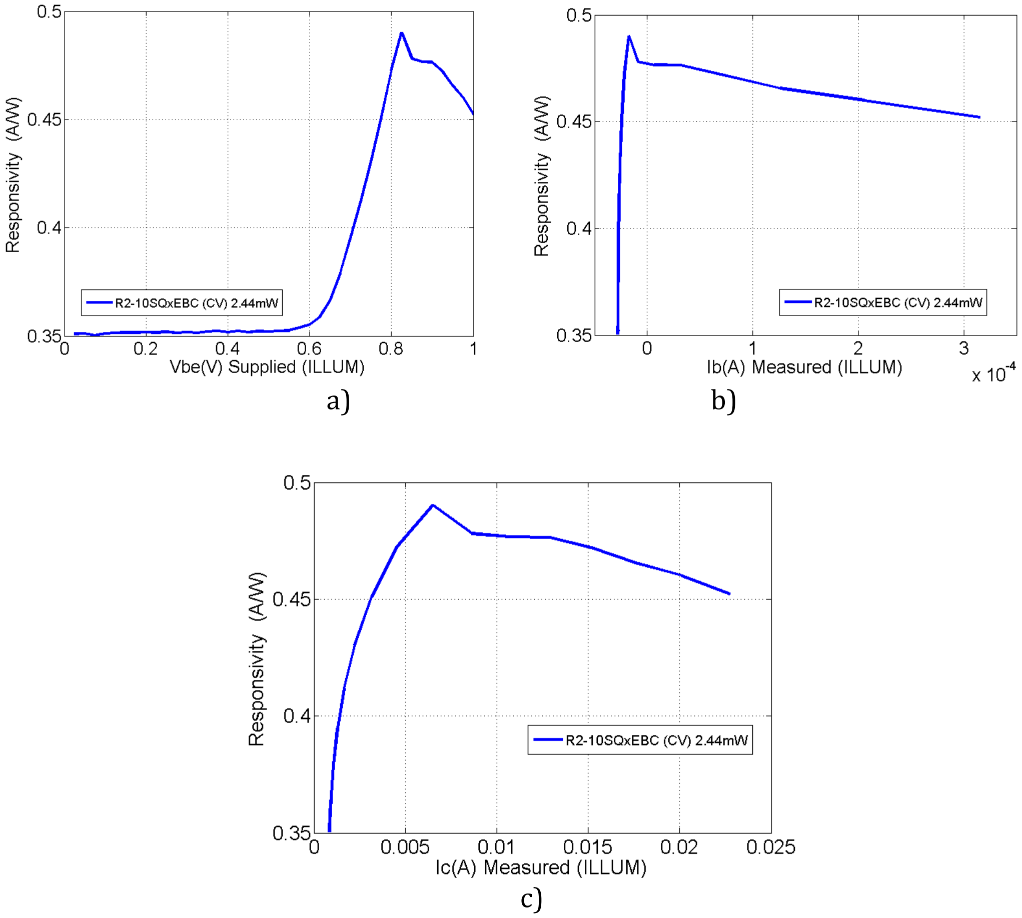

a) b)

c)

Figure 3.19 Extracted DC Responsivity of the R2-10SQxEBC HBT under constant voltage bias from Gummel measurements where Vbe = Vce with: (a) DC Responsivity vs. Vbe(supplied) ,(b) DC Responsivity vs. Ib(measured),(c) DC Responsivity vs. Ic(measured)

Table 3.5 summarizes the measured collector and base currents under constant voltage bias in the base, which has the highest, extracted responsivity.

	Vc (V)	Ic (mA)	Vb (V)	Ib (μA)	Ic dark (mA)	Pin (mW)	Responsivity
R1-10xEBC	2	6.508	0.825	-17.6	5.312	2.44	0.4902

Table 3.5 Measured collector and base currents of R1-10xEBC HPT with the highest extracted DC responsivity

The DC responsivity extracted from the Gummel measurements reflects a biasing wherein Vce = Vbe. However, In the common emitter operation of the HPT, the voltage bias in the collector is at fixed value that is typically higher than the Vbe (1.5,2,2.5V).

Figure 3.20 shows a summary of the extracted DC responsivity as function of Vbe of a 30x30μm^2 HPT (R3-30xEBCeO) as an example at different values of Vce. It can be seen that the extracted responsivity is within the range of each other. The extracted DC responsivity shows no significant difference. It can be concluded that the DC responsivity that is extracted from illuminated Gummel measurements (Vce = Vbe) is sufficient for DC responsivity estimation under 3T-HPT constant voltage operations.

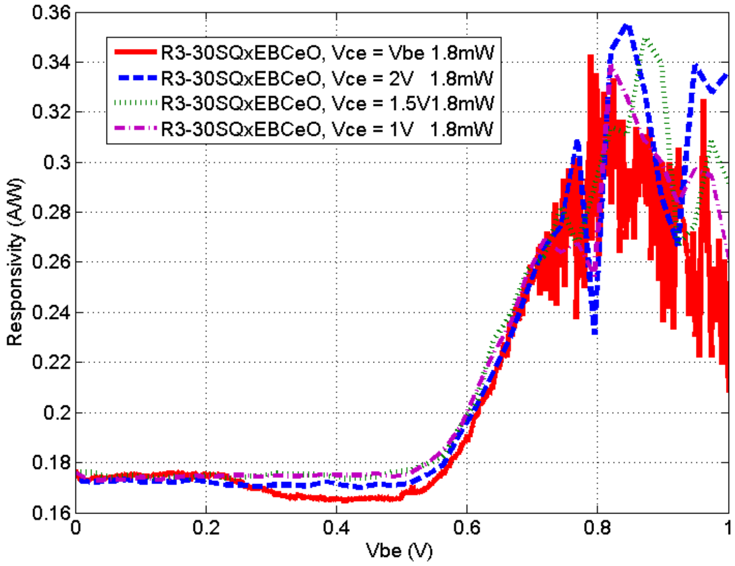

Figure 3.20 DC responsivity vs Vbe of R3-30xEBCeO HPT at different values of Vce.

Figure 3.21 shows the extracted DC responsivity from Gummel measurements of three HPTs ; R3-05SQxEBCeO, R3-10SQxEBCeO and R3-30SQxEBCeO. In (a), Vce is equal to Vbe, i.e., standard Gummel conditions. In (b) is the extracted responsivity versus Vbe with Vce = 2V. This shows that both approaches could be used in the estimation of DC responsivities under 3T HPT operation with constant voltage bias. Vbc value has very less influence on the responsivity.

Under the PD mode of operation (Vb =0V) the extracted responsivity increases in value as the optical window is increases. This shows the decreasing optical mismatch losses as the optical window fully covers the optical beam width. In the HPT mode operation, the HPT with the optical window of 30x30µm² HPT provides the highest peak responsivity and the highest current gain at the specific bias point. The 5x5µm² HPT exhibits lowering of the DC responsivity, as Vbe has a value greater than 0.7V. This means that with the power of the illumination that is used, the HPT bias is shifted to the very high current region where the collector current and current gain starts roll off.

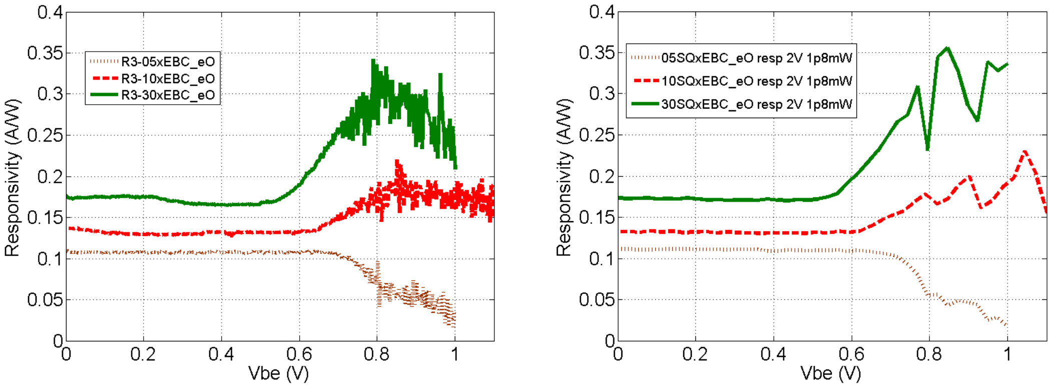

a) b)

Figure 3.21 Responsivity of different R3-SQxEBCeO HPT vs. Vbe in 3T HPT constant voltage mode (a) Vce = Vbe and (b) Vce = 2V, including coupling losses

Table 3.6 shows a summary of the HPTs that were measured with a constant voltage base biasing.

	Vce (V)	Ic(mA)	Vbe (V)	Ib (µA)	Resp (A/W)
R3-05SQxEBCeO	2	6.55	0.90	18.6	0.05
R3-10SQxEBCeO	Vbe	0.244	0.85	-10.35	0.22
R3-10SQxEBCeO	2	15.93	0.90	59.09	0.20
R3-30SQxEBCeO	Vbe	9.84	0.80	1.79	0.34
R3-30SQxEBCeO	2	21.71	0.85	25.08	0.36

Table 3.6 Summary of extracted DC Responsivity for constant voltage base biasing

3.3.2.2 Constant Current Biasing

3.3.2.2.1 Photogenerated currents and voltages.

The effect of illumination of a 2.44mW optical beam on the Ic-Vce curves of an HPT is shown in Figure 3.22. Highlighted in the figure are the dark Ic and illuminated Ic with current bias in the base of 1µA.

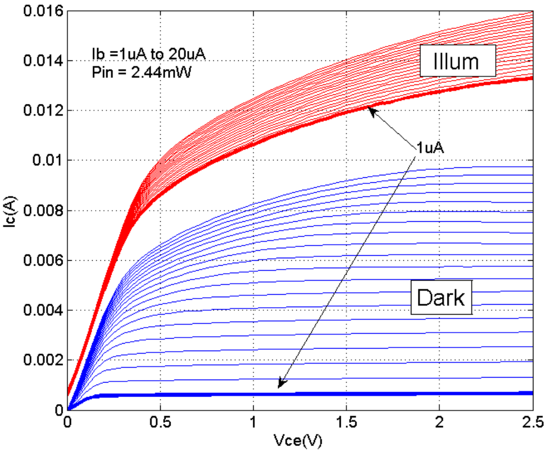

Figure 3.22 IC-Vce curve at Ib =1uA to 20uA under dark and 2.44mW illumination conditions respectively

The high value in the illuminated Ic is attributed to the generated photocurrent that adds to the initial base bias and that is amplified by the transistor action of the HPT. Without illumination, the supplied bias current in the base Ib_{bias} sets the bias point of the HPT. The illumination pushes the bias point of the HPT to Ib = (I_{ph} + Ib_{bias}) where the current gain β will have a new value that is dependent on the new bias point. As a result, in a first approximation, the measured collector current Ic_{illum} for the HPT will be given by:

$$Ic_{illum} = (I_{ph} + Ib_{bias}) * \beta + I_{ph} \quad \text{Eq. 3.1}$$

$$Ic_{illum} = (\beta + 1)I_{ph} + \beta Ib_{bias} \quad \text{Eq. 3.2}$$

Under constant base current biasing, illumination of the HPT causes an increase in the Vbe voltage. This is primarily due to the addition of the photocurrent in the base to the initial base bias Ib. Figure 3.23 shows a Vbe vs. Vce plot, which is extracted from the Ic-Vce measurements of the HPT under dark and illuminated conditions. It shows Vbe as a function of Vce at a constant base current bias of 1uA. In the dark condition, Vbe is 0.66V at Vce = 0V. It then increases to 0.72V when Vce is 0.2 V and is approximately constant until 2.5V Vce. As the HPT is illuminated Vbe increases by 0.08V and is now 0.74V at 0V Vce. This value increases up to 0.87V when Vce increases to 0.7V and is the same value until Vce = 2V. In the linear region the change in Vbe due to the optical illumination of 2.44mW is 0.15V illumination. Further examination of the Ic-Vce measurements shows that the difference in Vbe for the linear region when Ib = 10µA is 0.06V

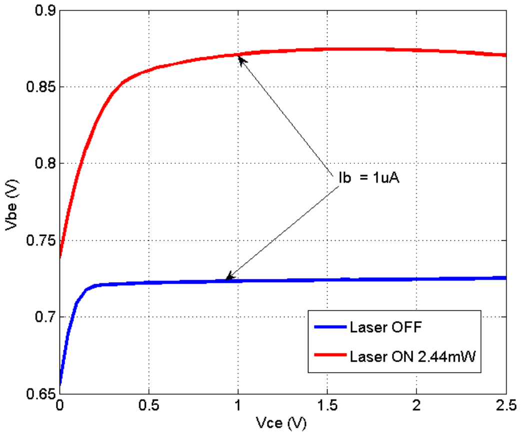

Figure 3.23 R210xEBC Vbe vs Vce for Ib_{bias} of 1μA

Shown in Figure 3.24(a) is the Ic vs. Vbe curve that is extracted from the dark and illuminated measurements of the HPT. It shows that with an initial 1μA base current bias, the measured Vbe increases, and the collector current increases to a value that is estimated by the equation. The illuminated collector current is the sum of two effects: the light induces bias shift and then Ic is increases; the light adds up to Ic and additional photogenerated current that is not controlled by the transistor effect. It does follow the Eq. 3.2. The solid curve shows that dark Ic of the HPT with a bias of 2V Vce and the current is from 1μA to 100μA. The curve with blue tick marks shows the subset dark IC with 1μA up to 20μA. The red tick marks shows the illuminated Ic with ib = 1μA to 20μA. The location of Ic when Ib is 1μA is at Vbe equal to 0.87V but its value is higher than the Ic at 0.87V in dark conditions. The effect of the illumination intensity the in the collector current behavior under constant current biasing in base of the HPT is seen in Figure 3.24(b). This indicates the lower photo generated current by the 1.22mW illumination as compared to the 2.44mW illumination.

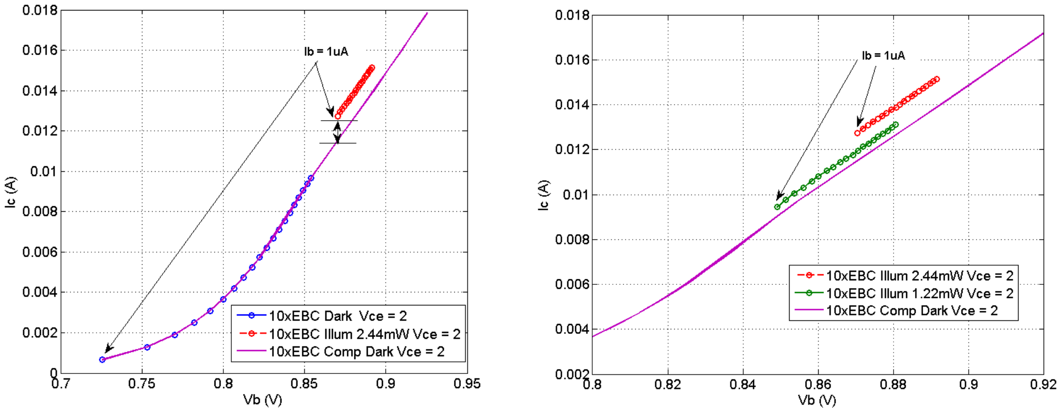

a) b)

Figure 3.24 Ic-Vbe curve form Ic-Vce measurements 1μA – 20μA in dark and illuminated conditions.

In summary, the illumination of the HPT under constant current biasing pushes the base biasing point from Ib_{dc} to $Ib_{dc} + I_{photo}$ with I_{photo} generated from the base -collector region. The initial Vbe is shifted to higher Vbe value. This results to an increased measured collector current Ic. The difference between the dark and illuminated collector current is the induced photocurrent Ic_{opt} due to optical injection.

3.3.2.2.2 Responsivity behavior

The measured collector current in dark and illuminated conditions can be used to extract the DC Responsivity of the HPT. Figure 3.25(a) shows it as a function of the current base bias Ib. The peak responsivity occurs at the lowest Ib value. It is 4.95A/W at 2V Vce and 1μA Ib. Figure 3.25(b) shows the same extracted DC responsivity values as a function of the measured Vbe under illumination. It shows that the peak responsivity occurs when the measured illuminated Vbe is 0.87V, which is consistent with Ib =1μA. Figure 3.26 shows the responsivity curves as a function of Vce at different constant base currents. It can be seen the lowest supplied base current (1μA) exhibits the highest extracted responsivity. The extracted DC responsivity goes lower as higher base currents are supplied at specific values of Vce. Finally, Figure 3.27 shows the responsivity vs. Ib curve over the entire range of supplied Ib of 1ua to 100uA at different Vce values of 1V, 2V and 2.5V. The lowest Ib and higher Vce exhibits the highest responsivity as high as 5.1A/W.

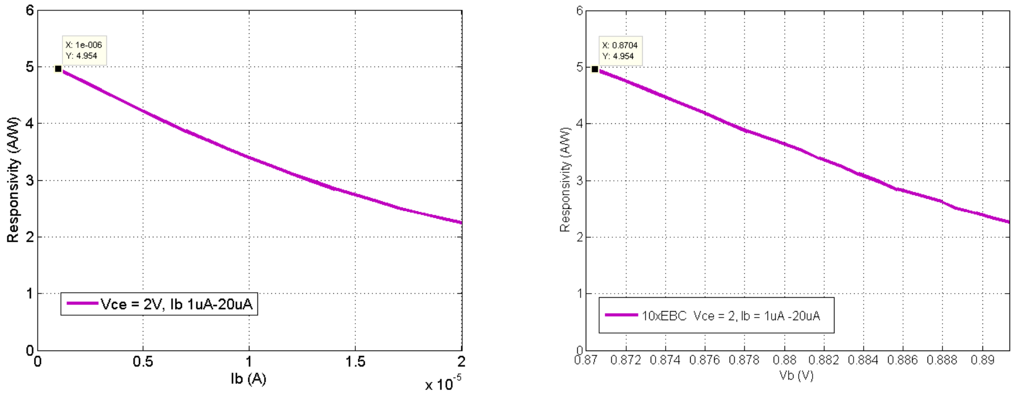

a) b)

Figure 3.25 DC Responsivity of R2-10SQxEBC vs Ib at Vce = 2V for constant current biasing in the base under 2.44mW of illumination

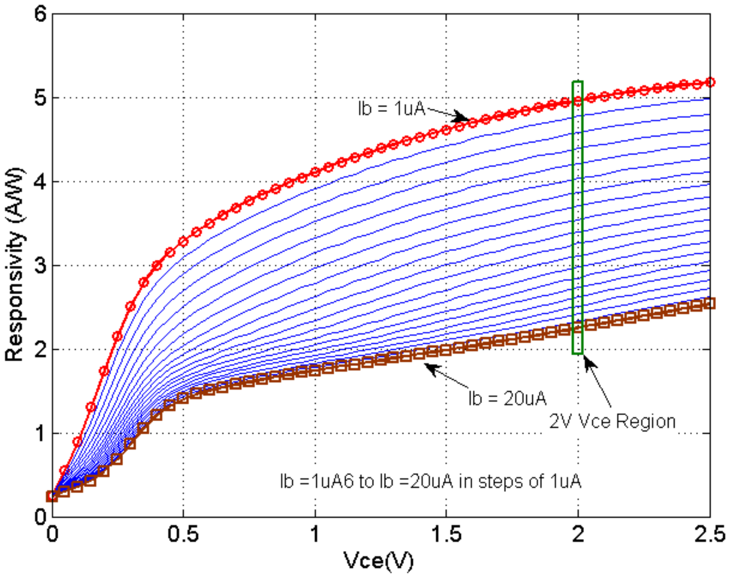

Figure 3.26 R2-10SQxEBC HPT DC Responsivity vs. Vce at diffent Ib under 2.44mW of illumination

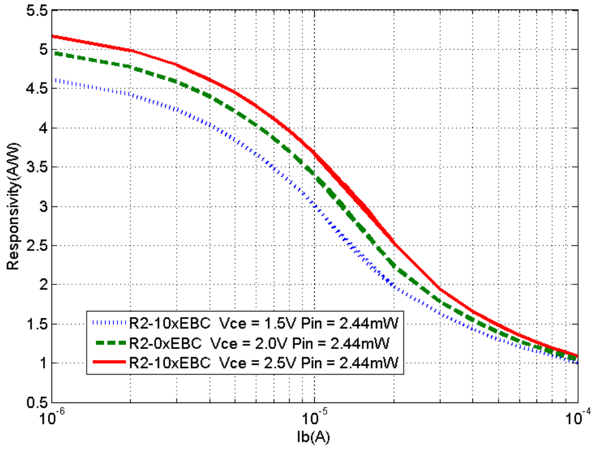

Figure 3.27 R2-10SQxEBC Responsivity (A/W) vs Ib (Ib =1uA – 100uA) under 2.44mW of illumination.

Such a behavior versus Ib is quite important. It shows peak responsivity much higher than what was observed with constant Vbe measurements. In the next curve, we verify the phenomenon as a function of the optical power with an xEBC with etched oxide HPT (R3_10SQxEBCeO). In this case, we consider Ib currents as low as 100nA and up to 100µA. At 100nA Ib, which is a very low bias in the base, the HPT could be considered as 2T HPT configuration where average optical power of the illumination provides the needed base current to bias the HPT. Figure 3.28(b) shows the measured collector current in the HPT with Ib bias of 100nA with different optical powers.

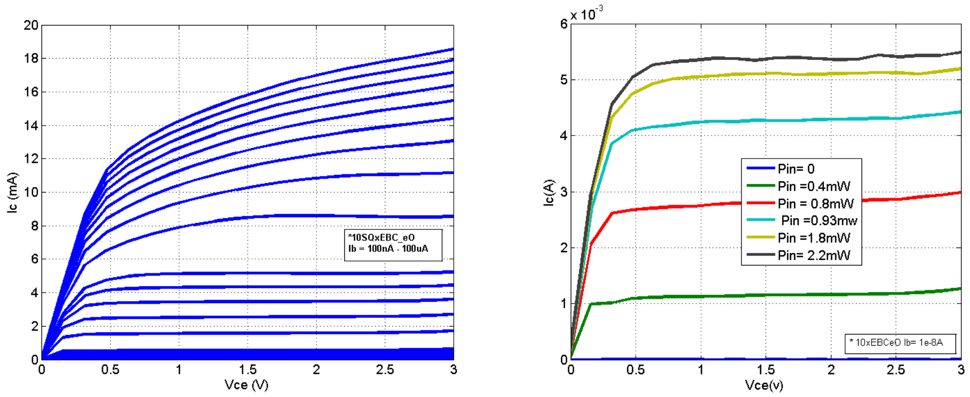

a) b)

Figure 3.28 R3-10SQxEBCeO a)Ic-Vce curved in non-illuminated condition b) Ic-Vce curves with Ib =100nA at different optical power levels

Figure 3.29 shows the responsivity of this HPT as function of (a) Vce at different values of Ib and (b) Ib at specified values of Vce under 1.8mW of illumination. For this HPT, the extracted responsivity is 2.82A/W from an Ib of 100nA -1µA. The DC responsivity from this very low bias region is almost constant. This means that the measured collector current under the illuminated condition provides the dominating base bias. It could be considered that this biasing range is similar to the 2T HPT operation. Higher base currents in constant base current biasing results in lower extracted DC responsivity, when the HPT operates in the high bias region, the collector current is severely limited by high current effects. Finally, Vce values, as long as it lies in the linear region, have minimal impact on the responsivity.

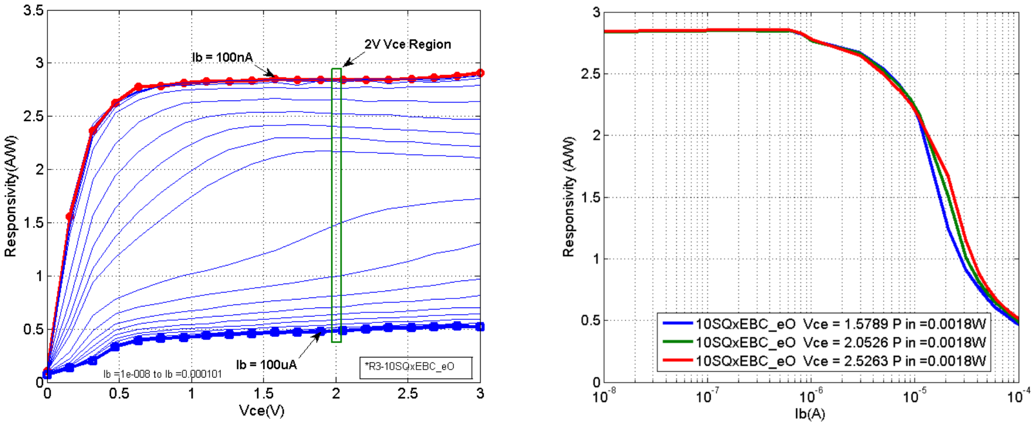

a) b)

Figure 3.29 Extracted DC responsivity of R3-10SQxEBCeO with 1.8mW optical input a) vs Vce at different values of supplied Ib b) vs Ib at Vce = 1.5V, 2V, and 2.5V

3.3.2.2.3 Effect of the HPT structure on responsivity curves

Figure 3.30 shows the comparison of the extracted DC responsivity from the different sized xEBC HPT of Run2 under 1.22mW illumination. Figure 3.30 (a) shows the responsivity versus Vce when the supplied base current is 1µA. The highest responsivity is from the 50SQxEBC HPT where 100% of the optical beam passes thru the optical window. This is followed by the 20SQxEBC HPT with 75% of the optical beam pass thru the optical window and finally the lowest response is from the 10SQxEBC HPT with only 15% of the optical signal which enters the optical window A record responsivity of 12.83A/W was exhibited with the 50x50µm^2 HPT in EBC structure R2-50SQxEBC. Figure 3.30 (b) present the responsivity versus Ib when the supplied Vce is 2V. It shows the general trend of lowering of the extracted DC responsivity as the supplied base current is increased.

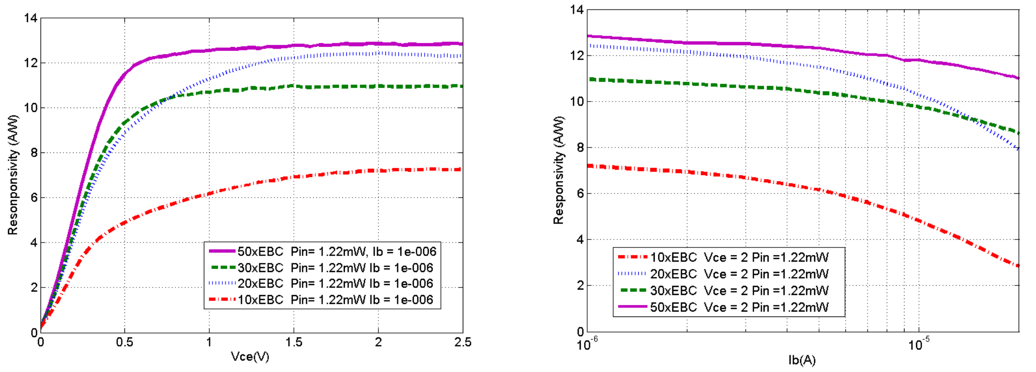

a) b)

Figure 3.30 Extracted DC responsivity of different R2-SQxEBC HPTs (a) vs. Vce at supplied Ib=1uA (b) vs. Ib at Vce = 2V

Finally, Figure 3.31 shows the comparison of the extracted DC responsivity from the different sized xEBCeO HPT of Run3 under 1.8mW of illumination. The general characteristic in terms of increasing responsivity as the optical window increases and coupling of the optical beam increases is also observed. Very low current biasing in the order of nA shows constant extracted responsivity.

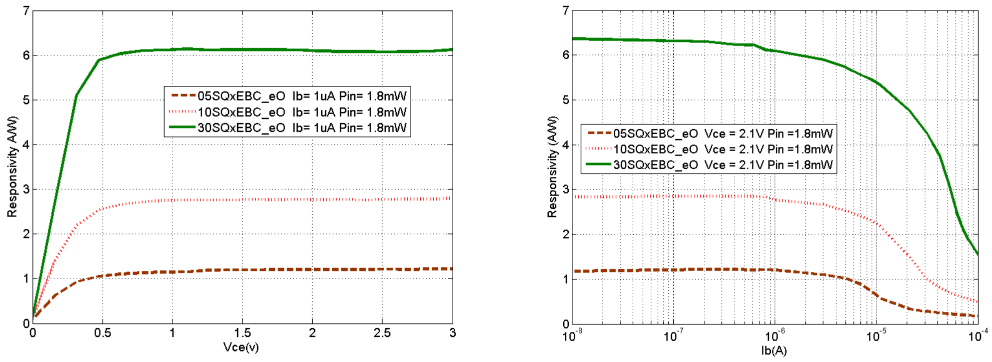

a) b)

Figure 3.31 Extracted DC responsivity of different R2-SQxEBC HPTs (a)vs Vce at supplied Ib=1uA (b) vs Ib at Vce = 2V

The difference between xBC and xEBC HPTs are shown in Table 3.7. It shows a summary of the measured peak DC responsivity of the different HPTS under constant current (CC) base bias. Similar behaviors are expected for all topologies. A peak responsivity of 12.83 A/W is demonstrated for R2-50SQxEBC HPT at 1.2mW

	Vce (V)	Ic (meas) (mA)	Vbe (meas) (V)	Ib (supplied) (µA)	Pin_{OPT} (mW)	DC Responsivity (A/W)
R1-10SQxBC	2	4.6	0.87	20	1.22	0.06
R1-50SQxBC	2	1.6	0.76	5	1.22	0.43
R1-10SQxBCrT	2	2.46	0.84	5	1.22	0.85
R1-50SQxBCrT	2	6.45	0.81	5	1.22	4.42
R1-10SQxBCrTeO	2	2.50	0.83	5	1.22	1.02
R1-50SQxBCrTeO	2	7.00	0.82	5	1.22	4.79
R1-10SQxEBC	2	5.16	0.81	5	1.22	2.54
R2-10SQxEBC	2	12.7	0.87	1	2.44	4.95
R2-10SQxEBC	2	9.4	0.85	1	1.22	7.20
R2-20SQxEBC	2	15.76	0.84	1	1.22	12.3
R2-30SQxEBC	2	14.14	0.81	1	1.22	10.96
R2-50SQxEBC	2	16.49	0.79	1	1.22	12.83
R3-05SQxEBC_eO	2	2.21	0.81	0.01	1.8	1.18
R3-10SQxEBC_eO	2	5.18	0.81	0.01	1.8	2.84
R3-10SQxEBC_eO	2	9.00	0.85	11	1.8	2.17
R3-30SQxEBC_eO	2	11.42	0.80	0.01	1.8	6.40

Table 3.7 Summary of extracted DC Responsivity for constant current base biasing (CC).

3.3.2.3 Conclusion and comparison between CC and CV modes

In summary, illumination of the HPT shifts the bias point of the HPT. For the case of a constant voltage (CV) that is applied in the base, the measured illuminated base current Ib will have lower values as compared to the base current of non-illuminated HPT, which is the sum of the forward dark current and of the reverse photocurrent. Part of the photocurrent is going out the HPT through the base contact. However part of it is amplified with the current gain β. Maximum responsivity of 6.4 A/W has been found for a R3-30SQxEBCeO HPT. On the other hand, the illumination of an HPT with a constant current (CC) bias in the base results in an increase of the measured Vbe. This means that the base bias of the HPT is increased to higher values that are multiplied with the shifted current gain β. This results in very high measured collector currents. Finally, the extracted DC responsivity from CC measurements will have higher values as high as 12.83A/W for a R2-50SQxEBC HPT under 1µA Ib and 2V Vce. Such a high responsivity is obtained only at very low Ib values where the HPT operates as 2T-HPT. This ensures that all photocurrent generated in the base is reinjected in the HPT and then amplified.

Figure 3.32 shows the comparison between the extracted DC responsivity from CC and CV as a function of the measured illuminated collector current. The CV biased HPT with Vbe= 0V to 1V, results in Ic illuminated range of 855µA to 22.76mA with a peak value of 0.49A/A in the Ic = 6.5mA. The CC biased HPT with Ibe= (1µA-100 µA) results in Ic illuminated range of 13.29mA to 21.56mA with a peak value of 5A/W under 2.4mW

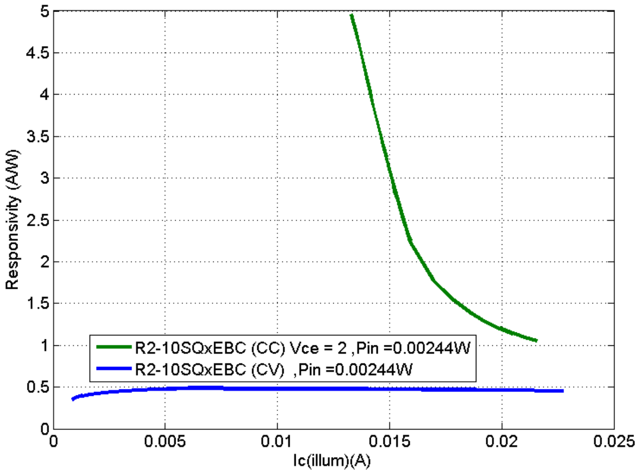

Figure 3.32 Extracted DC Responsivity of R2-10SQxEBC vs. Ic illuminated under constant current and constant voltage bias in the base of the HPT with illumination power of 2.44mW

3.4 Opto-microwave response

This section shows the HPT mode opto-microwave response of the fabricated HPTs. In the HPT mode of operation, the base of the HPT is biased. The detected optical signal is amplified by the transistor operation of the HPT.

For HPTs of RUN1, opto-microwave measurement were implemented using constant current in the base. The HPTs are operated in the forward active mode with Vce values at 1V, 1.5V, and 2V. and the Ib values are from 5µA to 90 µA. Figure 3.33 shows the opto-microwave link gain G_{OM_Link} at 50 MHz as a function of Ib with a Vce of 2V. The a G_{OM_Link} of the xBC HPT shows of an average value of -40 dB across the Ib sweep range. A the lowest bias of 5µA an increase of 4dB with the removal of silicided titanium (TiSi) in the xBCrT G_{OMLink}. Further improvement of at most 2dB is seen with the etching of the oxide in the xBCrTeO HPT. Finally the G_{OMLink} of the xEBC HPT shows the best performance with at most 6dB improvement in response over the xBCrTeO HPT.

Compared to the PD mode improvement of 6.5dB when moving from an xBC topology to an xEBC one, it can be extracted from this figure that the xEBC topology provides a better amplification of the photocurrent by typically 4.5dB more.

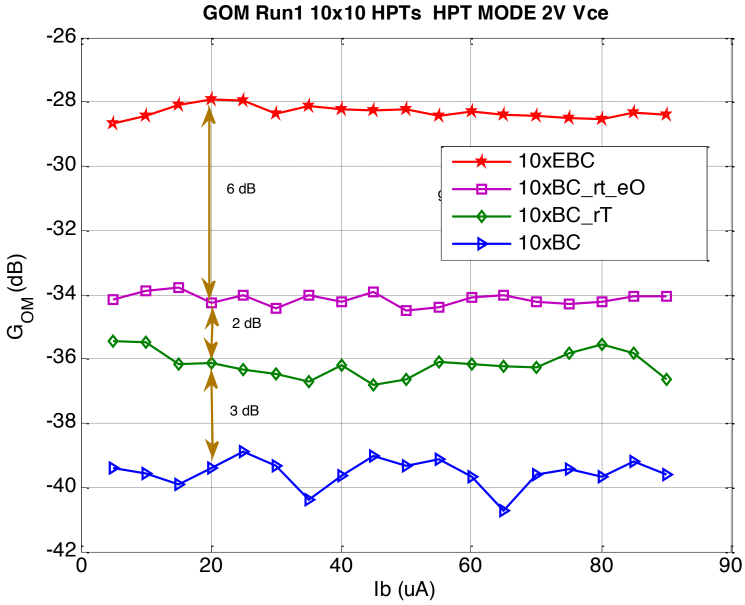

Figure 3.33 G_{OM_Link} (dB) @ 50 MHz vs. Ib. The HPT is in HPT MODE operation with 2V Vce and Ib from 5uA to 90 uA under a 1.08mW optical beam with a 26um diameter spot size.

Figure 3.34 shows the -3dB cutoff frequency of an opto-microwave link measurement as a function of the base current and a Vce of 2V. The laser used for this measurement has a bandwidth of 9GHz. The -3dB cutoff frequencies shown here are from the influence of the HPTs only. The -3dB cutoff frequencies of the xBC based HPTs has an average value of 200MHz. These HPTs have the same peak f_T value of 40GHz as seen in Figure 2.46. On the other hand the xBC HPT has an average value of 260MHz. The measurements tells us that the xEBC HPT has faster opto-microwave response at 850nm. This is due to its higher peak f_T value of 44GHz.

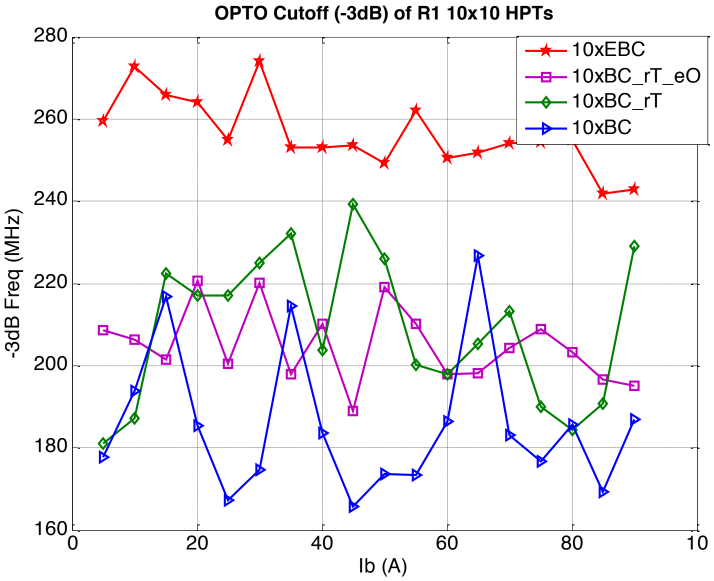

Figure 3.34 Optical Cut off frequency (-3dB_{Link}) vs. Ib (change the colors to be consistent)

Figure 3.35 shows the measured link gain of the laser + HPT with the HPT under constant base current of the different 10x10μm² and 50x50μm² HPTs at 50MHz. The collector voltage is at 2V, Ib is swept from. 0.5μA to 90μA. The 50SQxBC HPT shows a 2dB-3dB increase in response with respect to the 10SQxBC HPT. For the 50SQxBCrt and

50SQxBCrTeO, an increase of 9-10dB was observed with respect to the smaller optical window counterparts. The order of G_{OM} response from lowest to highest will be from xBC, xBCrt, xBCrTeO. This is a similar performance as seen in the 10x10µm² HPTs. The same is observed for the 50x50µm² HPTs however the increase from etching the oxide with bigger HPTs is only around 1 dB as compared to 3dB for the smaller sized HPTs. The opto-microwave cutoff frequency of the bigger devices are approximately 140 MHz as shown in Figure 3.36, and the smaller HPTs are in the area of around 200MHz. The larger HPTs are slower both in electrical and opto-microwave response as expected.

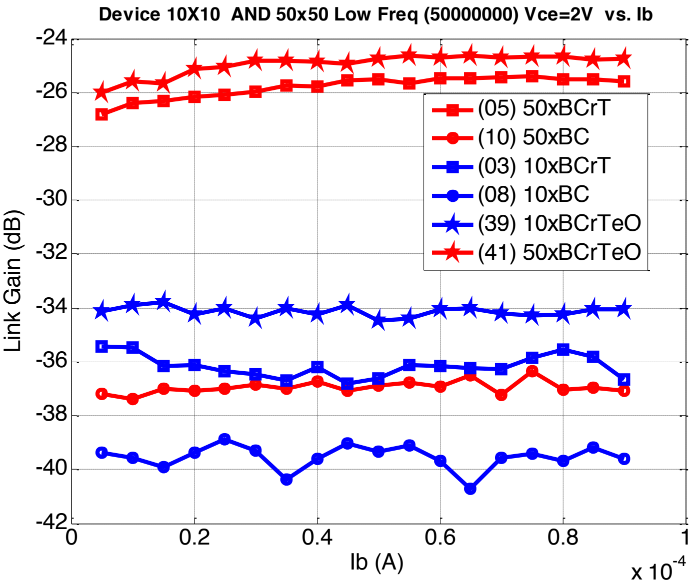

Figure 3.35 Gom at 50 MHz of differerent sized HPTs as function of Ib and Vce = 2V

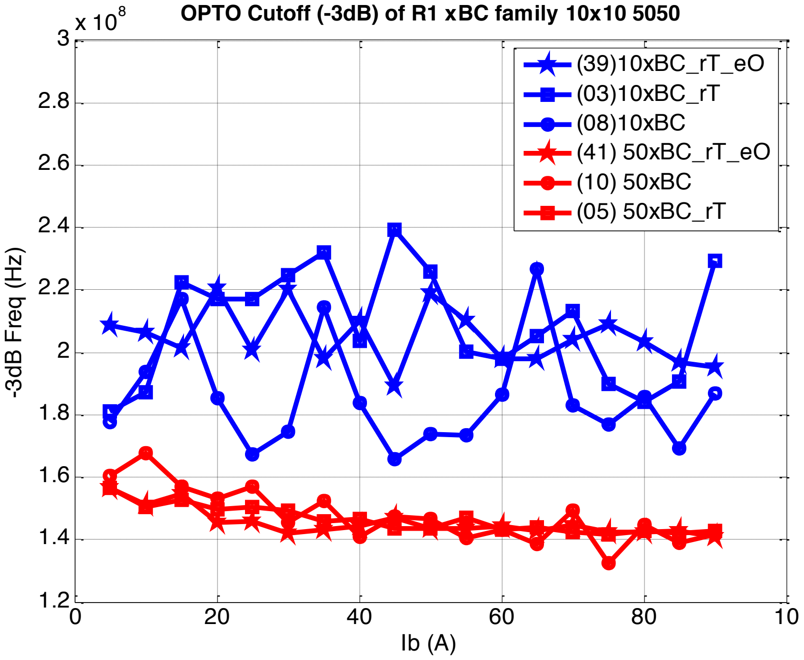

Figure 3.36 Opto Cutoff frequency as a function of Ib for different sized HPTs.

For HPTs of RUN1, the G_{OM} of the HPTs in relative units are plotted in Figure 3.37. It shows the highest measured responsivity from a Vce = 2V and a sweep of base currents.

Table 3.8 shows the complete bias values for the opto-microwave response shown in Figure 3.37. At 50MHz of operation, the lowest response is seen from the R1-10SQxBC HPT with a value of -33dB. The removal of titanium in the R1-10SQR1xBCrT HPT results in a 4dB increase in response. An addition increase of 2dB is seen with the etching of oxide in the R1-10SQR1xBCrT_eO HPT. Finally, the R1-10SQxEBC HPT has a 10dB increase as opposed to the R1-10SQR1xBCrT_eO HPT. This order is initially observed in the PD mode of operation. The amount of increase for each HPT type shows the effect of the amplification of the optical signal in the HPT mode of operation.

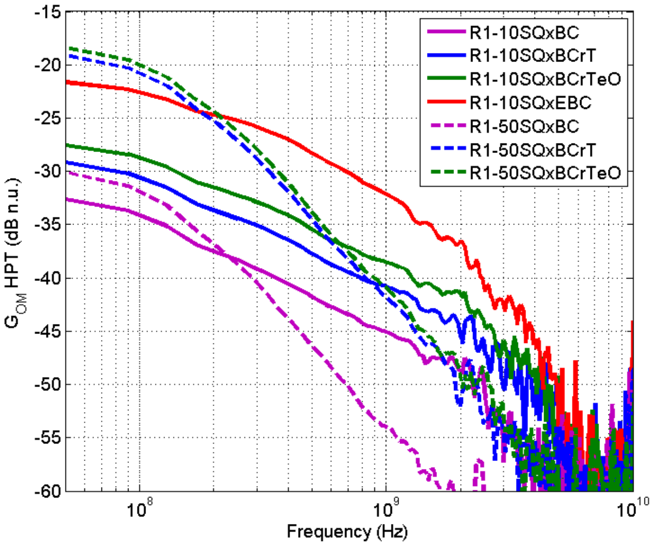

Figure 3.37 G_{OM} (dB n.u) of the different HPT from prototyping run 1 in HPT mode of operation

The 50x50µm² HPT shows significant increase in responsivity in the low frequency as compared to their 10x10µm² HPT counterparts. This is due to the decrease in the mismatch loss between the optical beam and the optical window of the HPT. However, it suffers from a lower opto-microwave cutoff frequency. These measurements show that the R1-10SQxEBC HPT has the highest response in the GHz range of operation.

	Vce (V)	Ic (mA)	Vbe (V)	Ib (µA)	G_{OM}(50 MHz) (dB n.u)	Cutoff Freq (MHz)
R1-10SQxBC	2	5.10	0.88	25	-32.59	205
R1-50SQxBC	2	14	0.86	75	-30.08	133
R1-10SQxBCrT	2	2.47	0.84	5	-29.15	181
R1-50SQxBCrT	2	17.24	0.87	75	-19.11	142
R1-10SQxBCrTeO	2	4.31	0.87	15	-27.5	202
R1-50SQxBCrTeO	2	16.25	0.87	65	-18.35	143
R1-10SQxEBC	2	9.27	0.85	20	-21.64	264

Table 3.8 Summary of G_{OM} (dB n.u) of different HPTS with optical input power of 1.08mW in HPT mode

The xEBC HPT shows the best results from prototyping run 1. Prototyping run 2 provides HPT structures with different sized xEBC HPT. The measurement of the opto-microwave response of the Laser + HPT link provides the $G_{OM\ Link}$ provides the starting point for the extraction of the HPT responsivity. The resulting measurements are shown in Figure 3.38. In this figure, the one axis is the $G_{OM\_Link\text{-}HPT}$ and another axis which is the Frequency. The measurements are made from 11MHz up to 24GHz. Each slice in the Vbe axis shows the Link Gain vs. frequency plot when Vce = 2V. This shows that for a 0V Vbe Base biasing, we observed a G_{OM} of -26 dB at 50 MHz and a peak G_{OM} value of -20.86dB at 50 MHz for a base voltage of 0.85V.

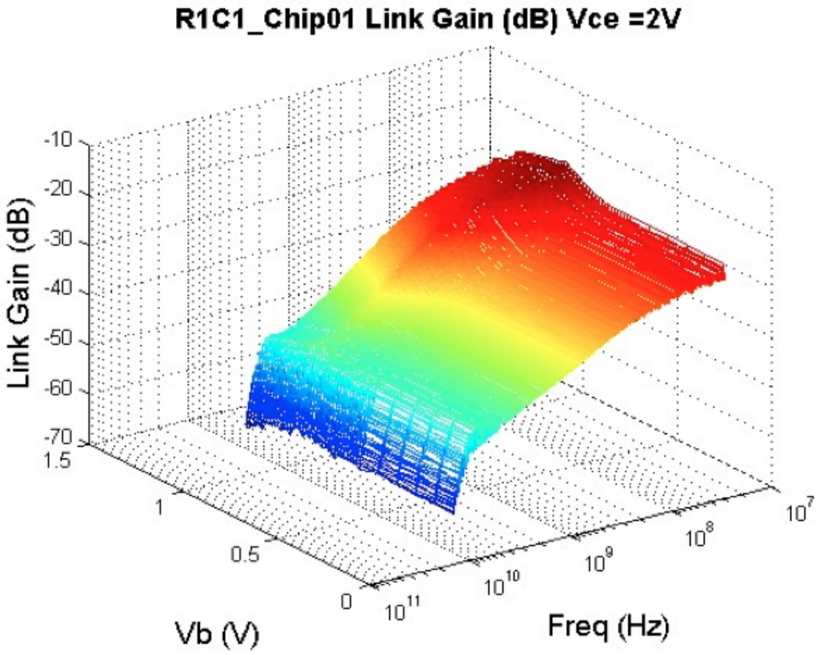

Figure 3.38 GoM at Vce = 2V and Vb from 0V to 1.1V

Figure 3.39 a and b shows the $G_{OM\,Link}$ at 50 MHz as a function of the base bias voltage Vbe at a fixed Vce of 2V for the different sized xEBC HPTs. The G_{OM} measurements at 0V-0.55V could be considered as the PD mode biasing of the HPT. In this biasing region, the Base Collector junction is reverse biased and the BE junction is not yet forward biased. The G_{OM} increases from 0.6V and reaches its peak at around 0.85V Vbe, it then starts to fall off as the HPTs are in the high injection region of operation for voltages greater than 0.85V. The difference between the peak G_{OM} and the G_{OM} At 0V is G_{OPT}. It is the gain enhancement between HPT mode and PD mode of operation.

Table 3-9 summarizes the G_{OM} under PD mode and HPT mode (peak) of operation under 2.44mW of illumination.

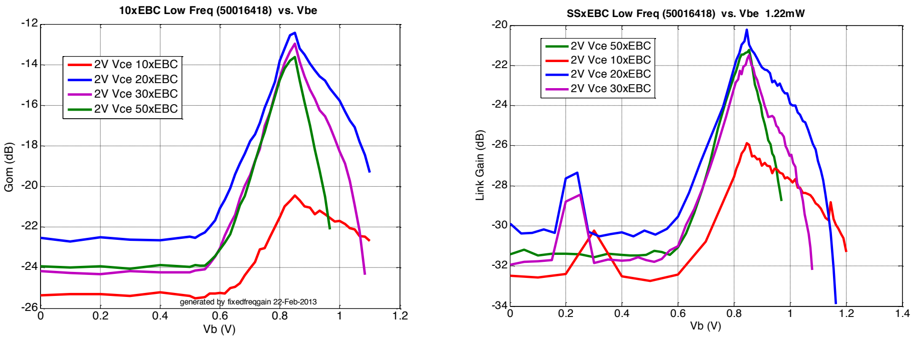

Figure 3.39 $G_{OM\_Link\text{-}HPT}$ with extended Emitter Base and Collector (xEBC) HPTs at different optical windows as a function of Vbe. (a) under 2.44mW and 26um spot size b) 1.22mW and 26um spot size.

Table 3-9 Summary of R2-SQxEBC HPTs under 2.44mW Popt in constant voltage biasing

	G_{OM} link (50 MHz) PD Mode	G_{OM} link (50 MHz) HPT Mode	Gopt	Peak Vb(V)	Elec beta a peak
R2-10SQxEBC	-25.37	-20.46	4.91	0.85	420.5
R2-20SQxEBC	-22.53	-12.44	9.91	0.85	451
R2-30SQxEBC	-24.18	-12.97	11.21	0.85	444.7
R2-50SQxEBC	-23.92	-13.62	10.3	0.85	378

In terms of the estimated optical gain, the 20xEBC has 10dB, the 30xEBC has 11dB and the 50xEBC has a 10dB. This shows that the optical gain for the devices with near 100% coupling is the same.

Figure 3.40 shows the measured $G_{OM\_Link-HPT}$ as a function of the measured collector current as Vb is swept from 0V to 1.1V. In the 10xEBC HPT, the peak link gain occurs when Vbe is equal to 0.85V at Vce value of 2V. In the illuminated condition, a 9.7mA collector current is measured. As Vbe is raised above 0.85, the measured $G_{OM\_Link-HPT}$ goes lower and the measured collector current decreases. The measured collector current, which corresponds to the peak, measured $G_{OM\_Link-HPT}$ has a value that increases as the size of the optical window increases. The 20xEBC has 18.9mA , 30xEBC has 24.8mA and the 50xEBC has 37.35mA. These values, shows the start of the high current operation region of the HPT. Collector currents above these causes the gain of the intrinsic transistor to starts the fall off. In Figure 3.41 the measured $G_{OM\_Link-HPT}$ as a function of the measured base current Ib as Vb is swept from 0V to 1.1V is presented. This shows that the peak $G_{OM\_Link-HPT}$ could generally be achieved at negative values of Ib under the illuminated condition. In term of positive Ib values, the highest $G_{OM\_Link-HPT}$ could be achieved in the lowest possible base current that allows for the forward-active mode operation of the HPT.

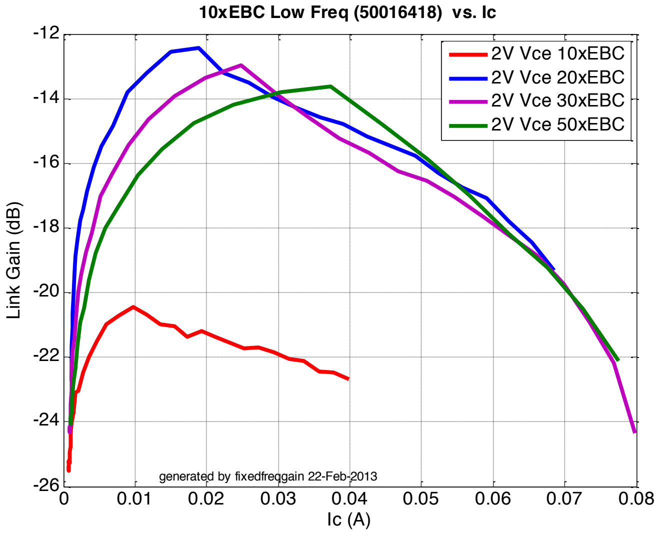

Figure 3.40 Gom Vs. Ic xEBC different optical windows

The optical cutoff frequency using 50MHz as a reference low frequency response is shown in Figure 3.42. It is the -3dB frequency of the G_{OM} measurements. In the PD mode operation. The 10x10µm^2 has a 175MHz, 20x20µm^2 is 152MHz, 30x30 is 149 MHz and the 50x 50MHz is 130MHz. The cutoff frequency at peak G_{OM} is a follows: 295MHz,199MHz, 125MHz ,97.5MHz for increasing optical window size. It can be observed that the peak cutoff for the 10x10 and 20x20 HPT is when Vbe = 0.85V . The

HPT mode operation has a higher cutoff frequency in the HPT mode as supposed to the PD mode. However for the 30x30µm^2 and 50x50µm^2 HPT the inverse is observed.

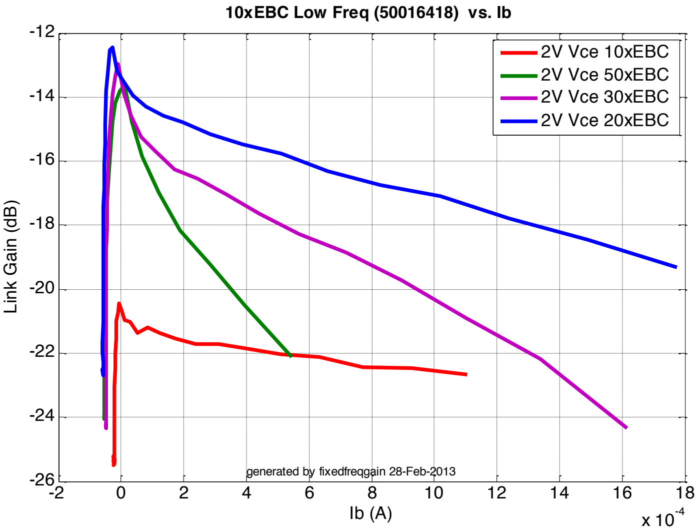

Figure 3.41 Gom Vs. Ib xEBC different optical windows

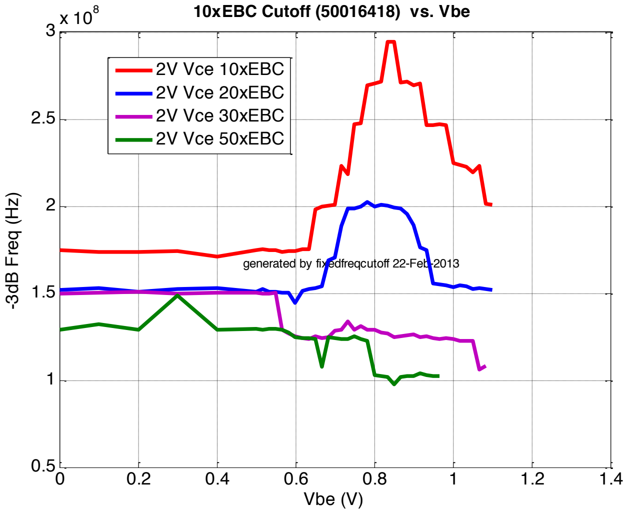

Figure 3.42 Opto cutoff vs. Vbe

Figure 3.43 (a) shows the peak measured responsivity (dB) for the xEBC HPTs of run 2. Similar to the previous HPT types, HPT with optical windows that are equal or greater than 20x20µm^2 show improvements over 10x10µm^2 from the minimization of coupling losses. However such improvement in the low frequency HPT responsivity could not be seen in the high frequency operation. The R2-10SQxEBC HPT and R2-20SQxEBC HPT shows similar results from 6 GHz onwards. Figure 3.43 (b) presents the measured peak response from xEBCeO HPTs with 5x5µm^2, 10x10µm^2, 20x20µm^2, and 30x30µm^2 optical windows. In low frequency, the larger the size of the optical window dictates the higher response. The 30x30µm^2 HPT shows the highest response at low frequency. However, in the GHz range, the 10x10µm^2 HPT exhibits the best response. The high collector current collector current in the 5x5µm^2 HPT under the illuminated condition pushes it in the high current region wherein it has lower response in the high frequency. Finally, Table 3.10 show the summary of the extracted responsivity from opto-microwave measurements.

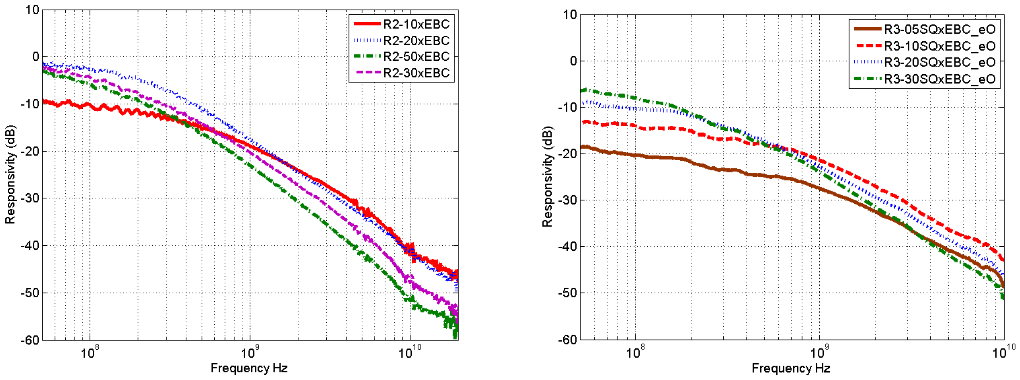

a) b)

Figure 3.43 Opto-microwave response of different HPT a) Run 2 xEBC HPTs and b) Run3 xEBC_eO HPTs.

	Vce	Ic mA	Ib uA	Vb V	Pin_{OPT}	Resp A/W	$F_{-3dB\ opt}$ (MHz)	GBW GHzA/W
R2-10SQxEBC	2	9.71	-6.24	0.85	2.44	0.33	295	0.099
R2-20SQxEBC	2	18.86	-26.27	0.85	2.44	0.84	198	0.166
R2-30SQxEBC	2	24.81	-8.68	0.85	2.44	0.78	125	0.097
R2-50SQxEBC	2	37.35	10.88	0.85	2.44	0.70	102	0.072
R3-05SQxEBC_eO	2	5.05	9.17	0.87	1.8	0.12	195	0.022
R3-10SQxEBC_eO	2.	5.36	5.54	0.82	1.8	0.21	247	0.053
R3-20SQxEBC_eO	2	9.60	4.17	0.82	1.8	0.34	215	0.074
R3-30SQxEBC_eO	2	13.85	3.01	0.82	1.8	0.47	152	0.072

Table 3.10 Summary of extracted HPT responsivity from opto-microwave measurements in HPT mode.

The extracted DC responsivity from constant (CC) and constant voltage (CV) which provides the same measured illuminated Ic shows that higher responsivity values are extracted with CC base bias. However, for opto-microwave measurements, the extracted responsivity of the HPT at the same resulting Ic bias level shows the same result for the extracted responsivity. This is illustrated in Figure 3.44, it shows the extracted responsivity R3-05xEBCeO HPT and R3-10xEBC_eO HPT in CC and CV biasing in the base. For the R3-10xEBC_eO HPT, an Ic of 14mA is achieved by 2V Vce and 25.5µA Ib, or by 2V Vce and 0.9V Vbe. In both biasing, the extracted peak responsivity is 0.21A/W and the resulting responsivity versus frequency curve shows no variation. This is due to the small signal nature of the responsivity extracted from the opto-microwave measurements. In both biasing conditions, the HPT are compared at exactly the same bias point as set the external bias and illumination power. The same result could be seen with the R3-05xEBCeO HPT that is biased at 7mA Ic, which results to a peak responsivity of 0.11A/W.

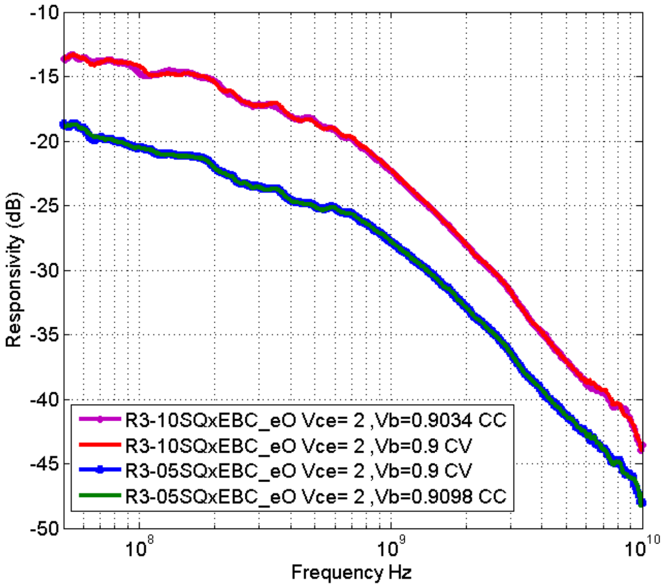

Figure 3.44 Comparison of opto-microwave responsivity of HPT extracted from CC and CV measurements with the same measured illuminated Ic for the R3-10SQxEBC_eO HPT and R3-5SQxEBC_eO HPT

3.5 Conclusion

The two operation modes of the HPT were analyzed to provide an understanding in the operation and characterization of the different HPT structures. In the photodiode mode (PD) mode, the effect on the optical path of the vertical stack of the different HPT structures is directly visible.

The removal of the silicided titanium and the etching of the oxide layers helps improve the DC responsivity of the HPTs. This is clearly seen on HPTs with optical windows that are equivalent or greater than the spot size of the optical beam that is used for the optical systems. Finally, using the full extended emitter structure (xEBC) HPT shows better performance by 6.5dB when compared to a Base-collector extended HPT only, even with the improvement of the removal of TiSi and oxide etching (xBCrTeO). The etching in the oxide in an xEBC HPT or an xBC HPT also improves further the optical response typically by 2dB.

The effect of the constant current CC and constant voltage CV bias in the base was studied and its effects could be summarized as follows: In the illuminated condition, the average power of the optical signal shifts the bias in the base of the HPT. In the CV condition, the measured current in the base has a lower value as compared to the non-illuminated base current from the same Vbe bias. This forces the HPT to operate in a lower base bias and shifted current gain. In the CC condition, the measured Vbe is higher that the non-illuminated Vbe. This indicates that base bias is shifted to a higher Ib bias due to the photocurrent and the current gain β is shifted as well. The extracted DC responsivity at the same illuminated Ic bias value shows that CC biased base will have higher responsivity compared to HPT in the CV bias, specially at low Ib where the 3T-HPT behaves has a 2T-HPT like behavior. However, the experiments have shown that the type of biasing in the base has no effect in the opto-microwave behavior, because the opto-microwave responsivity is a small signal property and the HPT is operated in an illuminated Ic bias that is fixed by the base bias and the average power of the optical beam. However the CV mode proved to allow a larger amplitude of biasing conditions, independent on the optical power that is injected.

It can also be concluded from this chapter that the xEBC topology has an advantage as compared to the xBC topology. The xEBC offers improved optical transmission as seen from the PD mode response and a its ability to amplify the photodetected signal in the HPT mode is improved by at least 4.5dB. This results in a 11dB improvement on the total G_{OM}.

Finally, the opto-microwave measurements show that R2-10xEBC HPT shows the highest measured opto microwave response at 5GHz. However, due to high coupling losses associated with the 26μm spot size used for the illumination, it has very low opto-microwave response at lower frequencies. The R2-20SQxEBC offers very high responsivity in the low frequency of operation due to better coupling with the optical beam. In the high frequency of operation, its response is only lower by 1 dB at 5GHz compared to the R2-10SQxEBC and is practically the same value for operation above 6GHz. This 20SQxEBC offers a good trade off between optical coupling and frequency response. The cutoff frequency on the HPT mode G_{OM} proved to be improved by the use of xEBC topology typically by a 30% ratio.

4 HPT Based Circuits and Amplifier Circuits

4.1 Introduction

This chapter focuses on the design and characterization of HPT based circuits and amplifier circuits that can be used in the implementation of a circuit subsystem for integrated optoelectronic receiver circuits.

Opto-microwave matching will be presented as it affects the performance of a single HPT device. The theory on opto-microwave matching, as well as simulations and measurements, will be discussed as a background on how single HPT performance could be optimized using only passive devices to provide input matching in the HPT. Output matching is also considered while strictly similar to the standard HBT case.

Characterization of several HPT-HBT pairs is then presented. This integration is expected to provide an efficient way to collect or amplify further the output signal of the HPT at a reduce cost in additional passive circuits. It is also a step toward the fabrication of simple OE-MMIC .The general idea of using multi stage amplification to improve single stage amplifier limitations is discussed.

A conclusion is then provided.

4.2 Opto-microwave Matching

In this section the effect of opto-microwave matching on HPTs is presented. A three-port configuration is used to represent phototransistors. The target is to optimize the gain between the optical input and the electrical output of the HPT as a function of the impedance that is presented in the base of the HPT. Port 1 is an electrical access in the base, Port 2 is a single direction access optical window and finally, Port 3 is an electrical access in the collector where the electrical emitter access is grounded in the common emitter configuration. The intensity modulated optical signal is injected in Port 2 and the modulating signal is collected in port 3. The opto-microwave S-parameters of the HPT can be defined as follows [130].

S_{11} reflection of the base	S_{12} transfer of the optical access towards the base	S_{13} transfer of the collector towards the base
$S_{21}=0$ transfer of the base towards the optical entry	$S_{22}=0$ reflection of the optical access are equivalent	$S_{23}=0$ transfer of the collector towards the optical access
S_{31} transfer of the base towards the collector	S_{32} transfer of the optical access towards the collector	S_{33} reflection of the collector.

The three ports, S_{22} , S_{21} and S_{23} are equal zero since the optical port is assumed to have only one direction. The parameters S_{11}, S_{33}, S_{31} and S_{13} are classical electrical parameters while S_{12} and S_{32} are the new defined opto-microwave S-parameters.

The resulting schematic of a three-port representation of the HPT is presented in Figure 4.1.

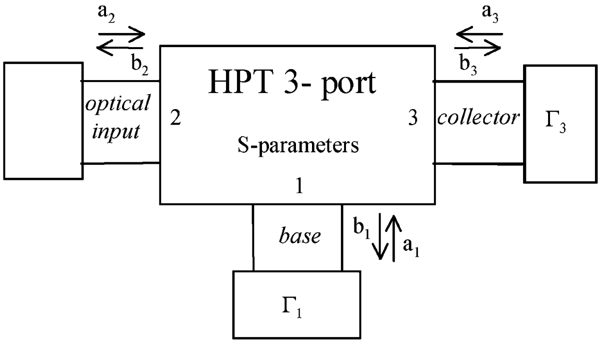

Figure 4.1 Three port representation of the HPT [230]

An equation to define opto-microwave gain G_{OM} of the HPT is formulated using the opto-microwave S-parameters and the load impedances in the base and collector [130]. The G_{OM} of the HPT is presented in Eq. 4.1 which takes into consideration of the single direction of the port $S_{21} = S_{22} = S_{23} = 0$.

$$G_{OM} = G_1 \cdot G_0 \cdot G_2 = \left|\frac{1 - M \cdot \Gamma_1}{1 - S_{11} \cdot \Gamma_1}\right|^2 \cdot |S_{32}|^2 \cdot \frac{1 - |\Gamma_3|^2}{|1 - sp_3 \cdot \Gamma_3|^2} \qquad \text{Eq. 4.1}$$

where

$$M = S_{11} - \frac{S_{31} \cdot S_{12}}{S_{32}}$$

$$sp_3 = S_{33} \cdot \frac{1 - D \cdot \Gamma_1}{1 - S_{11} \cdot \Gamma_1}$$

$$D = S_{11} - S_{31} \cdot \frac{S_{13}}{S_{33}}$$

sp_3 is the output reflection coefficient of the HPT when the base is loaded with R_0 = 50Ω. The equation for G_{OM} has three main terms; G_1 represented the influence of the load impedance presented to the base of the phototransistor (Port 1), G_0 represents the 50Ω-loaded gain of the phototransistor, and the term G_2 represents the effect of the output impedance that is connected to the collector of the phototransistor (Port 3).

Maximizing the gain terms G_1 and G_2 through adequate load impedances presented in the base and collector ports leads to a maximization of the opto-microwave gain G_{OM}. The gain of G_2 is maximized by impedance matching techniques to the collector port. The load impedance in the collector should be the conjugate of sp_3, $\Gamma_3 = sp_3^*$. It should be noted that G_2 is also dependent of the base load since sp_3 is a function of Γ_1. However, we will assume that this dependence is negligible and that Γ_1 has a strong influence in G_1 only.

In order to find the Γ_1 that maximizes G_1, it is essential to consider the values of the poles and zeroes of G_1. This is represented as Γ_{pole} and Γ_{zero}.

$$\Gamma_{pole} = 1/S_{11}$$

$$\Gamma_{zero} = 1/M$$

This means that if $|S_{11}| < 1$, the pole of the function will be located in the outside the Smith chart. An $|S_{11}| \geq 1$ presents a possibility of having an unstable operation of the phototransistor. The main consequence on the optimal base load for which the opto-microwave available gain is maximum, assuming a passive load is necessarily located at a place of constant gain that is tangent to the edge of the Smith chart. This means that the optimum impedance is purely reactive impedance.

At a specific frequency, the analysis of the gain component G_1 leads us to define the place of constant gain of this function in terms of load impedances Γ_1 of the base.

$$G_1 = \left|\frac{1 - M \cdot \Gamma_1}{1 - S_{11} \cdot \Gamma_1}\right|^2 = \left|\frac{\Gamma_{1(pole)}}{\Gamma_{1(zero)}}\right|^2 \cdot \left|\frac{\Gamma_1 - \Gamma_{1(zero)}}{\Gamma_1 - \Gamma_{1(pole)}}\right|^2 \qquad \text{Eq. 4.2}$$

The gain, computed as a function of Γ_1 is constant on complex circles. This is represented in Figure 4.2, using a physical simulation of the 1st generation SiGe HPT [130].

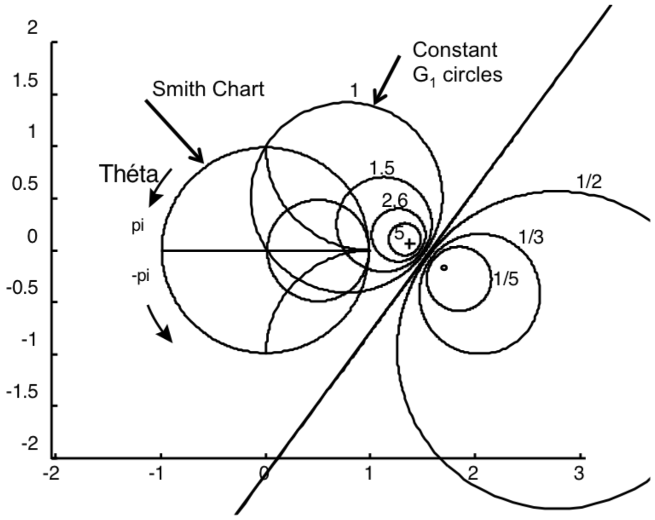

Figure 4.2 Circles of constant profit of G$_1$ in the plan 1Γ (pole represented by a `+', and zero by a `O')

The location of the pole (+) and zero (0) of G_1 plays a key role for both the optimum and minimum gain. The analysis of the orientation of the middle segment defined by these two points is particularly important. In the vicinity of the Γ_{pole}, the gain circles indicate an increase in the gain, and a decrease in the gain around the Γ_{zero}, for this particular HPT, at a specific biasing and frequency of operation. Base Loads influence in 1st generation SiGe HPTs.

Experimentally, the analysis of the impact of the base impedance in the behavior of the phototransistor was studied on an InGaAs/InP HPT and a 1st generation SiGe HPT pictured in Figure 4.3 [231]. In this study, Port 1 of the network analyzer is connected at the bias input of an 850nm laser, which illuminates the optical window of a SiGe HPT. Port 2 of the network analyzer is connected on the collector of the phototransistor, loaded with 50 Ω. The base is connected to a bias-T, allowing it to be connected to an electrical supply as well as connection to SMA connectorized RF impedance. A 1m-long low loss cable connects the bias-T to the load which is a 50Ω load, a short-circuit and open-circuit presented alternatively to the base. This makes possible a large variety of impedances to be connected to the base. This terminated line acts as an impedance generator as closed as possible to the border of the Smith chart. This measurement bench is illustrated in Figure 4.4.

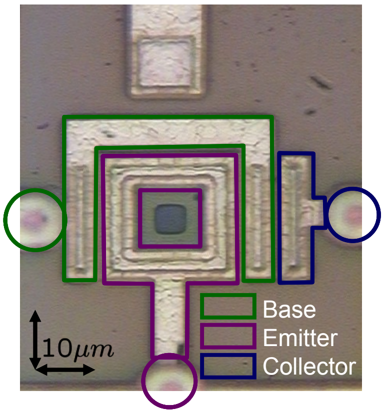

Figure 4.3 Chip photo of the 1st Generation SiGe HPT with a 10x10 μm² optical window.

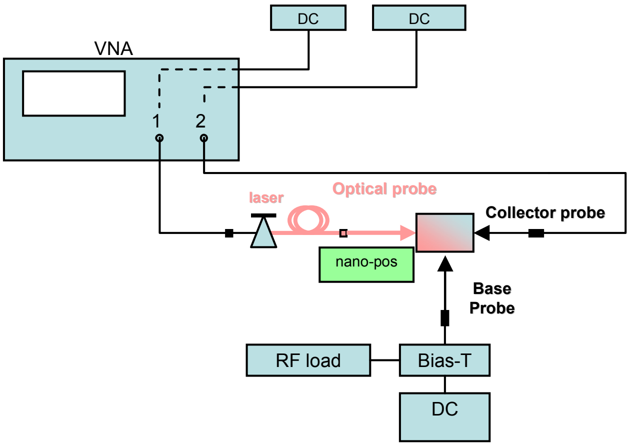

Figure 4.4 Measurement setup used to study the effects of different base load of the HPT.

The detected optical signal can flow in two directions. The main flow follows the direction towards the collector. This is amplified through the transistor action of the phototransistor. The other direction corresponds to the possibility for the photocurrent flowing out of the base access without being amplified by the transistor action. This signal is lost when the base is loaded with 50Ω. Nevertheless, when a reactive impedance is presented, the signal that flows out of the base can be reintroduced to the direction of the collector where it can be amplified. This direction presents a phase difference given by S_{12} and S_{31} combined with the terminal impedances. If this is in phase with the main flow, there will be an improvement in the G_{OM}. This is directly controlled by the Γ_1 load that is presented in the base of the phototransistor. The opto-microwave gain G_{OM} of the 1st generation SiGe HPT with the collector loaded with 50Ω and the base with varying base loads is shown in Figure 4.5.

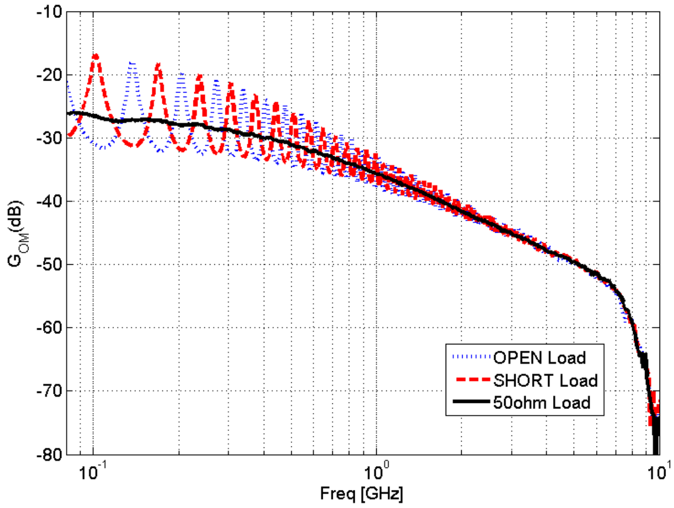

Figure 4.5 Measured opto-microwave gain in relative units of the SiGe link for a base load using a short-circuit (grey dotted curve), open-circuit (dark dashed curve) and 50 Ohms load (solid curve) in end of line. [231].

The presence of clearly visible extrema, in particular at the frequencies lower than 1GHz for the zone where the presented impedances are the closest of the edge of the plot validates experimentally the theory of the opto-microwave matching. The optimum impedances presented to the base shows improvement in response in the factor of 10dB as compared with 50Ω base load. On the other hand, worse case impedances degraded the opto-microwave gain.

The loads produced on the base of the HPT are then measured for the case of the open and short circuit RF loads. The values corresponding to the extrema are plotted on a Smith chart in Figure 4.6

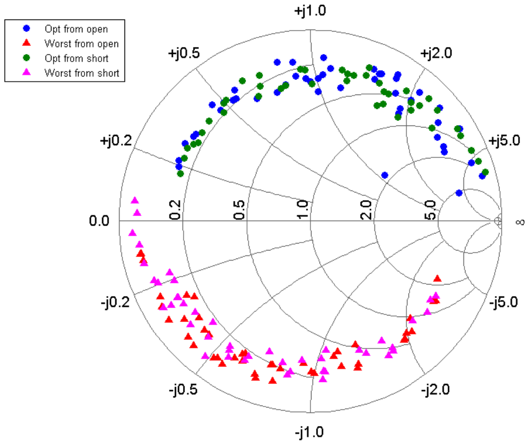

Figure 4.6 Locus of the impedances giving the maximum and the minimum values on G_{OM} extracted from measurements

The losses of the cable used to connect the base prevent from carrying out purely reactive loads. Thus, it is sure that an increase in the gain could be still obtained. Nevertheless, this figure shows a clear proximity of optimal impedances locus and $1/S_{11}$ one as predicted by the theory. The position of the "worse case" loads on the Smith chart, contrary to the "optimum" load impedances location, indicates a position of the zeroes of the G_1 function which is outside of the Smith chart beyond the pole and in a quasi-alignment with it and the 50Ω point. It is a particular characteristic related to the topology of this SiGe phototransistor. Figure 4.7(a) shows the opto-microwave measurements with the short loaded cable. The location of the optimum loads and worse case loads are marked. The phase of the optimum and worst case impedance presented to the base of the HPT at these specific frequencies are presented in Figure 4.7(b). The optimum loads occur when the phase angle is positive from 5°-150° for measurements until 4GHz and the worse case loads occur when the phase angle is negative valued form -150 °up to -50°

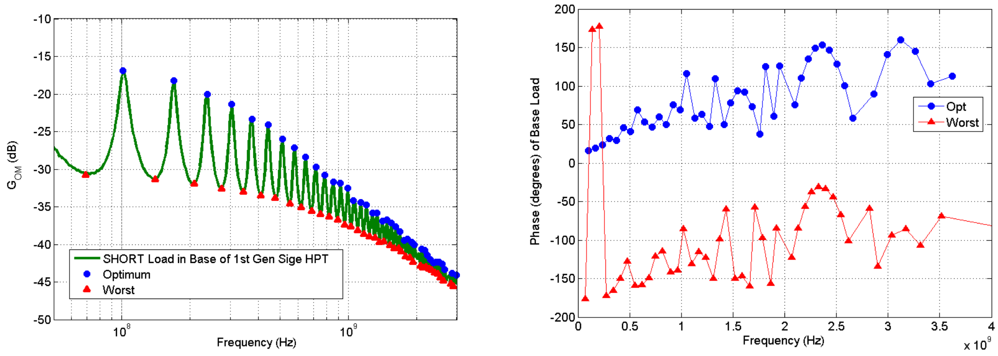

a) b)

Figure 4.7 Extracted optimum and worse case loads in a short loaded cable from measurements of 1st Generation ESYCOM SiGe HPT a) G_{OM} b) phase angle of G_{OM}

Base Loads influence in 2nd Generation SiGe HPTs.

The opto-microwave measurements of a 10x10µm^2 square extended emitter base and collector (R2-10SQxEBC) using a 4 port 24GHz Rhode and Schwarz network analyzer (R&SZNA24) are used to generate a 3-port model box. This model is generated when the HPT is biased with Vce =2V and Vbe = 0.85V and an optical illumination of 1.22mW feeding the lensed fiber. These are parameters from illuminated RF measurements and opto-microwave measurements of the HPT under the bias conditions mentioned earlier. The 3-port S-parameters of the HPT are presented graphically in Figure 4.8. It is used in the simulations (Agilent ADS) of the influence of base loads in the opto-microwave response of the HPT as well as in HPT base load circuits that are presented in the next section.

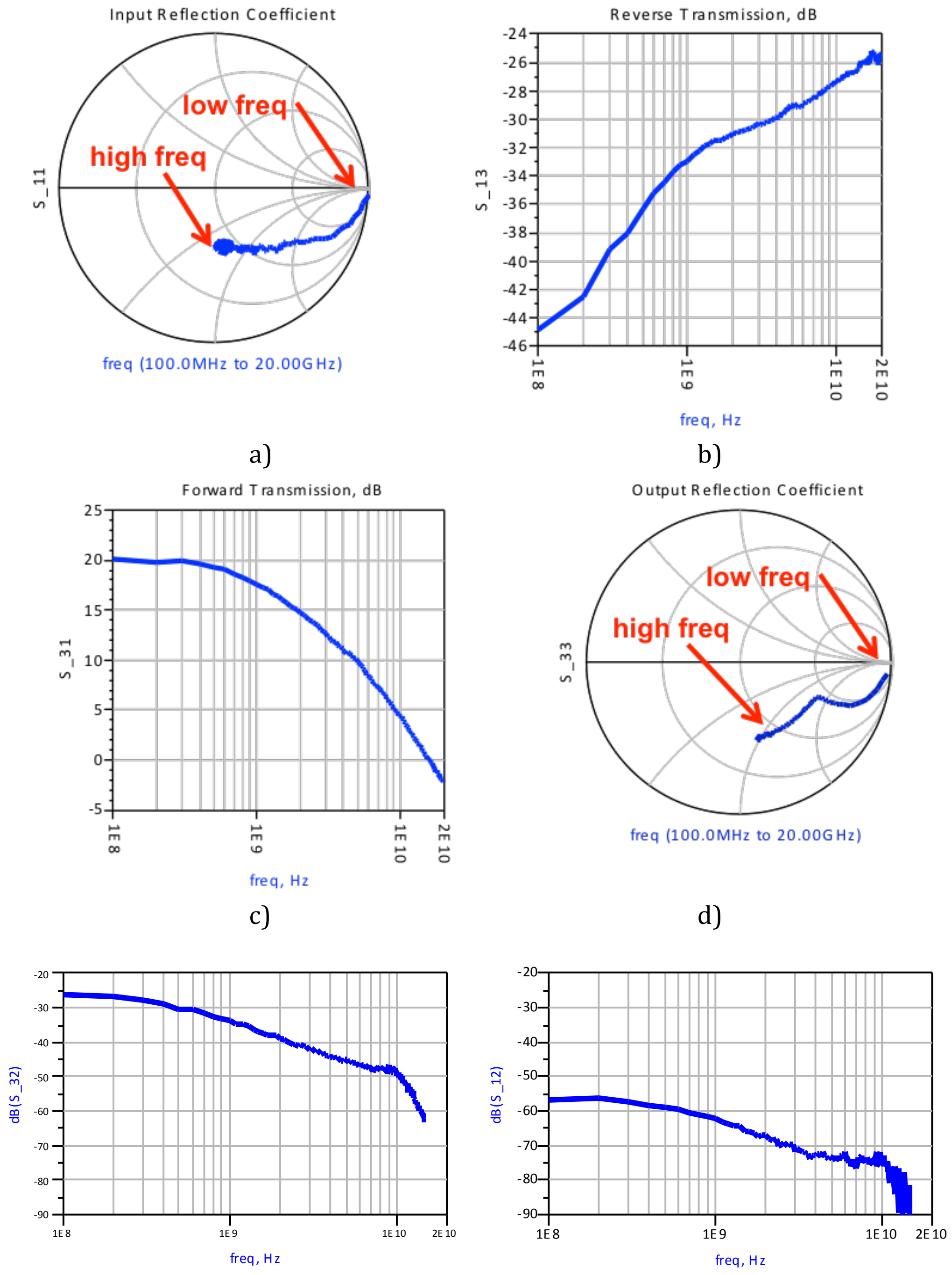

a) b)

c) d)

e) f)

Figure 4.8 3-port S-parameters of the HPT at Vce =2V and Vbe = 0.85V , P_{opt} = 1.22mW from measurements. a)S_{11} b) S_{13} c)S_{31} d)S_{33} e)S_{32_OM} f)s_{12_OM} for a R2-10SQxEBC HPT

4.2.1 External distributed Base loads influence

Initial experiments on the effect of different loads on the R2-10SQxEBC HPT were facilitated with the use of simulations. The performed simulations follow the experimental setup used for studying the base load effect for the 1st generation of SiGe HPT. In simulations, the base of the 3port model HPT is connected to a coaxial cable with three different terminations of 50Ω, short and open. The schematic representation of this simulation setup is shown in Figure 4.9 .

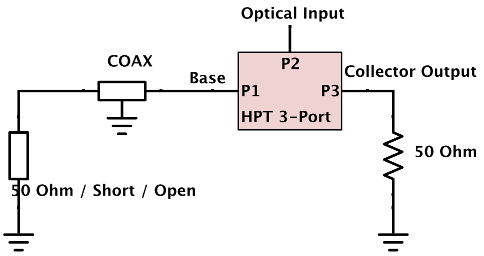

Figure 4.9 Schematic representation for the simulation the base load effect on the HPT.

The output reflection coefficient presented by an ideal 50Ω and 1m-length coaxial cable with three different terminations are presented on Smith chart as shown in Figure 4.10(a). The lossless nature of the coaxial cable means that the impedance presented to the base of the HPT by the short and open terminated cable is positioned in the border of the Smith chart with frequency (50MHz-24GHz) in 805 frequency points in logarithmic scale. The simulation results are shown in Figure 4.10b, from 50MHz up to 24GHz. They show similar behavior to the measurements on the 1st generation SiGe HPT. The simulations show higher gain peaks from some frequencies if the base is loaded by a stub. A 50Ω load absorbs the photogenerated carriers flowing to the base, they will not participate in the output signal. The simulated G_{OM} curves shows high and narrow peaks as compared to the measurements of the 1st generation SiGe HPT in Figure 4.7 This difference in the height of the peak is due the lossless nature of the coaxial cable used in the simulations; the narrow shape is due to the difference in the phase velocity of the coaxial cables. The peaks in G_{OM} curve shows that an improvement of at most 30dB at low frequencies and in ideal conditions could be possible. However, the minimum response is 2dB below the 50Ω terminated base load response. So, the worse case base load results to a degradation gain of 2dB.

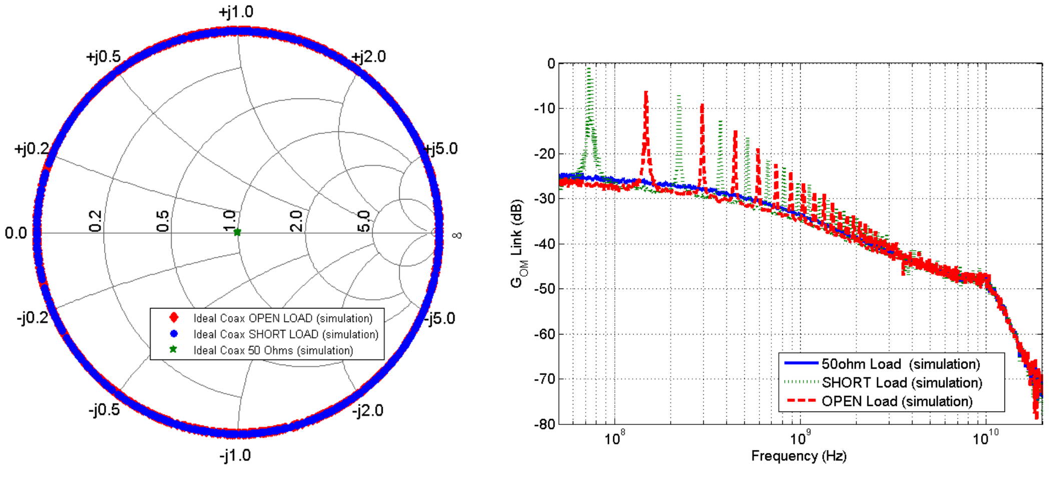

a) b)

Figure 4.10 Computed results for a R2-10SQxEBC HPT and a VI Systems VCSEL Link at 1.22mW a)Loads presented in the HPT using a lossless coaxial cable with a short, open and 50Ω termination b) G_{OM} form ideal coax 1m different terminations: 50Ω , short and open

Those computed results, despite obtained from a simulator are direct computation of measured results. Thus, it provides indirect measured quantities.. The peaks and valley of the short and open terminated stub loads correspond to a specific impedance load at that specific frequency. The peaks and valleys in the short stub loaded at the base of the HPT is shown in Figure 4.11 The corresponding impedance to the peak and the valleys are shown on Smith chart in Figure 4.12(a) , and the phase of the loads on Figure 4.12(b). As expected, the peaks in the G_{OM} correspond to purely inductive base loads with phase angle of 8° to 50°. The valleys correspond to purely capacitive loads with phase angles in -177° to -126°. However, as seen in the phase angle of the loads presented to the base of the HPT, the abrupt change in phase from a negative value to a positive value means that, certain inductive loads will also result in G_{OM} values lower than 50Ω-loaded G_{OM} value.

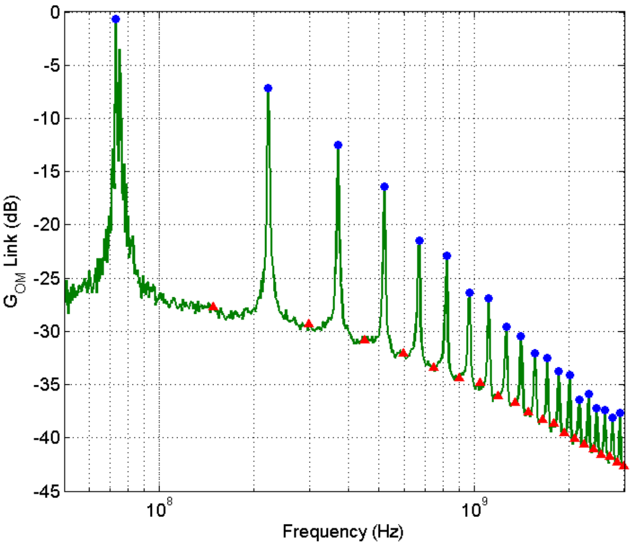

Figure 4.11. G_{OM} of optimum load and worse case loads with an ideal coaxial cable from 50 MHz to 10 GHz (Computations) for a for a R2-10SQxEBC HPT and a VI Systems VCSEL Link at 1.22mW

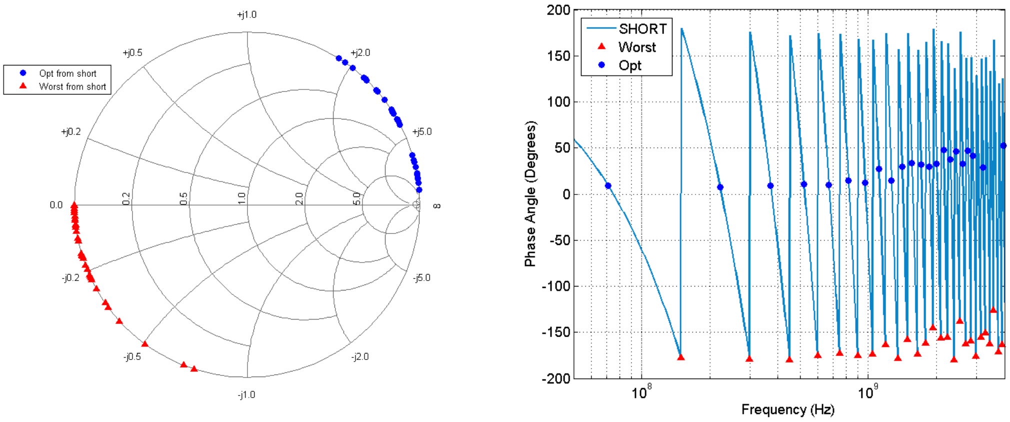

a) b)

Figure 4.12 Computed results for a R2-10SQxEBC and a VI Systems VCSEL Link at 1.22mW : a) Corresponding impedance of optimum load and worse case loads with an ideal coaxial cable from 50 MHz to 10 GHz b) Phase angle of the loads presented to the HPT, the phase angle of the optimum load is highlighted with circle and the phase angle of the worst case load is highlighted with a triangle.

The effect of a fixed 10Ω termination in a lossless coaxial cable and a lossy coaxial cable on the G_{OM} simulation is also studied. The resulting loads in the base are placed on Smith chart Figure 4.13(a). The lossy coaxial cable loads will be rotating inside the Smith chart as the frequency is swept from 50MHz to 24GHz as expected. The 10Ω fixed termination in lossless coaxial cable produces an impedance with a constant gamma and with different angles as the frequency is swept. Figure 4.13(b) shows the resulting G_{OM} for the different cases: ideal coax with short termination, ideal coax with 10Ω termination and lossy coax cable. The effects of the lossy coaxial cable is seen at the G_{OM} greater than 200MHz where the peak responses are slightly lower as compared to the lossless cable. The 10Ω terminated cable extinguishes the benefits in the peak response of the purely inductive loads. This gamma represents a realistic load but offers only a maximum peak increase of at most 5dB. This shows that more interesting loads should be located in between the fixed gamma from the 10Ω termination and the border of the Smith chart which shows purely reactive devices.

Nevertheless, using load and transmission line directly integrated to the SiGe HPT decreases the losses and so increases G_{OM} consequently.

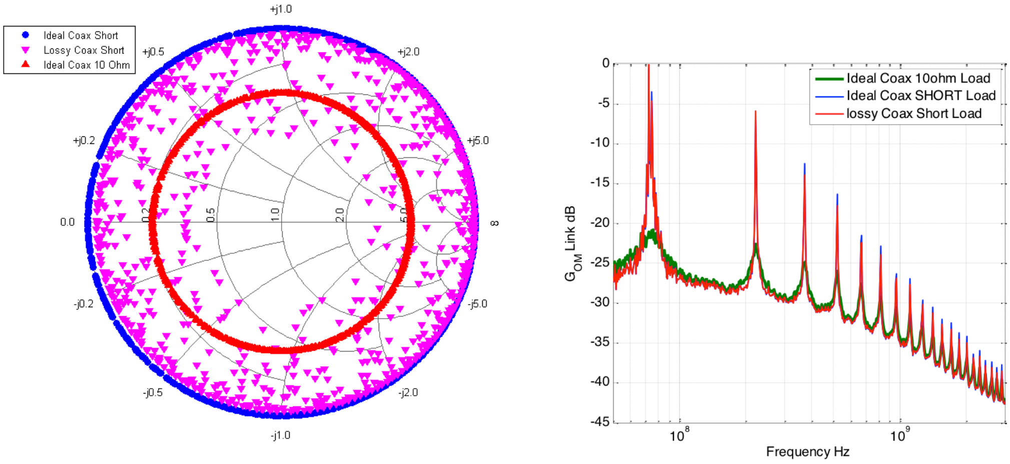

a) b)

Figure 4.13 Computed results for a for a R2-10SQxEBC HPT and a VI Systems VCSEL Link at 1.22mW of different loads in the base of the HPT by using 1m ideal coax terminated by short, 1m lossy coax terminated by short, and 1m ideal coax terminated by 10 ohm. b) G_{OM} link from different loads in the base by using 1m ideal coax terminated by short, 1m lossy coax terminated by short, and 1m ideal coax terminated by 10 ohm.

The location of the optimum and worst case loads for the 10Ω terminated coaxial cable is shown in Figure 4.14(a) in Smith chart and Figure 4.14(b), in terms of phase angle as a function of frequency. Similar with the short terminated, coaxial cable, the optimum loads which results in the peaks in the G_{OM} are inductive loads with phase angle in the range of 5°to 50°. The worse case loads, which are valleys in the G_{OM} curve, are capacitive loads with phase angles of between -170° to -130°.

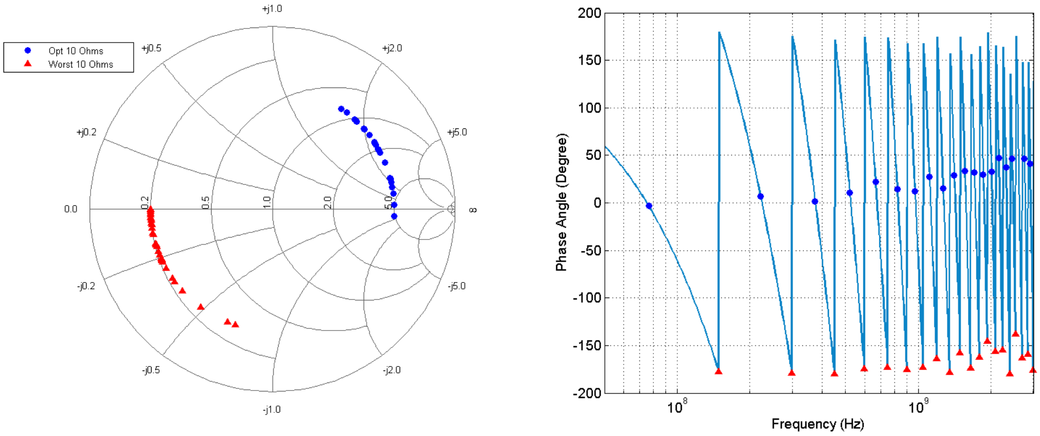

a) b)

Figure 4.14 Computed optimum and worst case loads for the 10Ω terminated cables for a for a R2-10SQxEBC HPT and a VI Systems VCSEL Link at 1.22mW a) impedance b) phase angle.

The G_{OM} peaks are higher at low frequencies, and diminish with an increased frequency. Indeed they are dependent on the frequency response of the HPT providing the initial limit in the electrical gain as could be seen in the relative H_{21} parameter of the HPT. However, the peaks of G_{OM} fall at a faster rate due to base transit time of the device where the signal flowing out of the base, comes back to the base to be amplified in the collector as seen in Figure 4.15.

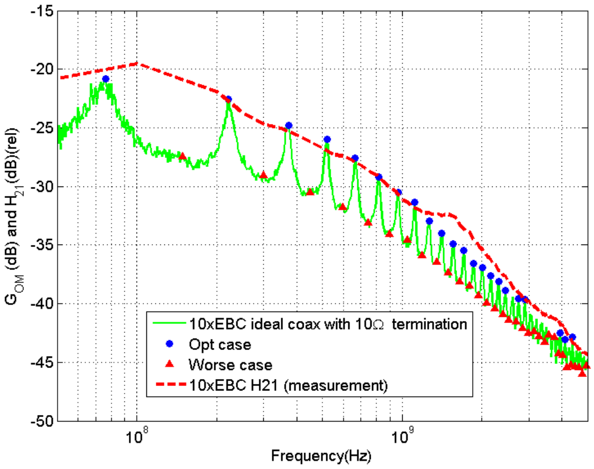

Figure 4.15 Measured H_{21} parameter frequency response (normalized to arbitrary units for comparison) and the of the G_{OM} with a 10Ω terminated ideal cable from computations for a for a R2-10SQxEBC HPT and a VI Systems VCSEL Link at 1.22mW

4.2.2 Integrated localized Base loads influence (Simulations)

Figure 4.16 shows the simulation circuit for an HPT with a single component integrated base load. The single component is a resistor, inductor and capacitor, corresponding to the previous cases (resistance, open and short circuit stubs).

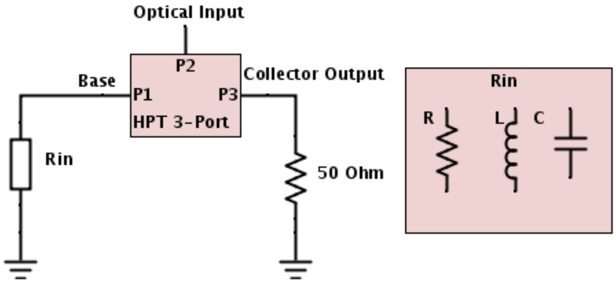

Figure 4.16 Schematic diagram of the HPT with different base loads a) resistor b)inductor and c) capacitor

A resistor can be easily integrated in the base of the HPT. The simulation results for the G_{OM} using different resistor values are shown in Figure 4.17. The 50Ω value is considered as the reference for the discussion. Lower values (10Ω and 3Ω) decrease G_{OM} at low frequencies and has no significant effect at high frequencies. A 1000Ω value is a very high impedance presented to the base of the HPT resulting to 10dB-15dB gain increase at the low frequency, the frequency response is similar corresponding to the HPT response.

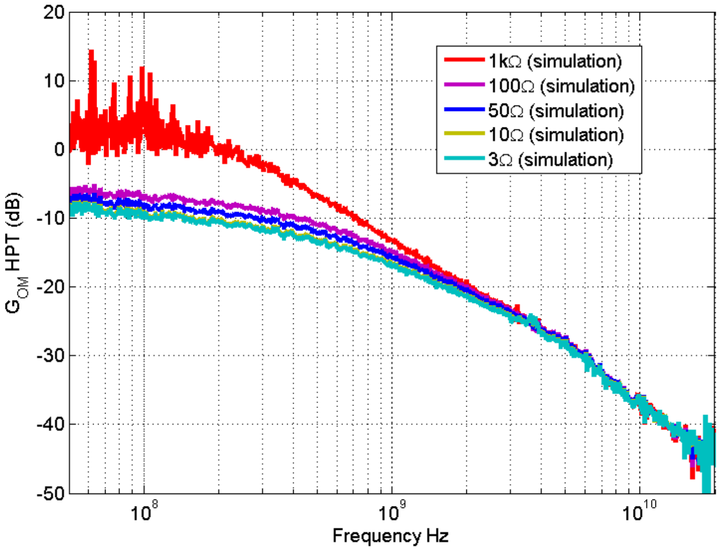

Figure 4.17 Simulation result of G_{OM} of the R2-10SQxEBC HPT and a VI Systems VCSEL Link at 1.22mW with resistor loads

The inductor load used in the simulation varies from 0.6nH up to 43nH. The upper limit on the inductor value is set by the maximum inductance available in the design kit. The inductors used in the simulation are summarized in Table 4.1. It includes its physical parameters, inductance and effective resistance. As can be seen in the table, the effective increases with the inductance value. This is due to the longer tracks that are needed to increase the number or loops to provide higher inductance value. The columns in the table indicated the metal layer of the inductor structure (MetVar),the width of metal strip that forms the spiral (WC) , is the metal spacing in between the turns(s), the number of ¼ turns (NOT) and the inner radius of the spiral (RI).

Table 4.1 Parameters of integrated inductors

Met Var	WC	S	NOT	RI	Inductance (nH)	R eff (Ω)
2-3	10	3	5	80	0.6	0.83
2-3	10	3	9	80	1.75	1.39
2-3	8	3	9	100	2.27	1.68
2-3	8	3	13	100	4.5	2.82
2-3	10	3	19	100	9.2	3.36
2-3	10	3	29	100	21.12	5.18
2-3	10	3	35	100	30.91	6.37
2-3	10	3	41	100	42.9	7.63

The frequency and phase responses of the inductor loads used in the simulation is shown in Figure 4.18, from 50MHz to 24GHz. The effect of the parasitic resistance can be seen on the S_{11} parameter, indeed for lower inductance values results in lower parasitic resistance S_{11} is placed near the edge of the Smith chart as compared to the inductance values with higher resistance values are positioned more inside the Smith chart. Because of its intrinsic resonant frequency, the inductors have capacitive response at high frequencies. This shows that the inductor models takes into consideration the inherent capacitance of the planar structure of the inductor. This is highlighted in its phase response, for example. The 43nH inductor has a zero phase crossing at around 1.5GHz while it is 2GHz for the 0.6nH inductor.

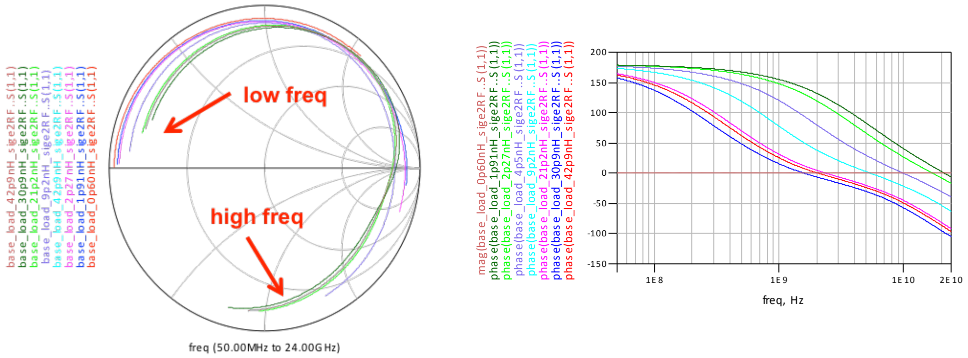

a) b)

Figure 4.18 S_{11} parameters of different inductors a) smith chart and b) phase angle.

In reference to the base load experiments on the R2-10SQxEBC HPT, an improvement in the G_{OM} response is observed when the phase angle of the base load is between 10° – 150°. A peak in the response is expected in this region as well. For the 43nH inductor, it's phase angle is 50° at 350MHz and 10° at 843MHz. In this region, an improvement in the G_{OM} of the HPT as well as a peak in response. The 4.5nH inductor has its phase angle valued at 50° at 3.3Ghz and 20° at 5.9GHz. Similarly, a peak and improvement in the G_{OM} is expected in this frequency region.

Using the 3-port model of the HPT, the G_1 term of G_{OM} of the HPT is computed for different values of the inductance that are used for the simulations. Shown in Figure 4.19 is the computed G_1 term. At low frequency (50MHz), all the inductor loads produce a G_1 term that has a negative value, decreasing G_{OM} of the HPT, this is attributed to the effective resistance of the inductor structure. For the 43nH, the G_1 term has a positive value from 350MHz up to 1.8GHz with a peak of 6.9dB at 650MHz and for the 4.5nH inductor; it has a positive value from 1.55GHz up to 7GHz and a peak at 3.4GHz. The location of peak is consistent with the initial estimates from the properties of the different inductors. So, that the opto-microwave response of the HPT can be improved using series inductor loads on to its base.

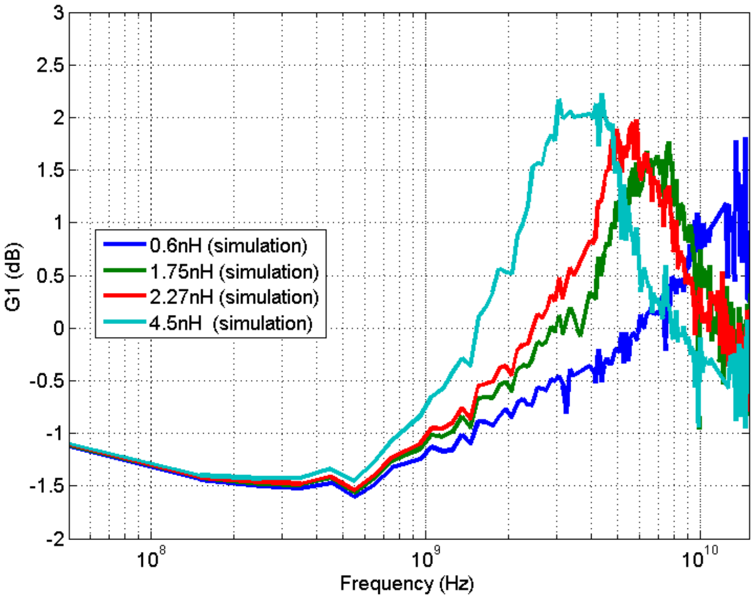

Figure 4.19 Simulated result for G_1 using the measured 3 port parameters of the HPT and a VI Systems VCSEL Link at 1.22mW with a bias of Vce =2V and Vbe = 0.85V.

Finally, the simulated G_{OM} from the different inductor base loads are presented in Figure 4.20. The effect of G_1 can be seen on G_{OM}. At low frequencies, the G_{OM} with the inductor base load has lower value compared to a 50Ω base loaded HPT. The different inductor loads produce a peak in G_{OM} when its frequency phase angle is between 10°–50°. The magnitude of this peak response is also frequency dependent due to the current gain limitations of the HPT and the transit time of the base since the peak comes from the reflected base signal.

The G_{OM} of the HPT base-loaded by a series inductor will generally have a response at low frequency that is lower due to the series resistance of the inductors. A peak occurs at the frequency where the load presented by the inductor value is in the region of the optimal loads. For the 4nH inductor this is at around 3.4GHz and for the 43nH inductor around 670MHz.

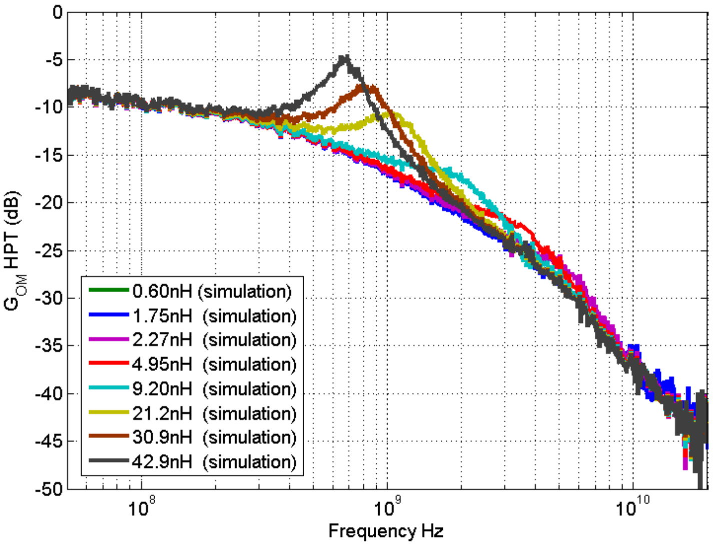

Figure 4.20 Simulation results of G_{OM} of the R2-10SQxEBC HPT and a VI Systems VCSEL Link at 1.22mW with inductor loads

Simulations were also performed to see the effect in the G_1 term of the opto-microwave gain when the base is loaded with different capacitor values. The frequency and phase response of the capacitor loads used in the simulation is shown in Figure 4.21 This response is from 50MHz up to 24GHz. It shows that at low frequencies the capacitor approaches an open circuit. The Smith chart also shows that some capacitors are moving in the inductive region at high frequencies because of their intrinsic resonance frequency. Table 4.2 shows low frequency S_{11} parameters of the capacitors.

The capacitor increases G_1 at 50 MHz then G_1 decreases sharply up to 300MHz with a minimum value of -2dB. So, the capacitor is similar to an open circuit, and the photocurrent cannot exit to the base terminal and it goes out of the collector and at a high enough frequency, the photocurrent charges up the capacitor. The G_1 response slowly increases up to 0dB in the 15GHz. Figure 4.22 shows the simulated G_1 values with the different capacitor loads. The capacitor values used showed no expected improvement in the overall opto-microwave response from 300 MHz up to 15 GHz.

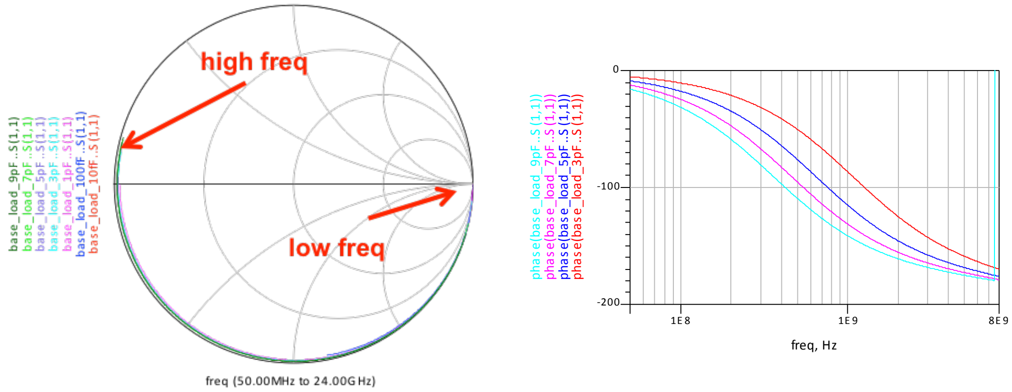

a) b)

Figure 4.21 S_{11} Parameters of different capacitors a) Smith chart and b) phase angle.

Table 4.2 Parameters of integrated capacitors

C	Impedance at 50 MHz	Magnitude_ angle
10 fF	2.69-j318000	1<-0.018
100 fF	1.55-j32000	1<-0.18
1pF	0.870-j3200	1 -1.799
3pF	0.667-j1000	1 < -5.396
5pF	0.587-j636	1 < -8.9818
7pF	0.534-j454	1< -12.55
9pF	0.501-j353	1<-16.94

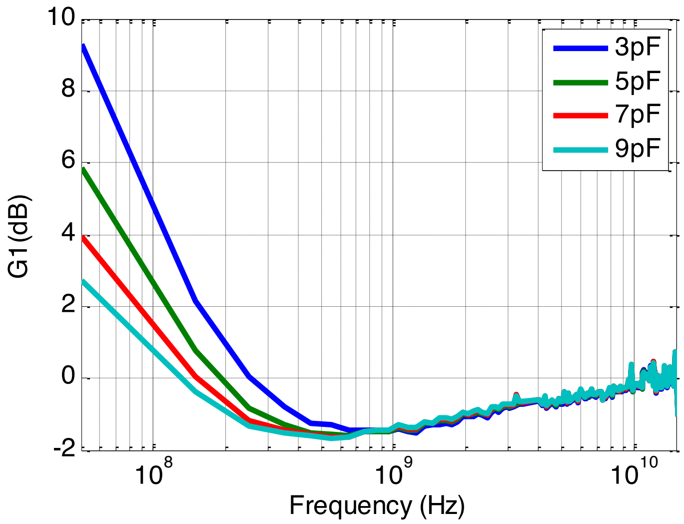

Figure 4.22 Simulated G1 term of the opto-microwave gain of the base loaded HPT, using the measured 3 port parameters of the HPT with a bias of Vce =2V and Vbe = 0.85V and an optical power of 1.22mW

Finally, the total simulated G_{OM} from the different capacitor base loads are presented in Figure 4.23. The effect of the G_1 term is seen on the total G_{OM}. At low frequencies, the G_{OM} with the capacitor base load in the HPT has very high values compared to 50Ω base loaded HPT. The different capacitor loads produce a peak in G_{OM} in the lowest frequency of measurements. The magnitude of this peak response is dependent on the capacitance value.

The G_{OM} of the HPT with different series capacitor load presents have a response at low frequency higher than the ones with the inductor loads because of the series resistance of the inductors. A peak occurs at the lowest frequency where the load presented by the capacitance has the highest low frequency impedance. However, at high frequencies, the series capacitor acts as a short circuit and does not reflect back the photocurrent that exits the base.

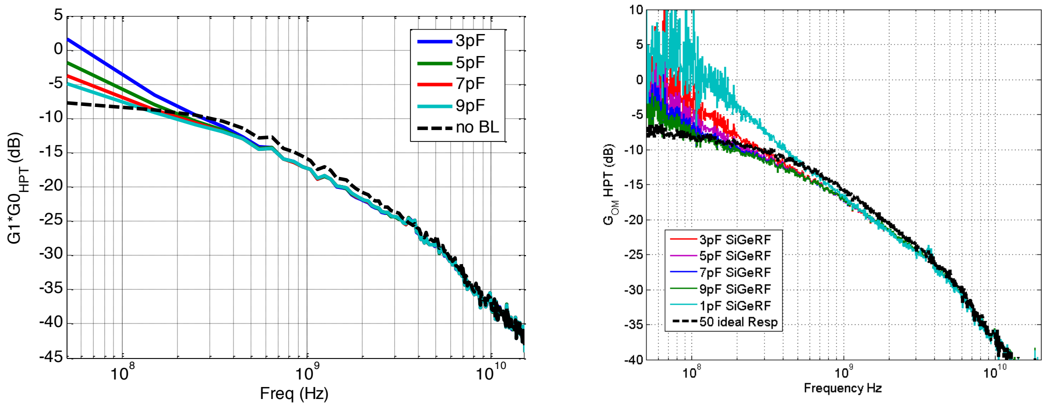

a) b)

Figure 4.23 Simulation of G_1*G_0 (dB) of the R2-10SQxEBC HPT and a VI Systems VCSEL Link at 1.22mW with capacitor base loads

4.2.3 Integrated localized Base loads influence: fabricated circuits

The final fabricated HPT with different base loads include a 10pF bypass capacitor connected to the pad that is used to bias the base of the HPT. The resulting schematic diagram for the inductor and capacitor loaded HPT is shown in Figure 4.24. The final layout of the HPT, loaded with a 1.91nH inductor is shown in Figure 4.25(a) the two GSG pads bias the base and the collector of the HPT and the RF access.

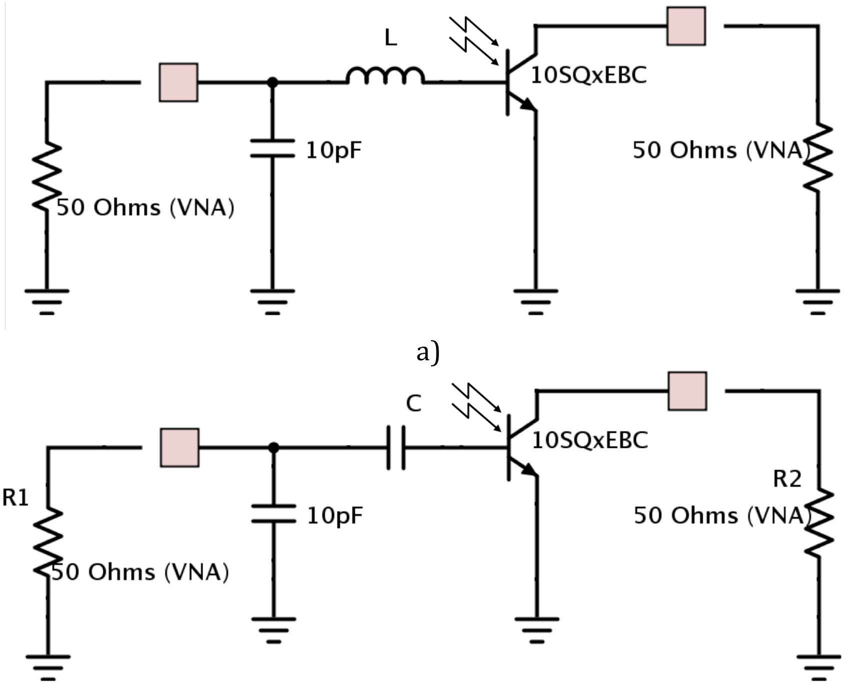

b)

Figure 4.24 Final schematic of the HPT with different base loads a) inductor b) capacitor.

These structures are measured by a 4 port VNA from Rhode and Schwarz R&SZVA24. Thus each port is ensured to be loaded with 50Ω.

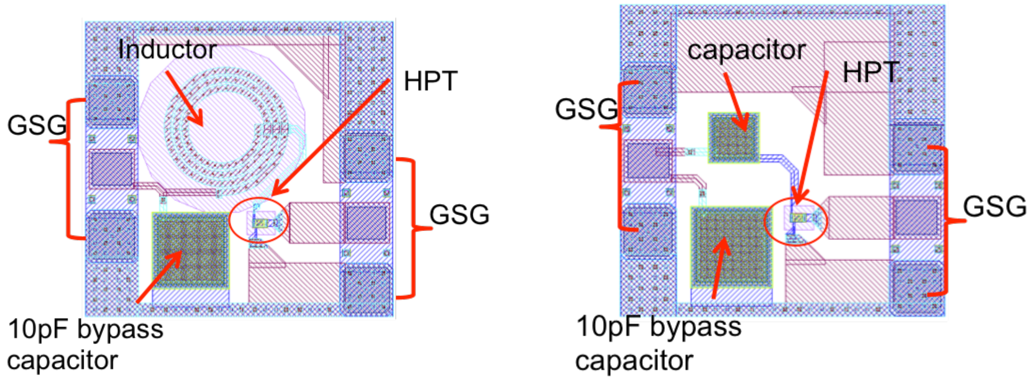

a) b)

Figure 4.25 Layout view of the HPT with a) series inductor base load b) a series capacitor base load.

The fabricated HPTs with integrated inductor and capacitor loads were measured using an opto-microwave measurement bench set-up described earlier in Chapter 2. The measured link gain at 50MHz, is composed of the Laser and HPT combination as a function of Vbe for the different HPTs with different inductor loads as well as the HPT without the integrated load is presented in Figure 4.26. This case without load is actually the direct connection of the base to the 50Ω load of the VNA.

At 50 MHz, all the HPTs with the inductor loads have lower gain as compared to the HPT with no integrated base load. The worst-case gain decreases by of 1.5dB in the PD mode of operation and 2.6dB in the HPT mode of operation. This low gain at low frequency is observed in simulations, due to the effective resistance of the inductor as seen in Figure 4.20.

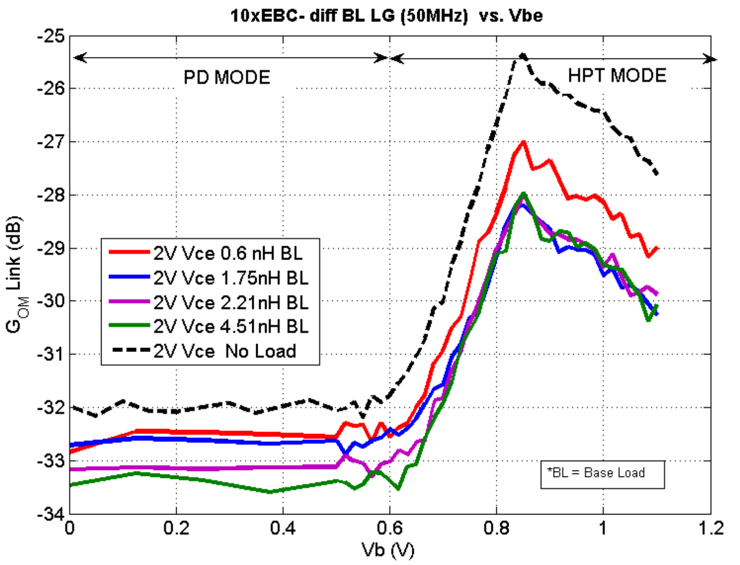

Figure 4.26 G_{OM} link (50 MHz) vs. Vbe of the 10SQxEBC HPT with different inductor series base loads (no load = 50Ω).

The peak response appeared at the bias point Vce =2V and Vbe = 0.85, whatever the HPT and inductor values. The extracted G_{OM} of the HPT and inductor loaded HPT is shown in Figure 4.27. The inductor values of 0.6nH, 1.75nH and 2.21nH are expected to have a peak at higher frequencies near the 11GHz range. Their effect is not so visible because of the added noise in measurements in that frequency range.

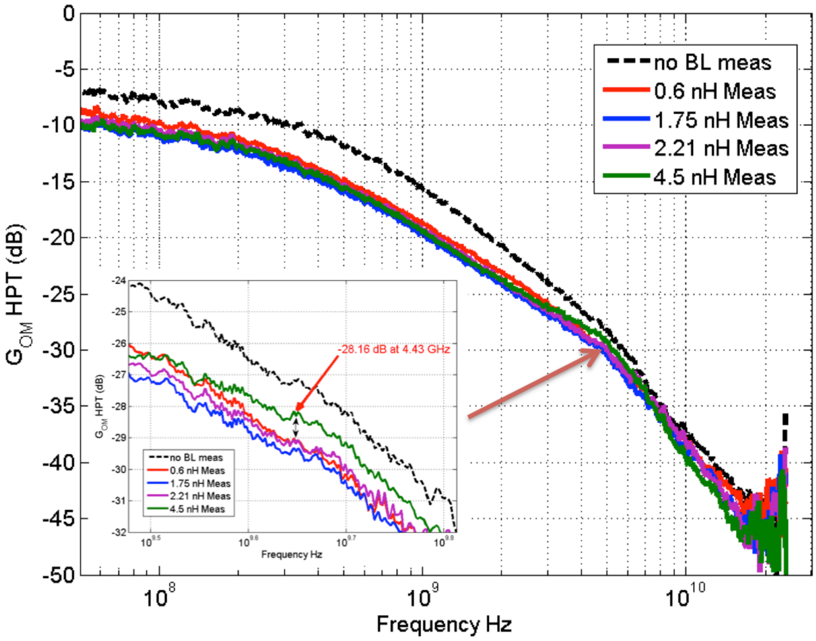

Figure 4.27 Extracted absolute G_{OM} of the HPT for different inductor base loads (Vce =2V and Vbe = 0.85V) and the optical power is 1.22 mW (Measurements). The inset is a region at 5GHz

The measured link gain at 50 MHz, which is composed of the laser illuminating the HPT, is presented as a function of Vbe for the different HPTs with different capacitor loads as well as the HPT without the integrated load in Figure 4.28. At 50MHz, the combination of capacitors and HPT has higher gain compared to the HPT with no integrated base load. As there is no dependence of the supplied Vbe voltages, the HPT is operating in a 2T-HPT configuration due to the series capacitor load. The measured responses are strongly dependent on the capacitor values increasing the gain value with a capacitance decrease at 50MHz.

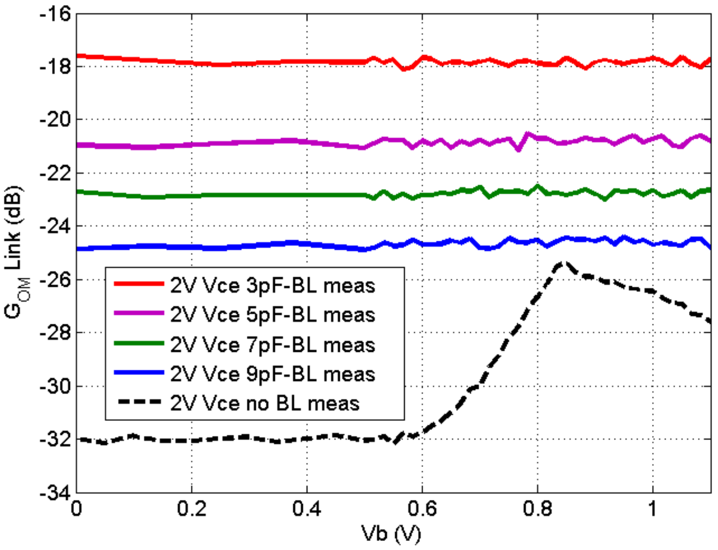

Figure 4.28 G_{OM} Link (50 MHz) vs. Vbe of the 10SQxEBC HPT with different capacitor series base loads and the VI Systems VCSEL with 1.22mW(Measurements)

Finally, the G_{OM} frequency response of the HPT with different capacitor loads is presented in Figure 4.29. The 3pF base load exhibits the highest G_{OM} at 0dB while the 9pF load has lower G_{OM} of -8dB. The cut-off frequency of the G_{OM} response is higher for the HPT without any load.

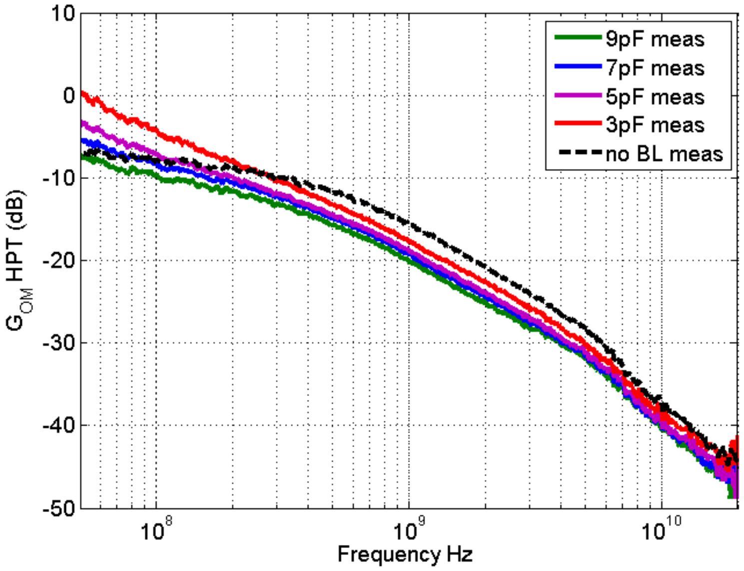

Figure 4.29 Extracted absolute G_{OM} of the HPT from opto-microwave measurements for different capacitor base loads (Vce =2V and Vbe = 0.85V) and the optical power is 1.22mW

It has been shown in this section that matching improvement on the base of the SiGe can provide an improvement of up to 25dB in the G_{OM} of a 10SQxEBC HPT (R2-10SQxEBC) at low frequency. This phenomenon has a cutoff frequency related to the H_{21} frequency limit and may decrease even further. In order to practically implement matching networks simple passive devices are considered. It has been seen and confirmed that capacitors helps to improve the opto-microwave response at low frequencies. Inductors simulated by taking into account the realistic model of the available integrated inductors from the SiGe2RF technology, may increase the gain by up to 10dB at 0.5-1GHz. In any case, the gain improvement is not more than 5dB above 2GHz in the case of the R2-10SQxEBC, event with an ideal optimum load.

The simulations and measurements show that resistor and capacitor loads is the best scenario to improve the low frequency response, while the inductors improve the gain response at higher frequencies. Integrated base load circuits could be designed to provide improvement in the operational bandwidth of the HPT in order to design a RoF system application.

4.3 HPT-HBT Pair Topologies

We present circuits that are composed of a phototransistor (HPT) and transistor (HBT) . These circuits are derived from classical transistor pair configurations with improved performance in gain, input impedance and cutoff frequency. These transistor pair configurations are: common emitter – common base (CE-CB), common emitter – common emitter (CE-CE), and common collector – common emitter (CC-CE) with each having a particular improvement in electrical and opto-microwave performances. The HPT-HBT pair is implemented by replacing the first transistor with a phototransistor in the classic transistor pair configurations. The performance of the HPT and HBT pair is characterized using opto-microwave measurements, which are compared to the OM measurement of a single R2-10SQxEBC HPT under the same illumination condition. Figure 4.30(a) shows the measured low frequency (50 MHz) link gain in dB vs. the supplied Vbe. The measurements were made with different values of Vce : 1V, 1.5V, and 2V. Figure 4.30(b) is the G_{OM} versus frequency measurement at the bias point with the highest measured low frequency G_{OM}.

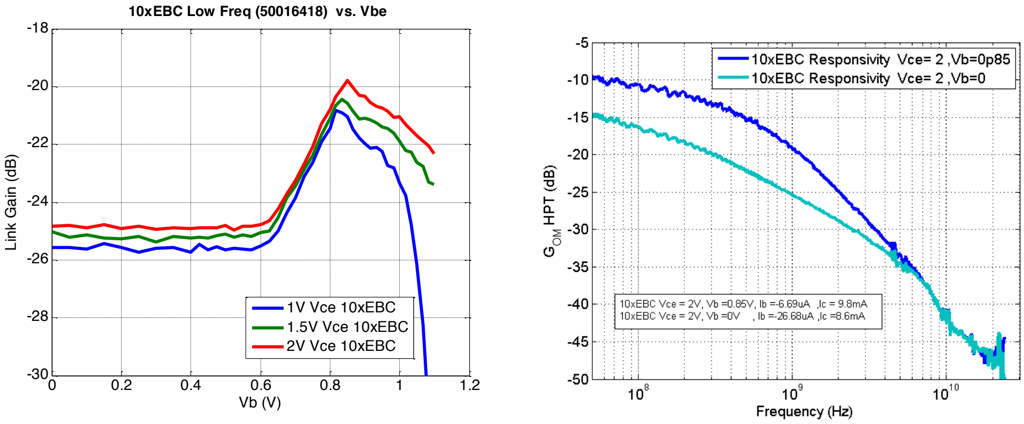

a) b)

Figure 4.30 Opto-microwave gain of the VI system VSCEL link with a) a single HPT 10SQxEBC at 50MHz at different Vce values (1V, 1.5V, 2V) and b) G_{OM} link vs. Frequency at Vce = 2V ,Vb = 0.85V and at Vce = 2V, and Vbe = 0V

Table 4.3 shows a summary of the measured G_{OM} of the R2-10SQxEBC HPT under different bias conditions. It shows a 5dB difference in G_{OM} between the HPT mode and PD mode of operation.

Table 4.3 Summary of G_{OM} Link (50 MHz) at different bias points

Vce(V)	Vb (V)	Link Gain (dB)	G_{OM} (dB)
1	0	-25.58	-15.32
1	0.8167	-20.81	-10.67
1.5	0	-25.02	-14.86
1.5	0.833	-20.44	-10.1
2	0	-24.84	-14.7
2	0.85	-19.79	-9.6

The electrical gummel properties from simulation of an HBT with a size of 30x0.5µm² are presented in Figure 4.31. These simulations are base on the process design kit from Telefunken. This will be used in the discussion of the operation of the HPT- HBT pair topologies

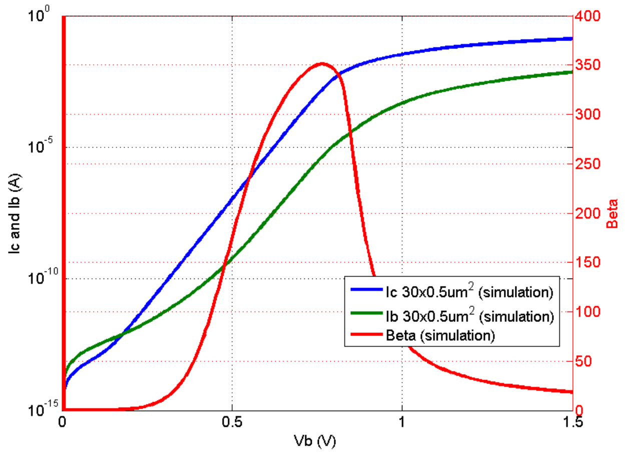

Figure 4.31 Gummel characteristics of a 30x0.5µm² HBT.

4.3.1 Common Emitter HPT -Common Base HBT (CE-CB) Topology

The two-transistor amplifier combination of a common emitter (CE) input stage and a common base (CB) output stage is envisioned to overcome the performance limitation of either CE or CB configurations. A CE amplifier offers moderately high input impedance (kΩ), high voltage gain and high output impedance, The CB amplifier on the other hand offers wider bandwidth. However, its low input impedance is a limitation for many applications. To mitigate this limitation on CB amplifiers, a low gain CE stage is placed before the CB stage. This results in a cascode amplifier configuration with a high voltage gain, a high input impedance, a wide bandwidth and a high output impedance. The current gain in the cascode is β since the current gain in a CB is 1 and the current gain in CE is β

The key element of the cascode amplifier's wider bandwidth is the CB amplifier output stage, which has better high frequency response. The CB amplifier is not subject to the Miller effect because the grounded base shields the collector signal from being fed back to the emitter input. However, in the CE configuration, the collector output signal is out of phase with the input at the base. The collector signal, capacitively coupled back opposes the base signal. Moreover, the collector feedback is (1-A_V) times larger than the base signal. Where (A_v) is the voltage gain. Thus, the small CB capacitance appears (1-A_V) times larger than its actual value. This capacitive gain reducing feedback increases with frequency, reducing the high frequency response of a CE amplifier.

In order to minimize the miller effect on the CE amplifier, its voltage gain (A_V) should be minimized, or ideally (A_V = -1) such that ,the resulting equivalent miller capacitance is only 2•CB. Since the gain of a CE amplifier is proportional to R_C/R_{EE} where R_C is the collector load and REE is the internal emitter resistance, a gain of 1 is achieved when the load to the CE amplifier is also R_{EE}. R_{EE} is the input impedance presented by a CB amplifier. The R_{EE} of the CE amplifier and the R_{EE} of the CB amplifier will have the same value if they are matched. The resulting cascode amplifier will have a CE stage with a high input impedance, a voltage gain of 1 or 0dB, with a maximize frequency response due to the reduction of the miller effect. Thus the HPT+HBT cascode with a 10SQxEBC HPT, the HPT is chosen with a total emitter size which is similar, i.e., 30x0.5µm^2 The CB stage provides a voltage gain proportional to R_C/R_{EE}, and high frequency response with high output impedance..

The CE HPT–CB HBT pair is implemented by configuring the 10SQxEBC HPT in a common emitter configuration, and the 30x0.5µm^2 HBT is configured as a common base. Figure 4.32a shows the schematic representation of the HPT-HBT pair. The emitter of the HPT is connected to the ground, the base of the HPT is connected to the signal pin of the GSG pad to provide the base bias to the HPT Vb_{HPT} and the collector of the HPT is connected to the emitter of the HBT. The collector of the HBT is connected to the signal pin of the second GSG pad, this provides the collector bias Vc_{HBT}, and output signal is also taken from the collector. The base bias of the HBT comes from the DC pad connected to the HBT base Vext. The final layout of the CE HPT- CB HBT pair is shown in Figure 4.32b.

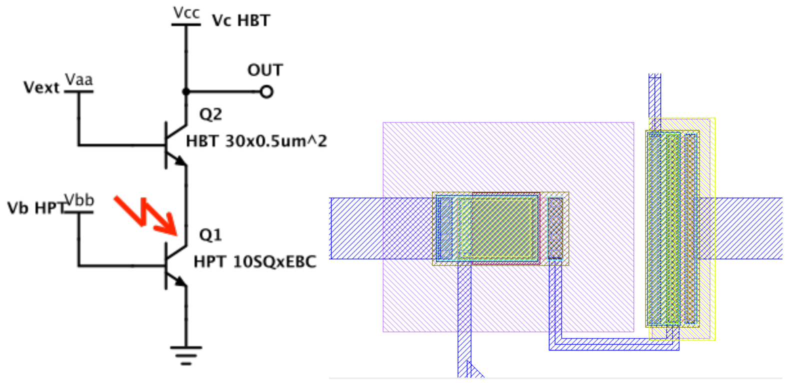

a) b)

Figure 4.32 Common emitter HPT and Common base HBT topology a)schematic representation b) layout view

Under proper biasing conditions, the small signal analysis of the HPT based cascode is a combination of the Common Emitter and Common Base small signal models

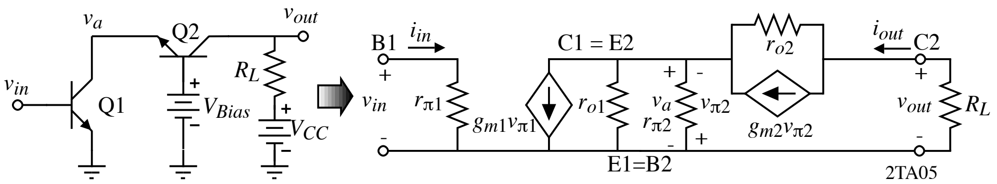

Figure 4.33 CE-CB circuit and circuit model in DC analysis

$$If\ \beta_1\ \approx\ \beta_2\ and\ r_0\ can\ be\ neglected, then:$$

$$R_{in} = r_{\pi1}$$

$$R_{out} = \beta_2 r_{o2}$$

$$\frac{v_{out}}{v_{in}} = \left(\frac{v_{out}}{v_a}\right)\left(\frac{v_a}{v_{in}}\right) = (g_{m2}R_L)\left(\frac{r_{\pi2}}{1+\beta_{o2}}\frac{-\beta_{o1}}{r_{\pi1}}\right) \approx (g_{m2}R_L)(-1) = -g_{m2}R_L$$

$$\frac{i_{out}}{i_{in}} = \alpha_2\beta_1$$

the advantage of the cascode is the gain of Q1 equals to -1 and therefore the Miller capacitor Cμ is not translated to the base-emitter as a large capacitor.

The small-signal model of the CE-CB pair with miller effect applied to $C_{\mu1}$ assuming $v_a/v_{in} = -1$ is shown Figure 4.34 .

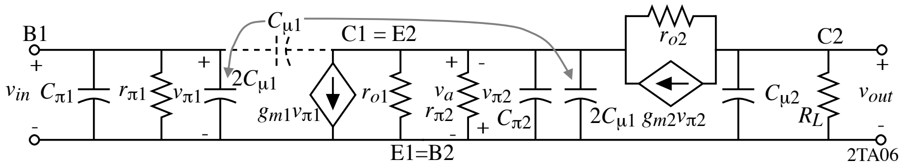

Figure 4.34 Small signal model of CE-CB pair in RF analysis

The cutoff frequency of the CE-CB is computed using the equations presented:

$$f_{-3dB} \approx \frac{1}{2\pi\Sigma(Open\ circuit\ time\ constants)} \approx \frac{1}{2\pi(\tau_{in}+\tau_{interstage}+\tau_{out})}$$

$$\tau_{in} = r_{\pi1}(C_{\pi1}+2C_{\mu1}),\tau_{interstage} = \frac{r_{\pi2}}{1+\beta_{o2}}(C_{\pi1}+2C_{\mu1}),and\ \tau_{out} = R_L C_{\mu2}$$

$$therefore:$$

$$f_{-3dB} \approx \frac{1}{2\pi\left(r_{\pi1}\left(C_{\pi1}+2C_{\mu1}\right)+\frac{r_{\pi2}}{1+\beta_{o2}}\left(C_{\pi1}+2C_{\mu1}\right)+R_L C_{\mu2}\right)} \approx \frac{1}{2\pi R_L C_{\mu2}}$$

The computations show that the cutoff frequency is dependent on R_L and $C_{\mu2.}$

4.3.1.1 Static characteristics under illumination

The operation of the CE HPT- CB HBT circuit under illumination is explained by using the measured collector current of the HBT Ic_{HBT} and the base current of the HPT Ib_{HPT} as a function of supplied HPT base voltage Vb_{HPT} at a fixed value for the HBT collector voltage Vc_{HBT} and Vext of the HPT. Figure 4.35 shows the circuit currents Ic_{HBT} and the absolute value of Ib_{HPT} in logarithmic scale as a function of Vb_{HPT} at Vc_{HBT} = 2V and Vext = 1.5V.

The operation of the circuit can be divided into two regions based on the value of Ib_{HPT}. In region 1 (Vbe = 0V -0.62V), the values of Ib_{HPT} and Ic_{HBT} are constant. At the bias point where Vbe = 0V, The measured Ib_{HPT} is -25.17µA and Ic_{HBT} = 681µA. The negative Ib_{HPT} indicates that the generated photocurrent in the base dominates the base current that is initially set by the Vb_{HPT} of 0V , Vext of 1.5V and Vc_{HBT} = 2V. In this bias condition, there will be a collector current in the HPT that will be flowing from the collector to the emitter of the HPT. Given that the Vext of 1.5V is applied to the base of the HBT, the measured collector current in the HBT Ic_{HBT} will have a value that will be similar to the Ie_{HBT} and from the circuit configuration Ie_{HBT} is equal to Ic_{HPT}. The measured HBT collector current remains constant as Vb_{HPT} is increased until Vb_{HPT} = 0.62V.

In region 2(Vbe >0.65), the external bias in Vbe influences the measured Ib_{HPT} and Ic_{HBT}. The measured Ib_{HPT} starts to increase with Vbe.. The notch observed in the Ib_{HPT} represents the change of its polarity and that the bias currents dominate the measured Ib_{HPT}. The measured Ic_{HBT} also starts to increase and at the Vbe value where the measured Ib_{HPT} has a positive value, the Ic_{HBT} starts to saturate. This means that the HBT is in the high bias region of operation and the high injection effects are present.

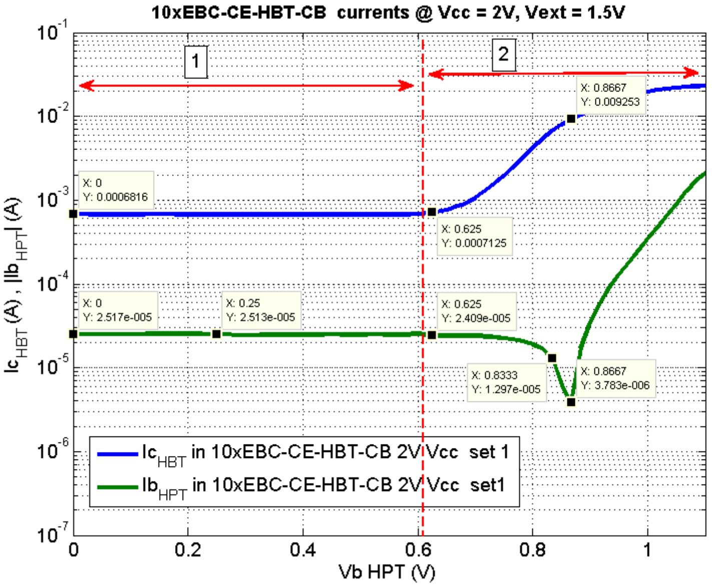

Figure 4.35 Measured currents in the CE HPT – CB HBT circuit with Vc_{HBT}=2V, Vext = 1.5V under illuminated conditions with Popt = 2.44mW

The external voltage Vext has a significant effect in the measured Ic_{HBT} are shown in Figure 4.36. Vext sets the voltage bias across the collector and base of the HBT Vcb_{HBT}. This also sets the voltage across the Vbe_{HBT} and the Vce_{HPT}. Vext has a value of 1.5V shown in Figure 4.35. A Vext of 0.9V in comparison with a Vext of 1.5V results in lower Ib_{HPT} values in region 1 and higher Ib_{HPT} values in region 2 with the notch appearing earlier at 0.8V. The resulting Ic_{HBT} in region 1 has slightly lower valuesand in region 2, the Ic_{HBT} increases in value as up to the location of the notch Ib_{HPT}. As Vb_{HPT} increases further, this causes the HPT to be operated in the high current region resulting in the decreasing value of Ic_{HBT}. A Vext of 2V results in higher Ic_{HBT} in both regions.

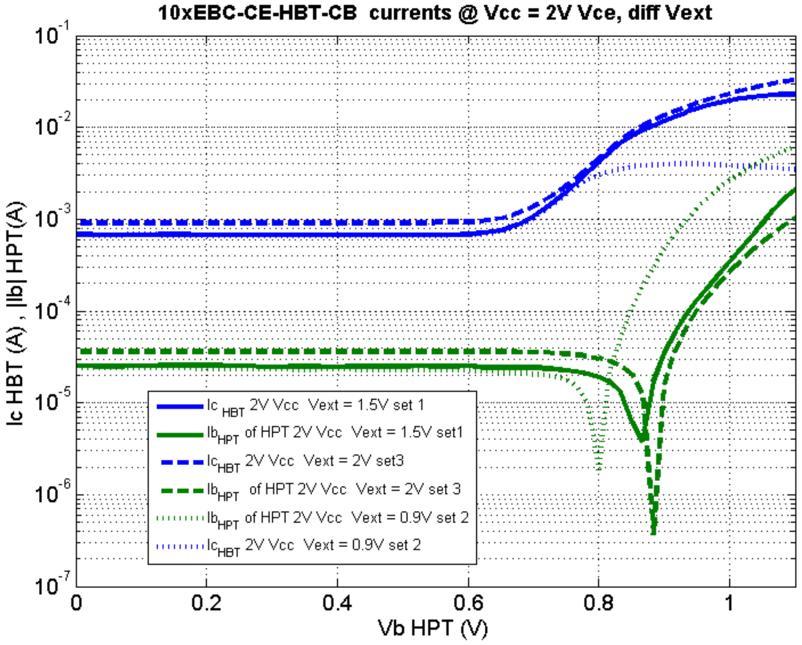

Figure 4.36 Measured currents in the CE HPT – CB HBT circuit with Vcc=2V, Vext = 0.9V, 1.5V and 2V under illuminated condition. with Popt = 2.44mW

4.3.1.2 Opto microwave response

Under the appropriate bias condition, the HPT in the common emitter configuration detects the modulated optical beam that illuminates it. The detected modulated signal is then fed to the emitter of an HBT, which is configured as a common base amplifier. The common base configuration does not suffer from Miller effect. This results in a total gain that could be similar or slightly higher than the single HPT common emitter stage and a cutoff frequency that is higher than the single common emitter HPT. Figure 4.37 shows the measured low frequency G_{OM} Link when Vcc = 2V at different Vext values (0.9V, 1.5V and 2V) as a function of supplied Vb_{HPT}. The single 10SQxEBC HPT low frequency G_{OM} is also included to provide a base line measurement. The G_{OM} Link of the single HPT in PD mode region (Vb = 0) is -24.84 dB and peak value of -19.79 dB in the HPT mode region(Vb = 0.85V). This corresponds to a G_{OPT} of 5dB. With the cascode HPT structure, a photodiode mode and phototransistor mode are also dissociated versus Vbe_{HPT} value, as shown in Figure 4.37

The G_{OM} Link response of the CE HPT- CB HBT pair thus shows that:

1. at Vext = 0.9V, the PD mode response is -28.84dB and the peak value in the HPT mode is -26.62dB corresponding to a G_{OPT} of 2.22dB. The low measured response is due to the low value in Vext which forces the early onset of the high injection operation of the HPT.

2. at Vext = 1.5V the PD mode response is -27.45dB and the peak value in the HPT mode is -21.45dB. Both values are lower as compared to the a single HPT which indicates that a Vext value of 1.5V sets the HPT to a lower bias point. A higher G_{OPT} of 6dB is however demonstrated that shows that the HPT pair exhibits higher gain.
3. at Vext = 2V, the PD mode response is similar to the single HPT indicating that the HPT in the pair is in the same bias region. The peak value in the HPT mode is -18.5dB resulting to a G_{OPT} of 6.35dB, thus improved slightly further with the gain of the CB HBT.

The optimum response in term of the low frequency G_{OM} link for the HPT CE – HPT CB is achieved with the bias of Vcc = 2V, Vext = 2V and Vb = 0.83V.

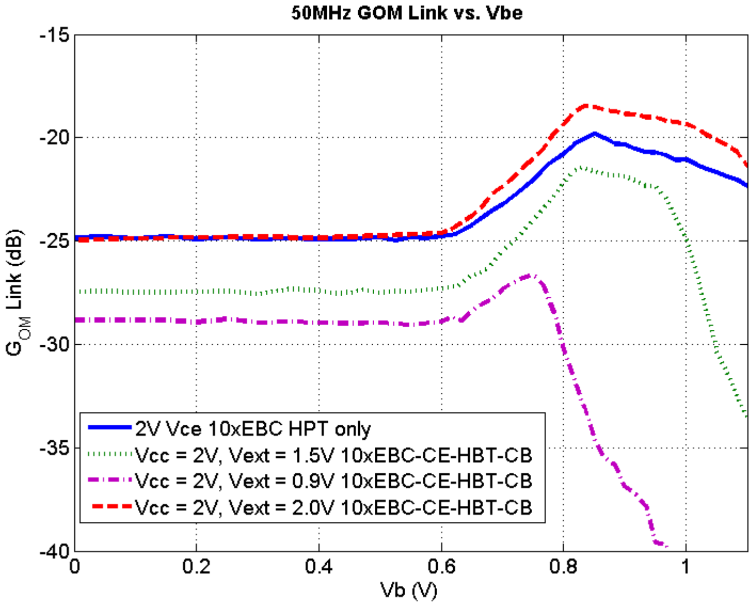

Figure 4.37 G_{OM} vs. Vbe at different values of Vext for the 10xEBC-CE-HBT CB plus VI Systems VSCEL at Vcc = 2V and P_{OPT} = 1.22mW(Measurement)

Figure 4.38 shows the opto-microwave cutoff frequency $f_{-3dB\ OM}$ at a given Vc_{HPT} value of 2V. The single R2-10SQxEBC HPT cutoff frequency curve is also included. It has a peak cutoff frequency of 275 MHz at a bias condition of 2V Vce, 0.83V Vbe. The CE HPT - CB HBT shows improved frequency response at with a peak value of 344 MHz for Vb_{HPT} 0.83V and Vext 2V.

The figure is also separated in 3 regions: region 1 (Vbe_{HPT} < 0.6V) where the cutoff frequency is constant and is related to the PD mode; region 2 (0.6V < Ve_{HPT}< 0.85V) for which the cutoff frequency increases, and ; region 3 (Vbe_{HPT} > 0.85V) where the cutoff frequency decreases drastically.

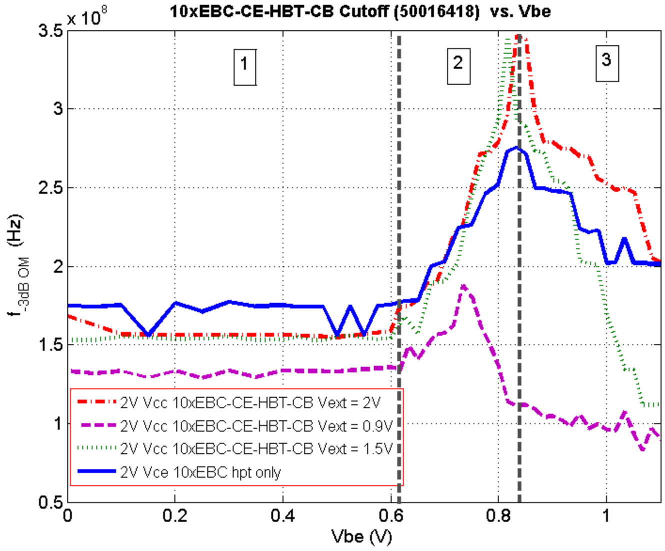

Figure 4.38 Opto-microwave gain -3dB cutoff frequency of the HPT CE- HBT CB vs. Vbe at different Vext (Measurement) at Vcc = 2V and 1.22mW P_{OPT}

Figure 4.39 shows the extracted HPT G_{OM} vs frequency response of the HPT-HBT pair in the biasing condition with the highest extracted opto microwave response from the different supplied Vext. Table 4.4 shows the summary of the CE HPT – CB HPT pair of G_{OM} and the cutoff frequency at different bias points, and provides with the value the indeed maximizes the opto-microwave cutoff frequency.

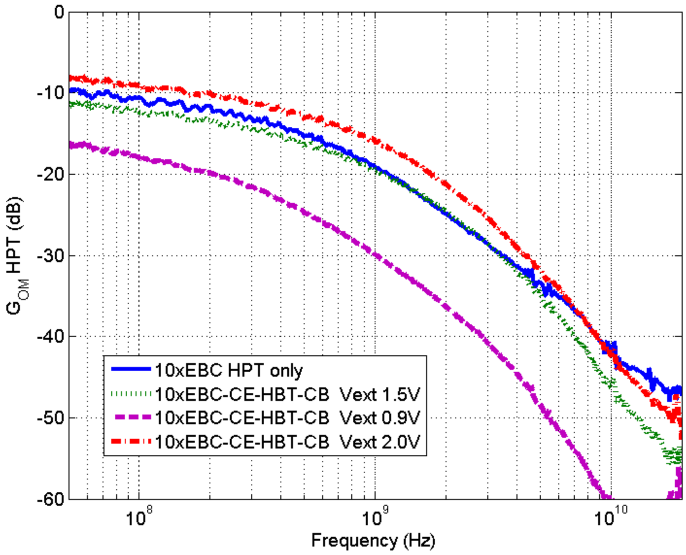

Figure 4.39 Extracted absolute G_{OM} of the HPT circuits (Measurements) Vce =2V and optimumVb_{hpt} biasing point that maximizes f_{-3dB_OM} as given in Table 4.4

Table 4.4 Summary of the opto-microwave performance of the CE HPT-CB HBT pair at maximum opto-microwave cutoff frequency and Vcc = 2V.

Structure	Vc (V)	Ic_{HBT} (mA)	Vb_{HPT} (V)	Ib_{HPT} (uA)	Vext (V)	G_{OM} HPT	Cutoff (MHz)
10xEBC	2	7.76	0.83	-12.11	---	-9.6	275.6
HPT CE-HBT CB	2	7.33	0.833	-25.05	2V	-8.22	344.8
HPT CE -HBT CB	2	5.4	0.817	-16.93	1.5V	-11.35	341.9
HPT CE -HBT CB	2	1.85	0.733	-17.88	0.9v	-16.35	187.8

The CE HPT- CB HBT pair provided a 1.4dB improvement in the extracted G_{OM} and an increase of 25% in the -3dB cutoff frequency of the opto-microwave link as compared to a single HPT structure with the same sized HPT in the same illumination condition..

4.3.2 Direct coupled Common Emitter HPT and Common Emitter HBT topology (CE-CE)

A cascaded common emitter amplifier is typically used when a very high voltage gain is required. The gain equals to the product of the voltage gain of the individual stages. A main disadvantage of this architecture is its low cutoff frequency that is influenced by the Miller capacitance at each stage. When capacitive coupling is used to couple the two stages this further affects the frequency response of the circuit. However, directly coupling the two common emitter stages avoids the degradation of the frequency response since no capacitor is used between the stages. Biasing the two common emitter stages then becomes a challenge since the bias at the first stage collector is shared with the base of the second stage. This may present another problem such that the output current of the 1st stage attacks the base of the 2nd stage thus causing saturation.

An implementation of a direct coupled common emitter HPT - common emitter HBT pair is shown in Figure 4.40a The 10xEBC HPT is configured as a common emitter and its output is directly connected to the input of a $30x0.5\mu m^2$ common emitter HBT. The base of the HPT is connected to a GSG pad to provide Vb_{HPT}. The emitter of the HPT is connected to ground and the collector of the HPT is directly connected to the base of the HBT. The HBT collector is connected to another GSG pad as an access to provide Vc_{HBT} bias and to measure the output signal. A DC pad is connected to the collector of the HPT and the base of the HBT provides the bias for both devices. Figure 4.40 b) shows the layout view of the CE HPT – CE HBT module.

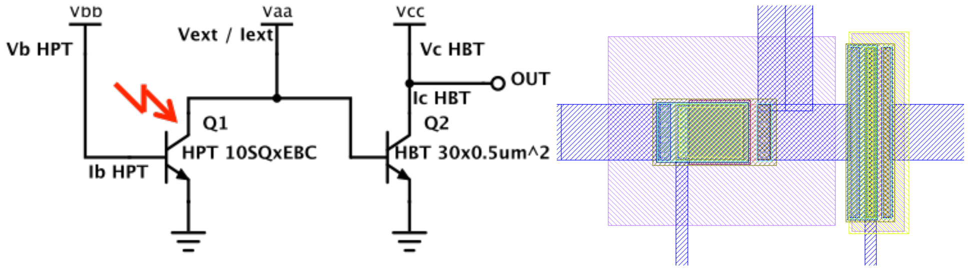

a) b)

Figure 4.40 Common emitter HPT -common Emitter HBT topology (a) schematic representation (b) layout view

In the direct coupled CE HPT – CE HBT pair, the two stages are not DC isolated. The first stage essentially acts as a bias circuit for the second stage. Since there is no DC isolation, the AC output of the first stage is superimposed on the DC operating point of the second stage. The absence of the coupling capacitors improves the frequency response of the pair.

The operation of this HPT-HBT pair requires careful consideration of the bias points of the two stages. In order to maximize the achievable gain of this configuration, both devices should be in the forward active mode and no device should be in cutoff mode. However, with the collector bias and the base bias of the HPT being tied up to one source, it will be difficult to put the two stages in the optimum bias point at the same time.

There are different scenarios that can be considered regarding the biasing of this circuit.

One critical voltage is Vext or Iext that should be chosen such that the supplied Vb_{HBT} and Vce_{HPT} will simultaneously put both the devices in the forward active mode of operation. This will result in a total gain which is a product of the individual gain stages as set by the biasing point.

4.3.2.1 Static characteristics: Operation under illumination

The operation of the CE HPT - CE HBT under illumination presents another complicated situation in the proper selection of the bias points. The DC power of the optical source shifts the bias of the first stage HPT which then affects the bias of the second stage due to its direct coupling. The DC operation of this circuit under illuminated conditions will be discussed using the measured currents of the circuit. The voltage in the base of the HPT Vb_{HBT} is swept from 0V – 1V. The voltage across the collector of the HBT Vc_{HBT} is set at different values of 1V, 1.5V, 2V and 2.5V. The external bias provided in the collector of the HPT and the base of the HBT is a current source with values of 4mA resulting to a 2V voltage drop at Vb_{HPT} = 0V and a 3mA value resulting to a 1.5V voltage drop Vb_{HPT} = 0V. Figure 4.41 shows the measured currents under illuminated conditions. The collector current of the HBT Ic_{HBT} and the base current of the HPT Ib_{HPT} are shown as a function of the supplied Vb_{HPT} from 0V-1V at Vc_{HPT} = 2V with Iext is 4mA.

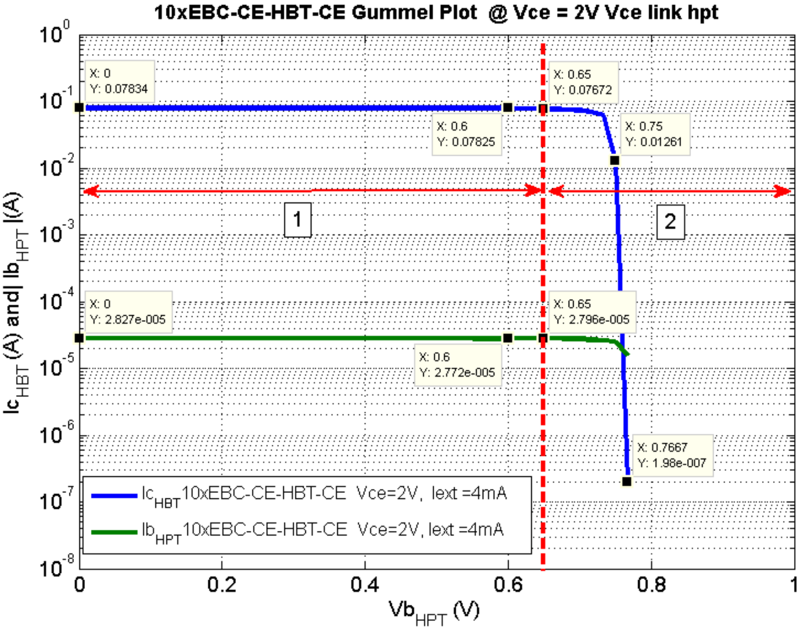

Figure 4.41 Measured currents in the CE HPT – CE HBT circuit with Vc_{HBT}=2V, Iext = 4mA under illuminated conditons with Popt = 2.44mW

A discussion is started depending on the Vb_{HPT} value:

At Vb_{HPT} = 0V

The measured Ib_{HBT} is -28µA and Ic_{HBT} = 78mA. The negative value of Ib_{HPT} indicates the presence of the base photocurrent with a higher value than that of the base current as set by the initial external bias. An Ic_{HPT} will be present due to the illumination. The illuminated Gummel measurements of this HPT in common emitter configuration shows that the Ic_{HPT} will be few hundreds of µA. This is seen in Figure 3.17. The HPT is therefore in the PD mode of operation. The current supplied by the Iext will be divided between Ic_{HPT} and Ib_{HBT} with the resulting Ib_{HBT} in the mA range which then results to a measured Ic_{HBT} of 78mA. The Gummel characteristics of HBT shows that at this level of

Ic_{HBT} is in the very high current region of operation of the device. Given this biasing values, and taking into consideration the DC power from the illumination, both the devices are in forward active mode with the HPT in PD mode operation and the HBT operating in the high current region.

At $Vb_{HPT} > 0.6V$

The HPT base current Ib_{HPT} starts to increase in value, which also results to an increase in the HPT collector Ic_{HPT} value. As Ic_{HPT} increases, the bias to the base of the HBT decreases. It can be seen in the decrease in the measured collector current in the base of the HBT Ic_{HBT}. Referring the Gummel plot of the HBT in Figure 4.31, the biasing point of the HPT moves from the high current region back to the linear region. As Vb_{HPT} increases, there is a point where in the collector current in the HBT is at 12mA which means that the collector current in the HPT is high enough for proper forward active operation and the base current is low enough to put the HBT in forward active operation in the linear Gummel region, Further increase in Vb_{HPT} increases causes the Ib_{HPT} to increase in value, until its value becomes 0A, turning off the HPT and all the external supply current Iext of 4mA will be supplied to the HBT producing very high collector current in the HBT. At this point, the automated measurements stops the measurements due to the compliance setting of the HBT supply pin at 100mA.

In this Vb HBT region, an optimum bias point is observed when both devices are in the forward active mode. The HPT will be in HPT mode of operation and the HBT is in the linear Gummel region. Moreover, the HPT could work in the cutoff mode because the HPT base current in the from a negative to a positive value.

4.3.2.2 Opto microwave response

The opto-microwave operation of the directly coupled CE HPT – CE HBT can be illustrated by using two operation points as explained for analysis of the measured illuminated bias current of this topology. The first operation point is when the HPT is in PD mode of operation and the HBT is biased in the high current region. This occurs when $Vb_{HPT} < 0.6V$, Vc_{HBT} is 2V and Iext is 4mA. The opto-microwave gain G_{OM} of the HPT has lower value compared to the G_{OM} of the HPT under HPT mode of operation and the CE HBT that is biased in the high current region provides also lower gain values. The second operation point considered an optimum biasing under a current Iext biasing of 4A is when Vb_{HPT} is greater than 0.65V which results in a collector current that is high enough that pushes the CE HPT to operate in the HPT mode of operation while setting the bias point of the CE HBT back in the linear region where CE HBT gain is optimum. Figure 4.42 shows the 50MHz opto microwave link gain G_{OM} of the CE HPT- CE HPT and a single HPT device as a function of the supplied Vb_{HPT}. If we consider one Vc_{HBT} value of 2V is at zero Vb_{HPT}, it has a response of -9dB which is 16dB higher than the single HPT at Vbe = 0 V and Vce = 2V. This HPT pair has a peak response of 11.08dB. It is 30dB higher than that of the peak response of the single HPT. But this gain decrease is very strong, indeed at Vb_{HBT} equals to 0.75V G_{OM} is maximum and it drops to -71dB when Vb_{HBT} is 0.77V!

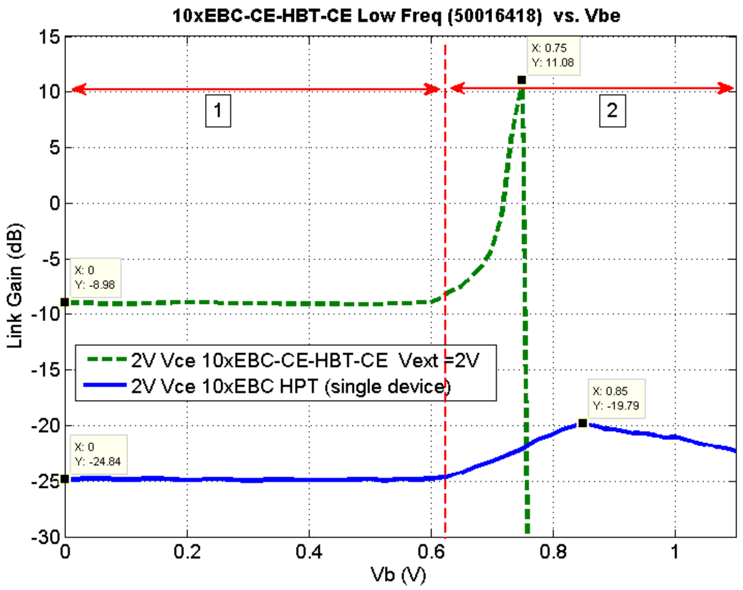

Figure 4.42 G_{OM} vs Vb_{HPT} at 2V Vc_{HBT} and Iext of 4mA of the 10xEBC-CE-HBT-CE plus VI Systems VCSEL at 1.22mW (Measurements)

This direct coupled CE HPT-CE CHBT configuration results in very high opto-microwave gain. However, its opto-microwave cutoff frequency suffers severely. Figure 4.43 shows the opto-microwave cutoff frequency of the reference HPT and the cascade pair bias peak G_{OM} bias point, the cutoff frequency is 146MHz.

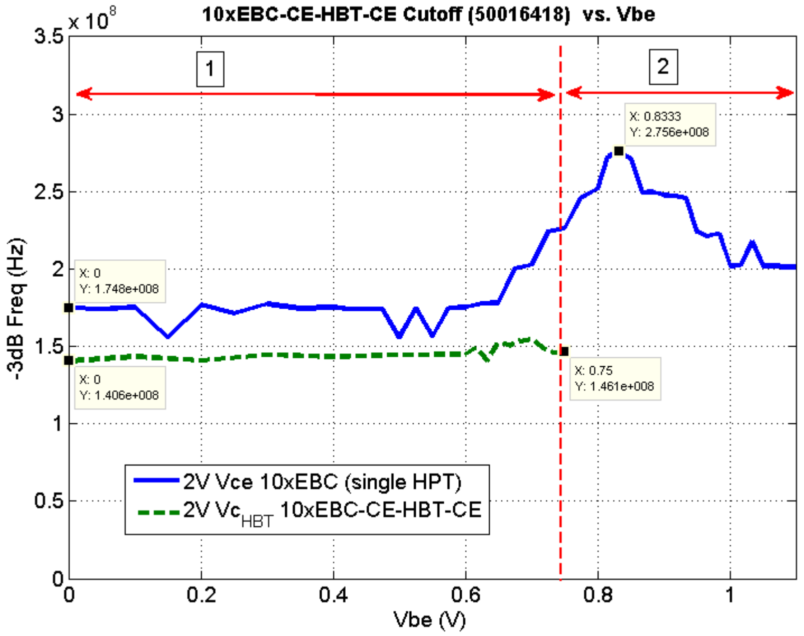

Figure 4.43 Opto-microwave -3dB cutoff frequency of the HPT CE- HBT CB vs. Vb_{HPT} at Iext of 4mA and P_{OPT} = 1.22mW (Measurements)

The opto-microwave frequency response is shown in Figure 4.44. It is compared with the single HPT response at a bias point that maximizes the low frequency G_{OM}. The curve at Vb_{HPT} = 0, Vc_{HBT} = 2V and Iext = 4mA shows an improvement in the low frequency values. However, it exhibits a lower cutoff frequency. The response at Vb_{HPT} 0.75V, Vc_{HBT}= 2V and Iext =4mA maximize the gain (as shown in Figure 4.43) low frequency d while it still has a lower cutoff frequency, it exhibits a higher G_{OM} up to 10GHz. This shows that HPT-HBT topology, even with its low cutoff frequency has interesting response values in the GHz range of operation as compared to the single HPT. At 275.6 MHz which is the cutoff frequency of the single HPT, G_{OM} of the CE HPT- CE HBT pair is higher by more than 20dB to the single HPT.

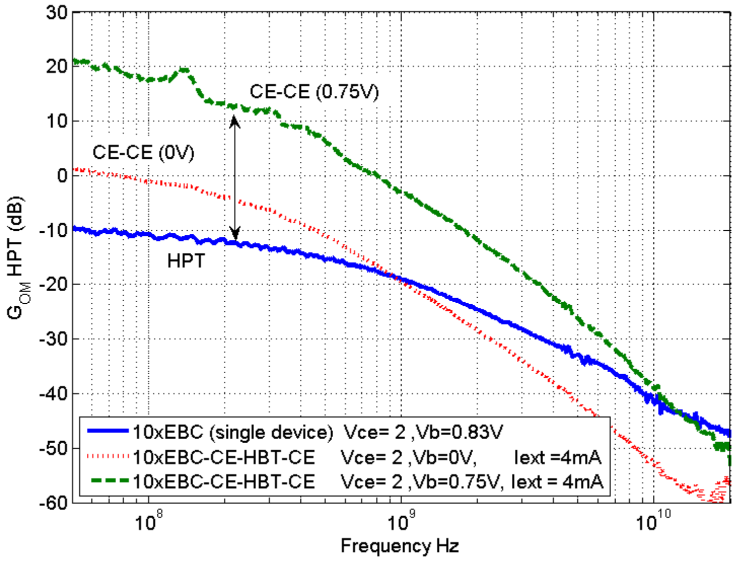

Figure 4.44 Comparison of extracted opto-microwave responsivity of a 10xEBC HPT and HPT-HBT pairs with a 10xEBC HPT. (Measurements)

Table 4.5 presents the measured responses in he CE HPT-CE HBT topology.

Table 4.5 Summary of extracted opto-microwave responsivity of a 10xEBC HPT and HPT-HBT pairs with a 10xEBC HPT.

Structure	Vc (V)	Ic_{HBT} (mA)	Vb_{HPT} (V)	Ib_{HPT} (µA)	Iext (mA)	Link Gain (dB)	Cut (MHz)
10xEBC	2	7.76	0.83	-12.11	---	-19.8	275.6
HPT CE-HBT CE	2	78.34	0	-28.27	4	-8.97	141
HPT CE -HBT CE	2	12.61	0.75	-25.15	4	11.08	146

In summary, CE HPT – CE HBT configuration offers very high G_{OM} even at its simplest configuration of cascading the two devices. This HPT-HBT configuration shows that with its high opto-microwave response and a low cut off frequency still results in good performance even in the GHz range of operation. Further experiments on this configuration, such as using a voltage source instead of current source as the external bias would give a full characterization of the opto-microwave response of this HPT-HBT pair. Also, separation of the DC biasing of the two devices with the use of capacitive coupling between the two common emitter stages, may provide optimizations in the opto-microwave response of the HPT-HBT pair.

4.3.3 The HPT-HBT pair topologies:

The different HPT-HBT pair topologies present some advantages in terms of the opto-microwave response in amplitude and cutoff frequency. One way to compare their performance in frequency is to consider two frequencies (2GHz and 5GHz) modulating the optical signal. Figure 4.45 shows the measured G_{OM} of the link constituted by the VI systems VCSEL and the HPT+HBT configurations (single HPT, CE-HPT+ CB HBT, and CE-HPT+ CE-HBT) at these 2 RF frequencies as a function of Vb_{HPT}. Considered Vc_{HBT} and

Vext are selected values that provide the highest opto-microwave response. At 2 GHz operation, the CE HPT- CE HBT pair exhibits the highest opto-microwave link gain of -27.75dB, the CE HPT- CB HBT with -31.79dB and the lowest response comes from the single HPT with -34.82dB. At 5 GHz, the highest response is from the CE HPT- CE HBT pair with a value of -32.45dB and the lowest response is still from the single HPT with a value of -41.85dB. The peak values, together with the biasing information are summarized in Table 4.6 for the 2GHz operation and Table 4.7 for the 5GHz operation.

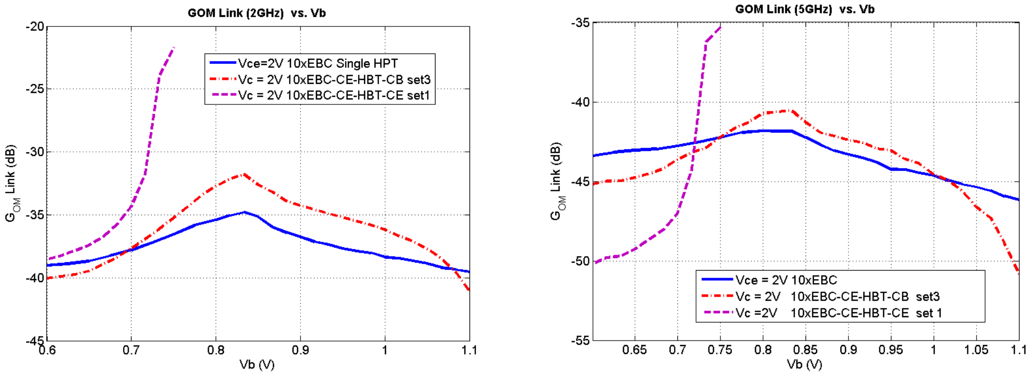

a) b)

Figure 4.45 G_{OM} Link vs. Vb$_{HPT}$ of the different HPT-HBT pair under an illumination of 2.44mW using a VI-Systems VCSEL a) at 2 GHz b) at 5 GHz

Table 4.6 Summary of HPT-HBT pairs at 2 GHz and illumination of 2.44mW

HPT-HBT	Vbe(V)	Vce(V)	Bias$_{ext}$	G_{OM} Link (dB)
CE (single HPT)	0.83	2	NA	-34.82
CE-CB	0.83	2	2V	-31.79
CE-CE	0.75	2	4mA	-21.75

Table 4.7 Summary of HPT-HBT pairs at 5 GHz and illumination of 2.44mW

HPT-HBT	Vbe(V)	Vce(V)	Bias$_{ext}$	G_{OM} Link(dB)
CE (single HPT)	0.83	2	NA	-41.85
CE-CB	0.83	2	2V	-40.54
CE-CE	0.73	2	4mA	-35.30

Figure 4.46 shows the absolute G_{OM} of the three topologies (single HPT, CE-HPT+CB HBT, CE-HPT+ CE-HBT) versus frequency. It is observed a crossing of the curves at 10GHz . The improvement of the CE-HPT+CE-HBT is clearly seen.

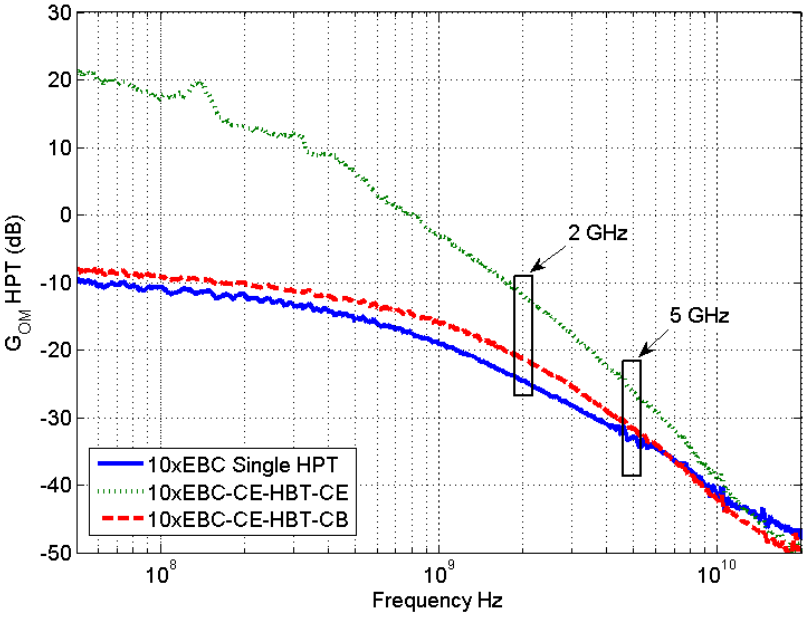

Figure 4.46 G_{OM} HPT vs. Frequency of a single HPT and the HPT-HBT pairs under optimum bias conditions with illumination of 2.44mW

The opto-microwave responses of different HPT -HBT pairs are analyzed and identified. The CE HPT –CB HBT pair offers a 25% higher -3dB$_{OM}$ cutoff frequency as compared to the single CE HPT. The CE HPT – CE HBT circuit offers a very high G_{OM} with an improvement of up to 30dB at low frequency and around 10dB at 5 GHz. despite a reduction in the -3dB$_{OM}$ cutoff frequency of almost two times as compared to the single CE HPT.

4.4 Conclusion

In this chapter, we have presented the study and analysis of the opto-microwave response of various circuits utilizing HPT: passive base loads on an HPT and HPT-HBT pairs.

Experiment on the external HPT base loads shows that the opto-microwave response in high frequencies could be optimized with the use of impedances that have a positive phase angle. The simulations on the passive internal base loads showed that the resistor, and capacitor loads shows improvement up to 25dB in the low frequency region and the inductor loads shows improvement up to 5dB in the 0.5GHz-1GHz region. This means that the HPT opto-microwave frequency could be tailored with the use of an adequate base load circuit. The measurements using an HPT with an internal base load shows that the base load effect on the HPT can be properly observed by configuring a biasing of the HPT that is independent on the base load. The fabricated modules with an inductor in series to the base of the HPT is severely affected by the DC bypass capacitor of to provide the base bias to the HPT. The fabricated modules with a capacitor in series to the base of the HPT allowed for the 2T HPT mode of operation of the HPT in DC.

Measurements in the HPT-HBT pair shows that the HPT-HBT pair shows improved performances as compared to a single HPT. The HPT cascode exhibits a 1.4dB increase in response as well as an increase in the cutoff frequency by 25% up to 344MHz for a R2-10SQxEBC HPT. The simple HPT-HBT cascade has a very tight biasing range but offers at most a 30dB increase in the low frequency. While its cutoff frequency is almost reduced by 40% as compared to a single HPT it still provides a 10dB improvement at 5GHz and reach the level of the single HPT configuration at 10GHz.

The comparison of the opto-microwave response of a single HPT and the HPT-HBT pairs showed that the direct coupled CE HPT -CE HBT amplifier response has the highest value in the low frequency operation (50 MHz) and high frequency operation at up to 10GHz.

5 SiGe HPT for Radio over Fiber applications

5.1 Introduction

In the previous chapters, we have studied the performance of a single device as well as the influence of additional circuit components. These were simple HPT circuits with either a single passive component on the base or a basic HPT and HBT pair. In this chapter the SiGe HPT is packaged as a ROSA module, where it is a major component in a RoF system and thus measured in a complete circuit. In Section 2, a 60 GHz transceiver module is discussed to provide an overview of the system where the HPT ROSA will be used. Section 3 focuses on electronic low noise amplifiers that could be used as individual circuit modules for the RoF system and as a basis for SiGe HPT ROSA implementations. Section 4 presents the SiGe HPT cascode circuits that are targeted to be used in the first generation SiGe ROSA modules. These circuits are characterized on wafer to determine the optimum circuit that will be used for the fabrication of the SiGe HPT ROSA. Section 5 presents the actual resulting ROSA. The processes and steps in the fabrication and assembly of this module are detailed, together with the characterization results. Finally, a second version of the ROSA which is based on the hybrid cascading of a SiGe HPT and two LNA are designed and fabricated.

5.2 IF over RoF Transceiver Module for 60 GHz application

The architecture of a 60GHz IF over RoF transceiver module as developed in the FUI8-ORIGIN Project is presented in Figure 5.1 [232],[226]. It is divided into two sections: the millimeter (mm) wave section and the centimeter (cm) wave section. The wireless (receiving section) of mm wave part is responsible for the down conversion of the received 60GHz wireless signal to an intermediate frequency (IF) of 5GHz with a bandwidth of 2GHz. The mm wave transmit part up converts the 5GHz signal to 60GHz. In the cm wave module down converted wireless signal is conditioned for direct modulation of a VCSEL for optical transmission. The other part of the cm wave section receives the optical signal and is converted to an electrical signal by the HPT. An HPT with a 4A/W responsivity and a cutoff frequency of 50 MHz is expected to have a response of -28dB at 5GHz. A 10dB amplifier integrated with the HPT will result in a response of -18dB at 5GHz for the integrated HPT and amplifier chip. In order to reach the overall link requirements of the system as defined in the ORIGIN project [232] [226], two amplifying stages with 14 dB gain are further needed after the HPT+LNA. An attenuator inserted between the two amplifiers provides the necessary control to adapt for the response of the HPT and amplifier chip module, and for the amplitude of the received 60GHz signal.

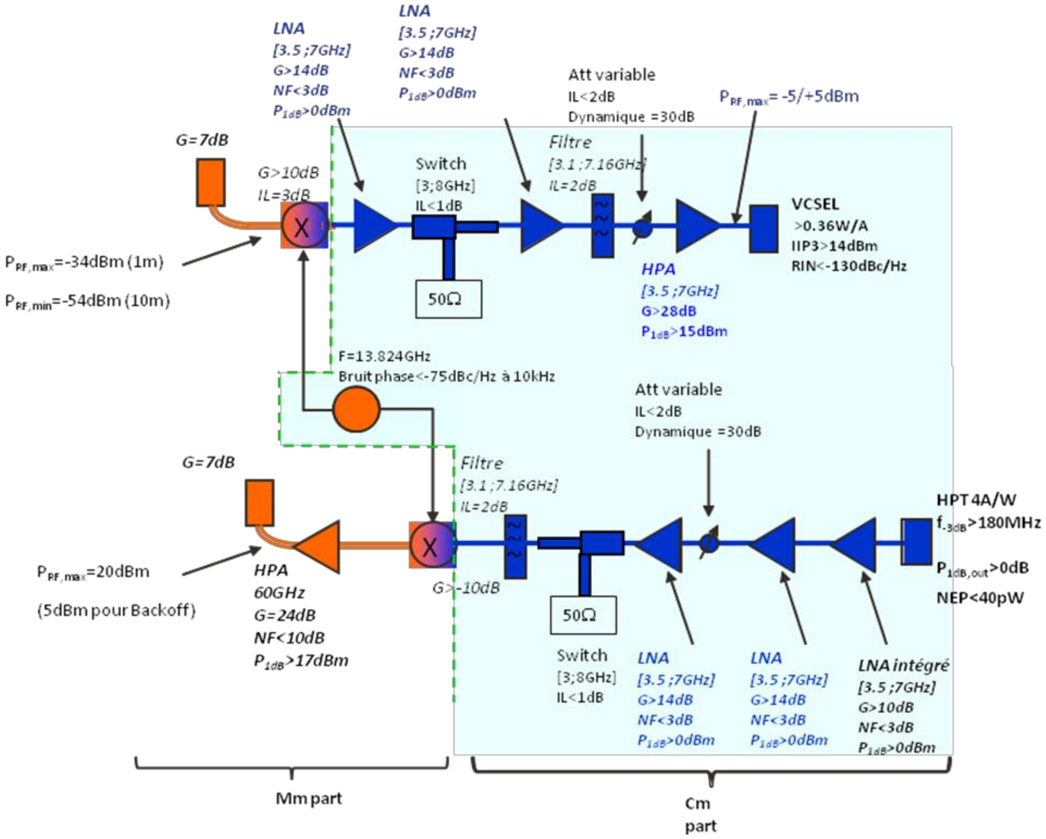

Figure 5.1 Proposed architecture of 60 GHz IF over RoF

5.3 Low noise amplifier circuits

This section presents the different circuits that can be used in the implementation of a radio over fiber link. These circuits are designed and implemented using the same processing technology used in the fabrication of SiGe HPTs. This allows the design of fully integrated optoelectronic receiver circuits.

A low noise amplifier plays an important role in a receiver side of a radio over fiber link. These circuits are intended to be used as post amplifying stages after a SiGe HPT detector or SiGe HPT amplifier circuit. For a generic wideband application, several preliminary specifications are chosen as design guides: a minimum bandwidth of 3.1GHz to 10.6GHz; a noise figure (NF) below 3dB and a gain greater than 20dB.

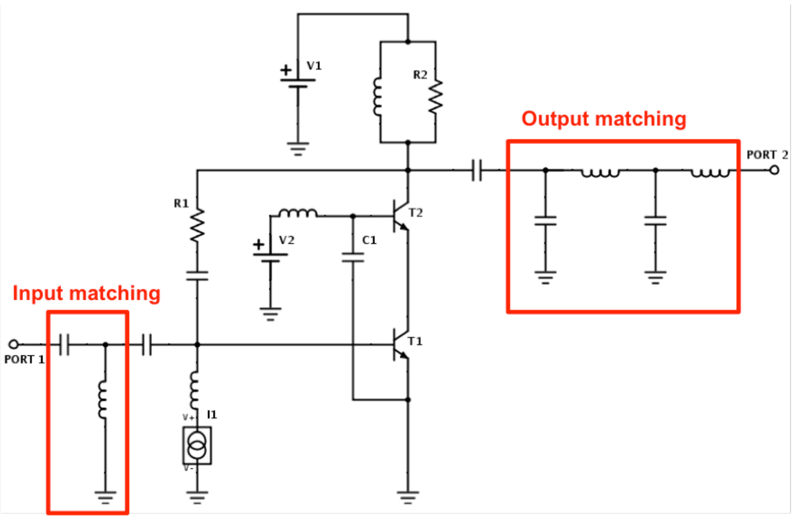

Figure 5.2 Schematic of the cascode LNA using two 0.5x30µm SIC SiGe HBTs and ideal lumped elements

The cascode topology is considered shown in Figure 5.2. It consists of an input common emitter transistor (T1) driving an output common base transistor (T2). It eliminates the Miller effect and thus contributes to a higher bandwidth. The cascode also improves input-output isolation since there is no direct coupling from the output to input. The choice of transistor is a key concern to achieve both the gain and the noise figure in the desired bandwidth. This choice is dictated by the need to select some transistor size that may not require inductance for their matching circuit, which may have low Q and low resonance frequency.

Three components are also key to the optimization of the cascode circuit. The resistive feedback resistor R1 with a value of 1.9kΩ . This resistor is located between the collector of T2 and the base of T1, the output and the input current of the cascode respectively. It helps to stabilize the transistor, but also has an effect on its performances. High R1 values increase the gain and decrease the noise figure. This also extends the bandwidth of the desired noise figure goal. The limitation comes from the degradation of output reflections leading to some difficulties for the output impedance matching across the bandwidth (3.1GHz - 10.6GHz). The capacitive feedback capacitor C1 with a value of 5pF, is a grounded capacitor connected to the base of T2. It works to compensate the imaginary part of the input impedance of the transistor, thus improving the gain bandwidth. Increasing this capacitor value raises the upper maximum available gain (MAG) and the S_{21} parameter. Increase in this capacitance value also results in improving the upper frequency gain by around 7dB (from the lower to the upper frequency) maintaining the low frequency behavior unchanged. This capacitor also affects the NF bandwidth in a similar way. This action is less important than the one on the gain, but still provides an improvement on NF. The drawback of using this capacitor is that it degrades the S_{22} parameter. Increasing the value of C1 also increases reflections. That should be considered as a limitation on C value. The effect on the Rollet stability factor is negligible. The output stabilization resistor R2 with a value of 340Ω is a parallel resistor to the inductor between the T2 collector and the voltage source or RF ground. This low value resistor helps to decrease S_{22}, therefore improving matching to a 50Ω loads. In fact this low resistor value makes S_{22} closer to the 50Ω matching point. This effect is easily visible on the Smith chart. Even without matching component a S_{22} is lower than 15dB in the whole bandwidth. This resistance does not degrade the noise figure. The degradation on the gain is controlled. Using ideal components, the simulation results are presented in Figure 5.17.

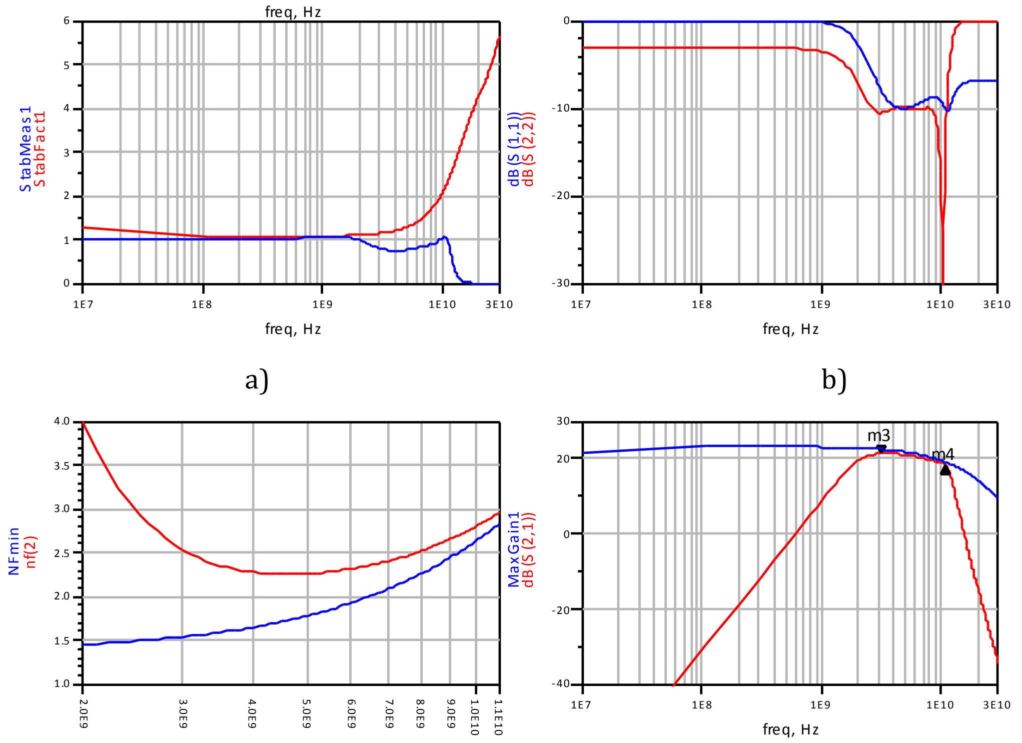

a) b)

c) d)

Figure 5.3 Simulation of the cascode LNA designed with ideal components: Shown is the (a) stability figures (b) reflection parameters , (c) achieved noise figure, nf(2) and its theoretical limit NFmin and (d) achieved S21 gain compared to the theoretical limit

The gain is higher than 20dB on the desired range of frequency, with a ripple less than 3dB. Noise figure is lower than 3dB and can reach 2.3dB for some channels of the ultra wideband radio standard. The output reflection however presents a limitation of that circuit but is lower than 10db in the whole range. Non-linear simulations are also performed with the computation of the 1dB Gain compression point (CP) and the Input IP3 (IIP3). At 6GHz, the input 1dB Gain compression point equals to -15.2dBm and the IIP3 is -1.8dBm, fulfilling expected targets . The simulations are shown in Figure 5.4 and Figure 5.5

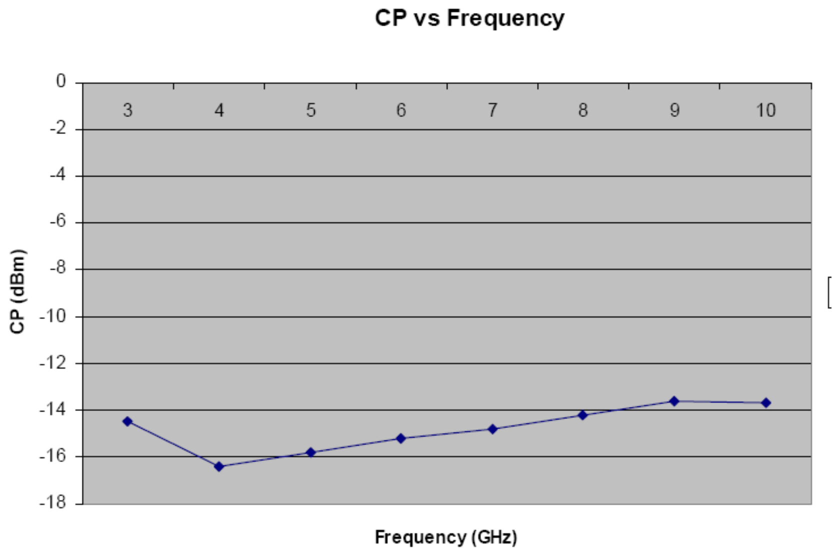

Figure 5.4 Simulation of the input power at the compression point (CP) vs. frequency of the ideal LNA.

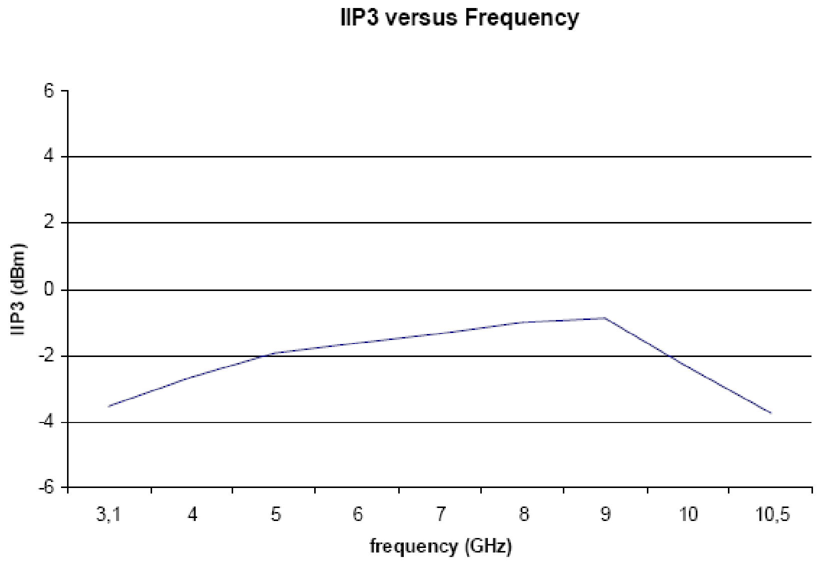

Figure 5.5 Simulation of the input 3rd order intercept point (IIP3) vs. frequency of the ideal LNA.

These simulations are performed with ideal passive components. The non-idealities of the lumped components are very critical in the design of an LNA. Simulations using non-ideal component model to optimize their values with respect to the desired circuit performance, showed that the value of the feedback capacitance C1 is severely affected, which drops down to 0.1pF with initial value of 5pF. This very low capacitance value could be removed in the final version of the circuit. Other changes are illustrated in Figure 5.6, where the circuit has been simplified and optimized to take into consideration the parasitics of the non-ideal components.

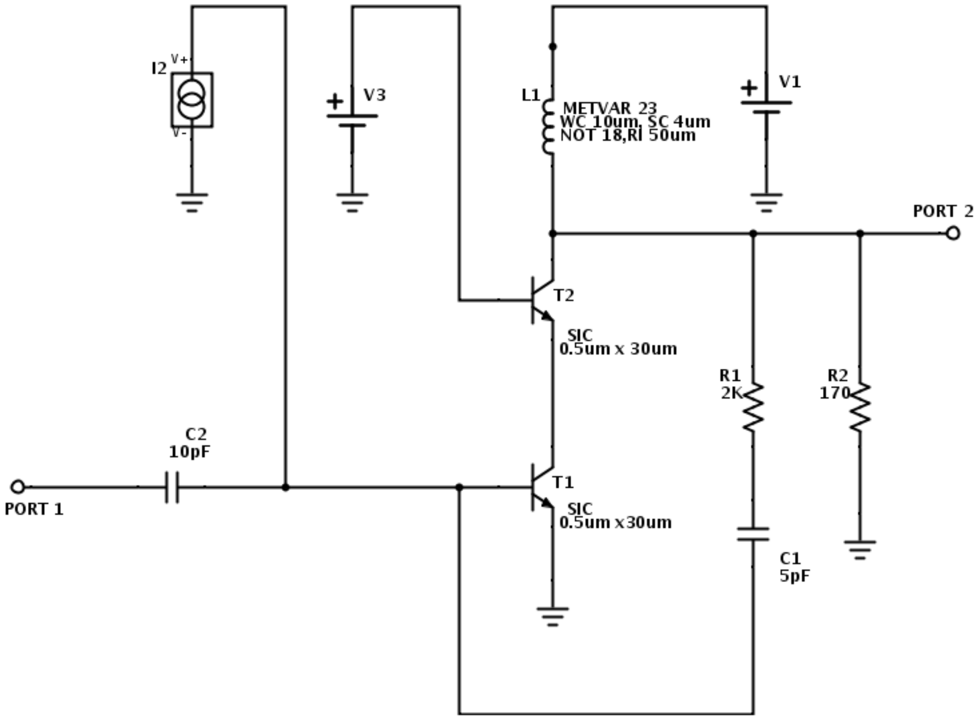

Figure 5.6 Schematic of the cascode LNA using passive components from the SiGe2RF process technology

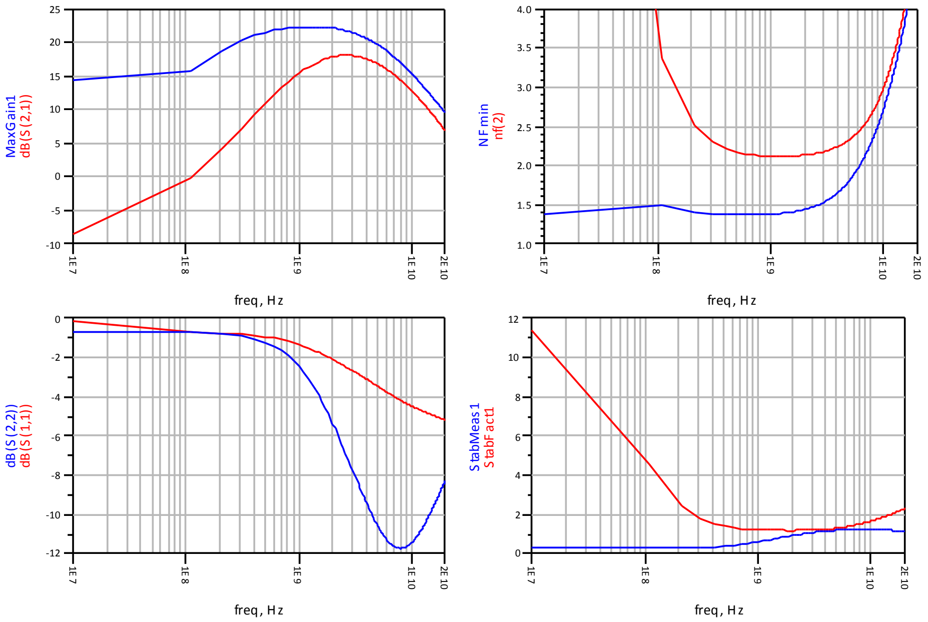

Figure 5.7 Simulation results of the cascode LNA using the passive components of the SiGe2RF process technology.

Final simulations of the cascode LNA circuit is shown in Figure 5.7 which exhibits a gain of 15dB ±2dB, i.e. 5dB-6dB lower than the circuit with ideal components. The noise figure is lower than 3.5dB with a minimum value over the band of 2.9dB. On the contrary, the output reflection coefficient is improved with a value lower than -10dB at 10GHz. The main limitation in the gain arises from the resistive nature of the feedback used to stabilize the transistor.

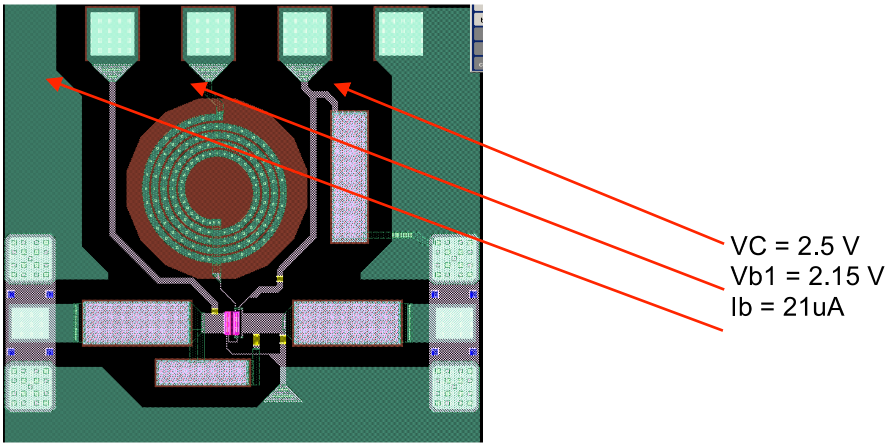

Figure 5.8 Layout view of the R2-LNA01 circuit

Figure 5.8 shows the final layout of R2-LNA01 circuit. The input and output ports of the LNA are connected to GSG pads. The LNA bias is established via the DC pads. Pin 1 is biased with 21μA, Pin 2 with 2.15V and Pin 3 with 2.5V.

The on-probe measurement results are compared to simulation results are presented on Figure 5.9. It shows that the measured response is 15dB at around 2 GHz. The central frequency was shifted and does not fit the 5GHz objective. Nonsteady behavior was also observed.

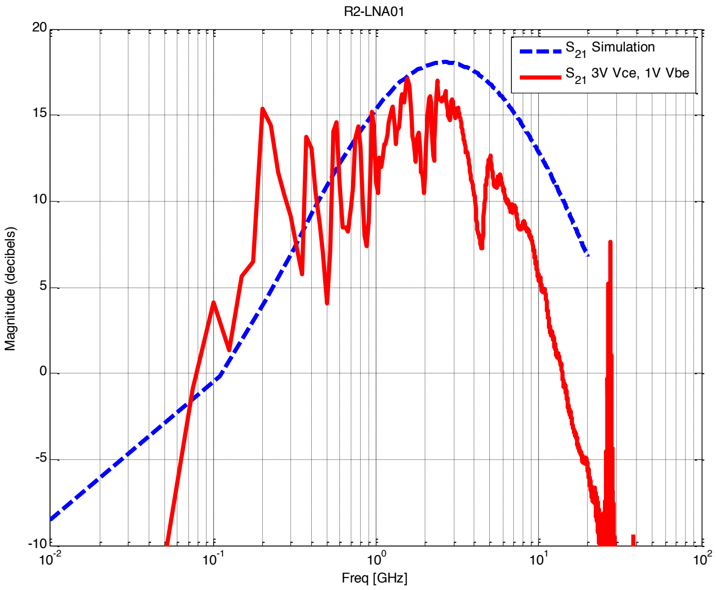

Figure 5.9 Simulated and measured S21 of the R2-LNA01 amplifier.

Another amplifer, named R3-LNA0 was designed to operate at a frequency of 5.185GHz and a bandwidth of 2GHz. It uses a simple cascode architecture similar to R2-LNA01 as seen in Figure 5.2. Figure 5.10 shows the schematic diagram of the R3-LNA01 with matching circuits to facilitate the operation at 5.185GHz .

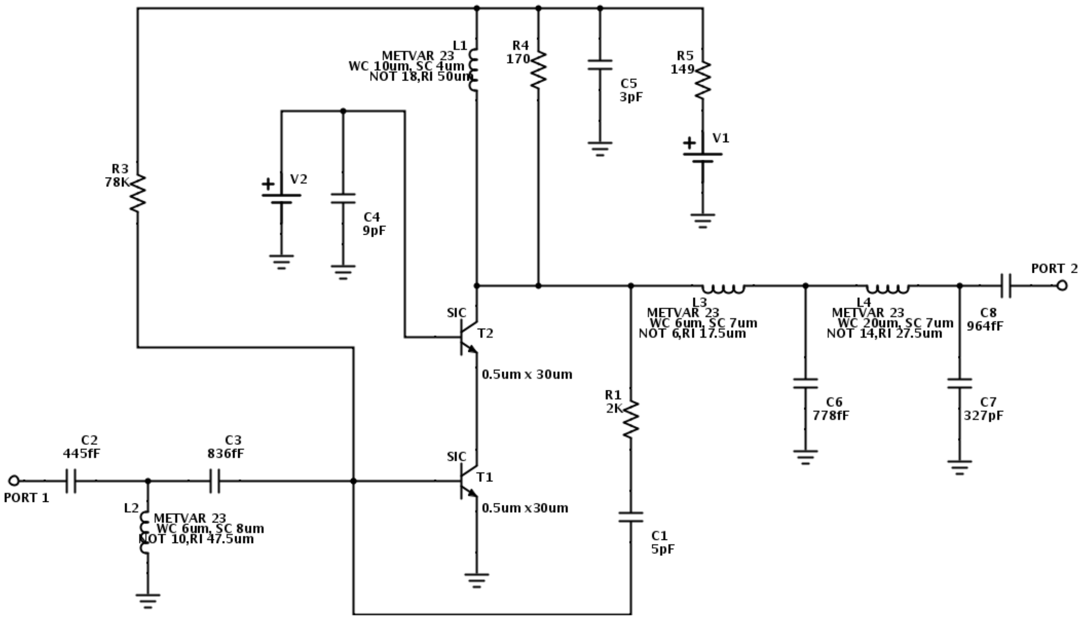

Figure 5.10 Schematic diagram of R3-LNA01 using a simple cascode operation

Figure 5.11 shows the simulation of the gain and noise figure of the R3-LNA01. It shows that the peak gain is a 13.86dB at 5.1 GHz. At 4.1 GHz, the gain is 9.7dB and at 6.1 GHz the gain is 10.1dB thus giving a +/-2dB variation within the band. The noise figure simulation shows a 3.8dB noise figure at 5.1 GHz.

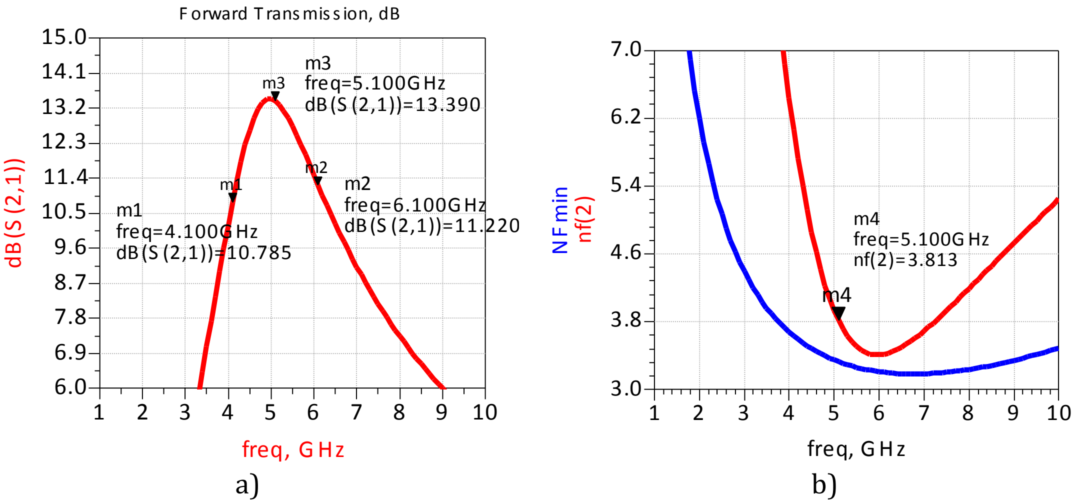

Figure 5.11 Simulation results of the R3-LNA01 amplifier (a) S_{21} and (b) NF

Figure 5.12 shows the layout diagram of the R3-LNA01 amplifier. The input and output ports of the LNA are connected to GSG pads and DC biasing are provided by the DC pads.

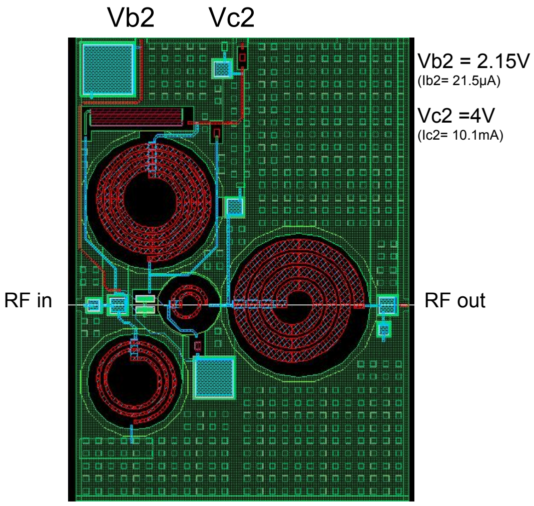

Figure 5.12 Layout view of the R3-LNA01 amplifier without the GSG pads and DC pads.

Figure 5.13 shows the on-probe measured S_{21} of the R3-LNA-01 compared to the simulation results. It shows a peak value of 10dB at 5GHz. The measurement results exhibit a lower gain and a shift in the center frequency of operation.

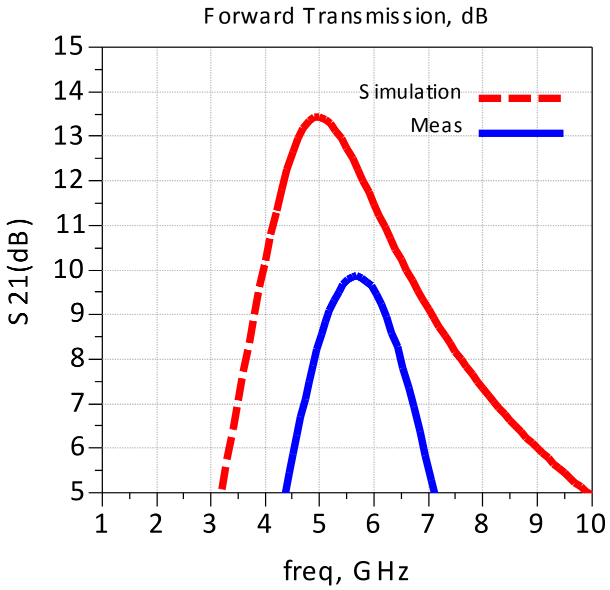

Figure 5.13 Measured S_{21} of R3-LNA01 vs. simulation results

5.4 HPT-based Receiver Optical Sub-Assembly (ROSA)

This section presents the development of an HPT based ROSA for the previous architecture. The circuit is described first. Then opto-electrical characterizations are provided with the goal to define the best method to realize the optical fiber alignment.

5.4.1 HPT cascode amplifier circuits

An opto-electronic HPT-based amplifier is designed using the R2-LNA01 architecture without its matching network. Where the common emitter transistor of the cascode has been replaced by an HPT. Figure 5.14 shows the schematic of the diagram of the resulting HPT cascode amplifier. The output resistance R1 is unaffected and the parallel feedback resistance R2 should be adjusted for the HPTs but this was not done at this stage as not enough information were available on the HPTs as they were developed simultaneously in the same run. The simple replacement of the HBT with an HPT provides insights in the operations, which could be used as reference for the future iterations. Four HPT cascode amplifiers are fabricated and characterized using the 10xEBC, 20xEBC, 30xEBC and 50xEBC.

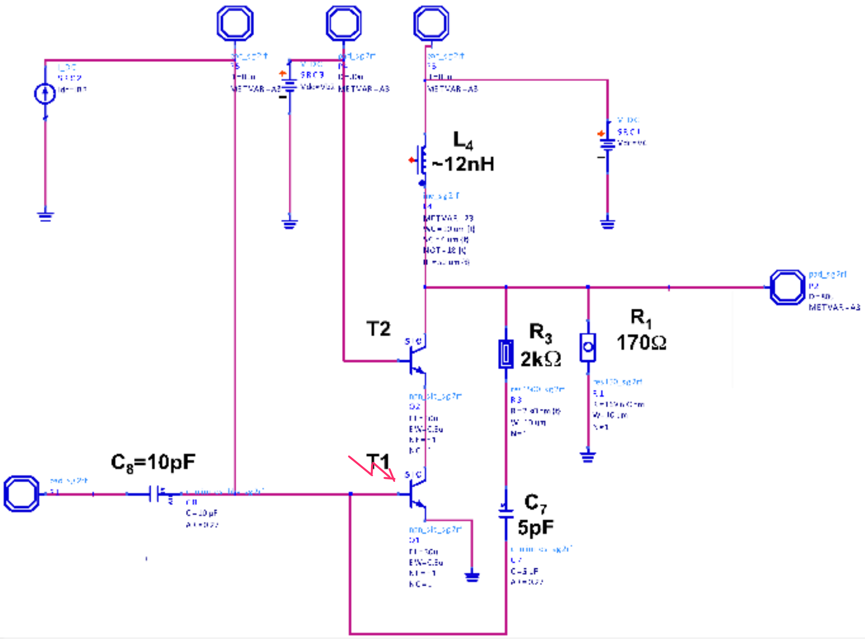

Figure 5.14 HPT cascode circuit schematic diagram

Figure 5.15 shows the measured G_{OM} link vs. frequency of the HPT cascode amplifier and a VI-Systems VCSEL with Vb1= 0.85V, Vc2 = 2.5V and Vb2 = 2.2V. The highest response is seen from the OE amplifier with the 30SQxEBC HPT and the lowest response is from the OE amplifier with the 10SQxEBC HPT. Similar to previous characterizations of similar type HPTs with different optical window sizes. The size of the optical beam used in the opto-microwave measurements will have significant effects in the peak measured OM response. The 30SQxEBC has no optical losses associated with the optical window and the 10SQxEBC has a high amount of associated optical losses.

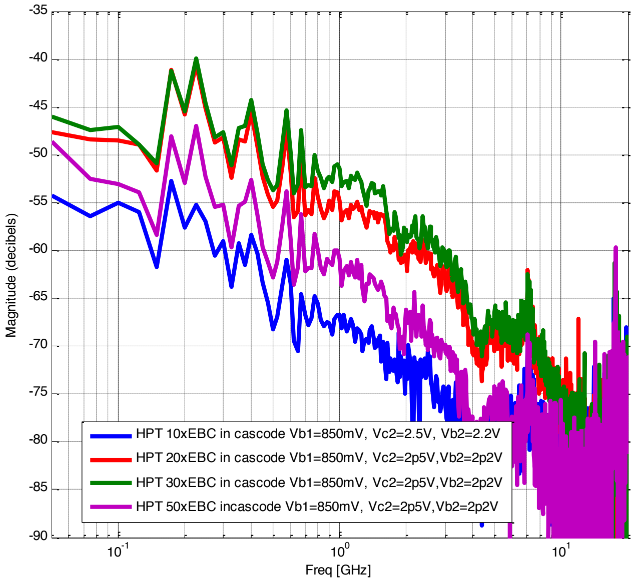

Figure 5.15 G_{OM} vs. frequency of the HPT base OE amplifier using different sized SQxEBC HPTs at a biasing condition of Vb1 = 850mV, Vc2 = 2.5 V and Vb2 = 2.2V (Measurements)

Figure 5.16 shows the comparison of the opto-microwave response of the HPT-based OE amplifier when as compared to the opto-microwave response of a single HPT of the same size as used in the OE amplifier circuit. Generally, the low frequency response of the OE amplifier circuits will have lower value compared to their single HPT counterpart. However, at high frequencies, i.e., 2GHz, The opto-microwave response of the HPT cascode amplifier with a 30SQxEBC and 50SQxEBC show better response .

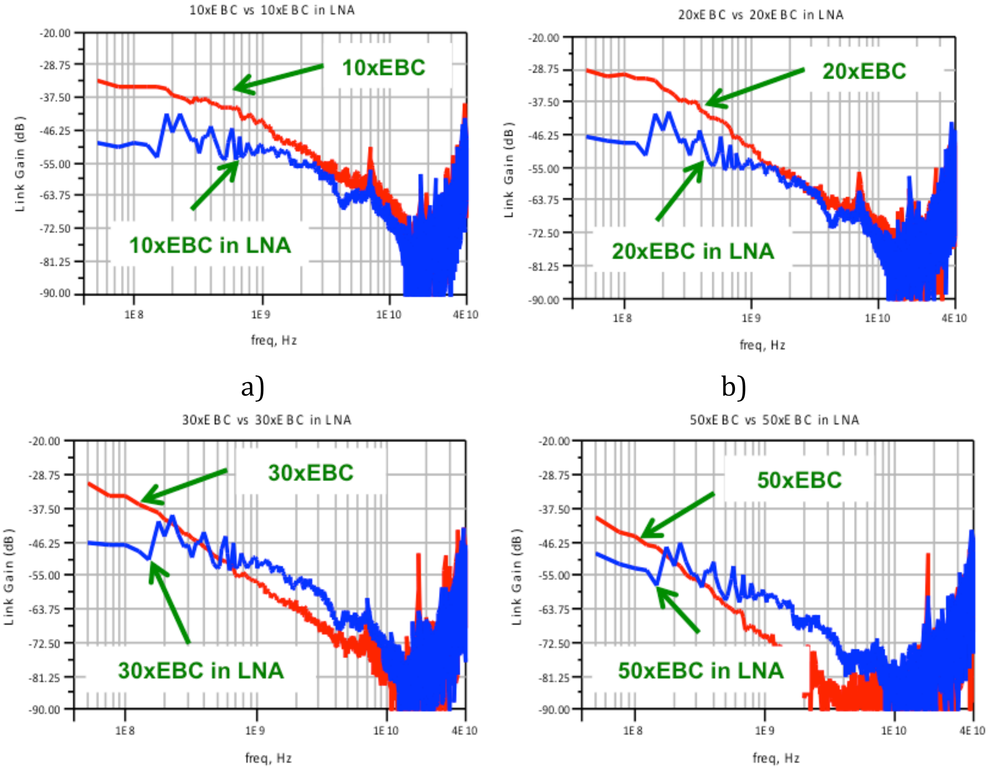

a) b)

c) d)

Figure 5.16 G_{OM} vs Frequency of the different HPT based OE amplifiers as compared to their counterpart single HPT.

From these measurements, the 30µm HPT cascode circuit is retained as a good candidate for integration in a ROSA module. Next section deals with the technique to prepare the optical packaging and how to monitor a proper optical alignment to the circuit.

5.4.2 Chip preparation for the packaging

The idea of this section is to discuss the packaging of the 30µm HPT cascode circuit. The die is described and then DC opto-electronic tests are performed that will be the basis of further optical alignment procedure.

Figure 5.17 shows two chip photographs of the HPT cascode circuit. Figure 5.17(a) shows the circuit with a 150um pitch GSG pads (GSG HPT in cascode) and Figure 5.17(b) shows the HPT cascode circuit with 200µm pitch pads. The 200µm pitch pads are compatible to flip chip and thermo-compression. These processes are used to attach the HPT to a glass transparent substrate that will be described later on. This is one of the steps in the fabrication and assembly of the HPT- based ROSA.

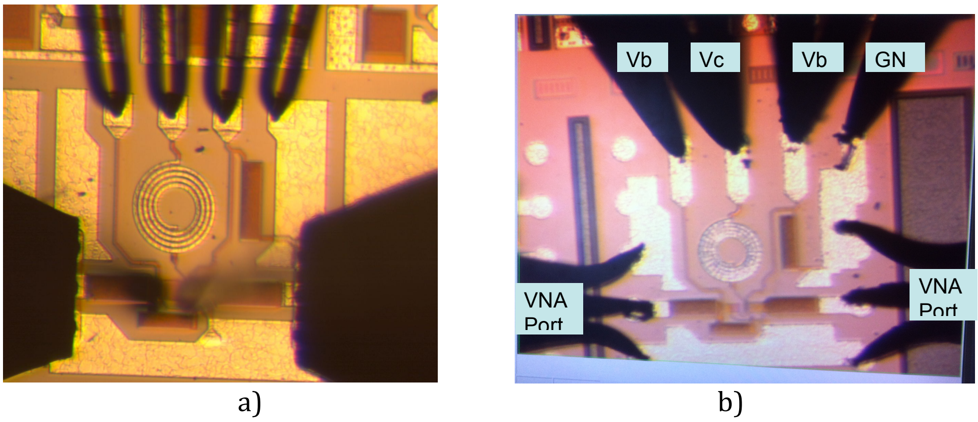

a) b)

Figure 5.17 HPT in cascode in a) 150µm pitch GSG Pads b) 200µm pitch pads

On-wafer DC tests on the GSG HPT cascode was performed to verify its operation and to define the best condition for the alignment of the optical probe to the HPT optical window.

Verification of the optical alignment using only DC currents offers a simplified bench for the assembly of the ROSA module. The circuit was biased with 2.5V Vc1, 2.2V Vb1 and Vb2 was swept from 0-1V. The first test condition is when there is no illumination from the laser. The second test condition is when the optical probe is aligned to the optical window and the laser is turned on. The current Ic2, which is the collector current on the transistor T2 and the Ib1, which is the base current in the HPT (T1) are monitored. Figure 5.18 shows Ic2 vs. Vb1 when the laser is turned on and turned off. Ic2 is approximately 15mA until the point where the HPT is forward biased. The HPT starts going on when Vb1 is around 0.7V and then Ic1 increases as Vb1 is increased. The other trace shows Ic2 when the laser is ON. We used a VCSEL with 6mA bias. The collector current Ic2 shows an increase of collector current all over the Vb1 range. The increase is little compared to the dark current value. The observation of the base current of the HPT thus provides a more clear view of the photogenerated currents

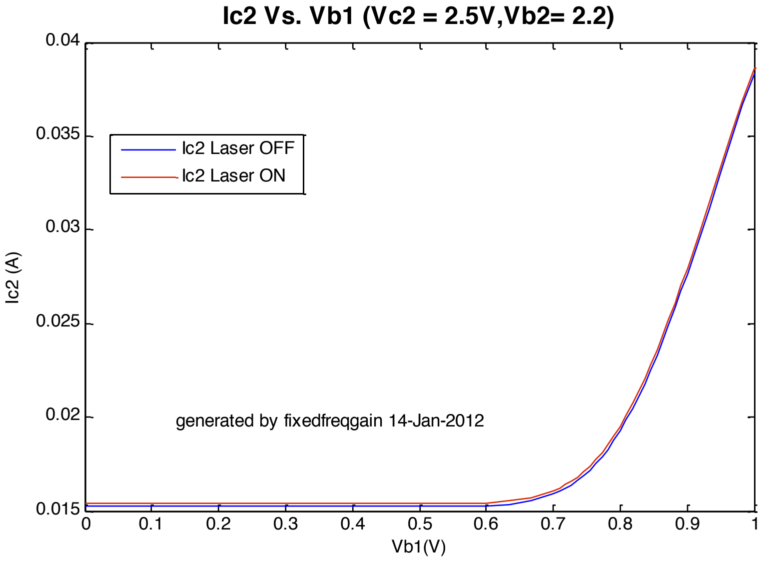

Figure 5.18 Ic2 vs. Vbe of the HPT-base OE Chip

Figure 5.19 shows the plot of the Ib2 vs Vb1. The first trace shows the Ib vs Vbe behavior when there is no illumination. At 0V Vbe Ib1 is approximately 0A, and when the HPT is forward biased, Ib1 will increase. When the HPT is illuminated, at 0V Vbe, Ib1 is negative until HPT is forward biased. Ib1 starts to increase and reach a positive value when Vb1 is equal to 0.85V. It continues to increase as Vb1 is increased. It can be observed that the illumination results in the decrease of Ib1, which is due to the opposite direction of the base photocurrent.

In summary, these observations are useful to identify the best criteria to realize the optical alignment of the fiber above the HPT. The GSG HPT cascode is aligned when we see a slight increase in the Ic2 in the region where Vb1 >0.7V, and when we observe a negative current on the Ib when Vb1 = [0, – 0.85V].

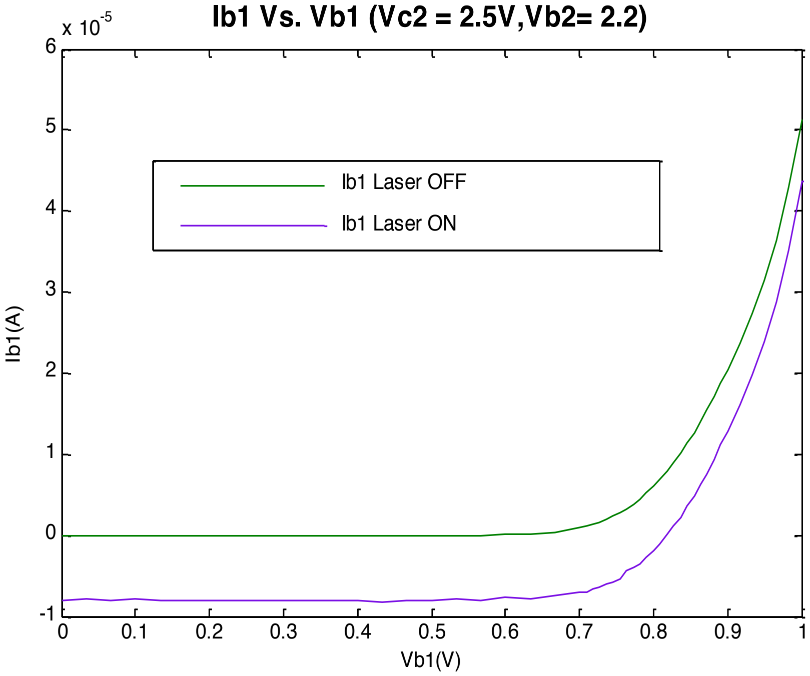

Figure 5.19 Ib1 vs Vbe of the HPT-base OE Chip

The HPT cascode circuit in the 200µm pads are then diced, assembled and packaged in an HPT-based ROSA module. Innoptics is primarily responsible for the packaging of the ROSA module. Figure 5.20 shows a layout representation of the HPT-based opto-electronic amplifier chip and the dimension and placement of the electrical pads (circles) and the optical window (squares). The chip also contains three single HPTs to optimize the die surface. The die is 1250µm x 2500µm in size which has been normalized for all of them.

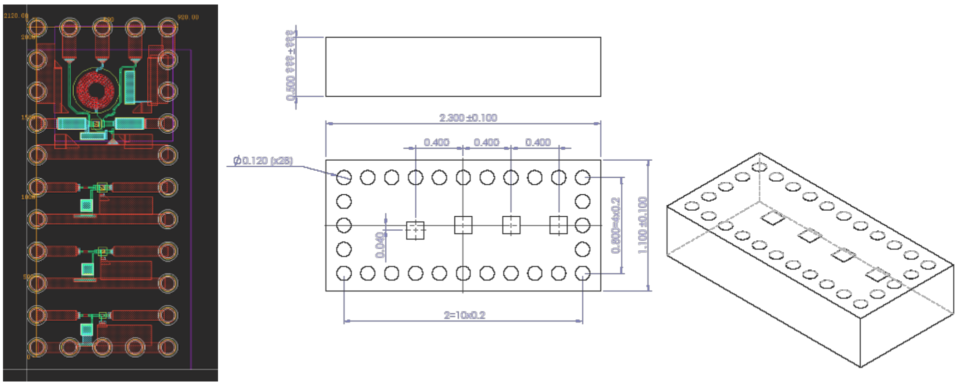

a) b)

Figure 5.20 HPT based OE chip a) layout b) dimension and placement of the optical windows

5.4.3 Interconnection substrate and Electrical contacts

The transparent interconnection substrate is an essential element in the architecture of the ROSA module. It allows for the reception of the optical signal thru the substrate while providing electrical contacts to the pads of the HPT circuit chip. The electrical routing to the pads of the HPT chip are designed and converted to lithographic masks for the substrate processing. The mask design for the HPT-based ROSA is shown in Figure 5.21(a). The fabrication of the interconnection substrate consists of depositing different metallic layers on a transparent substrate, which is either glass or sapphire. The final metallization layer is 1.5µm gold layer to allow for good electrical conductivity and to ease the thermo-compression process. The final interconnection substrate is shown in Figure 5.21(b). It has been fabricated in ESIEE cleanroom.

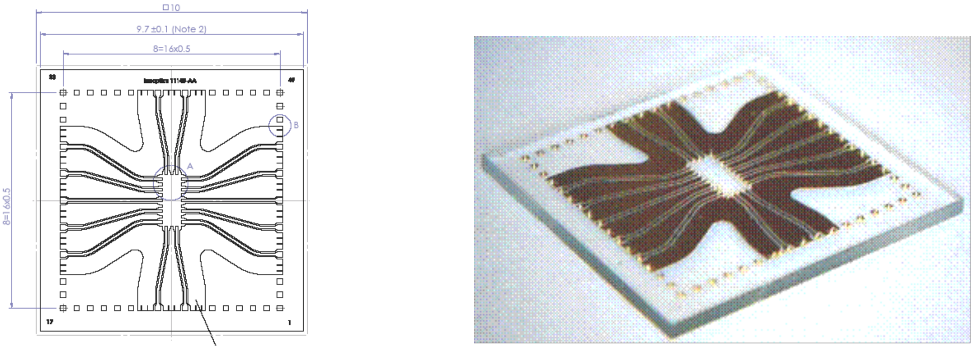

a) b)

Figure 5.21 Interconnection substrate a) mask layout b) final implementation.

Stud bumps are placed in the connection pads of the interconnection substrates. These stud bumps are small gold balls, which are used in soldering via thermal compression. Each stud bump allows for the realization of an electrical connection to the substrate. Some of the stud bumps are used for the interconnection to the HPT die while non-electrically active pads are used for the mechanical fixture reinforcement of the die to the transparent substrate.

Figure 5.22(a) shows the close up view to the stud bumps and Figure 5.22(b) shows a cross section of the interconnection substrate with the stud bumps.

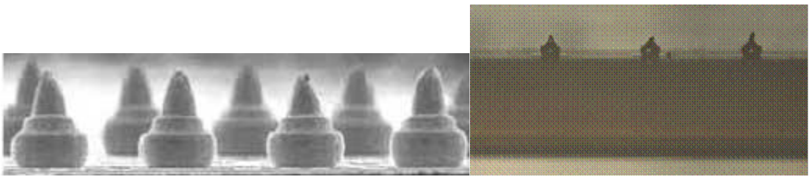

a) b)

Figure 5.22 The interconnection substrate with the stud bumps: a) stud bumps b) cross section

The HPT chip is connected to the interconnection substrate via flip chip process and thermal compression. Figure 5.23 shows the view to the HPT chip that is attached to the interconnection substrate. A flexible PCB circuit is designed to provide electrical access to the rest of the system. A layout representation is shown in Figure 5.24(a). Figure 5.24(b) show the final electrical connection system of the HPT based ROSA, the interconnection substrate is attached to the flexible PCB via thermal compression.

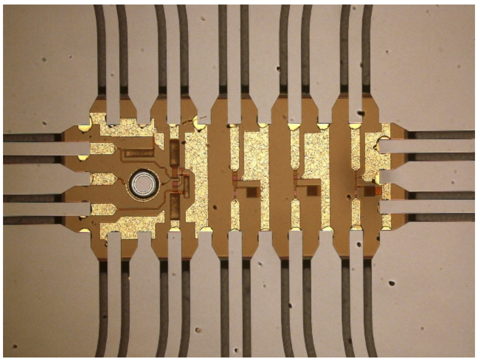

Figure 5.23 Top view of HPT OE chip that is attached to the interconnection substrate

The transparent substrate is a rigid material that will support the optical coupling fixture described in the next section. It is however mandatory to take electrical connection from this substrate to the external system. This is provided through a flex-PCB figure, sketched in Figure 5.24(a). The transparent substrate is then mounted on it through a similar thermo-compression procedure using pads from the outer region of the substrate. The flex-PCB is drilled etched in its center to keep an open access to the full surface of the transparent substrate. Figure 5.24(b) shows the final result of this flex-PCB glass SiGe HPT circuit fixture.

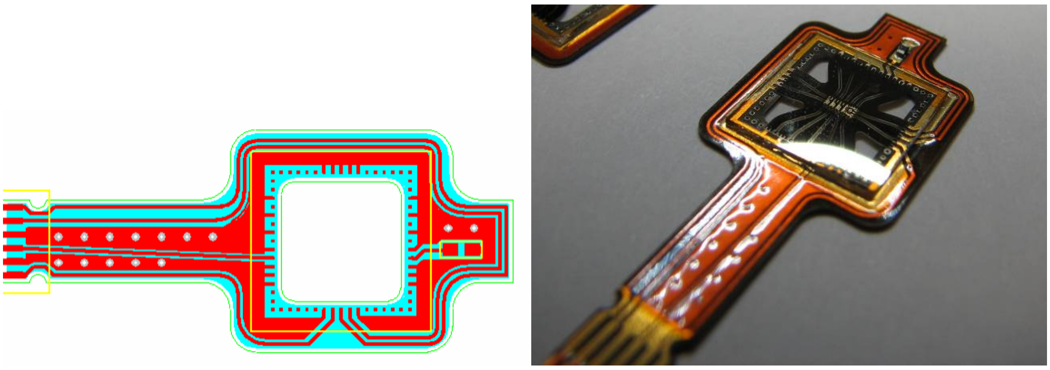

a) b)

Figure 5.24 HPT based ROSA: a) layout diagram of the flexible PCB circuit. b) final electrical connection system

5.4.4 Optical coupling and alignment

The optical coupling system is designed and fabricated by Innoptics. Shown in Figure 5.25 is a sketch of this system. A ferule holds a multimode fiber sot that the optical beam passes through a ball lens. The focused optical beam passes through the transparent interconnection substrate and finally hit the HPT die optical window with an optical spot size of 30µm in diameter. The mechanical drawing is shown in Figure 5.26a which shows the actual components of the optical coupling system: the body, ball lens, ferule for MMF connections, a sleeve to assure the alignment of the ferule to the receptacle and to connector, and a shield to protect the assembly. Figure 5.26 shows the final optical coupling system. The ball is a 1mm sapphire ball lens, in direct contact to the transparent substrate. The MMF position is controlled to by typically 1160µm. A typical 67% optical coupling efficiency is achieved on the 30x30µm^2 HPT.

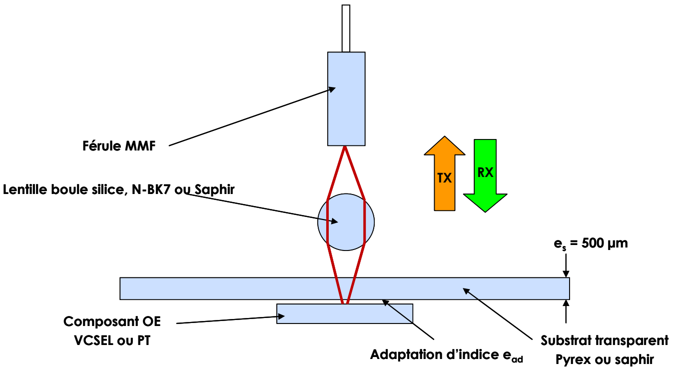

Figure 5.25 Sketch of the optical coupling system

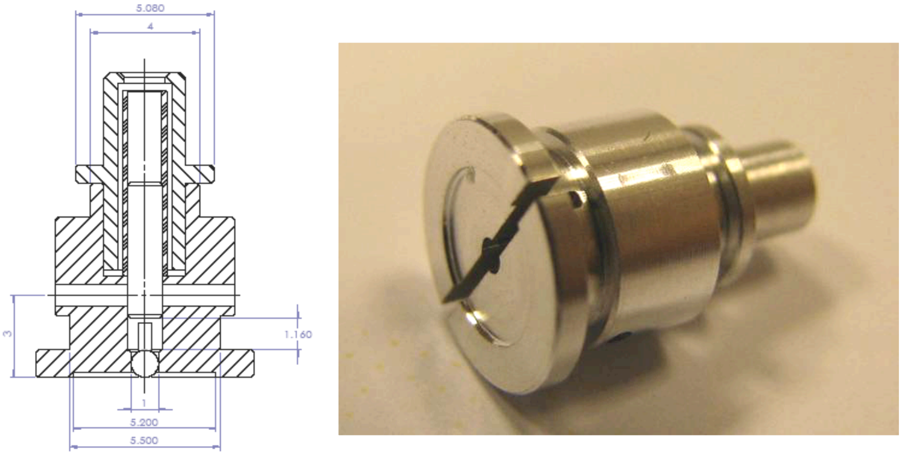

a) b)

Figure 5.26 optical coupling system a) mechanical drawing b) final implementation

The optical coupling system is aligned and glued over the electrical interconnection system shown in Figure 5.23. This is accomplished using a micropositioning lens alignment bench shown in Figure 5.27. The resulting HPT based ROSA is show in Figure 5.28

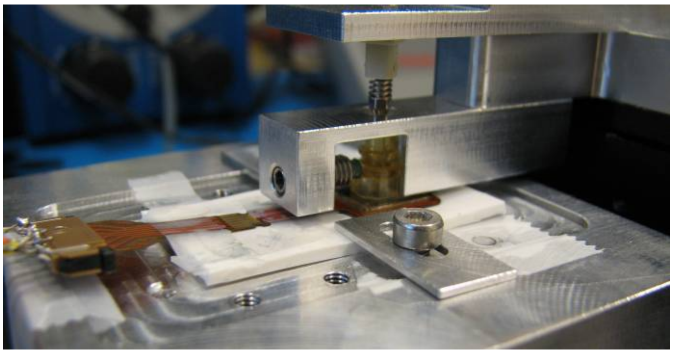

Figure 5.27 Lens alignment micro positioning system

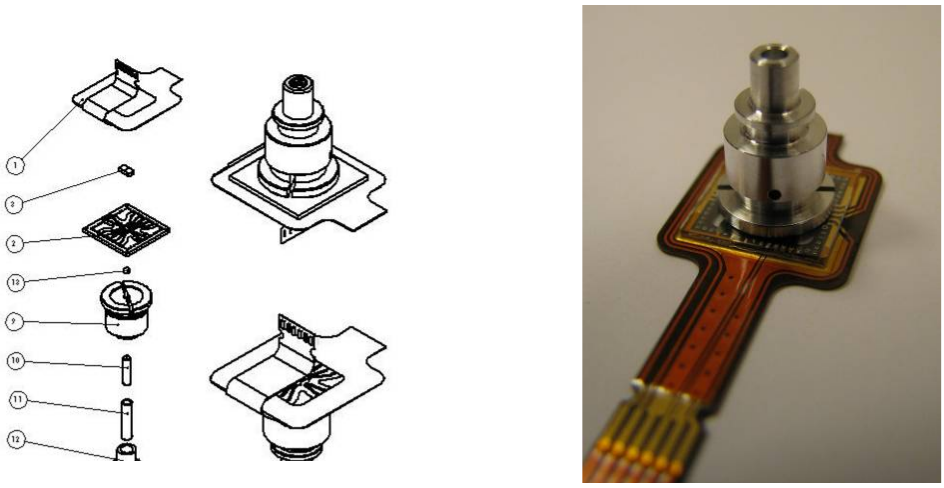

a) b)

Figure 5.28 a) Component breakout of the HPT-based ROSA and b) final assembled and packaged HPT-based ROSA

The alignment of the optical fixture to the electrical system is accomplished by observing the currents in the base of the HPT (Ib1) and in the collector of the HBT (Ic2). The on-wafer measurements were used as reference values for the alignment of the electrical system to the optical system. A negative value in the µA range in the measured Ib1 when Vb1 = 0V, Vb2 = 2.2V, and Vc2 = 2.5V shows that the optical system and electrical system are aligned. However, detecting differences in the µA range to determine alignment relaxes the requirement on the precision of the measurement instruments that will be used. Using a resistor in the Vb1 pin provides a way to lower the base current that is supplied to the HPT. Figure 5.29 shows the electrical system of the HPT-based ROSA before the optical system is positioned on top. The placement of a resistance value in the Vb1 pin is highlighted in the figure.

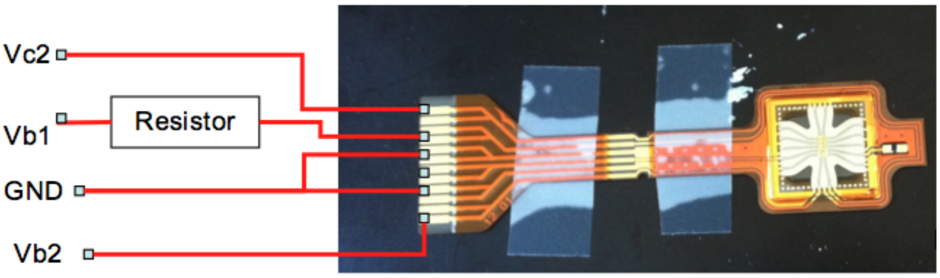

Figure 5.29 HPT-based ROSA without the metal receptacle

Figure 5.30 shows the Ib1 vs. Vbe1 curves with the laser on and laser off with the optical and electrical systems aligned. Measurement with the laser off is similar to when both systems are not aligned. It has three sets of curves showing the different resistance values used for the external resistor (0Ω, 20KΩ, and 200KΩ). Similar to the on-wafer measurement of the GSG HPT cascode, illumination results in the lower of Ib1. In the region before the HPT is forward biased (0V -0.7V, Vb1), the effect of illumination is more pronounced when there is no resistance connected and becomes less pronounced as the external resistance increases. This means that if the base current in the HPT is used in order to verify the alignment, an external resistor in not necessary. However, precise measurement equipment is needed in the alignment bench.

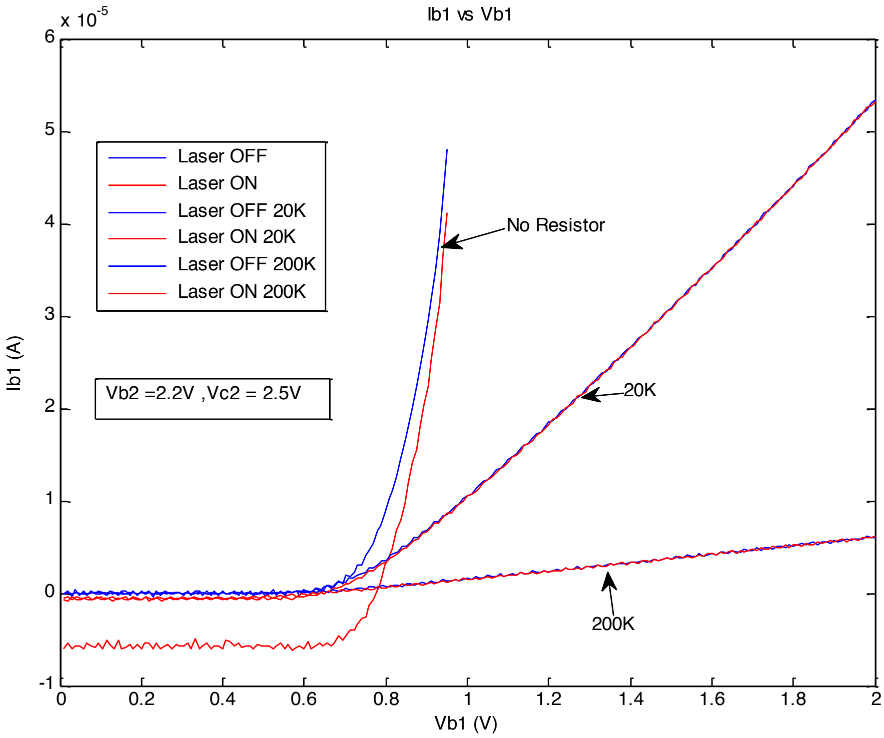

Figure 5.30 Measured Ib1 vs. Vb1 with laser turned ON and OFF for an aligned HPT-based ROSA

Figure 5.31 shows the Ic2 vs. Vb1 curves for the different illumination conditions and the external resistances. In general, HPT illumination causes Ic1 to increase. This increase is more pronounced as the external resistance increases. For Ic1, the external resistance of 200KΩ shows the highest increase in Ic2. This means that if the collector current in the HBT will be used to verify the alignment, a resistor with a minimum value of 200KΩ should be used in the alignment bench. The voltage biasing of the base trough a resistor essential convert the voltage base biasing into current base biasing. The higher resistance value gives lower base currents. The lower base current supplied in the base allows for the extraction of higher responsivity of the HPT. The measured illuminated Ic2 show consistent results with the constant current base bias DC measurement of the HPTs as presented in Chapter 3. One advantage with the use of external resistors is that the measured DC responsivity increases and having the additional benefit of reducing the dark Ic2. Equipment with less precision could be used in the alignment bench setup.

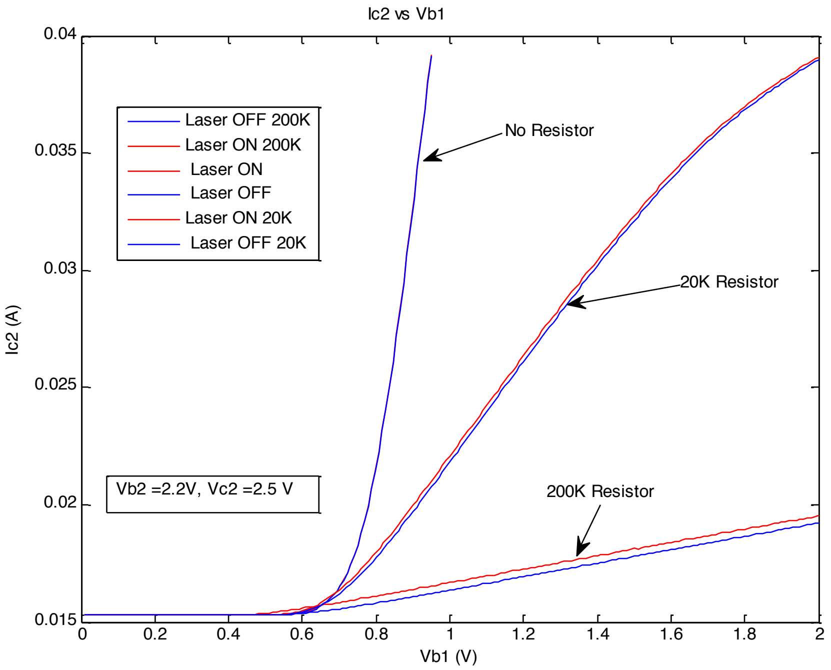

Figure 5.31 Measured Ic2 vs. Vb1 with laser turned ON and laser OFF for an aligned HPT-based ROSA

The final alignment of the optical and electrical systems of the HPT-based ROSA is implemented using the alignment bench shown in Figure 5.27. An external resistor with 200KΩ value is used to easily monitor the increase in Ic1 of an aligned system. Figure 5.32 (a) shows the shows that the Ic1 increases from 15mA to 28mA when Vb1 =0, Vc2 = 2.5V and Vb2 is 2.2V. Figure 5.32 (b) shows the measured Ib1 for the illuminated and non-illuminated conditions.

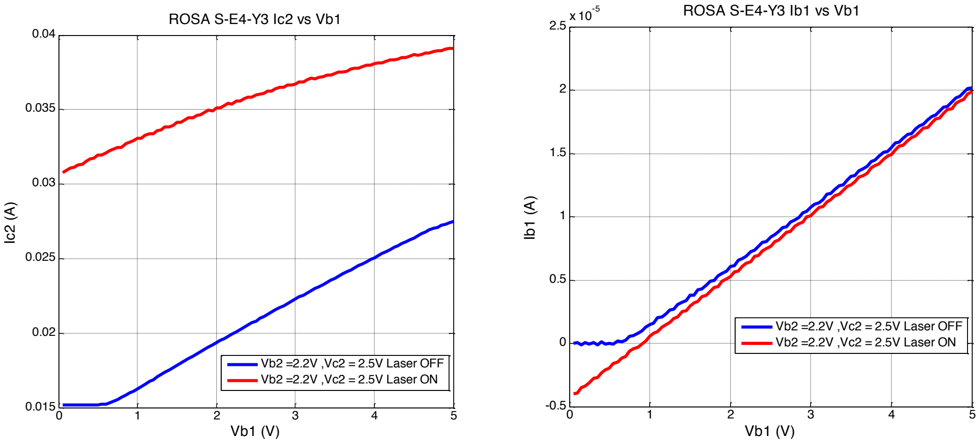

a) b)

Figure 5.32 ROSA measurements with 200KΩ external resistor aligned and non aligned a) Ic vs. Vb1 and b)Ib vs. Vb1

5.4.5 Opto-microwave measurements

This section describes the opto-microwave response analysis of the fabricated HPT cascode ROSA. To proceed with the characterization the ROSA is attached to a test board which provides the biasing voltage from a single bias voltage of 4V. It also provides an SMA connector for the output of the ROSA. Figure 5.33(a) shows the HPT Cascode ROSA test board. Opto-microwave measurements with two different VCSEL were performed. A VI Systems VCSEL, and an ULM photonics TOSA were used the internal voltages were set by the biasing network in the test board to measure at the opto-microwave response of the line as shown in Figure 5.33(b).

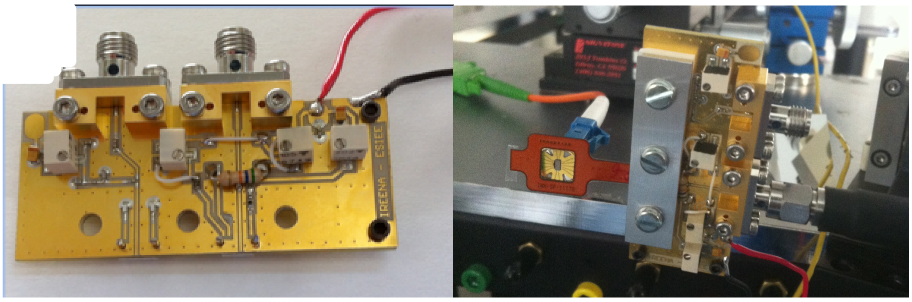

a) b)

Figure 5.33 a) HPT-based ROSA test board b) HPT-based ROSA connected to the HPT-based ROSA test board

Figure 5.34 shows G_{OM} link gain of the link made up VI Systems VCSEL and the HPT-based ROSA (SR7) when the laser is ON and when it is OFF. The measurement with laser OFF shows the noise floor of the system. The measurement with the laser ON shows a dip at 500MHz. This is due to the parasitics in the bias board module.

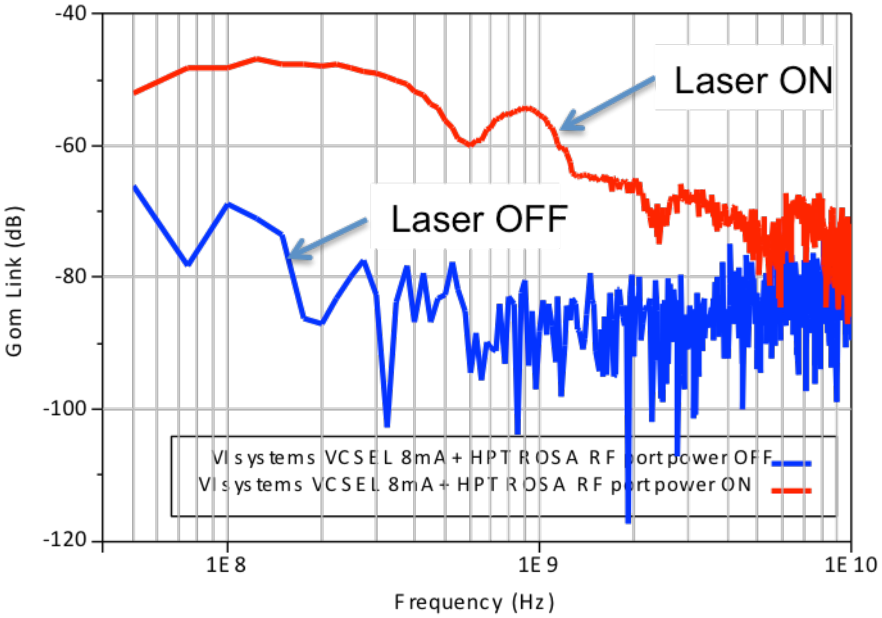

Figure 5.34 G_{OM} vs. frequency of VI systems VCSEL 8mA and HPT-based ROSA Link

Figure 5.35 shows a comparison between the opto-microwave measurements with the VCSEL(1) and HPT cascode ROSA and a VCSEL(2) and HPT cascode response measured on chip. The difference in magnitude in the low frequencies is attributed to the different output power of the VCSELs used. At high frequencies, all the components that are external to the HPT chip affect the response of the link with the HPT-based ROSA.

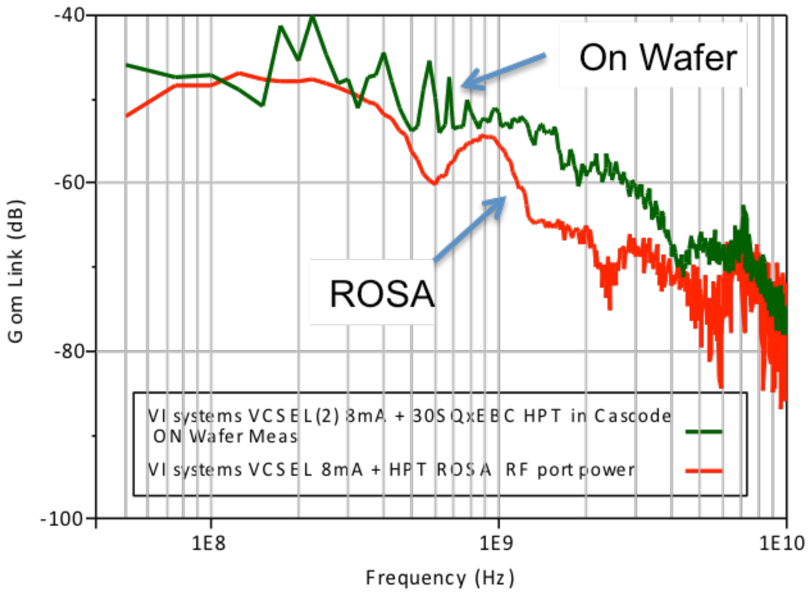

Figure 5.35 GOM vs. frequency of VI systems VCSEL 8mA and HPT-based ROSA and VI systems VCSEL 8mA and CE HPT on chip measurements.

Link measurements were also performed using the ULM Photonics TOSA and the HPT cascode ROSA optical link. Figure 5.36 shows the opto-microwave response of this optical link. A dip is observed in the 200MHz range that is due to the bias board for the TOSA and the second dip at 500MHz is due to the bias board for the ROSA. The opto-microwave link gain measurements of a VCSEL and an HPT ROSA link shows a response of around -70dB to -75 dB in the 4GHz to 6GHz bandwidth. These signal levels are very low to see a response in the EVM test bench. It can be seen in the measurement that by adding an 30dB 12GHz amplifier (Photline) results in a increase in the opto-microwave link gain by 30dB.

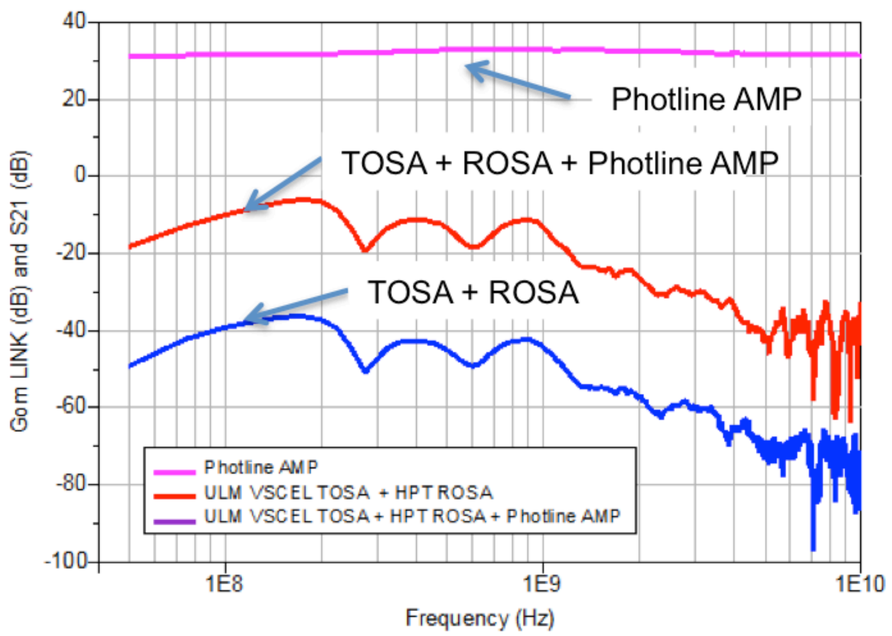

Figure 5.36 Link gain of ULM Photonics TOSA SS3 and Cascode SiGe HPT ROSA SR7

The low response in the 4GHz-6GHz can be attributed to the opto-microwave response of the 30SQxEBC HPT. It can be improved by changing the HPT type to: an extended EBC with etched oxide (30SQxEBCeO), and extended EBC with sic (30SQxEBCsic), or a combination of etched oxide and sic (30SQxEBCeOsic). Another source of improvement could be made by using a smaller optical window to have higher cutoff frequencies at the expense of high optical loses. Another solution is to use a CE HPT- CE HBT pair which was measured to have link response in the -30dB range centered at 5GHz as the core element in the HPT-based OE amplifier. It is also clear in Figure 5.35 that the TOSA electrical interconnections were not optimum and provides a 10dB degradation at some frequencies.

5.5 HPT and Cascaded LNA ROSA

A second generation of ROSA is built up in this section. It is implemented through a hybrid packaging of the 10SQxEBC HPT, and two LNA module, and SMT chip inductors [226]. The schematic of the circuit is shown in Figure 5.37 The HPT is loaded in the base by 50Ω and is configured as in a 2T HPT configuration. The LNA module used is the R3-LNA01 and the inductors are used to bias the HPT collector and match the HPT output to the LNA input impedance.

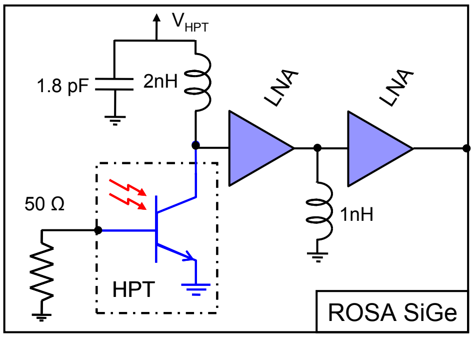

Figure 5.37 Schematic of the Hybrid ROSA

The complete ROSA was mounted on a glass interconnection substrate as shown in Figure 5.38(a) where the two LNA dies and the HPT dies are connected altogether with Gold RF transmission lines and thermo-bumping. The glass substrate is then mounted on a flex PCB and an optical package with its mechanical receptacle is assembled. Figure 3 shows the photo a) from the bottom view and b) from the top view. The dies are mounted through thermo-compression while SMT devices were fixed using conductive glue. The ROSA benefited from electromagnetic simulations and improvement on the electrical lines on the transparent substrate and on SMT devices interconnections [226]. This step was important to get rid off parasitics observed in Section 4 TOSA.

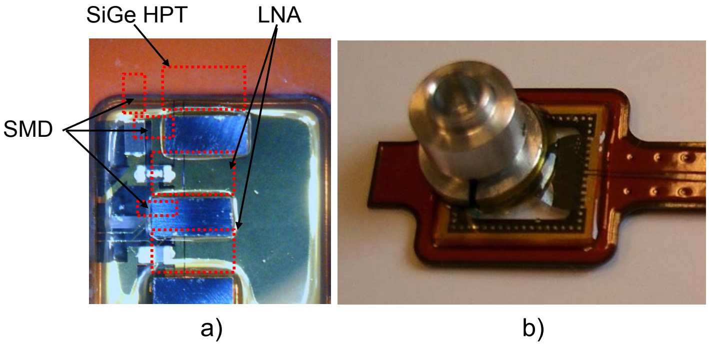

Figure 5.38 SiGe ROSA final integration and packaging: a) bottom view with electrical interconnections; b) Top view with optical mechanical receptacle mounted on the flex PCB

Figure 5.39 provides the extracted opto-microwave gain of the ROSA where both simulation (including the SMT elements) and measurement are shown. We can notice the amplification stage influence at 5 GHz, providing a final gain of -15 dB, which is 15 dB higher than the SiGe HPT gain. A 9dB loss compared to the simulated SiGe ROSA is found that is explained by a 35% coupling efficiency from the fiber to the HPT using the ball lensed coupling technique due to the small size of the HPT.

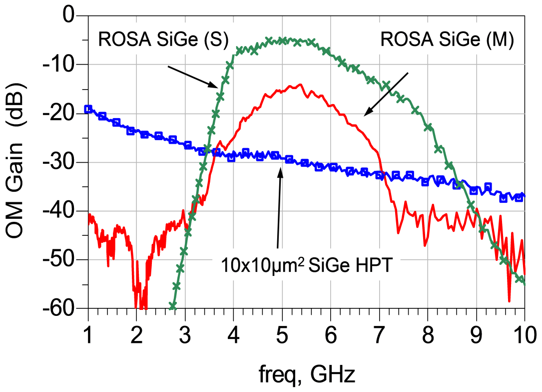

Figure 5.39 Measurements of opto-microwave response of the on probe 2T-HPT under Vce=2.5 V and of the complete SiGe ROSA (simulation and measurement

The fabricated 2T-HPT ROSA was integrated in a RoF link using 10Gbps Philips ULM photonics TOSA. The Error vector Magnitude (EVM) is measured with an Arbitrary Waveform Generator (AWG) with 12 bits resolution, 12 GSa/s sample rate and an analog bandwidth of 5 GHz (Agilent M8190A). An IF-OFDM signal is generated with QPSK modulation subcarriers working at 3.08 Gbit/s over a 1.815GHz channel bandwidth according to the IEEE 802.15.3c standard, HSI mode.

The comparison between the EVM of the link using the same VCSEL connected to a highly linear photodetector from NewFocus (NFPD) and the EVM of the link using the 2T- SiGe HPT is presented in figure 5 (including the back-to-back measurement B2B). A minimum EVM of 25 % is demonstrated at 0dBm input power, which represents a degradation of 16 % compared to Back-to-Back measurement. It is an error free transmission after Cyclic Redundancy Check (CRC) compensation. This is a first promising result that could be improved by further optimizations, both on the HPT and LNA stage design.

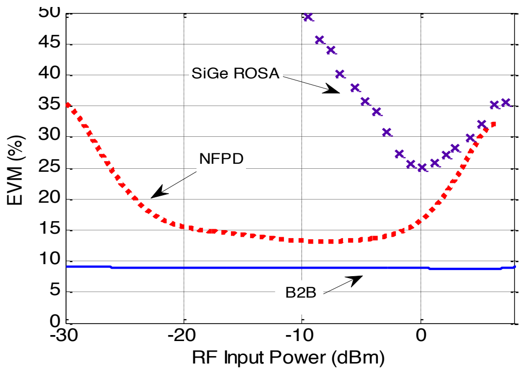

Figure 5.40 EVM curve of the light source module plus SiGe ROSA comparing with the NFPD at an IF of 5 GHz

In summary, a hybrid ROSA module was designed and fabricated that combines two cascaded LNAs to a 2T-SiGe-HPT. An overall -15dB opto-microwave gain is achieved at 5 GHz with a 35% optical coupling efficiency. A minimum EVM of 25 % was measured, which represents a degradation of 16 % compared to Back-to-Back measurement. These results, although preliminary, can be seen as very promising as it shows an error free transmission of a 3.08 Gbps IEEE 802.15.3c HSI signal at 5 GHz, after CRC correction.

5.6 Conclusion

This chapter presented a proposed architecture of a 60 GHz IF RoF system. It uses a directly modulated VSCEL as the optical source and an HPT as the optical detector. In the system modeling and design, the HPT should have a responsivity of at least 28dB at 5 GHz which translates to 4A/W and a cutoff frequency of 50MHz. An amplifier with a gain of 10dB should be integrated with the HPT in the same SiGe process to provide suitable signal levels for external processing. An adjustable RF gain system is included in the optical receiver chain to provide the necessary amplification to compensate for a lower response in the HPT block.

Different cascode amplifier circuits were designed for operation at the 5GHz and 17GHz. The circuits are intended to be used as post amplifying stages for the SiGe HPT.

The design and fabrication of the preliminary version of the HPT based ROSA was also presented. It is a collaborative work between ESYCOM and Innoptics. It uses an 30x30µm^2 HPT based cascode circuit which has better response at 5GHz taking into account optical losses. Characterization of the fully assembled version 1 of HPT-based ROSA showed responses in the range of -70dB to -75dB which is due to additional coupling losses from the optical assembly and parasitic losses in the electrical packaging.

An HPT and LNA circuit is chosen to be the circuit configuration for the implementation of the second version of the HPT based ROSA using a hybrid packaging of the 10SQxEBC HPT configured in the 2T-HPT configuration together with, two LNA_01 circuits and two SMT inductors. An overall -15dB opto-microwave gain is achieved at 5 GHz with a 35% optical coupling efficiency. A minimum EVM of 25% was measured, which represents a degradation of 16 % compared to Back-to-Back measurement. These results, although preliminary, can be seen as very promising as it shows an error free transmission of a 3.08 Gbps IEEE 802.15.3c HSI signal at 5 GHz, after CRC correction.

These characterization show that a photodetection module could be implemented in a SiGe process technology without additional processing steps. This means that we can implement a fully integrated OEIC receiver using a single process technology.

6 Conclusions and Perspective

Radio over Fiber technology is a key technology that merges wireless and optical networks. It is traditionally used to extend the reach of wireless signals in an external environment. Current advances in wireless media communication technologies transforms the indoor environment such as building and large area households to become high data rate environments. Higher frequency bands in the 60GHz range are used to accommodate the very high-speed wireless requirements. However, the 60GHz offers only high speed short range point to point communications. Radio over fiber is seen as a solution to extend its reach with the use of remote antenna units in distributed antenna configuration. Implementation cost is key consideration for the deployment of such RoF system in a home environment. A tight integration of the electronic modules and the use low cost optical component is essential. The core of this PhD was focused on the advantage of SiGe to provide a full Silicon integration of the 850nm detectors to prepare further OE-MMIC on silicon together with SiGe ICs.

The developments in SiGe based process technologies with transistor f_T in the range of a few hundred GHz makes it a good candidate to implement the RF and microwaves circuits that are essential to the implementation of RoF system. SiGe based technologies also benefits from its compatibility with Silicon CMOS circuits that are needed to implement dense and high-speed digital circuits whenever it is needed. A key benefit of SiGe based process technology is capability to have optical detection in the optical wavelength range of 800nm up to 1000nm. This offers the possibility of integrating a photodetection element with the electronics circuit. SiGe-based phototransistors as photodetectors in these systems would offer lower cost remote antenna units. Thus resulting to the implementation of a monolithically integrated optoelectronic receiver chip as well as driver circuits.

In this research, we have chosen to implement the SiGe HPT structures using an 80GHz SiGe Bipolar process (SiGe2RF) from Telefunken GmbH. The basic HBT structure from the process technology is modified in order to design the HPT structures. This resulted in two main SiGe HPT topologies: 1) the Base and Collector regions are extended to collect the light and become the optical window (xBC HPT), 2) the Emitter, Base and Collector regions are altogether extended to function as the optical window (xEBC HPT). Additional enhancements to improve the optical reception are applied whenever possible. These include the removal of the silicided titanium (TiSi), etching of the topmost oxide and nitride layers, and variations in the optical window sizes.

The different methods for the characterization of the HPT were presented. The performances of a 0.5x10μm^2 HBT and a 10SQxBC HPT with identical intrinsic transistor size of 0.5x10μm^2 are compared. It showed decrease in current gain β, increase in Early Voltage, lesser maximum RF gain at 50 MHz, reduction in cutoff frequency at maximum RF gain bias thus still achieving a maximum f_T of 41.54GHz. The different HPT structures were verified electrically and the modifications in a reference HBT to design an HPT showed process compatibility despite process rule violations. This confirms the viability of our approach.

The DC optical measurements showed that simply extending the base and collector as seen in xBC HPTs results in measurable optical responsivities. The removal of silicided titanium (TiSi) and the etching of the oxide provide the needed vertical stack variation to improve responsivites by a factor of 5.7 times and 6.7 times with values of 0.85A/W

(Vce = 2V, Ib = 5µA) and 1A/W (Vce = 2V, Ib = 5µA) respectively, with only a slight decrease of the transistor current gain from 305 to 292.

Comparisons of different 10x10µm^2 HPT shows however that the extended emitter base collector (xEBC) HPT exhibits the highest DC responsivity with a value of 2.5 A/W (Vce = 2V, Ib = 5µA), including the coupling losses from the optical probe. This is due to the high electric current gain of this structure which is as high as 447. It also proved that illumination through the emitter does not interfere with the optical absorption in the base and collector.

We used an on wafer opto-microwave measurement bench to characterize the HPT in terms of its opto-microwave gain G_{OM} and frequency response. Using the full extended emitter structure (xEBC) HPT shows better performance by 6.5dB when compared to a Base-collector extended HPT only, even with the improvement of the removal of TiSi and oxide etching (xBCrTeO). The etching in the oxide in an xEBC HPT or an xBC HPT also improves further the optical response typically by 2dB.

The two operation modes of the HPT were analyzed to provide an understanding in the operation and characterization of the different HPT structures. In the photodiode mode (PD) mode, the effect on the optical path of the vertical stack of the different HPT structures is directly visible.

The fabricated HPTs have a three terminal (3T-HPT) configuration. This means that the base could be biased by a current source or a voltage source. The study in the type of biasing in the base has a strong influence on the DC responsivity of the HPT. The effect of the constant current CC and constant voltage CV bias in the base was studied and its effects could be summarized as follows. In the illuminated condition, the average power of the optical signal shifts the bias in the base of the HPT. In the CV condition, the measured current in the base has a lower value as compared to the non-illuminated base current from the same Vbe bias. This forces the HPT to operate in a lower base bias and shifted current gain. In the CC condition, the measured Vbe is higher that the non-illuminated Vbe. This indicates that base bias is shifted to a higher Ib bias due to the photocurrent and the current gain β is shifted as well. The extracted DC responsivity at the same illuminated Ic bias value shows that CC biased base will have higher responsivity compared to HPT in the CV bias, specially at low Ib where the 3T-HPT behaves has a 2T-HPT like behavior. Responsivities as high a 12A/W are reported in the CC mode with a 50x50µm^2 (R2-50SQxEBC) while the maximum value of 0.7A/W are 17 times lower

However, the experiments have shown that the type of biasing in the base has no effect in the opto-microwave behavior, because the opto-microwave responsivity is a small signal property and the HPT is operated in an illuminated Ic bias that is fixed by the base bias and the average power of the optical beam. However the CV mode proved to allow a larger amplitude of biasing conditions, independent on the optical power that is injected.

PD mode measurements show that the xEBC topology has an advantage as compared to the xBC topology as the optical transmission is improved. However, the xEBC's abilities to amplify the photodetected signal in the HPT mode is also further improved by at least 4.5dB as compared to xBC HPTs. This results in a total 11dB improvement on the total G_{OM} xEBC HPTs as compared to xBC HPTs . The cutoff frequency on the HPT mode G_{OM} proved to be improved by the use of xEBC topology typically by a 30% ratio.

The opto-microwave characterization of 10x10µm^2 HPT (R1-10xSQxBCrT) showed a 2dB optical gain G_{OPT} when comparing the PD and HPT mode, with an opto-microwave cutoff frequency of the HPT in the 170MHz range. Further characterizations on the 10xEBC HPT structure (R2-10SQxEBC) shows that it exhibits the highest measured opto-microwave response at 5GHz with a value-32dB as compared with the R2-50SQxEBC HPTs with a value of -42dB. Despite high coupling losses associated with the 26µm spot size used for the illumination. The R2-20SQxEBC offers very high responsivity in the low frequency of operation due to better coupling with the optical beam. In the high frequency of operation, its response is only lower by 1 dB at 5GHz compared to the R2-10SQxEBC and is practically the same value for operation above 6GHz. The 20SQxEBC offers a good trade off between optical coupling and frequency response

Experiments on the external HPT base loads shows that the opto-microwave response in high frequencies could be optimized with the use of impedances that have a positive phase angle. The simulations on the passive internal base loads available in the SiGe2RF technology showed that resistor and capacitor loads shows improvement up to 25dB in the low frequency region and the inductor loads shows improvement up to 5dB in the 0.5GHz-1GHz region. This means that the HPT opto-microwave frequency could be tailored with the use of an adequate base load circuit. The measurements using an HPT with an internal base load shows that the base load effect on the HPT can be properly observed by configuring the biasing of the HPT to be independent on the base load. The fabricated modules with an inductor in series to the base of the HPT is severely affected by the DC bypass capacitor of to provide the base bias to the HPT. A redesign should be useful, but this design as a blind guess was still useful to validate our simulations in comparison to measurements. The fabricated modules with a capacitor in series to the base of the HPT allowed for the 2T HPT mode of operation of the HPT in DC.

Measurements in the HPT-HBT pair shows that the HPT-HBT pair shows improved performances as compared to a single HPT. The HPT cascode exhibits a 1.4dB increase in response as well as an increase in the cutoff frequency by 25% up to 344MHz for a R2-10SQxEBC HPT. The simple HPT-HBT cascade has a very tight biasing range but offers at most a 30dB increase in the low frequency. While its cutoff frequency is almost reduced by 40% as compared to a single HPT, it still provides a 10dB improvement at 5GHz and reach the level of the single HPT configuration at 10GHz.

An architecture of a 60 GHz IF RoF system is then proposed in the ORIGIN project. It uses a directly modulated VSCEL as the optical source and an HPT as the optical detector. In the system modeling and design, the HPT should have a responsivity of at least 28dB at 5 GHz which translates to 4A/W and a cutoff frequency of 50MHz. An amplifier with a gain of 10dB should integrated with the HPT in the same SiGe process to provide suitable signal levels for external processing. This consisted a target for the fabrication of a complete ROSA base on our SiGe HPT.

Different cascode amplifier circuits were then designed for operation at the 5GHz and 17GHz. The circuits are intended to be used as post amplifying stages for the SiGe HPT.

The design and fabrication of the preliminary version of the HPT based ROSA was also presented. It is a collaborative work between ESYCOM and Innoptics. It uses an 30x30µm^2 HPT based cascode circuit which has better response at 5GHz taking into account optical losses. The cascode topology was expected to prevent from the unknown output impedance of the HPT at the time of its first development and then to offer an ease and security in the ROSA design. On-chip characterization showed a gain in the range of -66dB to -69dB at 5GHz. However, characterization of the fully assembled version 1 of HPT-based ROSA showed responses in the range of -70dB to -75dB which is due to additional coupling losses from the optical assembly and essentially parasitic losses in the electrical packaging.

An HPT and LNA circuit is then chosen to be the circuit configuration for the implementation of a second version of the HPT based ROSA using an electromagnetically optimized hybrid packaging of the 10SQxEBC HPT configured in the 2T-HPT configuration. It integrates the HPT together with, two LNA_01 circuits and two SMT inductors. An overall -15dB opto-microwave gain is achieved at 5 GHz with a 35% optical coupling efficiency. A minimum EVM of 25% was measured. This represents a degradation of 16 % compared to Back-to-Back measurement. These results, although preliminary, can be seen as very promising as it shows an error free transmission of the signal (3.08 Gbps IEEE 802.15.3c HSI signal at 5 GHz), after CRC correction (BER $<10^{-5}$).

These characterization shows that a photodetection module could be implemented in a SiGe process technology without additional processing steps. This means that we can implement a fully integrated OEIC receiver using a single process technology.

In this research, several aspects of the HPTs were explored: implementation, characterization, and integration for amplifiers for OE-MMIC application. As the SiGe technologies continually evolve with faster transistors, the study on the implementation of further SiGe HPT should be present using these evolving technologies as well. This adds another dimension to the possible application of these high speed silicon based technologies.

The use of the SiGe HPT for opto-microwave amplifier applications offers fully integrated OE-MMIC functions for Radio over fiber applications. Further study on the SiGe HPTs use in other function in an optical system or radio over fiber system should also be pursued. These include OE-Mixers and OE oscillators and integrated RoF remote antenna front ends where in the optical receiver and receiving amplifiers are integrated with laser driver circuits.

Résumé

Ce travail de thèse présente le développement de phototransistors bipolaires à hétérojonction (HPT) SiGe/Si mis en œuvre dans une technologie de processus 80GHz SiGe bipolaire pour des applications de transmission Radio-sur-Fibre. Le cas particuliers d'un réseau domestique sans fil à infrastructure optique est considéré pour lequel le critère de coût est prépondérant. Le fonctionnement des ce HPT SiGe/Si est étudié sous une longueur d'onde optique de 850 nm en exploitant des fibres optique multimode (MMF) suffisantes pour les besoins de bande passante dans un environnement de réseau domestique. Le HPT SiGe/Si est également développé dans l'objectif de permettre une intégration combiné du photorécepteur et circuit intégré monolithiquement, conduisant à des structures de type *Opto-electronic Microwave Monolithically Integrated Circuit* (OE-MMIC), visant à poursuivre l'intégration et la réduction des cours.

Deux topologies ont été explorées principalement: 1) une topologie avec élargissement de la base et du collecteur (xBC HPT) et 2) une topologi avec élargissement des trois régions de base, émetteur et collecteur simultanément (xEBC HPT). Des variations technologies ont été réalisées et analysées en détail, à la fois en terme de couches verticales que de dessin de masque (layout). Les mesures ont démontré la validité technologique de chacune de ces approches, et permis d'isoler l'impact sur les performances statiques et dynamiques de chacune de ces couches. Une solution de type xEBC se montre ainsi préférable pour le cas de composants de petites dimensions inférieure à 50x50µm^2, dans la bande du GHz.

Les phototransistors sont développés dans une configuration à trois terminaux (3T-HPT). Le type de polarisation de la base du HPT influe également sur la responsivité du phototransistor. Une polarisation de courant constant (CC) démontre une plus grande responsivité par rapport au cas d'une polarisation en tension (CV). Une anlyse détaillée montre aussi les différences de responsivité mesurées en continue et celles mesurées en basse fréquence à 50MHz. La connexion de base permet également de varier l'impédance de charge présentée sur celle-ci. La théorie de l'adaptation des phototransistors est rappelée. L'effet de différentes impédances de base sont étudiées par la simulation et la mesure des circuits réalisés technologiquement.

L'intégration du phototransistor au sein d'un circuit élémentaire est enfin explorée. Différentes configurations de paires HPT - HBT sont étudiées, formant des circuits élémentaires. Des caractérisations expérimentales permettent de vérifier l'amélioration apportées par ces topologies par rapport au phototransistor unique. Enfin, un phototransistor SiGe en configuraiton 2T-HPT est utilisé et intégré avec succès pour la première fois au sein d'un module de type Receiving Optical Sub Assembly (ROSA) pour la mise au point d'une transmission Radio-sur-Fibre multiGigabit par seconde pour un réseau domestique.

Acronyms

2STD	Two step de-embedding
3T-HPT	Three terminal heterojunction phototransistor
AMPS	Advanced mobile phone system
APD	Avalanche photodiode
CMOS	Complementary metal oxide semiconductor
COTS	Commercial off the shelf
CT2	Cordless Telephone 2nd Generation
D-OILO	Direct optical injection-locked oscillators
DAS	Distributed Antenna Systems
DFB	Distributed feedback
DGCIS	Générale de la Compétitivité, de l'Industrie et des Services
EA	Electro-absorption
EIRP	Effective Isotropic Radiated Power
EMB	enhanced modal bandwidth
EML	Externally modulated lasers
EVM	Error vector magnitude
FCC	Federal Communications Commission (US)
FDMA	frequency division multiple access
GSG	Ground-Signal-Ground
GSM	Global system for mobile communications
HD TV	High definition television
HDMI	High-definition multimedia interface
HPT	Heterojunction bipolar phototransistors
IEEE	Institute of Electrical and Electronics Engineers (US)
IF IM-DD	Intermediate frequency intensity-modulation direct detection
IM-DD	Intensity-modulation direct detection
LAN	Local area network
LO	local oscillator
MAG	Maximum available gain
MB-OFDM	Multiband Orthogonal Frequency Division Multiplexing
MMF	multi mode fiber
MQW	multi quantum well
MSM	metal semiconductor metal
MZI	Mach-Zender Interferometer
NUT	Network under test
OE-MMIC	Optoelectronic monolithic microwave integrated circuits
OEIC	Optoelectronic integrated circuits
OFL	Overfill launch
OIL-SOM	Optical injection locked
OM2	Optical multi-mode 2
ONoC	Optical network on chip
OPD	Open de-embedding

ORIGIN	Optical Radio Infrastructure for Gigabit Indoor Network
QAM	Quadrature amplitude modulation
RF IM-DD	RF intensity modulated-direct detection
RIN	Relative intensity noise
RoF	Radio over fiber
ROSA	Receiver optical sub-assembly
SCR	Space charge region
SFDR	Spurious-free dynamic range
SIC	Selectively implanted collector
SIMOX	Separation of by implantation of oxygen
SMF	Single mode fiber
SOI	Silicon on insulator
TDD	Time division duplex
TIA	Transimpedance amplifier
TiSi	Titanium Silicide
TOSA	Tranceiver optical subassembly
TROF	Transceiver Radio over Fiber
UMTS	Universal mobile telecomunications system
UWB	Ultra-Wideband
VCSEL	Vertical cavity surface emitting laser
VNA	Vector network analyzer
WCDMA UMTS	Wideband code division multiple access universal mobile telecomunications system
WiGig	Wireless gigabit
WirelessHD	Wireless high definition

Bibliography

[1] W. Alliance, "WiMedia MAC-PHY Interface Specification," WiMedia Alliance Inc., Dec. 2009.

[2] A. WiGig, "WiGig - Defining the Future of Multi-Gigabit Wireless Communicaitons," Wireless Gibabit Alliance, Jul. 2010.

[3] K. Mandke, H. Nam, L. Yerramneni, and C. Zuniga, "The evolution of UWB and IEEE 802.15. 3a for very high data rate WPAN," *EE381K-11 Wireless Communications UWB Group, the University of Texas at Austin*, 2003.

[4] A. WirelessHD, "WirelessHD Specification Overview ," Jun. 2010.

[5] Agilent, "Wireless LAN at 60 GHz - IEEE 802.11ad Explained," Agilent Technologies, May 2013.

[6] X. Yu, T. B. Gibbon, D. Zibar, and I. T. Monoroy, "UWB-over-multimode-fiber technology for short range communication networks," *Proceedings Symposium IEEE/LEOS Benelux Chapter*, pp. 79–83, 2008.

[7] S. Li, "UWB radio-over-fiber system using direct modulated VCSEL," University of Waterloo, 2007.

[8] A. Pizzinat, I. Louriki, B. Charbonnier, F. Payoux, S. Meyer, M. Terre, C. Algani, A. L. Billabert, J. L. Polleux, C. Sillans, H. Jaquinot, S. Bories, Y. Le Guennec, and G. Froc, "Low cost transparent radio-over-fibre system for UWB based home network," presented at the Optical Communication, 2008. ECOC 2008. 34th European Conference on, 2008, pp. 1–3.

[9] Y. X. Guo, V. H. Pham, M. L. Yee, L. C. Ong, and B. Luo, "Performance Study of MB-OFDM Ultra-Wideband Signals over Multimode Fiber," presented at the Ultra-Wideband, 2007. ICUWB 2007. IEEE International Conference on, 2007, pp. 429–431.

[10] M. Crisp, R. V. Penty, I. H. White, and A. Bell, "Wideband radio over fiber distributed antenna systems for energy efficient in-building wireless communications," *Vehicular Technology Conference (VTC 2010-Spring), 2010 IEEE 71st*, pp. 1–5, 2010.

[11] H. Al-Raweshidy and S. Komaki, "Radio Over Fiber Technologies for Mobile Communications Networks," no. 3, Artech House Publishers, 2002, p. 436.

[12] D. Wake, "Trends and prospects for radio over fibre picocells," *Microwave Photonics, 2002. International Topical Meeting on*, pp. 21–24, 2002.

[13] D. Wake, M. Webster, G. Wimpenny, K. Beacham, and L. Crawford, "Radio over fiber for mobile communications," *Microwave Photonics, 2004. MWP'04. 2004 IEEE International Topical Meeting on*, pp. 157–160, 2004.

[14] J. Guillory, E. Tanguy, A. Pizzinat, B. Charbonnier, S. Meyer, C. Algani, and J. O. Hongwu Li Lightwave Technology, "A 60 GHz Wireless Home Area Network With Radio Over Fiber Repeaters," *J Light Tech*, vol. 29, no. 16, pp. 2482–2488, 2011.

[15] J. Guillory, F. Richard, P. Guignard, A. Pizzinat, S. Meyer, B. Charbonnier, L. Guillo, C. Algani, H. Li, and E. Tanguy, "Towards a multiservice & multiformat optical Home Area Network," *Electronic Media Technology (CEMT), 2011 14th ITG Conference on*, pp. 1–6, 2011.

[16] H. B. Kim, "Radio over fiber based network architecture," Universitätsbibliothek, 2005.

[17] A. J. Cooper, "'Fibre/radio' for the provision of cordless/mobile telephony services in the access network," *Electron. Lett.*, vol. 26, no. 24, pp. 2054–2056, 1990.

[18] E. I. Ackerman and C. H. Cox, "RF fiber-optic link performance," *Microwave Magazine, IEEE*, vol. 2, no. 4, pp. 50–58, 2001.

[19] S. Weisser, J. D. Ralston, E. C. Larkins, I. Esquivias, P. J. Tasker, J. Fleissner, and J. Rosenzweig, “High-frequency characterization of 30 GHz p-type modulation-doped In/sub 0.35/Ga/sub 0.65/As/GaAs MQW lasers,” *Electron Devices Meeting, 1992. IEDM '92. Technical Digest., International*, pp. 1009–1011, 1992.

[20] D. Chen, H. R. Fetterman, A. Chen, W. H. Steier, L. R. Dalton, W. Wang, and Y. Shi, “Demonstration of 110 GHz electro-optic polymer modulators,” *Applied Physics Letters*, vol. 70, no. 25, pp. 3335–3337, 1997.

[21] S. Z. Zhang, V. Kaman, A. Keating, Y.-J. Chiu, P. Abraham, and J. E. Bowers, “30 Gbit/s operation of a traveling-wave electroabsorption modulator,” presented at the Optical Fiber Communication Conference, 1999, and the International Conference on Integrated Optics and Optical Fiber Communication. OFC/IOOC '99. Technical Digest, 1999, vol. 3, pp. 290–292.

[22] Bin Liu, J. Shim, Y.-J. Chiu, A. Keating, J. Piprek, and J. E. Bowers, “Analog characterization of low-voltage MQW traveling-wave electroabsorption modulators,” *J Light Tech*, vol. 21, no. 12, pp. 3011–3019, 2003.

[23] M. Möhrle, “1.3um Electroabsorption Modulated Laser Diodes.” Fraunhofer Heinrich Hertz Institute, pp. 1–2, 06-Feb-2012.

[24] D. Opatic, “Radio over Fiber Technology for Wireless Access,” presented at the Ericsson MIPRO 2009, 2009, pp. 1–6.

[25] S. Iezekiel, “Measurement of microwave behavior in optical links,” *Microwave Magazine, IEEE*, vol. 9, no. 3, pp. 100–120, 2008.

[26] A. Flatman, “In-premises optical fiber installed base analysis to 2007,” presented at the IEEE 802.3 10GBE Over FDDI-Grade Fiber Study Group, Orlando, FL, 2004.

[27] L. Raddatz, D. Hardacre, I. H. White, R. V. Penty, D. G. Cunningham, M. R. T. Tan, and S. Y. Wang, “High bandwidth data transmission in multimode fibre links using subcarrier multiplexing with VCSELs,” *Electron. Lett.*, vol. 34, no. 7, p. 686, 1998.

[28] E. J. Tyler, M. Webster, R. V. Penty, and I. H. P. T. L. I. White, “Penalty free subcarrier modulated multimode fiber links for datacomm applications beyond the bandwidth limit,” *Photonics Technology Letters, IEEE*, vol. 14, no. 1.

[29] D. Wake, S. Dupont, C. Lethien, J. P. Vilcot, and D. E. L. Decoster, “Radiofrequency transmission of 32-QAM signals over multimode fibre for distributed antenna system applications,” *Electron. Lett.*, vol. 37, no. 17, p. 1087, 2001.

[30] P. Hartmann, M. Webster, A. Wonfor, and J. D. Ingham, “Low-cost multimode fibre-based wireless LAN distribution system using uncooled, directly modulated DFB laser diodes,” *Proc ECOC*, 2003.

[31] X. Qian, P. Hartmann, J. D. Ingham, A. Diab, R. V. Penty, and I. H. White, “Modelling and simulation-based prediction of radio transmission over multimode fibre,” presented at the 2004 IEEE International Topical Meeting on Microwave Photonics, 2004, pp. 165–168.

[32] C. Carlsson, H. Martinsson, A. Larsson, and A. M. P. 2. M. '. 2. I. T. M. O. Alping, “High performance microwave link using a multimode VCSEL and a high-bandwidth multimode fiber,” *Microwave Photonics, 2001. MWP '01. 2001 International Topical Meeting on*, Jan. 2001.

[33] M. Chia, B. Luo, M. L. Yee, and E. Hao, “Radio over multimode fibre transmission for wireless LAN using VCSELs,” *Electron. Lett.*, vol. 39, no. 15, pp. 1143–1144, 2003.

[34] K. A. Persson, C. Carlsson, A. Alping, A. Haglund, J. S. Gustavsson, P. Modh, and A. E. L. Larsson, “WCDMA radio-over-fibre transmission experiment using singlemode VCSEL and multimode fibre,” *Electron. Lett.*, vol. 42, no. 6,

Mar. 2006.

[35] C. Lethien, C. Loyez, and J. P. Vilcot, “Potentials of radio over multimode fiber systems for the in-buildings coverage of mobile and wireless LAN applications,” *IEEE Photon. Technol. Lett.*, vol. 17, no. 12, pp. 2793–2795, 2005.

[36] C. Carlsson, A. Larsson, and A. Alping, “RF Transmission Over Multimode Fibers Using VCSELs - Comparing Standard and High-Bandwidth Multimode Fibers,” *J. Lightwave Technol.*, vol. 22, no. 7, pp. 1694–1700, Jul. 2004.

[37] M. Sauer, A. Kobyakov, L. Fields, F. Annunziata, J. Hurley, and J. O. F. C. C. 2. A. T. 2. N. F. O. E. C. O. 2. George, “Experimental investigation of multimode fiber bandwidth requirements for 5.2 GHz WLAN signal transmission,” presented at the Optical Fiber Communication Conference, 2006 and the 2006 National Fiber Optic Engineers Conference. OFC 2006, 2006.

[38] M. Sauer, A. Kobyakov, J. E. Hurley, and J. M. P. 2. M. 2. I. T. M. O. George, “Experimental Study of Radio Frequency Transmission over Standard and High-Bandwidth Multimode Optical Fibers,” *Microwave Photonics, 2005. MWP 2005. International Topical Meeting on*, Jan. 2005.

[39] A. Nkansah, A. Das, C. Lethien, J. P. Vilcot, N. J. Gomes, I. J. Garcia, J. C. Batchelor, and D. Wake, “Simultaneous dual band transmission over multimode fiber-fed indoor wireless network,” *IEEE Microw. Wireless Compon. Lett.*, vol. 16, no. 11, pp. 627–629, 2006.

[40] M. L. Yee, L. C. Ong, C. K. Sim, B. Luo, and A. Alphones, “Low-cost Radio-Over-Fiber in-building distribution network for WLAN, UWB and digital TV broadcasting,” presented at the Microwave Conference, 2006. APMC 2006. Asia-Pacific, 2006, pp. 95–98.

[41] M. Y. Wah, C. Yee, and M. L. Yee, “Wireless ultra wideband communications using radio over fiber,” presented at the Ultra Wideband Systems and Technologies, 2003 IEEE Conference on, 2003, pp. 265–269.

[42] M. L. Yee, Y.-X. Guo, V. H. Pham, and L. C. Ong, “WiMedia Ultra-Wide Band Transmission in Radio over Fiber using Multimode Fiber,” *Lasers and Electro-Optics Society, 2007. LEOS 2007. The 20th Annual Meeting of the IEEE*, pp. 335–336, 2007.

[43] M. Yee, H. Chung, P. Tang, L. C. Ong, B. Luo, M. T. Zhou, Z. Shao, and M. Fujise, “850nm Radio-Over-Fiber EVM Measurements for IEEE 802.11g WLAN and Cellular Signal Distribution,” presented at the 2006 European Microwave Conference, 2006, pp. 882–885.

[44] M. J. Crisp, S. Li, A. Watts, R. V. Penty, and I. H. White, “Uplink and Downlink Coverage Improvements of 802.11g Signals Using a Distributed Antenna Network,” *J Light Tech*, vol. 25, no. 11, pp. 3388–3395, 2007.

[45] M. Sauer, A. Kobyakov, and J. George, “Radio over fiber for picocellular network architectures,” *J. Lightwave Technol.*, vol. 25, no. 11, pp. 3301–3320, 2007.

[46] L. C. Ong, M. L. Yee, and B. Luo, “Transmission of Ultra Wideband Signals through Radio-over-Fiber Systems,” *Lasers and Electro-Optics Society, 2006. LEOS 2006. 19th Annual Meeting of the IEEE*, pp. 522–523, 2006.

[47] A. Pizzinat, P. Urvoas, and B. Charbonnier, “1.92G bit/s MB-OFDM Ultra Wide Band Radio Transmission over Low Bandwidth Multimode Fiber,” *CORD Conference Proceedings*, pp. 1–3, Mar. 2007.

[48] T. K. Woodward and A. V. Krishnamoorthy, “1-Gb/s integrated optical detectors and receivers in commercial CMOS technologies,” *Selected Topics in Quantum Electronics, IEEE Journal of*, vol. 5, no. 2, pp. 146–156, 1999.

[49] I. Ogawa, “100-Gbit/s Optical Receiver Front-end Module Technology,” pp. 1–7, Nov. 2011.

[50] A. Moloney, “A CMOS Monolithically Integrated Photoreceiver Incorporating an Avalanche Photodiode,” 2003.

[51] S. Malyshev, *State of the art high-speed photodetectors for microwave photonics application. Microwaves, Radar and Wireless Communications*, no. 7499653. 2004 MICON, 2004.

[52] K. Kato, “Ultrawide-band/high-frequency photodetectors,” *Microwave Theory and Techniques, IEEE Transactions on*, vol. 47, no. 7, pp. 1265–1281, 1999.

[53] J. Bowers and C. J. Burrus, “Ultrawide-band long-wavelength p-i-n photodetectors,” *J Light Tech*, vol. 5, no. 10, pp. 1339–1350, 1987.

[54] J. Chazelas and B. Cabon, *Optoelectronique hyperfrequence*. 2003.

[55] J. Harari, G. Jin, J. P. Vilcot, and D. Decoster, “Theoretical study of p-i-n photodetectors' power limitations from 2.5 to 60 GHz,” *IEEE Trans. Microwave Theory Techn.*, vol. 45, no. 8, pp. 1332–1336, 1997.

[56] G. Wang, T. Tokumitsu, I. Hanawa, K. Sato, and M. Kobayashi, “Analysis of high speed p-i-n photodiode S-parameters by a novel small-signal equivalent circuit model,” *IEEE Microw. Wireless Compon. Lett.*, vol. 12, no. 10, pp. 378–380, Oct. 2002.

[57] K. Kato, A. Kozen, Y. Muramoto, Y. Itaya, T. Nagatsuma, and M. Yaita, “110-GHz, 50%-efficiency mushroom-mesa waveguide p-i-n photodiode for a 1.55-/spl mu/m wavelength,” *IEEE Photon. Technol. Lett.*, vol. 6, no. 6, pp. 719–721, Jun. 1994.

[58] I.-H. Tan, C.-K. Sun, K. S. Giboney, J. E. Bowers, E. L. Hu, B. I. Miller, and R. J. P. T. L. I. Capik, “120-GHz long-wavelength low-capacitance photodetector with an air-bridged coplanar metal waveguide,” *Photonics Technology Letters, IEEE*, vol. 7, no. 12.

[59] Y.-G. Wey, K. Giboney, J. Bowers, M. Rodwell, Silvestre, “110-GHz GaInAs/InP double heterostructure p-i-n photodetectors,” *J Light Tech*, vol. 13, no. 7, pp. 1490–1499, 1995.

[60] J. D. Schaub, R. Li, C. L. Schow, J. C. Campbell, G. W. Neudeck, and J. Denton, “Resonant-cavity-enhanced high-speed Si photodiode grown by epitaxial lateral overgrowth,” *Photonics Technology Letters, IEEE*, vol. 11, no. 12, pp. 1647–1649, 1999.

[61] M. Jutzi, M. Berroth, G. Wohl, M. Oehme, and I. E Kasper Photonics Technology Letters, “Ge-on-Si vertical incidence photodiodes with 39-GHz bandwidth,” *Photonics Technology Letters, IEEE*, vol. 17, no. 7, Jul. 2005.

[62] S. Klinger, W. Vogel, M. Berroth, M. Kaschel, M. Oehme, and E. Kasper, “Ge on Si p-i-n photodetectors with 40 GHz bandwidth,” presented at the 2008 5th IEEE International Conference on Group IV Photonics, 2008, pp. 188–190.

[63] S. Klinger, M. Berroth, and M. Kaschel, “Ge-on-Si pin photodiodes with a 3-dB bandwidth of 49 GHz,” *... photonics*, 2009.

[64] J. Osmond, L. Vivien, J.-M. Fedeli, D. Marris-Morini, P. Crozat, J.-F. Damlencourt, E. Cassan, and Y. A. P. L. Lecunff, “40 Gb/s surface-illuminated Ge-on-Si photodetectors,” *Applied Physics Letters*, vol. 95, no. 15, Oct. 2009.

[65] H. Temkin, T. P. Pearsall, J. C. Bean, R. A. Logan, and S. Luryi, “GexSi1−x strained-layer superlattice waveguide photodetectors operating near 1.3 μm,” *Applied Physics Letters*, vol. 48, no. 15, p. 963, 1986.

[66] T. Tashiro, T. Tatsumi, and M. Sugiyama, “A selective epitaxial SiGe/Si planar photodetector for Si-based OEIC's,” *Electron Devices*, 1997.

[67] O. Qasaimeh, Z. Ma, Bhattacharya, “Monolithically integrated multichannel SiGe/Si p-i-n-HBT photoreceiver arrays,” *J Light Tech*, vol. 18, no. 11, pp. 1548–1553, 2000.

[68] J.-S. Rieh, D. Klotzkin, O. Qasaimeh, L.-H. Lu, K. Yang, L. Katehi, P.

Bhattacharya, and E. Croke, “Monolithically integrated SiGe-Si PIN-HBT front-end photoreceivers,” *IEEE Photon. Technol. Lett.*, vol. 10, no. 3, pp. 415–417, 1998.

[69] J.-S. Rieh, O. Qasaimeh, D. Klotzkin, and L.-H. Lu, “Monolithically integrated SiGe/Si PIN-HBT front-end transimpedance photoreceivers,” *... Devices and Circuits ...*, 1997.

[70] M. W. Geis, S. J. Spector, M. E. Grein, R. T. Schulein, J. U. Yoon, D. M. Lennon, S. Deneault, F. Gan, F. X. Kaertner, and T. M. Lyszczarz, “CMOS-Compatible All-Si High-Speed Waveguide Photodiodes With High Responsivity in Near-Infrared Communication Band,” *IEEE Photon. Technol. Lett.*, vol. 19, no. 3, pp. 152–154.

[71] H. Zimmermann, T. Heide, and A. Ghazi, “Monolithic high-speed CMOS-photoreceiver,” *IEEE Photon. Technol. Lett.*, vol. 11, no. 2, pp. 254–256, Feb. 1999.

[72] S. M. Csutak, J. D. Schaub, W. E. Wu, R. Shimer, and J. C. Q. E. I. J. O. Campbell, “CMOS-compatible high-speed planar silicon photodiodes fabricated on SOI substrates,” *IEEE J. Quantum Electron.*, vol. 38, no. 2, pp. 193–196, 2002.

[73] S. M. Csutak, J. D. Schaub, W. E. Wu, and J. C. Campbell, “8 Gb/s CMOS compatible monolithically integrated silicon optical receiver,” *CORD Conference Proceedings*, pp. 585–586, Mar. 2002.

[74] S. M. Csutak, J. D. Schaub, W. E. Wu, R. Shimer, and J. C. Campbell, “High-speed monolithically integrated silicon photoreceivers fabricated in 130-nm CMOS technology,” *J Light Tech*, vol. 20, no. 9, pp. 1724–1729, Aug. 2002.

[75] B. Ciftcioglu, L. Zhang, and J. Zhang, “Integrated Silicon PIN Photodiodes Using Deep N-Well in a Standard 0.18-,” *Lightwave ...*, 2009.

[76] J. B. D. Soole and H. Schumacher, “InGaAs metal-semiconductor-metal photodetectors for long wavelength optical communications,” *Quantum Electronics, IEEE Journal of*, vol. 27, no. 3, pp. 737–752, 1991.

[77] L. Dobrzanski and J. K. Piotrowski, “Technology and characterization of a fast MSM photodetector,” *Microwaves*, 2000.

[78] J. S. Wang, C. G. Shih, W. H. Chang, J. R. Middleton, P. J. Apostolakis, and M. Feng, “11 GHz bandwidth optical integrated receivers using GaAs MESFET and MSM technology,” *IEEE Photon. Technol. Lett.*, vol. 5, no. 3, pp. 316–318, 1993.

[79] C. Yu, L. Mao, X. Xiao, S. Zhang, and I. '. P. O. T. 2. 1. I. S. O. Sheng Xie Integrated Circuits, “A metal-semiconductor-metal photodetector in Si-based, standard CMOS technologies,” presented at the Integrated Circuits, ISIC '09. Proceedings of the 2009 12th International Symposium on, 2009, pp. 616–618.

[80] M. Makiuchi, H. Hamaguchi, T. Kumai, M. Ito, O. Wada, and T. Sakurai, “A monolithic four-channel photoreceiver integrated on a GaAs substrate using metal-semiconductor-metal photodiodes and FET's,” *Electron Device Letters, IEEE*, vol. 6, no. 12, pp. 634–635, 1985.

[81] V. Hurm, W. Benz, M. Berroth, W. Bronner, T. Fink, M. Haupt, K. Kohler, M. Ludwig, B. Raynor, and J. Rosenzweig, “10 Gbit/s long wavelength monolithic integrated optoelectronic receiver grown on GaAs,” presented at the Indium Phosphide and Related Materials, 1996. IPRM '96., Eighth International Conference on, 1996, pp. 435–438.

[82] J. J. Morikuni, M. H. Tong, K. Nummila, J.-W. Seo, Ketterson, “A monolithic integrated optoelectronic photoreceiver using an MSM detector,” presented at the Solid-State Circuits Conference, 1993. Digest of Technical Papers. 40th ISSCC., 1993 IEEE International, 1993, pp. 178–179.

[83] P. Fay, W. Wohlmuth, C. Caneau, and I. Adesida, “18.5-GHz bandwidth

monolithic MSM/MODFET photoreceiver for 1.55-µm wavelength communication systems," *Photonics Technology Letters, IEEE*, vol. 8, no. 5, pp. 679–681, 1996.

[84] S. J. Koester, B.-U. Klepser, J. O. Chu, D. Kuchta, and K. Ismail, "1.1 GHz MSM photodiodes on relaxed Si1-xGex grown by UHV-CVD," presented at the Device Research Conference Digest, 1998. 56th Annual, 1998, pp. 60–61.

[85] Z. Lao, V. Hurm, A. Thiede, M. Berroth, M. Ludwig, H. Lienhart, M. Schlechtweg, J. Hornung, W. Bronner, K. Kohler, A. Hulsmann, G. Kaufel, and T. Jakobus, "Modulator driver and photoreceiver for 20 Gb/s optic-fiber links," *J Light Tech*, vol. 16, no. 8, pp. 1491–1497, 1998.

[86] X.-J. Li, J.-P. Ao, R. Wang, W.-J. Liu, Z.-G. Wang, Q.-M. Zeng, S.-Y. Liu, and C.-G. Liang, "An 850 nm wavelength monolithic integrated photoreceiver with a single-power-supplied transimpedance amplifier based on GaAs PHEMT technology," *Gallium Arsenide Integrated Circuit (GaAs IC) Symposium, 2001. 23rd Annual Technical Digest*, pp. 65–69, 2001.

[87] M. Y. Chen and I. Chung Cheng Chang Sensors Journal, "Integrated a ZnSe MSM Photodiode and an InGaP/GaAs HBT on a GaAs Substrate for High Sensitivity Short Wavelength Photodetector," *Sensors Journal, IEEE*, vol. 9, no. 8.

[88] S. B. Alexander, *Optical Communication Receiver Design*. SPIE Press, 1997.

[89] J.-W. SeoKetterson, "A comparative study of metal-semiconductor-metal photodetectors on GaAs with indium-tin-oxide and Ti/Au electrodes," *Photonics Technology Letters, IEEE*, vol. 4, no. 8, pp. 888–890, 1992.

[90] D. J. H. Lambert, B. Yang, T. Li, C. J. Collins, M. M. Wong, U. Chowdhury, B. S. Shelton, A. L. Beck, J. C. Campbell, and R. D. Dupuis, "High-performance back-illuminated solar-blind AlGaN metal-semiconductor-metal photodetectors," *Compound Semiconductors, 2000 IEEE International Symposium on*, pp. 525–530, 2000.

[91] J. H. Kim, H. T. Griem, and R. Friedman, "High-performance back-illuminated InGaAs/InAlAs MSM photodetector with a record responsivity of 0.96 A/W," *Photonics Technology Letters, IEEE*, vol. 4, no. 11, pp. 1241–1244, 1992.

[92] E. H. Bottcher, E. Droge, D. Bimberg, A. Umbach, and H. Engel, "Ultra-wide-band (>40 GHz) submicron InGaAs metal-semiconductor-metal photodetectors," *IEEE Photon. Technol. Lett.*, vol. 8, no. 9, pp. 1226–1228, 1996.

[93] B. J. Van Zeghbroeck and W. Patrick, "IEEE Xplore - 105-GHz bandwidth metal-semiconductor-metal photodiode," *... Device Letters*, 1988.

[94] E. Droge, E. H. Bottcher, D. Bimberg, and O. Reimann, "70 GHz InGaAs metal-semiconductor-metal photodetectors for polarisation-insensitive operation," *Electronics ...*, 1998.

[95] Y. Chen, S. Williamson, T. Brock, F. W. Smith, and A. R. Calawa, "375-GHz-bandwidth photoconductive detector," *Applied Physics Letters*, vol. 59, no. 16, pp. 1984–1986, 1991.

[96] S. Y. Chou, Y. Liu, W. Khalil, T. Y. Hsiang, and S. Alexandrou, "Ultrafast nanoscale metal-semiconductor-metal photodetectors on bulk and low-temperature grown GaAs," *Applied Physics Letters*, vol. 61, no. 7, p. 819, 1992.

[97] M. Y. Liu, S. Y. Chou, S. Alexandrou, C. C. Wang, and T. Y. Hsiang, "110 GHz Si MSM photodetectors," *IEEE Trans. Electron Devices*, vol. 40, no. 11, pp. 2145–2146, 1993.

[98] E. Chen and S. Y. Chou, "High-efficiency and high-speed silicon metal–semiconductor–metal photodetectors operating in the infrared," *Applied Physics Letters*, vol. 70, no. 6, pp. 753–755, 1997.

[99] M. Y. Liu, E. Chen, and S. Y. Chou, “140-GHz metal-semiconductor-metal photodetectors on silicon-on-insulator substrate with a scaled active layer,” *Applied Physics Letters*, vol. 65, no. 7, pp. 887–888, 1994.

[100] A. R. Hawkins, W. Wu, P. Abraham, K. Streubel, and J. E. Bowers, “High gain-bandwidth-product silicon heterointerface photodetector,” *Applied Physics Letters*, vol. 70, no. 3, pp. 303–305, 1997.

[101] A. Rochas, A. R. Pauchard, and P. A. Besse, “Low-noise silicon avalanche photodiodes fabricated in conventional CMOS technologies,” *Electron Devices*, 2002.

[102] J.-S. Youn, M.-J. Lee, K.-Y. Park, H. Rücker, and W.-Y. Choi, “7-Gb/s monolithic photoreceiver fabricated with 0.25-µm SiGe BiCMOS technology,” *IEICE Electron. Express*, vol. 7, no. 9, pp. 659–665, 2010.

[103] Hyo-Soon Kang, Myung-Jae Lee, and Woo-Young Choi, “Low-Cost Multistandard Radio-Over-Fiber Downlinks Based on CMOS-Compatible Si Avalanche Photodetectors,” *IEEE Photon. Technol. Lett.*, vol. 21, no. 7, pp. 462–464, 2009.

[104] J.-S. Youn, M.-J. Lee, K.-Y. Park, and W.-Y. Choi, “10-Gb/s 850-nm CMOS OEIC Receiver With a Silicon Avalanche Photodetector,” *IEEE J. Quantum Electron.*, vol. 48, no. 2, pp. 229–236, Feb. 2012.

[105] M.-J. Lee, H. Rücker, and W.-Y. Choi, “Effects of Guard-Ring Structures on the Performance of Silicon Avalanche Photodetectors Fabricated With Standard CMOS Technology,” *IEEE Electron Device Lett.*, vol. 33, no. 1, pp. 80–82, Jan. 2012.

[106] T. Shimotori, K. Maekita, T. Maruyama, and K. O.-E. A. C. C. O. 2. 1. Iiyama, “Characterization of APDs fabricated by 0.18 µm CMOS process in blue wavelength region,” presented at the Opto-Electronics and Communications Conference (OECC), 2012 17th, 2012.

[107] H.-S. Kang and W.-Y. Choi, “CMOS-compatible 60 GHz Harmonic Optoelectronic Mixer,” *Microwave Symposium, 2007. IEEE/MTT-S International*, pp. 233–236, 2007.

[108] K. Nishida, K. Taguchi, and Y. A. P. L. Matsumoto, “InGaAsP heterostructure avalanche photodiodes with high avalanche gain,” *Applied Physics Letters*, vol. 35, no. 3.

[109] T. Nakata, I. Watanabe, K. Makita, and T. E. L. Torikai, “InAlAs avalanche photodiodes with very thin multiplication layer of 0.1 µm for high-speed and low-voltage-operation optical receiver,” *Electron. Lett.*, vol. 36, no. 21.

[110] J. C. Campbell, A. G. Dentai, W. S. Holden, and B. L. Kasper, “High-performance avalanche photodiode with separate absorption ‘grading’ and multiplication regions,” *Electron Lett*, vol. 19, no. 20, p. 818, 1983.

[111] Ran Wei, J. C. Dries, Hongsheng Wang, M. L. Lange, G. H. Olsen, and S. R. Forrest, “Optimization of 10-Gb/s long-wavelength floating guard ring InGaAs-InP avalanche photodiodes,” *IEEE Photon. Technol. Lett.*, vol. 14, no. 7, pp. 977–979, 2002.

[112] L. E. Tarof, “Planar InP-InGaAs avalanche photodetectors with n-multiplication layer exhibiting a very high gain-bandwidth product,” *IEEE Photon. Technol. Lett.*, vol. 2, no. 9, pp. 643–646, 1990.

[113] L. E. Tarof, R. Bruce, D. G. Knight, J. Yu, H. B. Kim, and T. Baird, “Planar InP-InGaAs single-growth avalanche photodiodes with no guard rings,” *IEEE Photon. Technol. Lett.*, vol. 7, no. 11, pp. 1330–1332, Nov. 1995.

[114] I. Watanabe, T. Nakata, M. Tsuji, K. Makita, and K. Taguchi, “High-reliability and low-dark-current 10-Gb/s planar superlattice avalanche photodiodes,” *IEEE Photon. Technol. Lett.*, vol. 9, no. 12, pp. 1619–1621, Dec. 1997.

[115] I. Watanabe, T. Nakata, M. Tsuji, K. Makita, T. Torikai, and K. Taguchi, *High-Speed, High-Reliability Planar-Structure Superlattice Avalanche Photodiodes*

for 10-Gb/s Optical Receivers, vol. 18, no. 12. IEEE, 2000, pp. 2200–.

[116] K. Matsuo, M. Teich, and B. Saleh, “Noise properties and time response of the staircase avalanche photodiode,” *J Light Tech*, vol. 3, no. 6, pp. 1223–1231, 1985.

[117] F. Capasso, Won-Tien Tsang, and G. F. Williams, “Staircase solid-state photomultipliers and avalanche photodiodes with enhanced ionization rates ratio,” *IEEE Trans. Electron Devices*, vol. 30, no. 4, pp. 381–390, 1983.

[118] T. Kagawa, Y. Kawamura, and H. Iwamura, “A wide-bandwidth low-noise InGaAsP-InAlAs superlattice avalanche photodiode with a flip-chip structure for wavelengths of 1.3 and 1.55 µm,” *Quantum Electronics, IEEE Journal of*, vol. 29, no. 5, pp. 1387–1392, 1993.

[119] W. Wu, A. R. Hawkins, and J. E. O. F. C. O. 9. C. O. Bowers, “High-gain bandwidth product Si/InGaAs avalanche photodetectors,” presented at the Optical Fiber Communication. OFC 97., Conference on, 1997.

[120] T. Mitsuyu, S. Fujita, and A. Sasaki, “InGaAsP/InP wavelength-selective heterojunction phototransistors,” *IEEE Trans. Electron Devices*, vol. 31, no. 6, pp. 812–817, 1984.

[121] Z. Pei, L. Lai, H. Hwang, Y. Tseng, C. Liang, and M.-J. Tsai, “Si 1− x Ge x/Si multi-quantum well phototransistor for near-infrared operation,” *Physica E: Low-dimensional Systems and Nanostructures*, vol. 16, no. 3, pp. 554–557, 2003.

[122] T. Yin, A. Apsel, A. M. Pappu, C. Reungsinpinya, and A. Khimani, “Optical interconnects in commercial BiCMOS,” *Proceedings of SPIE*, vol. 5357, p. 1, 2004.

[123] D. Fritzsche, E. Kuphal, and R. Aulbach, “Fast response InP/InGaAsP heterojunction phototransistors,” *Electron. Lett.*, vol. 17, no. 5, pp. 178–180, 1981.

[124] S. Chandrasekhar, M. K. Hoppe, Dentai, “Demonstration of enhanced performance of an InP/InGaAs heterojunction phototransistor with a base terminal,” *Electron Device Letters, IEEE*, vol. 12, no. 10, pp. 550–552, 1991.

[125] H. R. Chen, S. W. Tan, W. T. Chen, T. S. Lin, and W. S. O. A. M. M. A. D. 2. C. O. Lour, “The Effect on Base Bias for InGaP/GaAs Heterojunction Phototransistors,” presented at the Optoelectronic and Microelectronic Materials and Devices, 2004 Conference on, 2004.

[126] S. W. Tan, H. R. Chen, W. T. Chen, M. K. Hsu, A. H. Lin, and W. S. Lour, “Characterization and Modeling of Three-Terminal Heterojunction Phototransistors Using an InGaP Layer for Passivation,” vol. 52, no. 2, pp. 204–210, Feb. 2005.

[127] Zingway Pei, C. S. Liang, L. S. Lai, Y. T. Tseng, Y. M. Hsu, P. S. Chen, S. C. Lu, M.-J. Tsai, and C. W. Liu, “A high-performance SiGe-Si multiple-quantum-well heterojunction phototransistor,” *IEEE Electron Device Lett.*, vol. 24, no. 10, pp. 643–645, 2003.

[128] A. Apsel and Z. Fu, “A 2.5 milliwatt SOS CMOS receiver for optical interconnect,” *CORD Conference Proceedings*, vol. 5, pp. V–5, May 2004.

[129] F. Moutier, “Modélisation et évaluation des Performances des Phototransistors Bipolaires à Hétérojonction SiGe/Si pour les Applications Optique-microondes Courtes Distances,” Universit´e de Marne-La-Vall´ee, 2006.

[130] J. L. Polleux, L. Paszkiewicz, A. L. Billabert, J. Salset, and C. Rumelhard, “Optimization of InP-InGaAs HPT Gain: Design of an Opto-Microwave Monolithic Amplifier,” *IEEE Trans. Microwave Theory Techn.*, vol. 52, no. 3, pp. 871–881, Mar. 2004.

[131] J.-L. Polleux, “Contribution a l'etude et a la modelisation de phototransistors bipolaires a heterojonction SiGe/Si pour les applications

opto-microondes" CONSERVATOIRE NATIONAL DES ARTS ET MÉTIERS, 2001.

[132] J. L. Polleux, F. Moutier, A. L. Billabert, C. Rumelhard, E. Sonmez, and H. Schumacher, "A strained SiGe layer heterojunction bipolar phototransistor for short-range opto-microwave applications," presented at the Microwave Photonics, 2003. MWP 2003 Proceedings. International Topical Meeting on, 2003, pp. 113–116.

[133] L. E. M. J. De Barros, A. Paolella, P. R. Herczfeld, and A. A. A. De Salles, "Noise performance of HBT as photodetector in analog fiber-optic communication link," presented at the Microwave and Optoelectronics Conference, 1997. "Linking to the Next Century." Proceedings., 1997 SBMO/IEEE MTT-S International, 1997, vol. 1, pp. 338–343.

[134] Y. Betser, D. Ritter, C. P. Liu, A. J. Seeds, and A. Madjar, "Modeling and performance of a one stage InP/GaInAs optoelectronic HBT 3-terminal mixer," presented at the Indium Phosphide and Related Materials, 1997., International Conference on, 1997, pp. 380–383.

[135] N. Chand and P. Houston, "Gain of a heterojunction bipolar phototransistor," *IEEE Trans. Electron Devices*, vol. 32, no. 3, pp. 622–627, 1985.

[136] H. Kamitsuna, K. Ishii, T. Shibata, K. Kurishima, and M. Ida, "A 43-Gb/s clock and data recovery OEIC integrating an InP-InGaAs HPT oscillator with an HBT decision circuit," *Selected Topics in Quantum Electronics, IEEE Journal of*, vol. 10, no. 4, pp. 673–678, 2004.

[137] M. D. Rosales, J. Schiellein, C. Viana, J. Polleux, and C. G. I. P. G. 2. I. 9. I. C. O. Algani, "Full area emitter SiGe phototransistor for opto-microwave circuit applications," presented at the Group IV Photonics (GFP), 2012 IEEE 9th International Conference on, 2012.

[138] S. A. Bashar and A. A. Rezazadeh, "Optically transparent ITO emitter contacts in the fabrication of InP/InGaAs HPT's," *Microwave Theory and Techniques, IEEE Transactions on*, vol. 43, no. 9, pp. 2299–2303, 1995.

[139] C. Gonzalez, M. Muller, J. L. Benchimol, M. Riet, P. Jaffre, and P. Legaud, "A 28 GHz HPT/HBT monolithically integrated photoreceiver for hybrid fibre radio distribution systems," *High Performance Electron Devices for Microwave and Optoelectronic Applications, 2000 8th IEEE International Symposium on*, Jan. 2000.

[140] A. Bilenca, J. Lasri, B. Sheinman, G. Eisenstein, and D. Ritter, "Millimeter-wave generation and digital modulation in an InGaAs-InP heterojunction phototransistor: model and experimental characterization of dynamics and noise," *J Light Tech*, vol. 19, no. 9, pp. 1340–1351, 2001.

[141] C. Gonzalez, "InP-based bipolar phototransistors for microwave photonic applications," presented at the Microwave Photonics, 2003. MWP 2003 Proceedings. International Topical Meeting on, 2003, pp. 99–104.

[142] M. D. Rosales, J. L. Polleux, and C. Algani, "Design and implementation of SiGe HPTs using an 80GHz SiGe bipolar process technology," *Group IV Photonics (GFP), 2011 8th IEEE International Conference on*, pp. 243–245, 2011.

[143] J. Campbell, A. Dentai, and C. Burrus, "InP/InGaAs heterojunction phototransistors," *...*, 1981.

[144] J. Campbell, A. Dentai, G. Qua, and J. Q. E. I. J. O. Ferguson, "Avalanche InP/InGaAs heterojunction phototransistor," *Quantum Electronics, IEEE Journal of*, vol. 19, no. 6, Jun. 1983.

[145] A. Sasaki, H. Yano, S. Fujita, and Y. L. T. J. O. Takeda, "Integrated optical devices of InGaAsP/InP heterojunction phototransistor and inner stripe light-emitting diode," *J Light Tech*, vol. 3, no. 6, Dec. 1985.

[146] H. Fukano, T. Kobayashi, Y. Takanashi, and M. Fujimoto, “High-speed InP/InGaAs heterojunction phototransistors with emitter metal reflector,” *Electron Devices Meeting, 1993. IEDM '93. Technical Digest., International*, pp. 213–216, 1993.

[147] H. Kamitsuna, “Direct Optical Injection Locking of InP/InGaAs HPT Oscillator Circuits for Millimeter-Wave Photonics and Optoelectronic Clock Recovery,” pp. 1–4, Jun. 2003.

[148] V. Magnin, J. Van de Casteele, and J. P. Vilcot, “A three-terminal edge-coupled InGaAs/InP heterojunction phototransistor for multifunction operation ,” *Microwave and …*, 1998.

[149] M. Borgarino, R. Plana, M. Fendler, and J. Vilcot, “Low frequency noise behaviour of InP/InGaAs heterojunction bipolar waveguide phototransistors,” *Solid-State …*, 2000.

[150] P. Freeman, Xiangkun Zhang, I. Vurgaftman, J. Singh, and P. Bhattacharya, “Optical control of 14 GHz MMIC oscillators based on InAlAs/InGaAs HBTs with monolithically integrated optical waveguides,” *IEEE Trans. Electron Devices*, vol. 43, no. 3, pp. 373–379, Mar. 1996.

[151] J. L. Gautier, D. Pasquet, and P. Pouvil, “Optical Effects on the Static and Dynamic Characteristics of a GaAs MESFET (Short Paper),” *IEEE Trans. Microwave Theory Techn.*, vol. 33, no. 9, pp. 819–822, Sep. 1985.

[152] L. E. M. de Barros, A. Paolella, M. Y. Frankel, M. J. Romero, P. R. Herczfeld, and A. Madjar, “Photoresponse of microwave transistors to high-frequency modulated lightwave carrier signal,” *IEEE Trans. Microwave Theory Techn.*, vol. 45, no. 8, pp. 1368–1374, 1997.

[153] R. A. Milano, P. D. Dapkus, and G. E. E. D. I. T. O. Stillman, “An analysis of the performance of heterojunction phototransistors for fiber optic communications,” *IEEE Trans. Electron Devices*, vol. 29, no. 2, 1982.

[154] T. F. Carruthers, I. N. I. Duling, O. A. Aina, M. R. Mattingly, and M. Serio, “Responses of InP/Ga0.47In0.53As/InP heterojunction bipolar transistors to 1530 and 620 nm ultrafast optical pulses,” *Applied Physics Letters*, vol. 59, no. 3, pp. 327–329, 1991.

[155] E. Suematsu and H. Ogawa, “Frequency response of HBTs as photodetectors,” *IEEE Microw. Guid. Wave Lett.*, vol. 3, no. 7, pp. 217–218, Jul. 1993.

[156] D. Wake, D. J. Newson, M. J. Harlow, and I. D. Henning, “Optically-biased, edge-coupled InP/InGaAs heterojunction phototransistors,” *Electron. Lett.*, vol. 29, no. 25, pp. 2217–2219, 1993.

[157] D. P. Prakash, D. C. Scott, H. R. Fetterman, M. Matloubian, Q. Du, and W. Wang, “Integration of polyimide waveguides with traveling-wave phototransistors,” *Photonics Technology Letters, IEEE*, vol. 9, no. 6, pp. 800–802, 1997.

[158] M. Muller, M. Riet, C. Fortin, S. Withitsoonthorn, J. d'Orgeval, and C. Gonzalez, “Millimetre-wave InP/InGaAs photo-HBT and its application to a double-stage cascode optoelectronic mixer,” *Microwave Photonics, 2002. International Topical Meeting on*, pp. 345–348, 2002.

[159] A. Leven, V. Houtsma, R. Kopf, Y. Baeyens, and Y. K. Chen, “InP-based double-heterostructure phototransistors with 135 GHz optical-gain cutoff frequency,” *Electron. Lett.*, vol. 40, no. 13, p. 833, 2004.

[160] V. E. Houtsma, A. Leven, J. Chen, J. Frackoviak, A. Tate, N. G. Weimann, and Y. K. Chen, “High Gain-Bandwidth InP waveguide Phototransistor,” presented at the Indium Phosphide and Related Materials Conference Proceedings, 2006 International Conference on, 2006, pp. 247–251.

[161] J. Schiellein, “Etude de Phototransistors bipolaires à hétérojonction InP/InGaAs pour applications d’oscillateurs photo- injectés très faible bruit

de phase," université Paris-Est, 2012.

[162] S. Chandrasekhar, J. C. Campbell, A. G. Dentai, C. H. Joyner, G. J. Qua, A. H. Gnauck, and M. D. Feuer, "Integrated InP/GaInAs heterojunction bipolar photoreceiver," *Electron. Lett.*, vol. 24, no. 23, pp. 1443–1445, Nov. 1988.

[163] H. Kamitsuna, Y. Matsuoka, S. Yamahata, and K. Kurishima, "A monolithically integrated photoreceiver realized by InP/InGaAs double-heterostructure bipolar transistor technologies for optical/microwave interaction systems," *Gallium Arsenide Integrated Circuit (GaAs IC) Symposium, 1995. Technical Digest 1995., 17th Annual IEEE*, pp. 185–188, 1995.

[164] H. Kamitsuna, Y. Matsuoka, S. Yamahata, and N. Shigekawa, "Ultrahigh-speed InP/InGaAs DHPTs for OEMMICs," *Microwave Theory and Techniques, IEEE Transactions on*, vol. 49, no. 10, pp. 1921–1925, 2001.

[165] J. Thuret, C. Gonzalez, J. L. Benchimol, M. Riet, and P. I. P. A. R. M. 1. I. 1. E. I. C. O. Berdaguer, "High-speed InP/InGaAs heterojunction phototransistor for millimetre-wave fibre radio communications," presented at the Indium Phosphide and Related Materials, 1999. IPRM. 1999 Eleventh International Conference on, 1991.

[166] J. Lasri, A. Bilenca, G. Eisenstein, D. Ritter, M. Orenstein, S. Cohen, and V. Sidorov, "Self oscillation at millimeter-wave frequencies and modulation using optoelectronic mixing in a two-heterojunction bipolar photo-transistors configuration," *Photonics Technology Letters, IEEE*, vol. 13, no. 1, pp. 67–69, 2001.

[167] C.-P. P. Liu, A. J. Seeds, and D. Wake, "Two-terminal edge-coupled InP/InGaAs heterojunction phototransistor optoelectronic mixer," *Microwave and Guided Wave Letters, IEEE*, vol. 7, no. 3, pp. 72–74, 1997.

[168] Chang-Soon Choi, Jun-Hyuk Seo, Woo-Young Choi, H. Kamitsuna, M. Ida, and K. Kurishima, "60-GHz bidirectional radio-on-fiber links based on InP-InGaAs HPT optoelectronic mixers," *IEEE Photon. Technol. Lett.*, vol. 17, no. 12, pp. 2721–2723.

[169] J. Van de Casteele, J. P. Vilcot, and J. P. Gouy, "IEEE Xplore - Electro-optical mixing in an edge-coupled GaInAs/InP heterojunction phototransistor," *Electronics …*, 1996.

[170] J.-Y. Kim, J.-H. H. Seo, W.-Y. Y. Choi, H. Kamitsuna, M. Ida, and K. Kurishima, "60 GHz radio-on-fiber downlink systems using optically injection-locked self-oscillating optoelectronic mixers based on InP/InGaAs HPTs," presented at the Optical Fiber Communication Conference, 2006 and the 2006 National Fiber Optic Engineers Conference. OFC 2006, 2006.

[171] M. Muller, M. Riet, J. L. Benchimol, C. Fortin, and C. Gonzalez, "28 and 42 GHz narrow-band InP based phototransistor mixers for hybrid fibre radio distribution systems," presented at the 2001 International Symposium on Electron Devices for Microwave and Optoelectronic Applications. EDMO 2001, 2001, pp. 249–254.

[172] J. Kim, S. Kanakaraju, W. I. J. Johnson, and C. H. Lee, "High upconversion gain optoelectronic mixer using uni-travelling carrier phototransistors," *Electron. Lett.*, vol. 48, no. 10, pp. 583–585, 2012.

[173] Y. Betser, J. Lasri, V. Sidorov, S. Cohen, D. Ritter, M. Orentstein, G. Eisentstein, A. J. Seeds, and A. M. T. A. T. I. T. O. Madjar, "An integrated heterojunction bipolar transistor cascode opto-electronic mixer," *Microwave Theory and Techniques, IEEE Transactions on*, vol. 47, no. 7, 1999.

[174] H. Kamitsuna, "A 15-GHz Direct Optical Injection-Locked MMIC Oscillator Using Photosensitive HBTs," *IEICE TRANSACTIONS on Electronics*, vol. 79, no. 1, pp. 40–45, Jan. 1996.

[175] H. Kamitsuna, T. Shibata, K. Kurishima, and M. Ida, “10- and 39-GHz-band InP/InGaAs HPT direct optical injection-locked oscillator ICs for optoelectronic clock recovery circuits,” *Microwave Symposium Digest, 2002 IEEE MTT-S International*, vol. 3, pp. 1699–1702, 2002.

[176] H. Kamitsuna, T. Shibata, K. Kurishima, and M. Ida, “Direct optical injection locking of a 96-GHz MMIC oscillator using a back-illuminated InP/InGaAs HPT,” *Microwave Photonics, 2002. International Topical Meeting on*, pp. 341–344, 2002.

[177] H. Kamitsuna, M. Ida, and K. Kurishima, “A 60-GHz-Band Optical Injection-Locked Oscillator Using a Top/Back-Illuminated InP/InGaAs HPT,” presented at the Indium Phosphide & Related Materials, 2007. IPRM '07. IEEE 19th International Conference on, 2007, pp. 538–541.

[178] K.-H. Lee, J.-Y. Kim, W.-Y. Y. Choi, H. Kamitsuna, M. Ida, and K. Kurishima, “Low-Cost Optoelectronic Self-Injection-Locked Oscillators,” *Photonics Technology Letters, IEEE*, vol. 20, no. 13, pp. 1151–1153, 2008.

[179] Y. Zhu, Q. Yang, and Q. Wang, “Resonant cavity SiGe/Si MQW heterojunction phototransistor grown on the SIMOX substrate for 1.3 μm operation,” presented at the Electronic Components and Technology Conference, 1997. Proceedings., 47th, 1997, pp. 1199–1204.

[180] Z. Pei, C. S. Liang, L. S. Lai, Y. T. Tseng, Y. M. Hsu, P. S. Chen, S. C. Lu, C. M. Liu, M.-J. Tsai, and C. W. Liu, “High efficient 850 nm and 1,310 nm multiple quantum well SiGe/Si heterojunction phototransistors with 1.25 plus GHz bandwidth (850 nm),” *Electron Devices Meeting, 2002. IEDM '02. Digest. International*, pp. 297–300, 2002.

[181] J. W. Shi, Z. Pei, Y. M. Hsu, F. Yuan, C. S. Liang, and Y. T. Tseng, “Si/SiGe Heterojunction Phototransistor,” pp. 1–4, Jul. 2003.

[182] Z. Pei, J. W. Shi, Y. M. Hsu, F. Yuan, C. S. Liang, S. C. Lu, W. Y. Hsieh, M.-J. Tsai, and C. W. Liu, “Bandwidth Enhancement in an Integratable SiGe Phototransistor by Removal of Excess Carriers,” *IEEE Electron Device Lett.*, vol. 25, no. 5, pp. 286–288, May 2004.

[183] J. Polleux, F. Moutier, A. Billabert, and C. Rumelhard, “An SiGe/Si Heterojunction Phototransistor for Opto-Microwave Applications: Modeling and first Experimental Results,” *11th GAAS Symposium*, 2003.

[184] T. Yin, A. M. Pappu, and A. B. Apsel, “Low-cost, high-efficiency, and high-speed SiGe phototransistors in commercial BiCMOS,” *Photonics Technology Letters, IEEE*, vol. 18, no. 1, pp. 55–57, 2006.

[185] M. Egels and B. Delacressonnière, “Design of an optically frequency or phase-controlled oscillator for hybrid fiber-radio LAN at 5.2 GHz,” *... and optical ...*, 2005.

[186] A. Marchlewski and H. Zimmermann, “BiCMOS phototransistors,” *Proceedings of SPIE*, vol. 7003, p. 70030J, 2008.

[187] A. B. Apsel, T. Yin, and A. M. Pappu, “Photonic VLSI for on-chip computing architectures,” *Society of Photo-Optical Instrumentation Engineers (SPIE) Conference Series*, vol. 5597, pp. 1–12, 2004.

[188] A. Apsel, A. Pappu, and T. Yin, “Merging traditional VLSI with photonics,” presented at the Lightwave Technologies in Instrumentation and Measurement Conference, 2004. Proceedings of the, 2004, pp. 91–99.

[189] J.-W. Shi, Z. Pei, F. Yuan, Y. M. Hsu, C. W. Liu, S. C. Lu, and M.-J. Tsai, “Performance enhancement of high-speed SiGe-based heterojunction phototransistor with substrate terminal,” *Applied Physics Letters*, vol. 85, no. 14, p. 2947, 2004.

[190] Z. Pei, J. W. Shi, Y. M. Hsu, F. Yuan, C. S. Liang, C. W. Liu, T. M. Pan, S. C. Lu, W. Y. Hsieh, and M.-J. Tsai, “Integratable sige phototransistor with high speed (BW = 3 GRz) and extremely-high avalanche responsivity,” presented at the

International Semiconductor Device Research Symposium, 2003, 2004, pp. 18–19.

[191] F. Yuan, J. W. Shi, Z. Pei, and C. W. Liu, “MEXTRAM Modeling of Si-SiGe HPTs,” *IEEE Trans. Electron Devices*, vol. 51, no. 6, pp. 870–876, Jun. 2004.

[192] P. Lecoy and B. Delacressonnière, “Design and realization of an optically controlled oscillator for radio over fiber at 5.2 GHz,” *Microwave Photonics, 2006. MWP '06. International Topical Meeting on*, pp. 1–4, 2006.

[193] J. P. Helme and P. A. L. T. J. O. Houston, “Analytical Modeling of Speed Response of Heterojunction Bipolar Phototransistors,” *J Light Tech*, vol. 25, no. 5, May 2007.

[194] F. Moutier, J. L. Polleux, and C. Rumelhard, “Physical and Electrical Modelling of Photocurrent Sources in an SiGe/Si Heterojunction Phototransistor.”

[195] P. Lecoy, B. Delacressonniere, and D. Pasquet, “SiGe heterojunction bipolar phototransistor for optics–microwaves interfacing,” *Int. J. Microw. Wireless Technol.*, vol. 3, no. 6, pp. 633–636, Oct. 2011.

[196] J. L. Polleux and C. Rumelhard, “Optical absorption coefficient determination and physical modelling of strained SiGe/Si photodetectors,” *High Performance Electron Devices for Microwave and Optoelectronic Applications, 2000 8th IEEE International Symposium on*, pp. 167–172, 2000.

[197] A. Gupta, S. P. Levitan, L. Selavo, and D. M. Chiarulli, “High-speed optoelectronics receivers in SiGe,” presented at the VLSI Design, 2004. Proceedings. 17th International Conference on, 2004, pp. 957–960.

[198] A. M. Pappu, T. Yin, and A. B. Apsel, “A low-voltage supply optoelectronic detector-receiver in a commercial silicon-based process,” presented at the Circuits and Systems, 2006. ISCAS 2006. Proceedings. 2006 IEEE International Symposium on, 2006.

[199] Chen, P.C.P, A. M. Pappu, and A. B. Apsel, “Monolithic Integrated SiGe Optical Receiver and Detector,” presented at the Lasers and Electro-Optics, 2007. CLEO 2007. Conference on, 2007, pp. 1–2.

[200] J. C. Campbell, “Phototransistors for lightwave communications,” *Semiconductors and semimetals*, 1985.

[201] J. N. Shive, “The Properties of Germanium Phototransistors,” *J. Opt. Soc. Am.*, vol. 43, no. 4, p. 239, 1953.

[202] W. Shockley, “Circuit Element Utilizing Semiconductive Material,” 256934725-Sep-1951.

[203] H. Kroemer, “Theory of a Wide-Gap Emitter for Transistors,” presented at the Proceedings of the IRE, 1957, vol. 45, no. 11, pp. 1535–1537.

[204] H. Kroemer, “Heterostructure bipolar transistors and integrated circuits,” presented at the Proceedings of the IEEE, 1982, vol. 70, no. 1, pp. 13–25.

[205] H. J. O. V. S. T. B. M. A. N. S. Kroemer, “Heterostructure bipolar transistors: What should we build?,” *Journal of Vacuum Science & Technology B: Microelectronics and Nanometer Structures*, vol. 1, no. 2.

[206] R. Braunstein and A. Moore, “Intrinsic optical absorption in germanium-silicon alloys,” vol. 109, no. 3, pp. 695–710, Jan. 1958.

[207] E. Kasper, H. Herzog, and H. Kibbel, “A one-dimensional SiGe superlattice grown by UHV epitaxy,” *Appl Phys A Mater Sci Process*, vol. 8, no. 3, pp. 199–205, Nov. 1975.

[208] G. L. P. S. S. D. S. T. J. M. C. S. S S Iyer, “Silicon-Germanium base heterojunction bipolar transistors by molecular beam epitaxy,” pp. 1–3, Dec. 1987.

[209] E. Kasper, I. O. E. Engineers, and I. Information service, *Properties of Strained and Relaxed Silicon Germanium*. Institution of Electrical Engineers, 1995.

[210] S. M. Sze, *Physics of Semiconductor Devices, 2nd Edition*, 2nd ed. Wiley, 1998.

[211] M. E. Levinshteĭn and S. L. Rumyantsev, *Properties of advanced semiconductor materials*. Wiley-Interscience, 2001.

[212] J. W. Matthews and A. E. Blakeslee, "Defects in epitaxial multilayers," *Journal of Crystal Growth*, vol. 27, pp. 118–125, Dec. 1974.

[213] R. People and J. C. Bean, "Calculation of critical layer thickness versus lattice mismatch for GexSi1−x/Si strained-layer heterostructures," *Applied Physics Letters*, vol. 47, no. 3, p. 322, 1985.

[214] J. C. Bean, "Silicon-based semiconductor heterostructures: column IV bandgap engineering," presented at the Proceedings of the IEEE, 1992, vol. 80, no. 4, pp. 571–587.

[215] R. People, "Physics and applications of GexSi1-x/Si strained-layer heterostructures," *Quantum Electronics, IEEE Journal of*, vol. 22, no. 9, pp. 1696–1710, 1986.

[216] D. V. Lang, R. People, J. C. Bean, and A. M. Sergent, "Measurement of the band gap of GexSi1-x/Si strained-layer heterostructures," *Applied Physics Letters*, vol. 47, no. 12, pp. 1333–1335, 1985.

[217] A. Vonsovici, L. Vescan, and R. Apetz, "Room temperature photocurrent spectroscopy of SiGe/Si pin photodiodes grown by selective epitaxy," *Electron Devices*, 1998.

[218] D. Lin, B. Schleicher, A. Trasser, and H. U.-W. I. 2. I. I. C. O. Schumacher, "A highly compact SiGe HBT differential LNA for 3.1–10.6 GHz ultra-wideband applications," presented at the Ultra-Wideband (ICUWB), 2010 IEEE International Conference on, vol. 1.

[219] G. Liu, A. Trasser, and H. Schumacher, "33–43 GHz and 66–86 GHz VCO With High Output Power in an 80 GHz," *Microwave and Wireless …*, 2010.

[220] G. Liu, A. Trasser, and H. M. T. A. T. I. T. O. Schumacher, "A 64–84-GHz PLL With Low Phase Noise in an 80-GHz SiGe HBT Technology," *Microwave Theory and Techniques, IEEE Transactions on*, vol. 60, no. 12.

[221] A. Ç. Ulusoy, G. Liu, A. Trasser, and H. Schumacher, "Hardware efficient receiver for low-cost ultra-high rate 60 GHz wireless communications," *Int. J. Microw. Wireless Technol.*, vol. 3, no. 2, pp. 121–129, Mar. 2011.

[222] P. Ashburn, *SiGe heterojunction bipolar transistors*. Wiley, 2003.

[223] M. D. Rosales, F. Duport, J. Schiellein, J.-L. Polleux, C. Algani, and C. Rumelhard, "Opto-microwave experimental mapping of SiGe/Si phototransistors at 850 nm," *Int. J. Microw. Wireless Technol.*, vol. 1, no. 6, p. 469, Jan. 2010.

[224] "Pigtailed 850nm 10Gbps MM VCSEL w/ 50/125µm Fiber," Avalon Photonics, Dec. 2004.

[225] "10 GBPS 850NM PIN + PREAMP LC ROSA PACKAGE," Finisar, Sep. 2007.

[226] C. VIANA, "TECHNOLOGICAL DEVELOPMENT AND SYSTEM INTEGRATION OF VCSELS AND SIGE HPT RECEIVERS FOR 60 GHZ LOW COST RADIO-OVER-FIBER APPLICATIONS," Université Paris-Est, 2014.

[227] O. Grimm, "Infrared-Absorption-4," Jun. 2006.

[228] R. Sridhara, S. M. Frimel, K. P. Roenker, N. Pan, and J. L. T. J. O. Elliott, "Performance enhancement of GaInP/GaAs heterojunction bipolar phototransistors using dc base bias," *J Light Tech*, vol. 16, no. 6, 1998.

[229] Chung-Kun Song, Sang-Hun Lee, Kang-Dae Kim, Jae-Hong Park, Bon-Won Koo, Do-Hyun Kim, Chang-Hee Hong, Yong-Kyu Kim, and Sung-Bum Hwang, "Optical characteristics of InGaP/GaAs HPTs," *IEEE Electron Device Lett.*, vol. 22, no. 7, pp. 315–317, 2001.

[230] J. L. Polleux, L. Paszkiewicz, J. Salset, N. Chennafi, C. Gonzalez, C. Rumelhard, and J. Thuret, "A Large-Signal Millimeter-wave InP/GaInAs Phototransistor Model: Method of Parameters Extraction and Maximum Gain Investigation,"

presented at the Microwave Conference, 1999. 29th European, 1999, vol. 1, pp. 48–51.

[231] J. Schiellein, M. Rosales, J. Polleux, F. Duport, C. Algani, C. Rumelhard, T. Merlet, N. Zerounian, M. Riet, J. Godin, and A. Scavennec, “Experimental influence of the base load effect on SiGe/Si and InGaAs/InP HPTs,” *Microwave Photonics, 2009. MWP '09. International Topical Meeting on*, pp. 1–4, 2009.

[232] J. Guillory, “Radio over Fiber for the futureHome Area Networks,” UNIVERSITY OF PARIS-EST, 2012.

[233] A. KHOUMMERI, “Circuit hyperfréquences et opto-electroniques pour réseaux domestiques haut-débit sans fil-Conception, Réalisation, Mesure-,” Jan. 2010.

Appendix I

This section will show the complete characteristics of HPT with the highest observed response at 5GHz of operation. HPT Run1 showed that the extended emitter, base and collector (xEBC) HPT has the best response when compared to the variants of the extended base collector (xBC,xBCrT,xBCrTeO) HPT. In HPT Run 2, an optical window of 20x20μm^2 in an xEBC HPT provides higher opto microwave response at low frequency (50MHz) as compared to a 10x10μm^2 xEBC HPT. However, at high frequencies of operation such as 5GHz for example, the size of xEBC HPTs greater than 20x20μm^2 show lower response due to the limitations in the transit times of the larger HPTs. The R2-10xEBC HPT exhibits the optimum opto-microwave response at 5GHz of operation, This performance is also verified in HPT Run 3 where different sized HPTs of xEBC_eO types were measured. The difference in the substrate properties of HPT Run 3 vs HPT Run 2 were important beacuse the measured responsivity of the xEBC HPTs even with etched oxide showed lower results.

In the dark DC operation, the output characteristics and the gummel properties are shown in Fig. 1(a) and (b) respectively. It show and early voltage of -5V. The current gain of the HPT has peak value of 612 and a range of 610 to 612 in the 0.65 to 0.725 Vbe or 0.114μA to 1.07μA Ib or 28.45μA to 654.5μA in terms Ic. Fig. 2(a) and (b) shows extracted results from the bias dependent frequency response measurements of the HPT. Fig. 3 shows the measured 50MHz RF gain S_{21} of the HPT as a function of the collector current. It shows that a gain of 15dB-19dB is achieve with a collector current of 2.8mA to 19mA and 17dB at 7mA .In this bias range, the -3dB cutoff frequency of the HPT is from 1.39GHz at 2.8mA with a peak at 2.1GHz at 7mA and down to 566MHz at 19mA. This biasing range correspond a range of Beta from 597 to 84. This translates to 0.775V to 975 in Vb

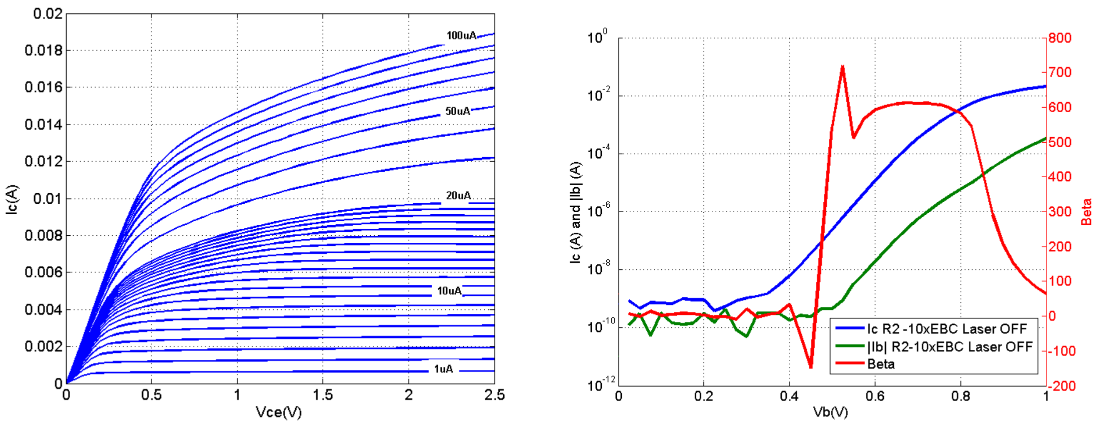

a) b)

Fig. 1

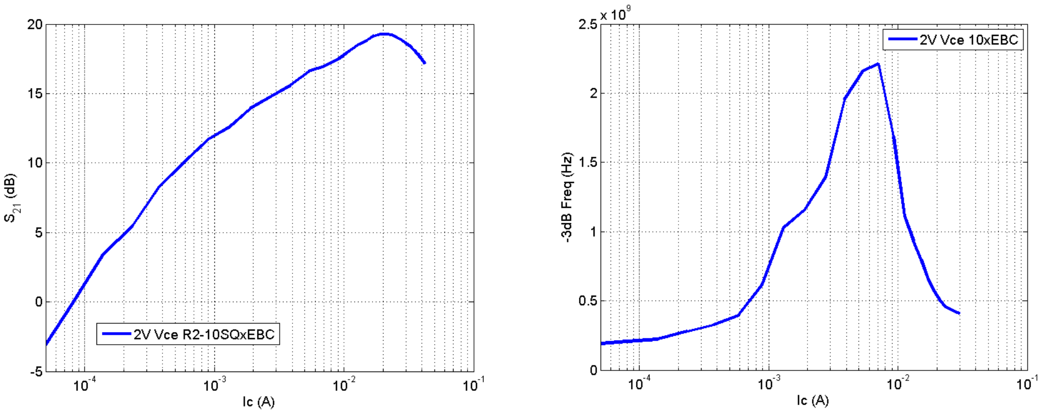

a) b)

Fig. 2

The DC responsitvity of this HPT as a function of the measured collector current shows that DC responsivity as high as 4.9A/W could be achieved with an HPT constant current bias in the base of of 1μA in the base with Vce of 2V. With a constant voltage bias in the base, a peak value of only 0.4A/W is achieved with 0.85Vbe bias in the base which is __ mA in Ic. However, a realistic collector bias in the HPT using a constant current in the base producing a 15dB RF gain is achieved with a collector bias of ____ mA. In this bias, the measured DC responsivity is ______. It is much lower than the peak DC responsivity but it is still higher than the measured DC responsivity with a constant bias in the base.

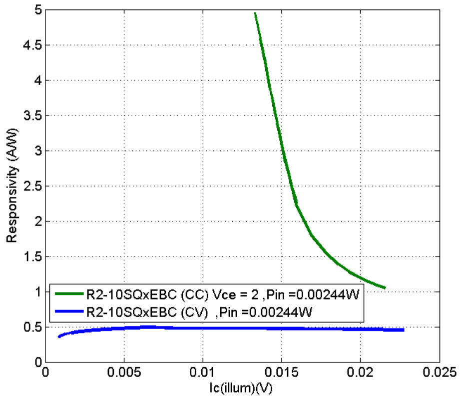

Fig. 3 Dc resonvity from gummel and icvce Vs. Ic

The opto-microwave responsitivity of the HPT as a function the frequency and Vbe bias with Vce set to 2V is presented in Fig. 4. (a) shows the 3D representation of the extracted opto-microwave responsivity. It shows that the peak responses are in the low MHz range with cutoff frequencies in the 200MHz-250 MHz range. The peak response in the 10MHz-50MHz range are seen in the bias of 2V Vce and 0.85V Vbe as can be seen in the darkest region of the top view of the responsivity plot as seen in Fig . 4(b).

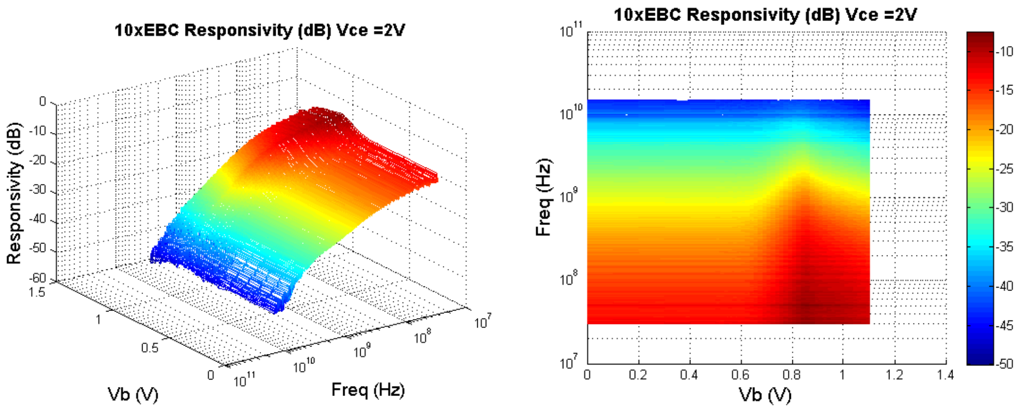

a) b)

Fig. 4

From the 3D plot of the responsivity, 2 bias point are localized, the PD mode with Vce = 2V and Vbe =0V and the HPT mode with the peak low frequency response. Fig. 5 shows the extracted responsivity (dB) as a function of frequency for both PD mode and HPT mode with a PD mode responsivity of -15dB and HPT mode responsivity of -10dB respectively. The difference between the two responses shows the GOPT of the HPT as function of frequency. This is shown in Fig.5(b) where at low frequency the Gopt is 5dB. It has peak value of 7dB at around 400-500MHz. And 1dB at 9 GHz. Fig. 6(a) show the extracted responsivity in A/W. At 10MHz, the responsivity is 0.4A/W. This extracted low frequency opto-microwave responsivity is near the 0.46 A/W extracted DC responsivity from at 0.85V Vbe bias as presented earlier in Figure 3.19(a).

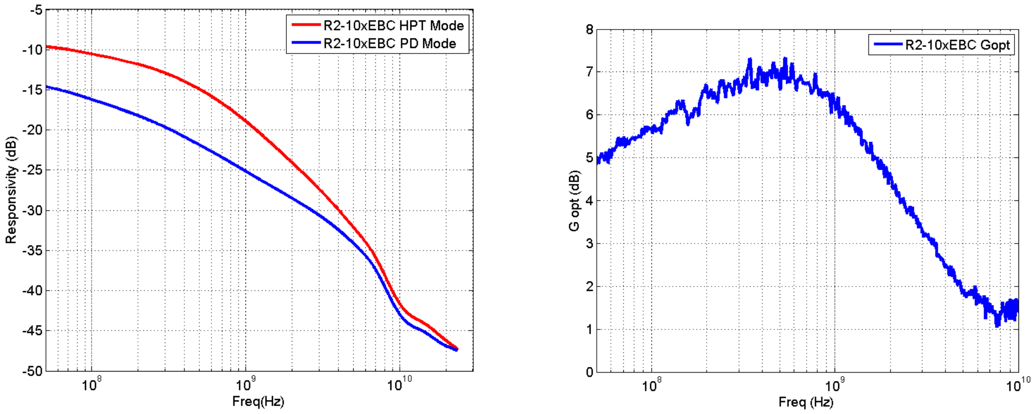

a) b)

Fig. 5 R2-10xEBC a)responsivity vs. Frequency (HPT mode and PD mode) (dB) b) GOPT vs. Frequency (dB)

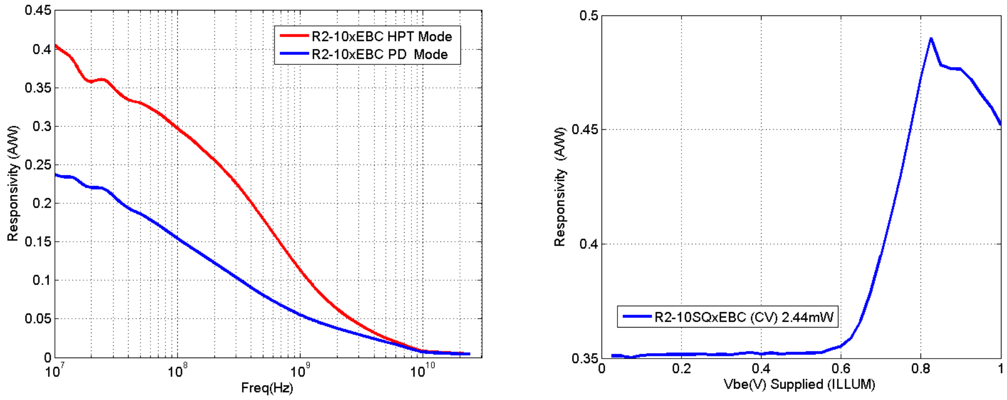

a) b)

Fig. 6 R2-10xEBC a)responsivity vs. Frequency (HPT mode and PD mode) (Linear) b) responsivity vs. Supplied Vbe

The R2-20xEBC HPT offers the better range of responsivity. It has a higher response in the low frequency operation and an adequate response in the GHz range of operation. It offers better optical coupling as supposed to a 10x10μm^2 HPT. Its size does not suffer severe penalties in the high frequency of operation as supposed to a 30x30μm^2 or 50x50μm^2 HPT. The DC, RF and optical and opto-microwave characteristics are presented in **Error! Reference source not found.**

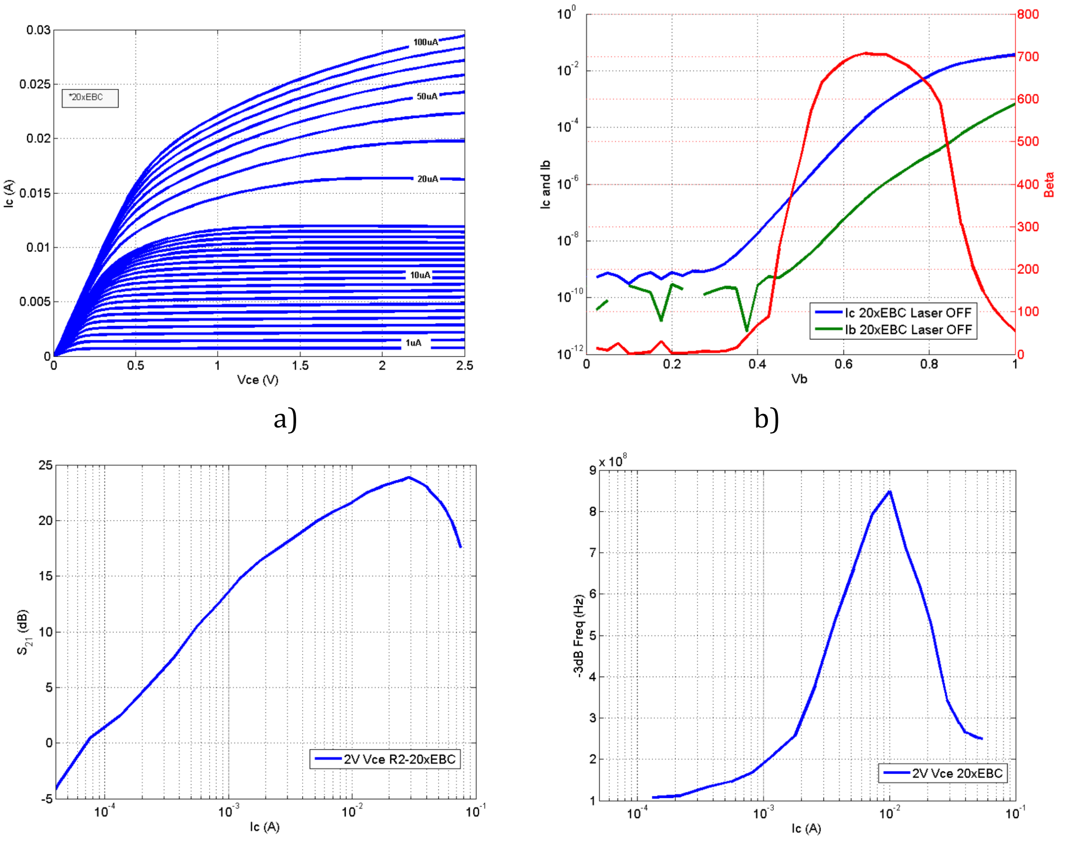

c) d)

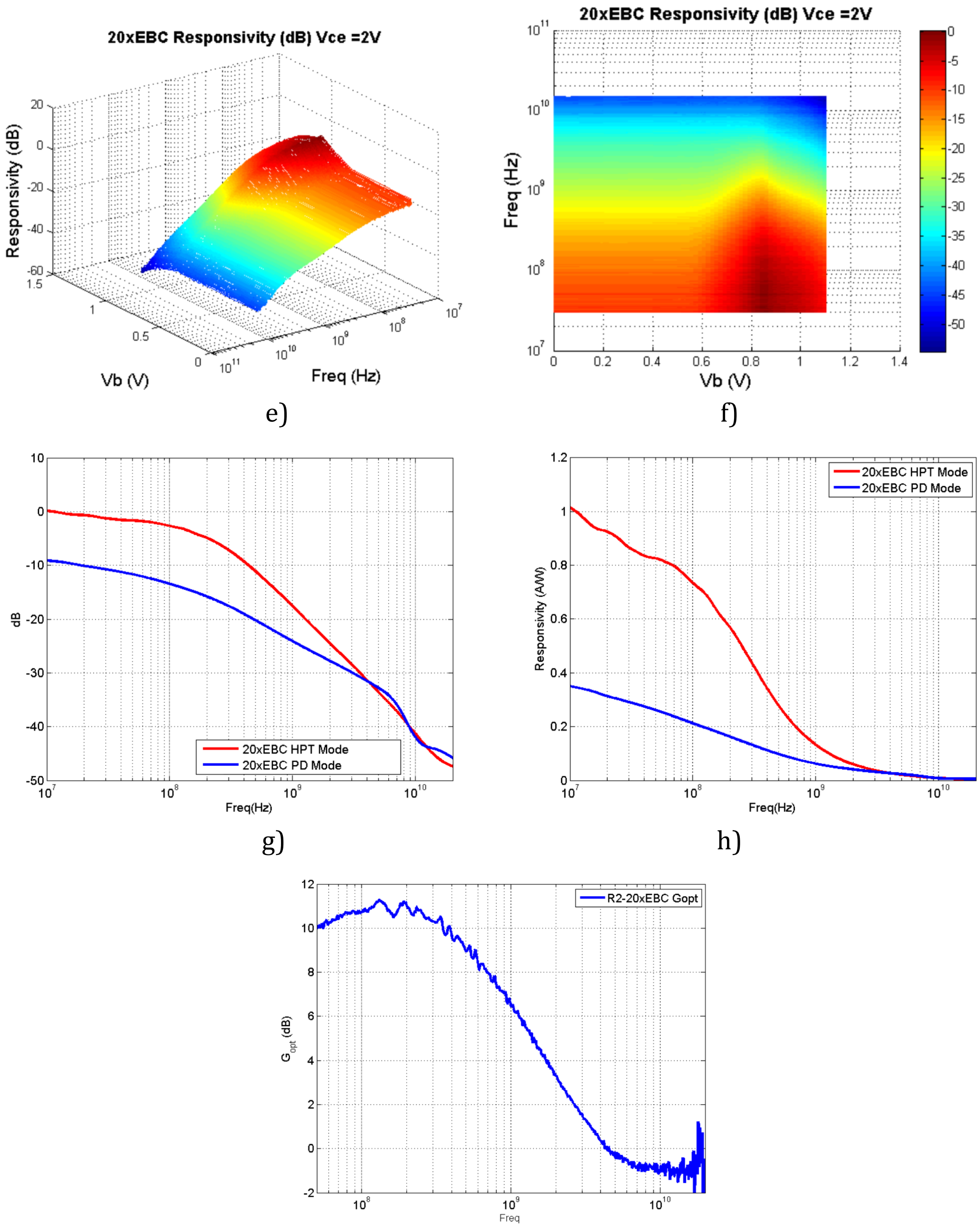

e) f)

g) h)

i)

Fig. 7 R2-20SQxEBC

Abstract

Essential to the deployment of indoor distributed antenna systems or remote antenna units is the total system cost. Using commercial of the shelf (COTS) components implies that MMF RoF systems could be easily implemented with performances meeting the requirements of different indoor wireless systems. Another aspect that will reduce implementation cost for IF-RoF systems is thru monolithic integration of the optical component with the electronics. In an IF-RoF system where high frequency electronics are needed for in both the transmitter side and the receiver side of the RoF link module, a reduction in size and power consumption are possible benefits that could be achieved if the TROF modules could be implemented using minimum integrated circuits as possible. For a remote antenna module wherein you have RF I/O and optical I/O, the received radio signal from one TROF will be transmitted in another TROF. The ROF Link serves as a tunnel and no demodulation of the received RF signal is needed. All the driver and amplifier and other circuits in IF-RoF could be implemented in a single MMIC or HF integrated circuit. Additional implementation cost is reduced if optoelectronic devices are implemented in the same MMIC. Thus, resulting to a single chip OE-MMIC. Integrating a Photodetector in the MMIC chip will produce a single chip OE-MMIC optical receiver/rf transmitter with laser driver.

This research is focused on the study of silicon germanium base heterojunction bipolar phototransistors (SiGe HPTs) implemented in an 80GHz SiGe Bipolar process technology. It's application in a radio over fiber system for home area networks are investigated. RoF for Home area networks are envisioned to implemented with a minimal system cost. Operation at 850nm is identified as a critical parameter to achieve this goal. Low cost off the shelf optical components are readily available at this wavelength. The use of multi mode fibers (MMF) as opposed to higher cost single mode fiber (SMF) is sufficient for the bandwidth requirements in a home network environment.

A monolithically integrated OE receiver chip would help in the overall reduction of the system cost by having the optical detector in the same chip with the electronic circuits. We have designed and implemented three terminal HPT (3T-HPT) structures. The two main groups of the HPT structures are: 1) HPTs with extended Base and Collector regions (xBC HPT) and 2) HPTs with extended Emitter, Base and Collector regions (xEBC HPT). Variations to improve optical coupling the though optimizations ins the vertical stack and lateral size of the HP. The measurements and characterization showed that all the structures are compatible with the process technology. The type of biasing used in the base of the HPT also influences the HPT performance. A constant current (CC) bias has higher extracted DC responsivity as compared to a constant voltage (CV) bias. The effects of the different passive base loads on the HPT responsivity are studied through simulation and measurement of fabricated circuits. The impedance presented on the base has a great influence on the HPT responsivity. The performance of an HPT as circuit component is studied using different HPT-HBT pair configurations. Tests and measurements verify that improvement in the classical transistor pair configurations are also present in the opto-microwave response of the HPT-HBT pair. Finally, SiGe hpt is used in the development of a ROSA module for a radio over fiber systems for home area network.